l'université nantes angers le mans
COMMUNAUTÉ D'UNIVERSITÉS ET ÉTABLISSEMENTS

UNIVERSITÉ DE NANTES

# Thèse de Doctorat

Zhihao SHI

*Mémoire présenté en vue de l'obtention du*
***grade de Docteur de l'Université de Nantes***
*sous le label de l'Université de Nantes Angers Le Mans*

**École doctorale : ED503 STIM**

**Discipline : Électronique et Génie Électrique**
**Spécialité : Génie Électrique**
**Unité de recherche : Institut de Recherche en Énergie Électrique de Nantes Atlantique (IREENA)**

**Soutenue le 6 Novembre 2014**

# Modeling and online aging monitoring of supercapacitors

## JURY

| | |
|---|---|
| Président : | **M. Demba DIALLO**, Professeur des Universités, LGEP, Université Paris Sud |
| Rapporteurs : | **M. Gildas BESANÇON**, Professeur des Universités, Gipsa Lab, Grenoble INP |
| | **M. Jean-Michel VINASSA**, Professeur des Universités, IMS, Institut Polytechnique de Bordeaux |
| Examinateurs : | **M. Vincent CHOQUEUSE**, Maître de conférences, LBMS, Université de Bretagne Occidentale |
| | **M. Emmanuel SCHAEFFER**, Maître de conférences, IREENA, Université de Nantes (co-encadrant) |
| | **M^me^ Tianzhen WANG**, Assistant Professor, Department of Electrical Automation, Shangai Maritime University, Chine |
| Directeur de thèse : | **M. François AUGER**, Professeur des Universités, IREENA, Université de Nantes |
| Co-directeur de thèse : | **M. Phillippe GUILLEMET**, MCF HDR, IMN, Université de Nantes |

# Acknowledgements

Working as a PhD student to finish my thesis during these three years was a precious experience for me. I would like to express my gratitude to everyone who supported me throughout my PhD period. Without their supports, I could hardly achieve what I have obtained today.

The first and the most important person that I would like to thank is my thesis director: Pr. Auger. His vast knowledge and rich experience in electrical engineering has given me an inspiring guidance on the thesis research. As a full professor, he was very busy with a lot of work as any other professor. But he was always available for helping me to solve the technical problems and showed a lot of patience to explain me everything in detail. His very series research attitude and the efficient way he manage his work have been highly influenced me as an excellent example. In front of research obstacles that I have met and when I was desperate for the problems, he was always positive and encouraged me and tried to find a solution with me together. What I have learned from him is not only useful for this thesis, but also will be very helpful for the rest of my career life.

Secondly, I would like to sincerely thank my supervisor, Dr. Schæffer. He has helped me a lot with his rich experience on modeling and diagnosis. Each time when I had questions, he showed a lot of patience to explain me and help me. He always encouraged me and tried his best every time to work with me and solve the problem together. I would like also to thank my third supervisor, Dr. Guillemet. His knowledge in supercapacitors have been guided me in the right research road and helped me a lot when analyzing the experimental results obtained in the laboratory. His affirmation on each presentation that I made gave me a lot of encouragement.

I would like to thank the jury members which gave me a lot of constructive suggestions which allow to improve the quality of my thesis and my future work.

I would like to thank the director of IREENA Pr. Machmoum, the technical supporter J. Frank and the secretary Ch. Brohan for their help in the laboratory.

I would like to express my warm thanks to all the researchers of IREENA and all my friends in France for their supports. Especially, I would like to thank Anne, Ahmed and Luc for accompanying me during the last hard months and for their huge warm supports and encouragements in laboratory and for the wonderful time that we have shared together. I would also like to thank my dear Chinese friends in

Saint-Nazaire, Wenli, Lin, the two Jian for their warm love and supports.

At last, I would like to thank my parents, my sister and Jifang Wang for their great love and encouragement from China which supported me to well finish my thesis in France.

# Résumé

Les supercondensateurs (SCs), également appelés condensateurs à double couche électrochimique (EDLC en anglais), sont de plus en plus utilisés comme dispositif de stockage d'énergie électrique, grâce à leur mécanisme de stockage purement électrostatique. Ils se composent principalement de trois parties : deux électrodes, un électrolyte et un séparateur ionique. Les électrodes sont souvent fabriquées avec des matériaux poreux qui, comme le carbone activé par exemple, ont de grandes surfaces d'échange, ce qui contribue à leur grande capacité (jusqu'à plusieurs milliers de Farads). La plage de température de fonctionnement des SCs est large, typiquement entre $-25°$ C et $+70°$ C [1]. En outre, ils ont une densité de puissance supérieure à celle des batteries, ce qui leur permet d'être chargés et déchargés beaucoup plus rapidement. Un autre avantage important des supercondensateurs par rapport à d'autres dispositifs de stockage d'énergie électrique est le grand nombre de cycles de charge-décharge qu'ils supportent comparativement à d'autres dispositifs. [2]. Toutes ces caractéristiques les rendent très attrayants dans certaines applications telles que les véhicules électriques hybrides ou les réseaux électriques autonomes multi-sources. Ils sont souvent utilisés pour répondre aux exigences de puissance de crête pendant les phases transitoires des applications, par exemple le démarrage ou l'accélération d'un moteur. Ils sont aussi souvent utilisés avec des batteries au sein de systèmes hybrides afin d'allonger la durée de vie des batteries [3] [4].

Cependant, les SCs présentent des problèmes de vieillissement causés par la dégradation des électrodes et l'électrolyte, en particulier quand ils fonctionnent dans des conditions critiques, telles que des températures ou des tensions élevées, ou des charges ou décharges excessives. Ces circonstances défavorables peuvent produire des réactions électrochimiques irréversibles, voire des gaz de décomposition ou des sous-produits organiques nocifs [5]. Les gaz et sous-produits peuvent diminuer la porosité accessible des électrodes, ce qui accélère le vieillissement des SCs et peut dégrader leur performances, en particulier leur capacité de stockage d'énergie. Le vieillissement des supercondensateurs peut donc mettre une application en défaut ou en danger. Quand le vieillissement d'un supercondensateur est trop important, la soupape de sécurité peut s'ouvrir [6] à cause de la pression interne accumulée, ce qui peut conduire à la fuite de l'électrolyte [7]. En conséquence, des événements

catastrophiques inattendus peuvent se produire tels que des incendies dans le cas d'un électrolyte organique [8]. La surveillance de l'état de santé des SCs est donc très importante afin de garantir la sécurité et la fiabilité d'un système de stockage d'énergie électrique.

Le vieillissement des SCs peut être perçu par l'évolution de leurs paramètres caractéristiques, tels que l'augmentation de leur résistance série ou la diminution de leur capacité. Une caractérisation appropriée des SCs durant leur phase d'utilisation permet donc de surveiller leur état de santé (ES). La plupart des méthodes de caractérisation d'un SC sont appliquées en laboratoire avec des conditions spécifiques telles que des profils de test particuliers [9] ou des techniques de caractérisation spécifiques telles que la spectroscopie d'impédance électrochimique (SIE) ou la voltamétrie cyclique (VC). Pour surveiller l'état de santé de SCs embarqués dans une application, par exemple dans un véhicule, toutes ces méthodes de caractérisation ont besoin d'interrompre le fonctionnement du système de stockage d'énergie et de déconnecter les SCs de leur application.

La Fig. 1 représente le principe d'un système de diagnostic sur site du vieillissement de SCs. L'objectif de cette thèse est de concevoir un tel système surveillance en ligne du vieillissement de SCs (comme celui mis en évidence dans le cadre en pointillés rouges sur la Fig. 1.) avec un faible coût. Ce système pourrait être embarqué dans une application industrielle de stockage d'énergie électrique. Il est réalisé en utilisant des observateurs d'état qui permettent d'estimer en temps réel les paramètres des modèles dynamiques caractéristiques des SCs. Pour étudier le vieillissement des SCs, une expérience de vieillissement calendaire accéléré a été réalisée sur des SCs fabriqués en série par Nichicon (type UM105) avec une capacité nominale de $1$ F et une tension maximale de $2.7$ V. Pour obtenir ce vieillissement accéléré, plusieurs lots de SCs ont été placés pendant $10$ semaines dans une enceinte climatique à $60°$ C avec une tension de maintien de $0$ V ou de $2,5$ V (fournie par une source de tension). La température et les tensions ont été choisies afin de ne pas vieillir les SCs en dehors de la plage d'utilisation typique des applications industrielles.

Pour observer le vieillissement d'un SC grâce à l'évolution de ses paramètres, la caractérisation hors ligne obtenue à l'aide des techniques de laboratoire peut être considérée comme un moyen fiable. Le premier chapitre de cette thèse est consacré à l'observation du vieillissement des SCs testés par des méthodes de caractérisation hors ligne et à la proposition d'indicateurs fiables pour la surveillance hors ligne du vieillissement. Cette étude va fournir une référence qui sera ensuite utilisée pour valider les résultats de la surveillance en ligne du vieillissement présentés dans le troisième chapitre. Tout d'abord, un aperçu des méthodes existantes de caractérisation hors ligne dans les domaines temporel et fréquentiel est présenté, et plusieurs techniques de caractérisation utilisées dans cette thèse, telles que la

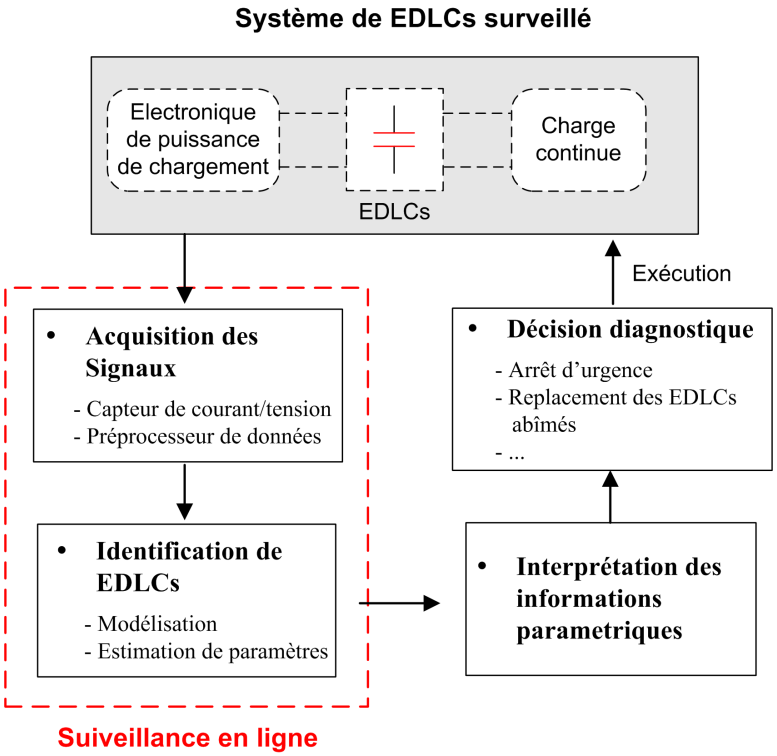


Figure 1: Système de diagnostique du vieillissement de SCs.

spectroscopie d'impédance électrochimique (SIE) ou la voltamétrie cyclique sont brièvement présentés. Les différents paramètres physiques des SCs sont définis et leurs expressions de calcul sont établies. Afin d'évaluer la qualité de ces paramètres, leur incertitude de mesure est utilisée et leur calcul est établi pour chaque paramètre. Enfin, des résultats expérimentaux ont permis de déterminer pour un SC neuf ses paramètres caractéristiques et l'incertitude de chaque paramètre, puis l'évolution des paramètres au cours de l'expérience de vieillissement accéléré. Les résultats ont montré que pour les SCs utilisés, les capacités intégrales et différentielles n'ont que légèrement diminué, tandis que les résistances séries et dynamiques présentent des augmentations importantes au cours du vieillissement et peuvent donc être utilisées comme de bons indicateurs pour la surveillance du vieillissement. Le rendement énergétique peut également constituer un indicateur fiable pour la surveillance du vieillissement des SCs testés grâce à sa diminution significative au cours du vieillissement et à son caractère indépendant de la tension.

Puisque l'objectif de cette thèse est de concevoir des systèmes de surveillance en ligne du vieillissement des SCs par l'observation sur leur site d'utilisation de l'évolution de leurs paramètres, le cœur de cette thèse est donc une identification des SCs basée sur un modèle dynamique à paramètres localisés. Différents modèles peuvent conduire à des décisions de diagnostic différentes donc le choix du modèle est très important pour la qualité du diagnostic en ligne du vieillissement des SCs. Dans ce mémoire, les modèles considérés sont des modèles de connais-

sance déduits des phénomènes physiques qui se produisent au sein des SCs, avec des paramètres caractéristiques de ces phénomènes. Ces modèles correspondent à des circuits électriques particuliers. L'objectif du deuxième chapitre de cette thèse est de proposer une méthodologie permettant de comparer différents modèles et de déterminer celui qui présente les meilleures potentialités de diagnostic pour des conditions d'utilisation données. Le premier paragraphe de ce chapitre présente plusieurs modèles de SCs qui ont déjà fait l'objet de publications. Certains modèles ont des structures très simples avec peu de paramètres à identifier, comme le modèle RRC du premier-ordre, tandis que d'autres, comme le modèle de ligne de transmission, sont plus complexes et comportent plus de paramètres, mais se rapprochent davantage du comportement réel des SCs. Ainsi, lors du choix d'une structure de modèle pour le diagnostic de vieillissement, il faut tenir compte à la fois de la complexité et de la conformité du modèle. Dans le paragraphe suivant, trois critères, l'erreur de sortie, l'incertitude des paramètres et la capacité de diagnostic du vieillissement, sont proposés pour choisir un "bon" modèle de SC. Plusieurs modèles concernant la dépendance en tension des capacités, la redistribution des charges et l'effet de ligne de transmission, ont été comparés grâce aux valeurs numériques de ces trois critères. Le modèle de ligne de transmission du second-ordre associé à une branche qui représente la redistribution des charges apparait alors comme un modèle approprié pour la surveillance en ligne du vieillissement des SCs testés dans cette thèse.

Le troisième chapitre est dédié à la conception d'observateurs d'état basés sur des modèles dynamiques à paramètres localisés pour surveiller sur leur site d'utilisation et en ligne le vieillissement de supercondensateurs. La stratégie de surveillance en ligne proposée dans cette thèse (représentée sur la Fig. 2.) consiste à utiliser les résultats fournis par un observateur à la fin de la phase de charge d'un SC. De cette manière, le système de surveillance ne perturbe pas la phase de décharge (donc de consommation de l'énergie par le "client") et les signaux de courant et de tension peuvent être rendus suffisamment excitants pendant la phase de charge afin d'obtenir des estimations précises des paramètres. Ce chapitre commence par un aperçu des méthodes existantes de surveillance en ligne du vieillissement des SCs. Ensuite, les estimateurs de l'état de santé (ES) et de l'état de charge (EC) d'un SC sont définis et la stratégie de surveillance du vieillissement en ligne est expliquée. Après cela, les principes conduisant à la conception d'observateurs linéaires et non linéaires basés sur le filtrage de Kalman et sur les observateurs de Luenberger sont rappelés. Les observateurs d'état conçus dans cette thèse sont basés sur deux modèles. Le premier est un modèle simple RRC avec trois paramètres, la résistance série, la capacité et la résistance parallèle. Le second est un modèle de ligne de transmission (TL) du quatrième-ordre qui est plus sophistiqué et plus précis. Mais il comporte cinq paramètres : la résistance série, la résistance dynamique, la ré-

sistance parallèle, la capacité et le coefficient de sensibilité en tension. Deux types d'observateurs, un filtre de Kalman étendu (FKE) et des observateurs interconnectés (OI) sont d'abord conçus en se basant sur le modèle RRC. Puis un filtre de Kalman étendu (FKE) et des filtres de Kalman tressés (FKT) sont conçus en se basant sur le deuxième modèle. Les résultats des simulations ont permis de vérifier les bonnes performances des deux observateurs dans chaque cas. Par rapport au FKE, les OI pour le modèle RRC et les FKT pour le modèle TL ont un coût de calcul plus faible et donc peuvent être plus intéressants dans une application industrielle. Ensuite, les observateurs conçus ont été appliqués à des SCs parvenus à différents stades du vieillissement calendaire accéléré, pour vérifier qu'ils permettent de percevoir les évolutions des paramètres au cours du vieillissement. Les résultats obtenus sont en accord avec ceux obtenus par la caractérisation hors ligne et présentés dans le premier chapitre, ce qui constitue une preuve de la validité des observateurs d'état proposés. Enfin, quelques exemples de calcul de l'état de santé sont donnés, permettant de connaître en temps réel l'ES de SCs embarqués dans une application industrielle.

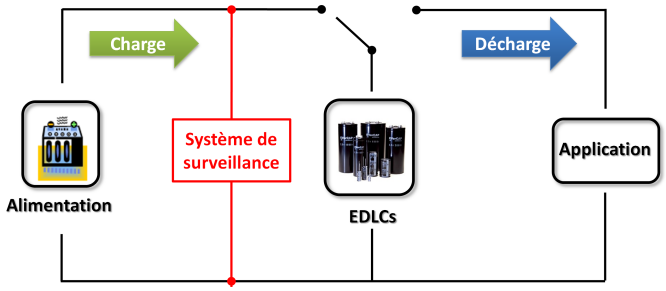


Figure 2: Système de surveillance du vieillissement de SCs.

Dans cette thèse, des systèmes de surveillance de vieillissement de SCs en ligne ont été conçus avec succès. Mais il y a encore de grandes possibilités d'améliorer et de continuer ce travail dans le futur. Parmi les perspectives envisageables, on peut citer les suivantes :

- Des observateurs d'état pourraient être conçus en s'appuyant sur le modèle considéré au chapitre 2 comme le plus approprié pour le diagnostic en ligne du vieillissement des SCs testés, afin de savoir si les résultats sont réellement meilleurs.
- Un modèle plus précis qui prend en considération l'influence de la température pourrait être développé et utilisé pour la surveillance en ligne du vieillissement de SCs.
- Les mêmes observateurs d'état basés sur des modèles dynamiques pourraient être appliqués à d'autres types SCs afin de vérifier sur un plus grand nombre de cas les performances des observateurs conçus et des indicateurs de l'état de santé.

- La mise en œuvre du système de surveillance en ligne du vieillissement conçu pourrait être réalisée sur une carte de développement à base de microcontrôleur à la place de Matlab/Simulink.
- Une expérience de vieillissement cyclique accéléré pourrait être considérée à la place de l'expérience de vieillissement calendaire pour vérifier les performances du système de surveillance du vieillissement conçu.

# Introduction

## Introduction to supercapacitors

Supercapacitors are known by different names such as electrochemical capacitors or ultracapacitors. The double-layer concept of the supercapacitors was firstly described by Hermann von Helmholtz, a German physicist, in 1853 [1]. Nowadays, supercapacitors with capacitance values in the range of thousands of farads are commercially available, thus making them a promising energy storage device and gaining increasing interest not only in their traditional field of application (electronics) but also in other sectors such as green power generation and transportation.

According to the different operation mechanisms, the supercapacitors can be divided into three general classes: electric double-layer capacitors (EDLCs), pseudocapacitors and hybrid capacitors. The EDLCs are non-faradaic (electrostatic) because there are no chemical reactions. The operation of pseudocapacitors is a faradaic process which involves the transfer of charge between electrodes and electrolyte such as oxidation-reduction reactions. The hybrid capacitors are a combination of the two, including both faradaic and electrostatic processes [10]. The supercapacitors studied in this thesis are EDLCs, but the designed methodology of monitoring systems presented in this thesis could be applied to other kinds of supercapacitors.

### Construction and operating principle

An EDLC consists of three main parts: two electrodes, an ionic electrolyte and an separator. These three parts are packed with two current collectors, some sealant, a shell and two tabs, and then an EDLC is produced [11]. The electrodes are immersed in the electrolyte and a separator is placed in the electrolyte between the electrodes.

- *The electrodes*

  The two electrodes of a supercapacitor can be made of various kinds of materials such as carbon, metal-oxides and conductive polymers. Activated carbon is one of the most widely used materials in EDLCs thanks to the accessibility, easy process ability, relatively low cost, non-toxicity, high chemical stability

and wide temperature range [11]. The activated carbon is a high surface area material with a huge quantity of pores. Fig. 3 is a SEM (scanning electron microscopy) view of the electrode of a Nichicon EDLC (UM series, 2.7 V/1 F) with activated carbon as electrode material. This SEM view clearly shows the porous feature of the activated carbon electrode. The capacitance $C$ of the EDLC is considered to be proportional to the surface area $A$ according to the following simple equation [1] [2]:

$$C = A\kappa/d \tag{1}$$

where $\kappa$ is the permittivity of the dielectric medium (electrolyte) and $d$ is the thickness of the double-layer. The high surface area of the special electrode material contributes to the high capacitance of the EDLCs.

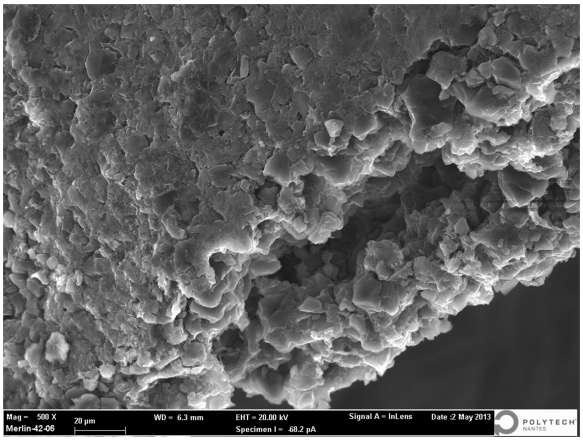


Figure 3: SEM view of the electrode of a Nichicon EDLC (UM series, 2.7 V/1 F).

– *The electrolyte*

The electrolyte used in EDLCs contains free ionic charges. The choice of the electrolyte of the EDLCs is very important because it is closely related to the energy density and power density of the EDLCs. The voltage of the EDLCs that can be attained depends on the breakdown voltage of the electrolyte and influences the energy density [12]. Each kind of electrolyte has a resistances which depends on the electrolyte conductivity. This resistance limits the power density of the EDLCs. The electrolyte of an EDLC can be an organic electrolyte, using the solvents such as acetonitrile and propylene carbonate, or an aqueous electrolyte, such as $\mathrm{H_sSO_4}$ and $\mathrm{KOH}$ aqueous solution [13]. Organic electrolytes are able to provide voltages as high as $3.5$ V, while aqueous electrolytes, have much lower breakdown voltages, typically $1$ V [12] [2]. On the other hand, aqueous electrolytes have a lower resistance, probably due to a higher ionic concentration and a smaller ionic radius [13]. For commercial EDLCs, organic electrolytes are the most commonly used [12].

– *The separator*

The separator is used to avoid the electrical contact of the electrodes surfaces. It acts as an electronic insulator but it allows the ionic charge transport [12]. Therefore, the separator with a high electronic resistance, a high ionic conductance and a low thickness could be a good choice for a competitive EDLC [12] [14]. The EDLCs with organic electrolyte often use polymer or paper separators while the glass fiber or ceramic separators are usually used for aqueous electrolyte [14].

The EDLCs work on the principle of the double electric charge layer effect at the interface of the electrodes and electrolyte. The energy storage of an EDLC is a non Faradaic process because there are only ions movements without chemical reactions between the electrolyte solution and the electrode [1]. Fig. 4 shows the energy storage principle of EDLCs with porous electrodes. When a bias voltage is applied to an EDLC, positive charges at the internal surface of one electrode attract anions from the electrolyte to keep local electro neutrality at electrode-electrolyte interface [11]. The negative charges at the other electrode force the cations to move to the negative electrode surface [15]. Thus, the cations and anions are separated and two electric charge layers are formed at the interfaces of the electrolyte and each electrode. These two layers capacitances form the overall capacitance of an EDLC [16].

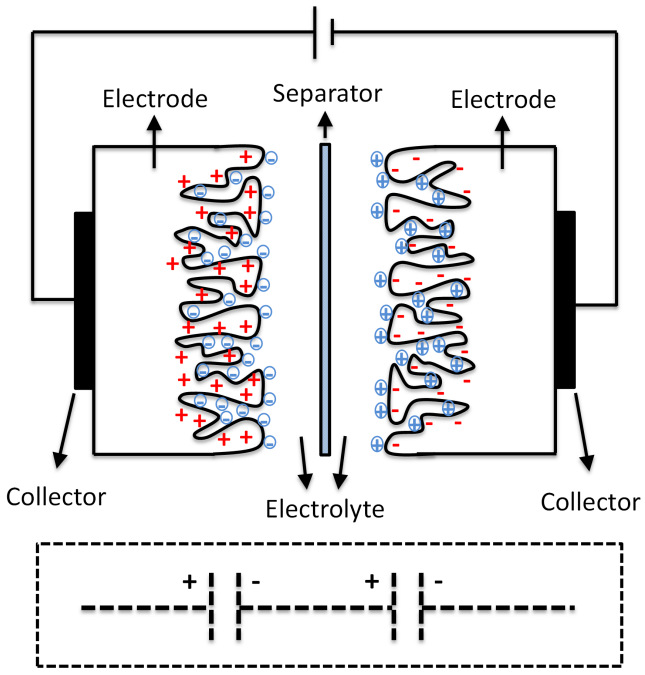


Figure 4: Operating principle of EDLCs.

**Advantages and challenges**

The "Ragone plot" shown in Fig. 5 is used for the performance comparison of various kinds of energy storage devices such as conventional capacitors, supercapacitors and batteries. The conventional capacitors may reach a power density of more than $10^6$ W/kg, but their possible energy density is extremely low compared to other energy storage devices [2]. On the other hand, the batteries and fuel cells have quite large energy density but with a very low power density. The supercapacitors fill the gap between the conventional capacitors and the batteries with improved performances in terms of power density compared to batteries and fuel cells and in terms of energy density compared to conventional capacitors.

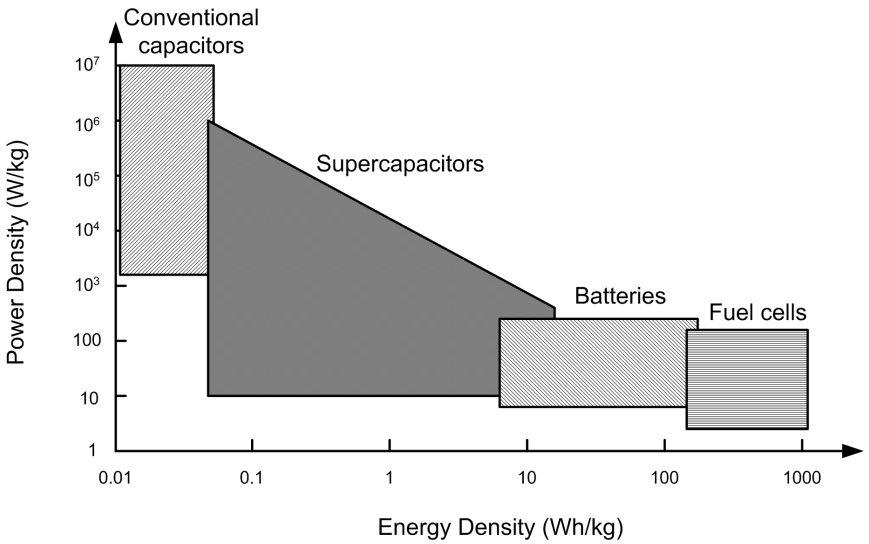


Figure 5: Ragone plot of various energy storage devices [2].

Table 1 summarizes some important properties including the power density and energy density of conventional capacitors, supercapacitors and lithium ion batteries. It can be seen from this table that the energy density of the supercapacitors is 10 times larger than that of the conventional electrostatic capacitors.

As we all known, batteries are today the most common electrical energy storage device, owing to their strong energy storage capability with a small volume and weight. However, they suffer from a slow power delivery and a short cycle life which can be clearly revealed from the corresponding data of the lithium ion batteries in Table 1. Compared to batteries, supercapacitors have shorter charge/discharge time, longer cycle life and higher cycle efficiency [17] [14] [11] [18]. Thanks to the relative high power density, the charging/discharging of a supercapacitor is of the order of a few seconds or less which is much faster than a battery. Supercapacitors have a much longer cycle life than batteries because of their different energy storage mechanisms. Batteries use a chemical process to store energy which can easily cause the degradation of the electrodes and electrolytes and the cycle life is

hence quite short. Unlikely, supercapacitors such as EDLCs, store energy through the ions separation and adsorption in which case there are no chemical reactions between the electrodes and electrolyte [1]. This important property of EDLCs contributes to their long cycle life. Another advantage of supercapacitors over batteries is the safety. Supercapacitors are much safer than batteries [13] because the fast aging of batteries may cause catastrophic events such as a fire caused by a thermal runaway [18]. Besides, supercapacitors have a wide operating temperature range, typically, $-40^{\circ}$ C to $+70^{\circ}$ C [13].

Table 1: Comparison of some properties of conventional capacitors, supercapacitors and lithium-ion batteries [17] [14] [11] [18].

| | **Conventional capacitors** | **Supercapacitors** | **Lithium ion batteries** |
|---|---|---|---|
| Charge/discharge time | $10^{-3} - 10^{-6}$ s | $0.3 - 30$ s | $3 - 5$ mins |
| Energy density (Wh/kg) | $< 0.1$ | $1 - 10$ | $70 - 100$ |
| Power density (W/kg) | $> 10000$ | $5000 - 10000$ | $500 - 1000$ |
| Cycle life | $> 500000$ | $> 500000$ | $< 5000$ |
| Cycle efficiency (%) | $> 95$ | $75 - 95$ | $50 - 90$ |

On the other hand, supercapacitors still need to improve their performances. One of the major disadvantages is the significantly low energy density caused by the low operating voltage, generally $1 - 3$ V per cell. For most applications, this low voltage is not high enough to meet the requirements. The solution used in practice is to connect single supercapacitor cells in series and in parallel to form supercapacitor modules which have a higher voltage. Another obvious disadvantage is the high self-discharge rate. The voltage of a supercapacitor decreases about $10\% - 40\%$ per day which could be a big obstacle to their practical use [13]. The high cost of supercapcitors is another disadvantage compared to batteries. The cost of using a lithium ion battery is $\$1 - 2$ per Wh while for a supercapacitor, the cost is up to $\$10 - 20$ per Wh [18]. Therefore, this high cost is still a major challenge for the supercapacitors to be popularized in commercial products [13]. However, the aging of the supercapacitors is much slower than the batteries which means that the batteries need to be replaced more frequently than the supercapacitors when they are used in an energy storage application for a long time. Thus, the cost of the supercapacitors during a long period, for example 10 years, may not necessarily be more expensive than the cost of batteries [19]. This is also an important point that should be considered when using supercapactiors or batteries in an application.

## Applications

Because of some significant advantages compared to other storage devices, the supercapacitors are rapidly developing and their applications range is quite wide which includes consumer electronics, traction, automotive and industry [20].

First of all, the supercapacitors can be used as main power sources for the applications which require short charging time or power for short time periods, such as toys, emergency flashlights [20]. They are also used as memory backup to replace the batteries in more and more products such as computers and mobile phones [13]. Because of their high power density, the supercapacitors are often used to provide bridge power in the cases where the standby power generation equipment is not instantaneously available. For example, in the application of a stand-alone fuel cell system, when the fuel cell cannot provide fast enough the required power to the load, the supercapacitors can be used as a "bridge" across the transients [21].

In most applications, the supercapacitors are used as a secondary energy source. The primary energy source such as generators, turbines and fuel cells provide the average power to the load. But these primary energy sources may fail to meet the peak power demand in very short time periods due to their limitations such as the low power density or the poor transient response. In this case, using the supercapacitors to store energy from the primary energy sources and to deliver the stored energy to the load as a secondary energy source whenever peak demand occurs for a short period, can significantly improve the performance of the system [17]. One interesting application is in the field of hybrid vehicles [22] [23] [24]. The peak power is always required when starting the electrical drives or accelerating the vehicles where the supercapacitors can be used to meet such a power requirement. Also the energy generated by the regenerative braking in a very short period can be stored by the supercapacitors. Another interesting application is the area of hybrid renewable energy systems such as PV system or wind energy system. In [25], the supercapactiors are combined with wind and fuel cell for sustained power generation in order to meet the load demand above the maximum power available from the FC system for short durations. In [26], supercapacitors are used as an auxiliary source for supplying the deficiency power from the PV and the FC. The most widely used energy storage device, the batteries, are less efficient when there is a peak power of load and the frequent charging and discharging may rapidly reduce their lifetimes. Therefore, the supercapacitors are also used together with the batteries as energy storage devices in order to meet the peak power demand and lengthen the life of the batteries [27] [28] [29] [24].

### Aging of supercapacitors

Although the EDLC is a purely electrostatic energy storage device which brings the EDLC a long cycle life, the aging problem is also unavoidable. With the use of EDLCs, especially under some critical conditions such as high temperature or over charge/discharge, irreversible electrochemical process can occur which may accelerate their aging [30]. Several studies have found that the electrolyte decomposes during the electrochemical process and thus creates decomposition gases such as CO, $H_2$ and related organic by-products [31] [5] [30]. For example, Azais et al. analyzed the positive and negative electrodes by X-ray photoelectron spectroscopy (XPS) and nuclear magnetic resonance (NMR) after the aging of EDLCs. The decomposition of the electrolyte has been observed on the electrode materials (i.e. activated carbon) [5]. The productions of this decomposition are produced on the surface of the electrode substrate and can block some pores of the porous materials such as the activated carbons. The decrease of the accessible porosity of the electrode leads to the deterioration of the electrodes and thus an increase of the series resistance [30]. Furthermore, the accessible surface area of the electrode decreases and thus results in a reduction of the capacitance. Therefore, the energy storage capability can be also decreased.

The aging of the supercapacitors may cause their failure and unsafe uses. When a supercapacitor is too much aged, the safety valve may open [6] due to the internal pressure built-up that can lead to an electrolyte leakage [7]. As a consequence, unexpected catastrophic events such as fire accidents may occur in case of organic electrolyte use [8].

## Objective of the thesis

Since the aging of the supercapacitors may cause failure and security problems for an energy storage system, it is hence very important to be able to monitor the state of health of the supercapacitors embedded in an application. Most of the existing methods to observe the supercapacitors aging are operated in laboratories with some specific conditions such as some particular testing profiles [32] [33] or specified measurement devices [34] [35], for example an impedance analyzer. To monitor the state of health of the supercapacitors embedded in an application, for example in an electrical vehicle, all of these offline methods require to interrupt the function of the energy storage system and to remove the supercapacitors from their application.

The global objective of this thesis is to design an online aging monitoring system (as the one highlighted in the red dashed box in Fig. 6) in order to maintain the proper function of the EDLCs. The online monitoring subsystem consists of the

signal acquisition and the identification of EDLCs. Firstly, the physical signals, such as voltage and current of EDLCs during their use (charging/discharging) in an application, are obtained by some embedded physical sensors. To get the useful information from these signals, the noisy raw data often need to be preprocessed (for example, filtering the signals in a required frequency band). Then, these processed signals are used for the EDLCs' identification. Since the EDLCs' aging can be revealed from their parameters evolution, for example the increase of the equivalent series resistance and the decrease of the capacitance [36], the aging monitoring problem can be converted to the EDLCs' identification.

Afterwards, the monitoring system using some online identification methods such as extended Kalman filters, provides the parameter estimations during the use of the EDLCs. With this information, a diagnosis can be made, for example, the aging degree of the EDLC or the determination of whether the EDLC has a failure, etc. According to the diagnostic conclusion, an executive decision is made to maintain the safety and reliability of the EDLC energy storage system. For example, the system can be stopped immediately if a significant default is detected or the worn EDLCs can be replaced by new ones if they are considered as aged enough.

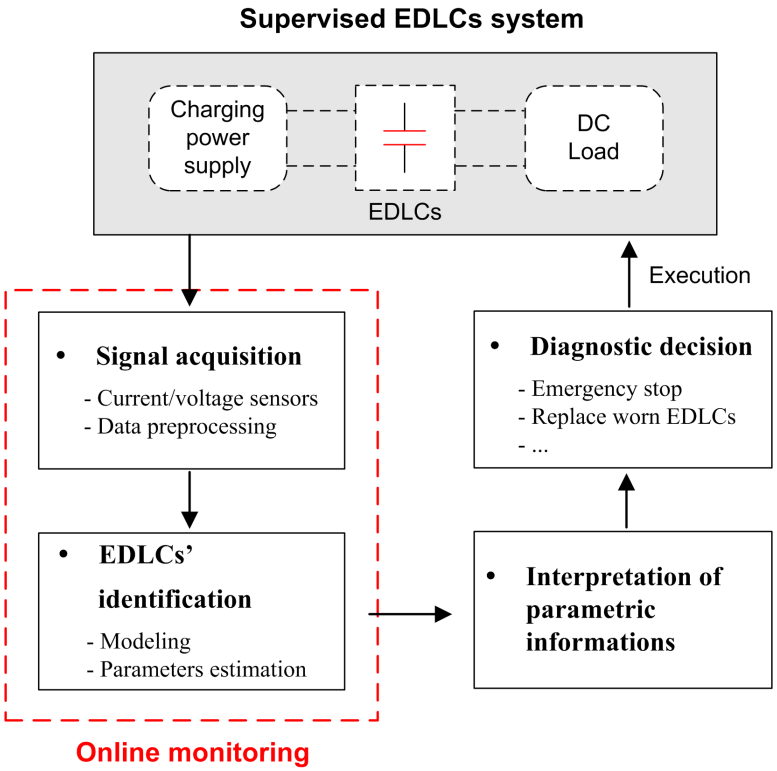


Figure 6: EDLCs aging diagnosis system.

The particular objectives of this thesis can be described as:

- To design an experimental setup allowing to carry out accelerated calendar aging on the chosen type of EDLCs with different levels of floating voltages

(0 V and 2.5 V) at a high temperature (60° C).

- To study the aging of the chosen EDLCs by using offline characterization methods and to analyze the characterization results.

- To select the most appropriate lumped model of EDLCs for the aim of online aging monitoring.

- To design EDLCs aging monitoring systems based on real-time state observers (Kalman filters, interconnected observers, etc.) that can be used in situ to observe the parameters evolution of the EDLCs during their aging process and to propose potential industrial aging indicators.

- To experimentally validate the designed systems by comparing the results obtained by online observers and by offline methods.

## Outline of the thesis

The content of this thesis is distributed through three chapters:

- Chapter 1 starts with a review of several popular characterization methods operated offline in laboratories. Different physical parameters of EDLCs are defined and estimated by using offline methods. The parameter uncertainty is proposed to be used to assess the quality of the parameter estimations. Experimental results are presented and analyzed for the fresh EDLCs. At last, the same characterization methods are applied to the EDLCs at different aging levels during an accelerated calendar aging experiment and the parameters evolution of the EDLCs during this aging process is presented.

- Chapter 2 is dedicated to look for a good model of EDLCs that could be used for online aging monitoring. A review of several classic and popular EDLC models are presented at first. To find the best trade-off between the model complexity and performance, three criteria are proposed to select a good model. Implementation methods of these criteria are presented based on geometric study of the hyper-surface of the output error energy. Then, several models are compared and analyzed according to the numerical values of the proposed criteria. At last, an "appropriate" model of the tested kind of EDLCs is suggested to be used for online aging monitoring.

- Chapter 3 is devoted to the design of real time observers for EDLCs dedicated to online aging monitoring. State observers are designed to estimate the parameters of two models of EDLCs: one is a simple RRC model and the other one is a more complicated transmission line model. The observability and sensitivity of these two models are studied. Two kinds of observers, an extended Kalman filter and interconnected observers are designed based on the first model while for the second model, an extended Kalman filter and braided Kalman filters are designed. The performance of the designed observers for both models are checked by simulated experiments. At last, the parameter estimations of real EDLCs at different aging levels are presented and validated by comparing with the offline characterization results obtained in Chapter 1. An example of potential online state of health indicator that could be used for industrial applications is proposed at last.

- Some conclusions of this work are then presented and potential ideas for a future extension of this work are also proposed.

# 1

# Offline monitoring of the supercapacitors aging

## Introduction

The aging of EDLCs can be detected from the evolution of their parameters, such as the increase of the equivalent series resistance $R_s$ or the decrease of the capacitance $C$ [1] [37]. To study the aging of an EDLC, offline characterization techniques could be considered as a reliable way to analyze their parameters' evolution with aging. This chapter is dedicated to investigating how the evolution of the EDLC parameters with aging can be observed by using different offline characterization techniques and to assessing the quality of the characterization results.

The first section reviews the existing offline characterization methods, both in the time and frequency domains. In the second section, several characterization techniques used in this thesis are firstly introduced. The different physical parameters of EDLCs are defined and their calculation expressions are derived. The third section proposes to use parameter uncertainty to asses the quality of the measurements. The calculation formulas of uncertainty of each parameter defined in second section are determined. Finally, the last section presents the experimental results of the proposed parameters and their uncertainties obtained on a fresh EDLC by offline characterization. Afterwards, the parameters evolution resulting from an accelerated aging experiment is presented and analyzed.

## 1.1 State of the art

A large amount of research has already been done to study the EDLCs aging through their parameters characterization [6] [32] [38] [39] [40]. The offline characterization methods used in these research works can be divided into two kinds, one gathering characterization methods in the time domain and the other in the frequency domain. In the time domain, two parameters, $R_s$ and $C$, are usually determined from some specific current and voltage profiles [41] [6] [32]. On the other hand, EIS (Electrochemical Impedance Spectroscopy) is most widely used in laboratories to determine the impedance spectrum of EDLCs [38] [39]. Besides the two main parameters, $R_s$ and $C$, EIS can furthermore determine other parameters, such as the electrolyte resistance which is related to the electrode porosity of an EDLC [40]. In [42], [3] and [43], different dynamic models of EDLCs have been derived and validated with experimental measurements obtained by EIS. Based on a model derived from impedance measurements, the impacts of calendar aging and cycling aging on the supercapacitor performance have been studied in [44].

This section will present different existing characterization methods used for EDLCs in both time domain and frequency domain.

### 1.1.1 Time domain characterization

The IEC-62391 standard [45] has defined a method, called Constant Current Constant Voltage (CCCV) method, to determine the parameters, $R_s$ and $C$ of an EDLC. This method applies a constant current to charge the EDLC until its voltage achieves the rated maximum voltage. Then, the EDLC is maintained 30 minutes at the rated voltage with the help of a constant voltage power supply. Subsequently, a specific negative constant current is applied to discharge the EDLC. The current and the voltage of the EDLC (see Fig. 1.1) are measured during such a cycle (charging, rated voltage maintenance and discharging) based on which the parameters can be derived. An estimation of the capacitance $C$ is calculated as

$$C = \frac{I(t_2 - t_1)}{U_1 - U_2} \tag{1.1}$$

where $I$ is the amplitude of the discharge current and the voltage measurements $U_1$ and $U_2$ at time $t_1$ and $t_2$ during the discharging phase are specified according to Table 1.1. An estimation of the equivalent series resistance $R_s$ is calculated as

$$R_s = \frac{\Delta U_3}{I} \tag{1.2}$$

where $\Delta U_3$ is the voltage drop at the beginning of the discharge phase defined as the difference between the rated voltage and the intersection of the auxiliary line

extended from the straight part of the discharge voltage and the time base at the beginning of the discharge. The value of the constant discharge current specified by the standard to determine $R_s$ is chosen according to Table 1.2, which is different from that used to determine $C$.

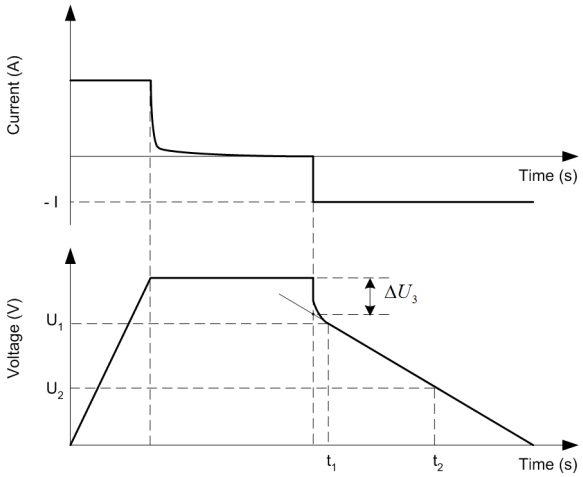


Figure 1.1: Current and voltage curves for the CCCV method [45].

Table 1.1: Discharge conditions to determine $C$ [45].

| Classification | Class 1 | Class 2 | Class 3 | Class 4 |
|---|---|---|---|---|
| Application | Memory backup | Energy storage | Power | Instantaneous power |
| $I$ (mA) | $1 \times C$ | $0.4 \times C$ | $4 \times C$ | $40 \times C$ |
| $U_1$ | The value to be 80% of the rated voltage ($0.8 \times U_R$) | | | |
| $U_2$ | The value to be 40% of the rated voltage ($0.4 \times U_R$) | | | |
| Note | $C$ (F) is the rated capacitance; $U_R$ (V) is the rated voltage | | | |

Table 1.2: Discharge conditions to determine ESR [45].

| Classification | Class 1 | Class 2 | Class 3 | Class 4 |
|---|---|---|---|---|
| $I$ (mA) | $10 \times C$ | $4 \times CU_R$ | $40 \times CU_R$ | $400 \times CU_R$ |
| Note | $C$ (F) is the rated capacitance; $U_R$ (V) is the rated voltage | | | |

For commercial EDLCs, manufacturers give the values of the rated capacitance and the equivalent series resistance based on this standard. For example, the characterization method used by the Nichicon company for their EverCAP products is nearly the same as CCCV [46]. The only difference is that the values of $U_1$ and $U_2$

used to calculate $C$ are not exactly the same as the ones shown in Table 1.1. They are respectively replaced by 2 V and 1 V.

Some manufacturers of EDLCs use other test procedures to characterize their EDLCs. The Maxwell company uses a test, called Constant Current Discharge Test (CCDT) [37], to determine the series resistance and capacitance of their supercapacitors. They also use the measurements from a constant current discharge phase which is similar to the one defined by the IEC-62391 standard. The procedure of this test is as follows:

1. The EDLC is charged to some appropriate voltage with an appropriate current;
2. Keep the EDLC in open circuit for some time, then discharge it with an appropriate current until the voltage decreases to a very small value, for example, 0.1V. Record the discharge time and the minimum discharged voltage.
3. Remove the load from EDLC for 5 seconds and record the voltage.

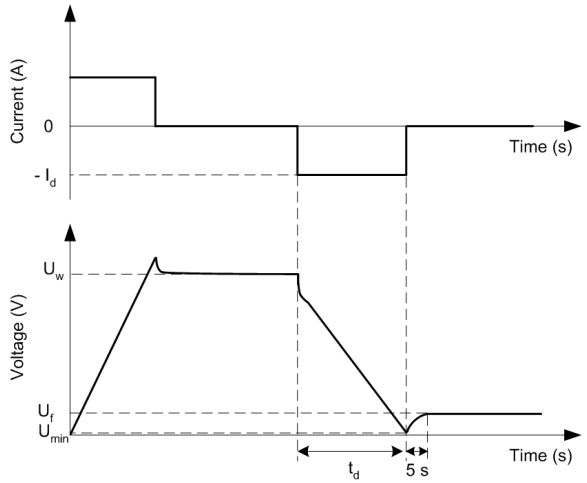


Figure 1.2: Current and voltage curves for the CCDT method used by Maxwell [37].

Fig. 1.2 shows the current and voltage curves in this test. The calculation of capacitance $C$ is in a similar way as equation 1.1:

$$C = \frac{I_d \times t_d}{U_w - U_f} \tag{1.3}$$

where $I_d$ is the amplitude of the discharge current, $t_d$ is the discharge time, $U_w$ is the working voltage and $U_f$ is the voltage 5 seconds after the removal of load. The voltage difference $U_w - U_f$ is used instead of $U_w - U_{\min}$ in the aim of eliminating the voltage drop due to the equivalent series resistance [37]. The resistance $R_s$ is defined as

$$R_s = \frac{U_f - U_{\min}}{I_d} \tag{1.4}$$

where $U_{\min}$ is the minimum discharged voltage of the EDLC.

A large amount of work about the time domain characterization of EDLCs is based on the two methods presented above. But some researchers also made some modifications depending on the different requirement of their applications. For example, in [4], Lajnef et al have calculated $C$ and $R_s$ based on a CCDT during not only the discharging period but also during the charging period. In [47], the authors defined these two parameters the same way as that of CCDT, except that they charge and discharge the EDLC with constant power instead of constant current.

### 1.1.2 Frequency domain characterization

The Electrochemical Impedance Spectroscopy (EIS), also called AC impedance method, is a popular and widely used technique to characterize electrochemical cells such as batteries, fuel cells and supercapacitors. Recognized as a frequency domain technique, EIS studies the response of an electrochemical cell to an applied excitation signal over a pre-determined frequency range, and calculates the corresponding impedance. It is usually operated by applying an AC excitation potential to the cell and then measuring the responding AC current [38]. Using EIS to analyze the impedance of a linear system is much easier than that of a nonlinear system. Unfortunately, electrochemical systems are nonlinear. But if the amplitude of the applied AC potential has a very small value, the system can be considered as approximately linear (pseudo-linear) [48]. Therefore, the experimental condition for a valid EIS measurement is that the amplitude of the applied excitation potential must be small enough (normally, between 1 mV and 10 mV) [39].

Usually in the EIS, a small sinusoidal voltage $v(t) = V\sin(\omega t)$, added to a steady state potential $v_0$, is applied to an electrochemical cell, where $V$ is the voltage signal amplitude and $\omega$ is angular frequency. Since the cell is assumed to be pseudo-linear, the response to the AC excitation potential is a sinusoidal current $i(t)$ with the same frequency but a shift in phase $\varphi$ which is expressed as $i(t) = I\sin(\omega t - \varphi)$, where $I$ is the amplitude of the current (see Fig. 1.3).

The sinusoidal voltage and current signals are expressed in complex form [49]: $V(t) = V \cdot e^{\jmath\omega t}$ and $I(t) = I \cdot e^{\jmath(\omega t - \varphi)}$. The resulting complex impedance can be written as $Z(\jmath\omega) = (V/I)\cdot e^{\jmath\varphi}$. Then, the values of the real and the imaginary parts of the impedance, $Z_{\text{re}}$ and $Z_{\text{im}}$, can be obtained from the following equations:

$$Z_{\text{re}} = \frac{V}{I}\cos(\varphi),\ Z_{\text{im}} = \frac{V}{I}\sin(\varphi) \tag{1.5}$$

The Nyquist plot of an electrochemical cell can be obtained by presenting the real part of the impedance on the abscissa axis and the opposite of the imaginary part on the ordinate axis at different frequencies. Fig. 1.4 shows Nyquist plots of

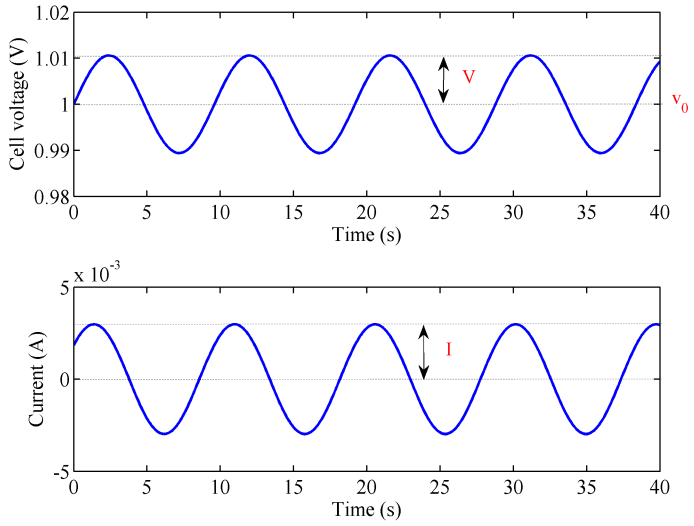


Figure 1.3: Applied voltage and responding current of an electrochemical cell.

simple elements and their combinations. For an ideal capacitor, the Nyquist plot in Fig. 1.4 (a) shows a vertical line at the ordinate axis with the real part of impedance being $0\ \Omega$. For a capacitor in series with a resistor (Fig. 1.4 (b)), the vertical line is shifted with the value of the resistor $R$ compared to the case of an ideal capacitor. The Nyquist plot of a capacitor in parallel with a resistor (Fig. 1.4 (c)) is a semi-circle centered on $(R_1/2, 0)$ with a radius of $R_1/2$ and the real part of the impedance is equal to the resistance $R_1$ when the frequency is zero. In the case of a resistor in series with a capacitor which is in parallel with another resistor shown in Fig. 1.4 (d), the semi-circle is shifted with the value of the series resistance $R_2$. This model is considered as the classical simple electrical model of an EDLC [50] [51].

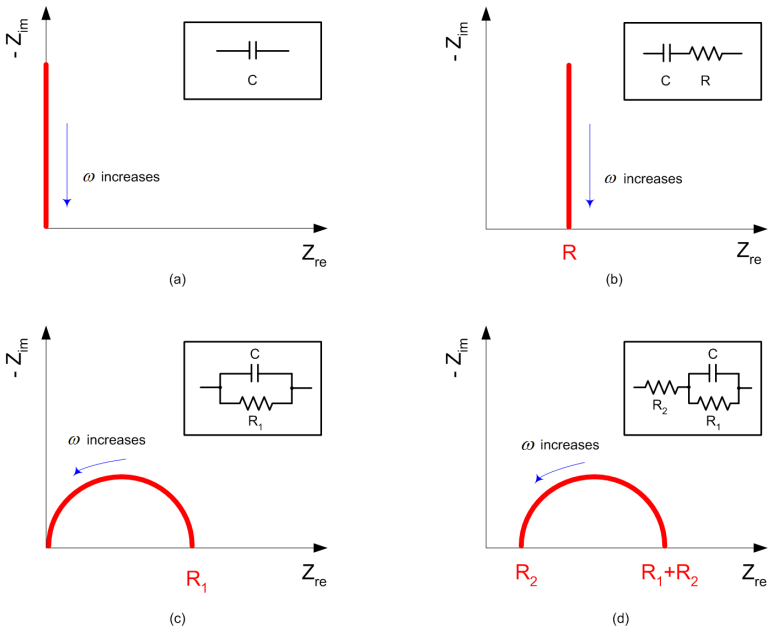


Figure 1.4: Nyquist plots of different elements [52].

However, in practice, the impedance plot of a real EDLC is not as simple as the plots illustrated above. Fig. 1.5 (left) is the Nyquist plot of a commercial Nichicon 1F/2.7V (UM105) EDLC obtained by EIS measurement at a 1 V DC potential with a frequency range between 10 mHz and 200 kHz. The nominal resistance specified by the manufacturer is 3 $\Omega$ and is shown by the red vertical line in the figure. It is clear from this figure that the impedance of this EDLC approaches the vertical line at very low frequencies. This means that at a very low frequency, the EDLC behaves almost but not exactly like a capacitor in series with a resistor as in Fig. 1.4 (b). The real part of the impedance decreases for higher frequencies. At a frequency where the imaginary part of the impedance is zero, the EDLC behaves as a pure resistor. The figure at the right side of Fig. 1.5 is an enlarged impedance spectrum at an intermediate frequency range. Between $0.3$ Hz and $5$ Hz, a $45^\circ$ slope area appears. It is caused by the electrode porosity and can be described by a transmission line RC network (more details will be given in Chapter 2) [53]. It should be noticed that at the frequencies higher than $1.5$ kHz, there exists a semi-circle in the impedance spectrum. The existence of this phenomenon is probably due to the contact at the interface between the electrode and current collector [7], which can be described by a contact resistance $R_{\text{int}}$ in parallel with a capacitance $C_{\text{int}}$. This capacitance can be calculated as

$$C_{\text{int}} = 1/(2\pi f_t R_{\text{int}}) \tag{1.6}$$

where, $f_t$ is the frequency at the top point of the semi-circle and $R_{\text{int}}$ is calculated as the diameter of the semi-circle. For this Nichicon 1F/2.7V (UM105) EDLC, $C_{\text{int}}$ is around $100\ \mu F$ which is small enough to be neglected with respect to the nominal capacitance (around 1 F).

With EIS method, the EDLCs are often characterized by calculating the equivalent resistance and capacitance [54] [55]. They are defined as

$$R_{\text{eq}} = Z_{\text{re}}, \quad C_{\text{eq}} = -1/(2\pi f Z_{\text{im}}) \tag{1.7}$$

Fig. 1.6 shows the equivalent resistance and capacitance versus frequency of a Nichicon 1F/2.7V (UM105) EDLC. At a high frequency, the ions of the electrolyte do not enter deeply into the pores of the electrodes. This is why $R_{\text{eq}}$ and $C_{\text{eq}}$ decrease with an increase of frequency. On the other hand, at a lower frequency, the ions can enter into the pores more deeply, which means that there are more charges stored in the EDLC. It leads to a higher capacitance at a lower frequency. Meanwhile, with the penetration of the ions in the pores, the electrolyte resistance increases which leads to a higher $R_{\text{eq}}$. When characterizing a commercial EDLC by EIS measurements, the rated capacitance $C$ is often determined as the maximum $C_{\text{eq}}$ obtained at the lowest frequency, and the equivalent series resistance $R$ is defined as $R_{\text{eq}}$ obtained at some high frequency $f_0$, for example 1 kHz for a Nichicon

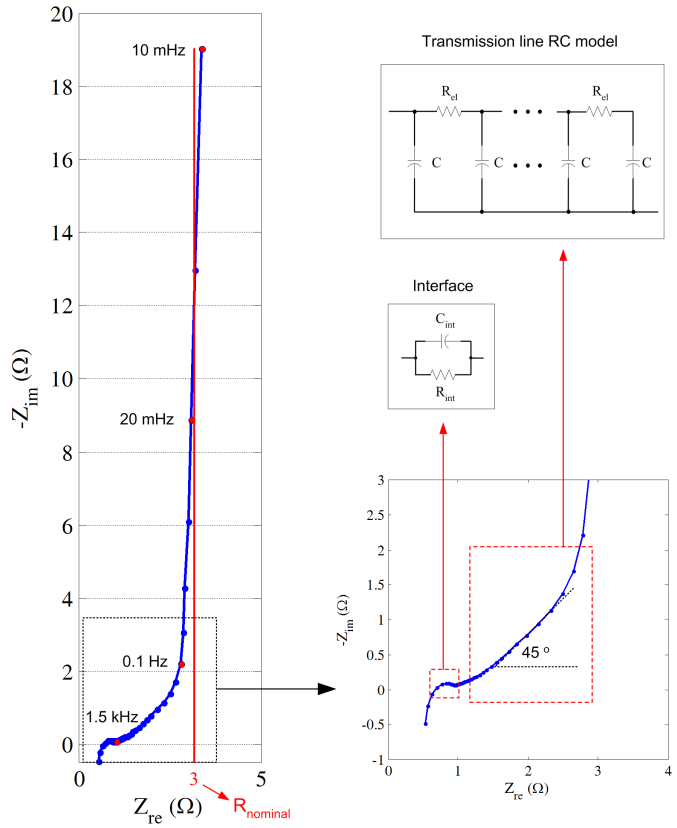


Figure 1.5: Nyquist plots of a Nichicon 1F/2.7V EDLC.

EDLC:

$$R = R_{\text{eq}}(f_0), \quad C = \max(C_{\text{eq}}) \tag{1.8}$$

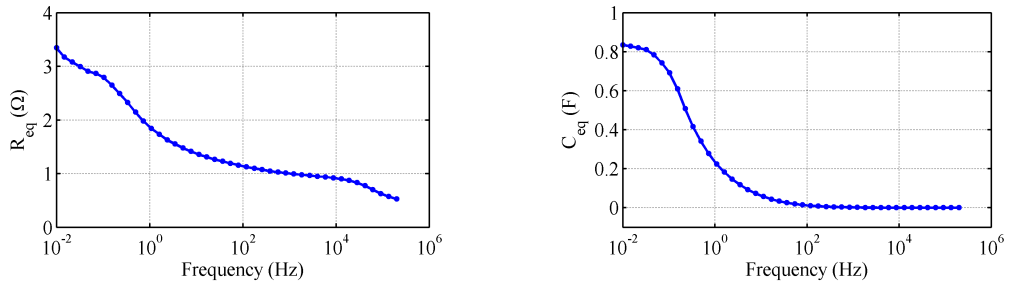


(a) $R_{\text{eq}}$ vs. frequency (b) $C_{\text{eq}}$ vs. frequency

Figure 1.6: The equivalent resistance and capacitance versus frequency.

## 1.2 Offline characterization of a commercial EDLC

### 1.2.1 Acquisition device and techniques

The supercapacitor used in this work is chosen as the Nichicon 1F/2.7V (type UM105) EDLC. To characterize this EDLC offline, a multipotentiostat called VMP3

Figure 1.7: VMP 3 device.

(see Fig. 1.7) provided by Bio-Logic is used. It can be connected to a computer by a USB link or by Ethernet. The EC-lab software shown in Fig. 1.8 is a platform for controlling the VMP3 potentiostat from a computer. The VMP3, together with EC-lab, can apply several techniques, such as EIS or Cyclic Voltammetry (CV) to electrochemical cells such as batteries or supercapacitors. They also allow to define personalized profiles to analyze or characterize the batteries or supercapacitors. The VMP3 is not only an analysis tool but also a data acquisition device. When analysis profiles are applied to a supercapacitor, the required data are recorded by the multipotentiostat and can be used through the EC-lab software.

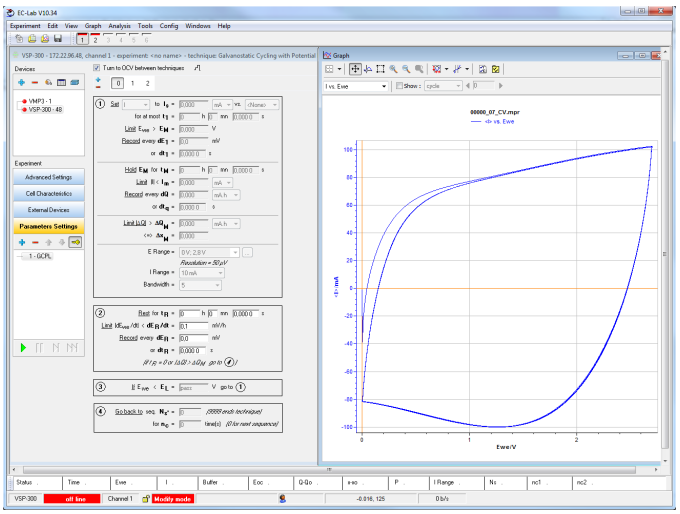

Figure 1.8: EC-lab software

The techniques used via VMP3 and EC-lab in our work for offline characterization of EDLCs are Potentiostatic Electrochemical Impedance Spectroscopy (PEIS), Cyclic Voltammetry (CV), Chronopotentiometry (CP) and Open Circuit Voltage (OCV).

– *Potentiostatic Electrochemical Impedance Spectroscopy (PEIS)*
  This technique has been presented in detail in §1.1.2.
– *Cyclic Voltammetry (CV)*
  The CV technique is frequently used by electrochemists to acquire informa-

tions on electrochemical reactions of batteries or supercapacitors [55] [56]. It applies a triangular potential waveform to the EDLC and the potential sweeps inside a given voltage range. Normally, the voltage increases linearly from $0$ V to the maximum voltage with a constant rate during the charging period and decreases from the maximum voltage to $0$ V during the discharging period with the same rate.

– *Chronopotentiometry (CP)*
Chronopotentiometry is a current controlled technique. With this technique, controlled constant current steps with desired values can be applied to an EDLC. The corresponding voltage is then recorded. This technique can be used for different kinds of EDLC analysis [56], such as the charge efficiency and energy efficiency in our case.

– *Open Circuit Voltage (OCV)*
The OCV technique disconnects the EDLC from power supply, which means that the EDLC is in open circuit state. There is no current and no voltage applied to the EDLC electrodes but the potential across the EDLC is measured by the VMP3. This technique is often used to observe the self-discharge phenomenon of an EDLC.

### 1.2.2 Parameters for EDLC characterization

According to the parameters which are frequently used in laboratories to characterize EDLCs offline [57], we consider the use for aging monitoring purposes of the following parameters:

#### Capacitive Parameters

– *The Integral Capacitance - $C_{\text{int}}$*
The integral capacitance is obtained by a CV technique. This parameter depends on the voltage scanning rate, because of the relatively low conductivity of the ions in the electrolyte within the pores. A higher voltage scanning rate can result in a smaller integral capacitance, because there is not enough time for the ions in the electrolyte to enter into the depths of the pores. Therefore, in our work, the integral capacitance $C_{\text{int}}$ of the chosen EDLC is calculated for two voltage scanning rates ($100$ mV/s and $10$ mV/s). The voltage and current signals obtained with a fresh EDLC during $3$ charge/discharge cycles and with a scanning rate of $10$ mV/s are shown in Fig. 1.9.
The integral capacitance can be calculated as the proportion of the accumulated/released charge and the voltage variation at charging/discharging phase.

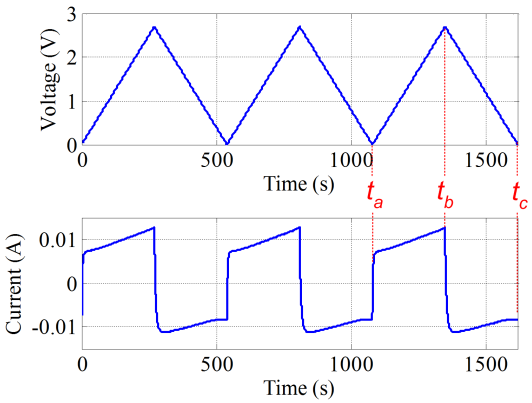


Figure 1.9: Current and voltage signals of a fresh EDLC obtained by CV technique during 3 charging/discharging cycles.

The integral capacitance $C_{\text{int1}}$ deduced from the charging phase is defined as

$$C_{\text{int1}} = \frac{\Delta Q_1}{\Delta v_1} = \frac{\int_{t_a}^{t_b} i(t)\,dt}{v(t_b) - v(t_a)} \tag{1.9}$$

This expression is closely connected to Eq. 1.1 and is based on the integration during the charging phase of an ideal capacitor model $i(t) = C\,\frac{dv}{dt}(t)$. Similarly, the integral capacitance $C_{\text{int2}}$ calculated from the discharging phase is defined as

$$C_{\text{int2}} = \frac{\Delta Q_2}{\Delta v_2} = \frac{-\int_{t_b}^{t_c} i(t)\,dt}{v(t_b) - v(t_c)} \tag{1.10}$$

Then the global integral capacitance $C_{\text{int}}$ is calculated as the average of $C_{\text{int1}}$ and $C_{\text{int2}}$:

$$C_{\text{int}} = (C_{\text{int1}} + C_{\text{int2}})/2 \tag{1.11}$$

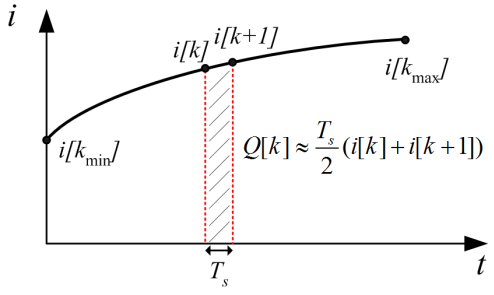


Figure 1.10: Integration approximated by a trapezoidal method.

Theoretically speaking, $v(t_b) - v(t_a) = v(t_b) - v(t_c) = 2.7$ V. But in practice, the current and voltage signals are recorded with a sampling period $T_s$. Therefore, the sampled voltage difference during the charging phase is not exactly equal to that during the discharging phase: $v[k_b] - v[k_a] \approx v[k_b] - v[k_c]$, with $t_a = k_a T_s$, $t_b = k_b T_s$ and $t_c = k_c T_s$. To calculate the accumulated charge

$\Delta Q_1$ and the released charge $\Delta Q_2$, the integral of the current is approximated by a trapezoidal method (see Fig. 1.10).
Finally, in discrete-time, the integral capacitance $C_{\text{int}}$ can be approximately calculated as

$$C_{\text{int}} \approx \frac{1}{2}\left(\frac{\widehat{\Delta Q_1}}{v[k_b]-v[k_a]} + \frac{\widehat{\Delta Q_2}}{v[k_b]-v[k_c]}\right)$$

$$\text{with} \quad \widehat{\Delta Q_1} = \sum_{k=k_a}^{k_b-1} Q[k] = T_s\left(\frac{i[k_a]+i[k_b]}{2} + \sum_{k=k_a+1}^{k_b-1} i[k]\right) \tag{1.12}$$

$$\widehat{\Delta Q_2} = \sum_{k=k_b}^{k_c-1} Q[k] = -T_s\left(\frac{i[k_b]+i[k_c]}{2} + \sum_{k=k_b+1}^{k_c-1} i[k]\right)$$

– *The Differential Capacitance - $C_{\text{diff}}$*
This capacitance is obtained by the EIS technique which was presented in §1.1.2. A voltage which sinusoidally oscillates around a constant DC continuous component $v_0$, is imposed to the EDLC and the corresponding current is measured. The amplitude of the small sinusoidal voltage oscillation is chosen in our case as $V = 10$ mV. The measured current amplitude $I$ and phase $\varphi$ allow to know the complex impedance $Z(j\omega) = Z_{\text{re}} + \jmath\, Z_{\text{im}}$, where $Z_{\text{re}}$ and $Z_{\text{im}}$ can be calculated from Eq. 1.5. The differential capacitance is defined as in Eq. 1.7 by

$$C_{\text{diff}} = -\frac{1}{Z_{\text{im}}\,\omega} = -\frac{I}{2\pi f V \sin(\varphi)} \tag{1.13}$$

This definition is based on the expression of the pure imaginary part of an ideal EDLC's impedance, $Z = -\jmath/(C\omega)$. The differential capacitance is calculated at the lowest frequency ($f = 10$ mHz) in the impedance spectrum and the phase $\varphi$ is thus close to $-\pi/2$. $C_{\text{diff}}$ is a capacitance obtained at a given DC voltage and thus is a voltage dependent parameter. In practice, this capacitance is calculated for $v_0$ equal to 0 V, 1 V, 2 V and 2.7 V.

**Resistive parameters**

– *The Series Resistance - $R_s$*
The series resistance $R_s$ is the sum of the ionic resistance of the electrolyte resulting from the ions migration through the separator between the electrodes and of the contact resistance at the interface between the current collector and the electrode material. This parameter is responsible for the immediate terminal voltage rise/drop at the beginning of charging/discharging phases. It can be characterized by EIS at high frequency. From the impedance spectrum shown in Fig. 1.11, $R_s$ is defined as the real part of the impedance at the right

intersection (denoted by $B$) of the semi-circle and the $Z_{\text{re}}$ axis:

$$R_s = \text{Re}(Z_B) = R_0 + R_{\text{int}} \tag{1.14}$$

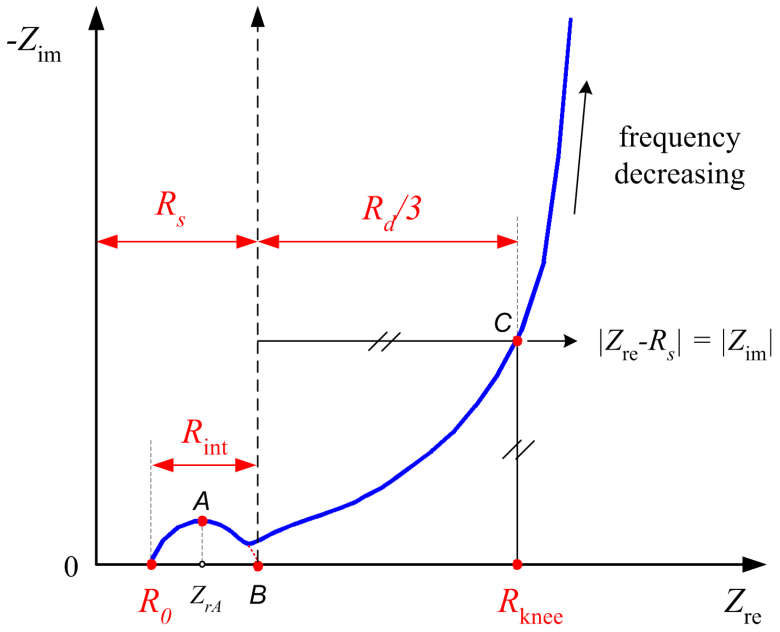


Figure 1.11: Definition of $R_s$ and $R_d$ from impedance spectrum.

$R_0$ is the real part of the impedance at the left intersection of the semi-circle and the $Z_{\text{re}}$ axis. This intersection is located where the imaginary part of the impedance, $Z_{\text{im}}$, is equal to zero ($\varphi = 0$ rad). In practice, the sinusoidal voltage is applied to the supercapacitor with a logarithmically sampled frequency which may lead to a lack of the sampled data to obtain $R_0$ at the required null imaginary part point. Therefore, the series resistance is obtained by a linear interpolation (see Fig. 1.12) between $Z_{r1}$, the real part of the impedance of the last sampled data which has the positive phase $\varphi_1$ and $Z_{r2}$, the real part of the impedance of the last sampled data whose phase, $\varphi_2$, is negative. Thus, the following relationship is obtained from the intercept theorem:

$$\frac{R_0 - Z_{r1}}{Z_{r2} - Z_{r1}} = \frac{\varphi_1}{\varphi_1 - \varphi_2} \tag{1.15}$$

Then, the parameter $R_0$ is calculated by

$$R_0 = \frac{\varphi_2\, Z_{r1} - \varphi_1\, Z_{r2}}{\varphi_2 - \varphi_1}, \text{ with } Z_{r1} = \frac{V_1\, \cos(\varphi_1)}{I_1} \text{ and } Z_{r2} = \frac{V_2\, \cos(\varphi_2)}{I_2} \tag{1.16}$$

$R_{\text{int}}$, represented as the contact resistance at the interface between the electrode and the current collector, is calculated as the diameter of the semi-circle

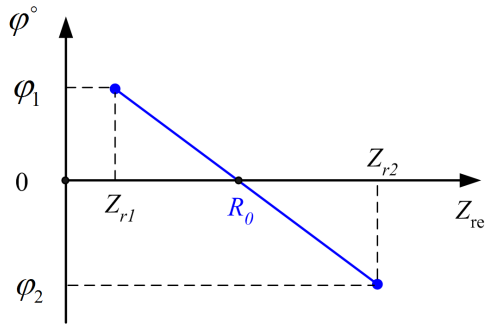


Figure 1.12: Determination of $R_0$ by interpolation.

which is twice the radius:

$$R_{\text{int}} = 2(Z_{rA} - R_0) \tag{1.17}$$

Combining Eqs. 1.14, 1.16 and 1.17, the series resistance $R_s$ is finally obtained:

$$R_s = 2Z_{rA} - R_0 = 2Z_{rA} - \frac{\varphi_2 Z_{r1} - \varphi_1 Z_{r2}}{\varphi_2 - \varphi_1} \tag{1.18}$$

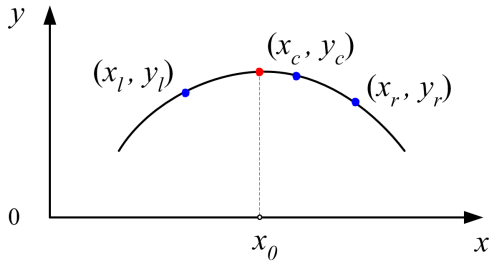


Figure 1.13: Method to find the maximum position of a parabola.

$Z_{rA}$ is considered as the real part of the highest point on the semi-circle and may not be directly obtained from the sampled data. It can be seen from Fig. 1.11 that the shape of the so called 'semi-circle' of an EDLC in the impedance spectrum is closer to a parabola. Thus, the following method can be used to find the maximum position of a parabola in order to obtain an accurate estimation of $Z_{rA}$. Let's suppose that three points (samples), $(x_l, y_l)$, $(x_c, y_c)$ and $(x_r, y_r)$, around the target maximum position are known. The point at the center of the three has the maximum $y$ axis value among all the samples (see Fig. 1.13). The equation of the parabola is assumed to be $y(x) = y_c + a(x - x_c)^2 + b(x - x_c)$, where $a$ and $b$ are constants. Then, at the left and right points, the following equations are established:

$$y_l = y_c + a(x_l - x_c)^2 + b(x_l - x_c) \tag{1.19}$$

$$y_r = y_c + a(x_r - x_c)^2 + b(x_r - x_c) \tag{1.20}$$

Combining the two equations above, $a$ and $b$ are obtained:

$$\begin{aligned} a &= \frac{(x_r - x_c)(y_l - y_c) - (x_l - x_c)(y_r - y_c)}{(x_l - x_c)(x_r - x_c)(x_l - x_r)} \\ b &= -\frac{(x_r - x_c)^2(y_l - y_c) - (x_l - x_c)^2(y_r - y_c)}{(x_l - x_c)(x_r - x_c)(x_l - x_r)} \end{aligned} \tag{1.21}$$

$x_0$ of the maximum position is obtained when the derivative of the function $y(x)$ is zero:

$$\frac{dy(x_0)}{dx} = 2a(x_0 - x_c) + b = 0 \quad \Rightarrow \quad x_0 = x_c - b/(2a) \tag{1.22}$$

Thus, $x_0$ is obtained from the three known samples:

$$x_0 = x_c + \frac{(x_r - x_c)^2(y_l - y_c) - (x_l - x_c)^2(y_r - y_c)}{2\left((x_r - x_c)(y_l - y_c) - (x_l - x_c)(y_r - y_c)\right)} \tag{1.23}$$

In our case, $x_0$ is replaced by $Z_{rA}$ and the three points, $(x_l, y_l)$, $(x_c, y_c)$ and $(x_r, y_r)$, are respectively replaced by the three highest sampled points on the "semi-circle" of the impedance spectrum, $(Z_{rl}, -Z_{il})$, $(Z_{rc}, -Z_{ic})$ and $(Z_{rr}, -Z_{ir})$. Therefore, $Z_{rA}$ can be calculated from:

$$Z_{rA} = Z_{rc} + \frac{(Z_{rr} - Z_{rc})^2(-Z_{il} + Z_{ic}) - (Z_{rl} - Z_{rc})^2(-Z_{ir} + Z_{ic})}{2\left((Z_{rr} - Z_{rc})(-Z_{il} + Z_{ic}) - (Z_{rl} - Z_{rc})(-Z_{ir} + Z_{ic})\right)} \tag{1.24}$$

– *The Dynamic Resistance - $R_d$*

The resistance responsible for the $45°$ slope area in the impedance spectrum is called the dynamic resistance of the electrolyte $R_d$. It corresponds to the ionic current caused by the movement of the ions in the electrolyte which fills the pores of the electrode [1]. Since this phenomenon is related to the porosity of the electrode, when determining the dynamic resistance, the series resistance $R_s$ is out of consideration. Thus, the dynamic resistance $R_d$ can be obtained by EIS measurement from the following definition [58]:

$$R_d/3 = R_{\text{knee}} - R_s \tag{1.25}$$

where $R_{\text{knee}}$ is the real part of the impedance at point $C$ of Fig. 1.11, called the knee point. This point indicates the limit of the use of an EDLC, where the capacitive character of the electrode is equal to its resistive character. Therefore, at this knee point, $Z_{\text{re}} - R_s = -Z_{\text{im}}$. In practice, the knee resistance $R_{\text{knee}}$ at point $C$ may not be directly deduced from the sampled data. Therefore, as for the determination of $R_0$, $R_{\text{knee}}$ is obtained by a linear interpolation (see Fig. 1.14) between $Z'_{r1}$, the real part of the impedance of the last sam-

pled data for which $Z_{\text{re}} - R_s + Z_{\text{im}}$ is positive and $Z'_{r2}$, the real part of the impedance of the last sampled data for which $Z_{\text{re}} - R_s + Z_{\text{im}}$ is negative.

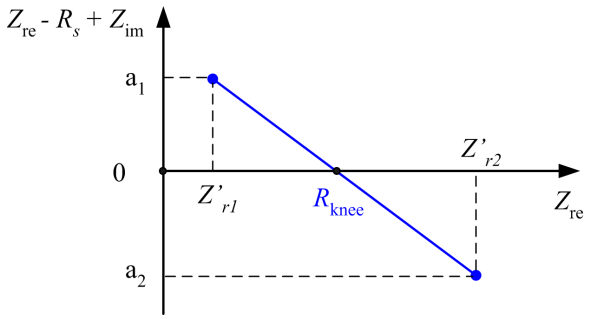


Figure 1.14: Determination of $R_{\text{knee}}$ by interpolation.

The knee resistance $R_{\text{knee}}$ is then obtained by:

$$R_{\text{knee}} = \frac{a_2\, Z'_{r1} - a_1\, Z'_{r2}}{a_2 - a_1} \tag{1.26}$$

with

$$a_k = Z'_{rk} - R_s + Z'_{ik} \quad (k = 1, 2) \tag{1.27}$$

$$Z'_{rk} = \frac{V'_k\, \cos(\varphi'_k)}{I'_k} \text{ and } Z'_{ik} = \frac{V'_k\, \sin(\varphi'_k)}{I'_k} \tag{1.28}$$

– *The Leakage Resistance* - $R_{\text{leak}}$
This parameter is obtained by imposing a constant voltage $v$ to the EDLC and measuring the current $i$ required to maintain the voltage constant. This current $i$ is called leakage current. The leakage resistance is defined as

$$R_{\text{leak}} = v/i \tag{1.29}$$

The leakage current comes from the circulation of the charge over the EDLC, caused by some parasitic chemical reactions between the electrodes and the chemical component in the electrolyte [40]. The leakage current depends on the voltage and temperature level. In our case, different DC voltages, 1 V, 2 V and 2.7 V, are maintained for 30 minutes at room temperature to ensure that the EDLC is completely charged. The measurement of the current is taken at the end of these 30 minutes.

– *The Self-discharge Resistance* - $R_{\text{sd}}$
Self-discharge is the voltage decay phenomenon of a charged cell after it is left on open circuit for some time [1]. The parameter $R_{\text{sd}}$ is obtained thanks to an OCV technique by measuring the voltage of EDLC over 30 minutes at open circuit after charging the EDLC to the rated voltage (i.e. 2.7 V in our case). The rated voltage is hold for 30 minutes before starting the open circuit state in order to ensure that the EDLC is completely charged. This

open circuit voltage is approximately equal to $v(t) = V_0 + V_1\, e^{-t/\tau}$, with $\tau = R_{\text{sd}}\, C_{\text{diff}}$. By measuring the voltage at three instants ($t = t_0 = 0$ s, $t = t_1$ and $t = t_2 = 2t_1$), the self-discharge voltage is obtained.

$$\begin{cases} v(t_0) = V_0 + V_1 \\ v(t_1) = V_0 + V_1 e^{\frac{-t_1}{\tau}} \\ v(t_2) = V_0 + V_1 e^{\frac{-t_2}{\tau}} \end{cases} \tag{1.30}$$

$$R_{\text{sd}} = \frac{\tau}{C_{\text{diff}}} \quad \text{with} \quad \tau = \frac{t_1}{\ln\left(\frac{v(0)-v(t_1)}{v(t_1)-v(2t_1)}\right)} \tag{1.31}$$

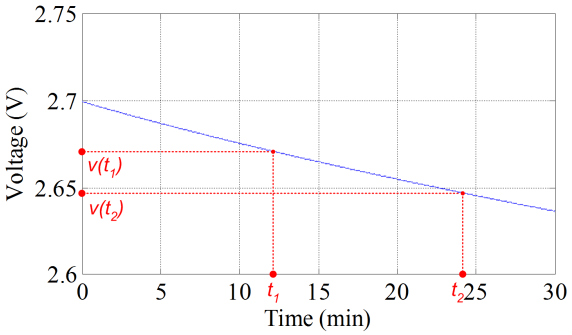


Figure 1.15: Measured voltage of a fresh EDLC in open circuit during 30 minutes, obtained by an OCV technique.

### Efficiency parameters

During the charging period, the charge and energy is accumulated and stored in an EDLC while at the discharging period, the charge releases and the energy is consumed. But even if there is no chemical reaction in EDLC, the charging/discharging efficiency can never reach $100\ \%$.

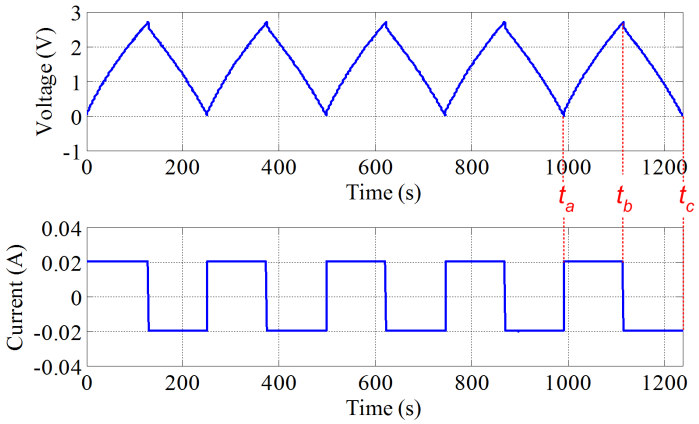


Figure 1.16: Constant charge/discharge current (below) and measured voltage (above) of 3 charging/discharging cycles of a fresh EDLC obtained by a CP technique.

To calculate the charge efficiency and energy efficiency of an EDLC, a chronopotentiometry technique is applied. Five constant current charge/discharge ($\pm 20$ mA) cycles are applied to achieve an external equilibrium of EDLC. The current and voltage signals of the last cycle are used for the calculation of the charge efficiency and energy efficiency (see Fig. 1.16). The voltage is controlled in a range of [0 V-2.7 V].

– *The Charge Efficiency - $\eta_c$*
The charge efficiency is defined as the ratio of electric charge quantity returned during the discharging period and the electric charge received during the charging period.

$$\eta_c = -\frac{\Delta Q_{bc}}{\Delta Q_{ab}} = -\frac{\int_{t_b}^{t_c} i(t)\,dt}{\int_{t_a}^{t_b} i(t)\,dt} \tag{1.32}$$

– *The Energy Efficiency - $\eta_e$*
The energy efficiency is defined as the ratio of the energy released during the discharging period and the energy accumulated during the charging period.

$$\eta_e = -\frac{E_{bc}}{E_{ab}} = -\frac{\int_{t_b}^{t_c} v(t)i(t)\,dt}{\int_{t_a}^{t_b} v(t)i(t)\,dt} \tag{1.33}$$

Generally, the charge efficiency is very close to one because there is very few irreversible chemical reaction during the charging and discharging phases. In contrast, the energy efficiency is lower because of the resistive behavior of the electrolyte in the pores and because of the interface resistance which give rise to Joule effect losses [40]. Therefore, the energy that is used by the load during the discharging phase is lower than the energy stored during the charging phase. This parameter allows to estimate globally the Joule losses at a certain current level without using an electrical model. It provides an indicator of the heating risk, thus, an indicator of the aging acceleration.
Although the current is controlled to $20$ mA during the charging period and to $-20$ mA during the discharging period, the measured current is very close to but not exactly equal to the constant current reference value. That is why Eqs. 1.32 and 1.33 are not simplified by eliminating the current term of the denominator and that of the numerator. In practice, the current and voltage signals are recorded with a sampling period $T_s$. The integrals of the current and the power are approximated by a trapezoidal method.

$$\eta_c \approx -\frac{\widehat{\Delta Q}_{bc}}{\widehat{\Delta Q}_{ab}} \quad \text{and} \quad \eta_e \approx -\frac{\widehat{E}_{bc}}{\widehat{E}_{ab}} \tag{1.34}$$

$$\text{with} \quad \widehat{\Delta Q}_{bc} = T_s \left( \frac{i[k_b] + i[k_c]}{2} + \sum_{k=k_b+1}^{k_c-1} i[k] \right) \tag{1.35}$$

$$\widehat{\Delta Q}_{ab} = T_s \left( \frac{i[k_a] + i[k_b]}{2} + \sum_{k=k_a+1}^{k_b-1} i[k] \right) \tag{1.36}$$

$$\widehat{E}_{bc} = T_s \left( \frac{v[k_b]i[k_b] + v[k_c]i[k_c]}{2} + \sum_{k=k_b+1}^{k_c-1} v[k]i[k] \right) \tag{1.37}$$

$$\widehat{E}_{ab} = T_s \left( \frac{v[k_a]i[k_a] + v[k_b]i[k_b]}{2} + \sum_{k=k_a+1}^{k_b-1} v[k]i[k] \right) \tag{1.38}$$

where $k_a \approx t_a/T_s$ such that $v[k_a - 1] > v_{\min}$ and $v[k_a] \leq v_{\min}$, $k_b \approx t_b/T_s$ such that $v[k_b - 1] < v_{\max}$ and $v[k_b] \geq v_{\max}$ and $k_c \approx t_c/T_s$ such that $v[k_c - 1] > v_{\min}$ and $v[k_c] \leq v_{\min}$.

For now, different parameters of EDLCs have been defined and their values can be calculated as long as the measurements are obtained by different characterization techniques. However, when presenting the parameters estimations obtained from measurements, it is also very important to show how much one can trust on these results. The next section will present how to evaluate the quality of the parameters estimations by analyzing their related uncertainties.

## 1.3 The parameter uncertainty estimation

### 1.3.1 Parameter uncertainty

The measurement provides some information about the value of a specific measurand, such as the voltage across an electrical circuit or the current through one branch of a circuit. However, this measurement cannot be exactly equal to the true value of the measurand because it can be affected by different factors such as the measuring system, the measurement procedure, the operation skills or the environment [59]. Therefore, when evaluating a measurement result, it is generally expressed as a measured quantity value and a measurement uncertainty [60]. In the 'International vocabulary of metrology', the measurement uncertainty is defined as "a parameter associated with the result of a measurement, that characterizes the dispersion of the values that could reasonably be attributed to the measurand" [60] [61]. The purpose of determining the measurement uncertainty is not to discredit the measurement result or the method by which it was obtained, but rather to assess the quality of a measurement system and to find a way to improve the measurement

accuracy (see [60], §2.13).

One part of the measurement uncertainty is due to the repeatability or reproducibility error. The remaining part comes from various sources, for example, the instrument effects, signal sampling or computational effects, etc [61]. When a physical quantity $y$, which cannot be measured directly, is related to a finite number of independent measurable physical quantities $x_1,\ x_2,\ ...x_N$ by a nonlinear function written as $y = f(x_1, x_2, ...x_N)$, the uncertainty of this quantity $y$ is called combined standard uncertainty [61]. The combined standard uncertainty $u(y)$ associated with $y$ is given by a quadrature combination of the product of the independent parameters uncertainty $u(x_i)$ and their corresponding sensitivity coefficient (see [59], §4.14 et §4.15):

$$u(y)^2 = \sum_{i=1}^{N} c_i^2\, u(x_i)^2, \quad \text{with} \quad c_i = \frac{\partial f}{\partial x_i}(x_1, x_2 \dots x_N) \tag{1.39}$$

The uncertainty of the quantity, $u(x_i)$, can be determined from the manufactures' specifications. When characterizing the EDLC with the VMP3 from the Biologic company, the limits of accuracy of the useful measurands are indicated by the manufacturer as the percentage of full scale range shown in Table 1.3.

Table 1.3: Specification of VMP3 multipotentiostat/galvanostat.

| **Measured Quantity** | Current | Potential | Frequency | Phase |
|---|---|---|---|---|
| **Accuracy** | < 0.1% FSR | < 0.1% FSR | 1% | 1° |

(FSR: Full Scale Range)

Since the specification provides neither a level of confidence nor a knowledge of the shape of the distribution of the measurand, it is normally appropriate to assume a rectangular distribution with a standard deviation of the accuracy divided by $\sqrt{3}$. Thus, the uncertainty of a measured quantity is calculated as [61].

$$u(x_i) = \frac{a}{\sqrt{3}} \tag{1.40}$$

where $a$ is the device accuracy (see Table 1.3), defined as the half-width of the rectangular distribution of the true value around the measured value shown in Fig. 1.17.

The uncertainty calculation given above in Eq. 1.39 is for the measurement of a single sample. But if the quantities $x_1,\ x_2,\ ...x_N$ are measured on several samples (in our case, several EDLCs), the total uncertainty should be composed of two parts. One is deduced from the measurement process, as calculated by Eq. 1.39. The other one is random uncertainty due to the repeated measurements on different samples and often represented by the standard deviation of the measurements of different samples. Therefore, the final estimation is then obtained by taking the average value

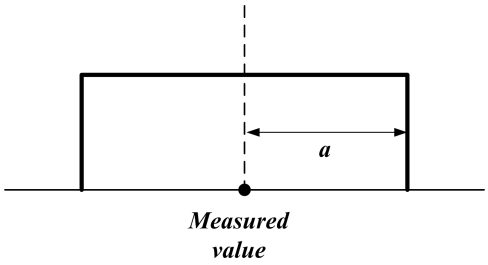


Figure 1.17: Plot of a rectangular probability distribution.

of $y_j$, and its total uncertainty is obtained by combining the experimental standard deviation of $y_j$ with the highest value of the measurement uncertainty $u(y_j)$:

$$\overline{y} = \frac{1}{M}\sum_{j=1}^{M} y_j, \quad \text{and} \tag{1.41}$$

$$u(\overline{y}) = \sqrt{S_{\overline{y}}^2 + \max_{j\in[1,M]} u(y_j)^2} \quad \text{with} \quad S_{\overline{y}}^2 = \frac{1}{M-1}\sum_{j=1}^{M}(y_j - \overline{y})^2 \tag{1.42}$$

where $M$ is the number of the samples ($M = 5$ in our case). Since the highest value of the measurement uncertainty is used to represent the systematic uncertainty, the estimation given in Eq. 1.42 corresponds to a conservative estimation of the uncertainty of $\overline{y}$.

### 1.3.2 Determination of the uncertainty of EDLC parameters

– *Uncertainty of the integral capacitance* - $u(C_{\text{int}})$
For the integral capacitance $C_{\text{int}}$, we assume that all the voltages and all the currents are measured with the same range, such that all voltage measurements have the same uncertainty $u(v)$ and all current measurements have the same uncertainty $u(i)$. Then, the uncertainty of $C_{\text{int}}$ defined by Eq. 1.11 can be calculated as

$$u(C_{\text{int}})^2 = \frac{1}{4}\left(u(C_{\text{int1}})^2 + u(C_{\text{int2}})^2\right) \tag{1.43}$$

where $C_{\text{int1}}$ and $C_{\text{int2}}$ are obtained from Eq. 1.9 and 1.10 and their uncertainties are calculated the following way:

$$u(C_{\text{intk}})^2 = (\frac{\partial C_{\text{intk}}}{\partial \Delta Q_k})^2 u(\Delta Q_k)^2 + (\frac{\partial C_{\text{intk}}}{\partial \Delta v_k})^2 u(\Delta v_k)^2 \quad (k = 1, 2)$$

$$\text{with} \quad \frac{\partial C_{\text{intk}}}{\partial \Delta Q_k} = \frac{1}{\Delta v_k}, \quad \frac{\partial C_{\text{intk}}}{\partial \Delta v_k} = -\frac{\Delta Q_k}{(\Delta v_k)^2} \tag{1.44}$$

Therefore, $u(C_{\text{int1}})$ and $u(C_{\text{int1}})$ can be obtained by the following simplified equation:

$$u(C_{\text{intk}})^2 = C_{\text{intk}}^2 \left( \frac{u(\Delta Q_k)^2}{\Delta Q_k^2} + \frac{2\,u(v)^2}{{\Delta v_k}^2} \right) \quad (k = 1, 2)$$

$$\text{with} \quad u(\Delta Q_1)^2 = T_s^2 u(i)^2 (k_b - k_a - \frac{1}{2}), \quad u(\Delta v_1)^2 = 2u(v)^2 \tag{1.45}$$

$$u(\Delta Q_2)^2 = T_s^2 u(i)^2 (k_c - k_b - \frac{1}{2}), \quad u(\Delta v_2)^2 = 2u(v)^2$$

The current and voltage are measured with two different voltage scanning rates, 100 mV/s and 10 mV/s in the cyclic voltammetry test. The full scale ranges of the current are respectively chosen as 100 mA (for 100 mV/s) and 10 mA (for 10 mV/s). The full scale range of the voltage for both cases is chosen as 3 V. The numerical values of the sampling period $T_s$, $u(i)$ and $u(v)$ needed for calculating the uncertainty of $C_{\text{int}}$ are shown in Table 1.4. The other variables, $\Delta v_k$, $\Delta Q_k$, $k_a$, $k_b$ and $k_c$, can be determined directly from the measured signals.

Table 1.4: The values of $T_s$, $u(i)$ and $u(v)$ in CV test.

| | $T_s$ [s] | $u(i)$ [A] | $u(v)$ [V] |
|---|---|---|---|
| 100 mV/s | 0.05 | $0.1\% \times 0.1/\sqrt{3}$ | $0.1\% \times 3/\sqrt{3}$ |
| 10 mV/s | 0.005 | $0.1\% \times 0.01/\sqrt{3}$ | $0.1\% \times 3/\sqrt{3}$ |

– *Uncertainty of the differential capacitance* - $u(C_{\text{diff}})$

Table 1.5: The uncertainties of the measurands in EIS test.

| $u(I)$ [A] | $u(V)$ [V] | $\frac{u(f)}{f}$ | $u(\varphi)$ [rad] |
|---|---|---|---|
| $0.1\% \times 0.01/\sqrt{3}$ | $0.1\% \times 3/\sqrt{3}$ | 1% | $1 \times \pi/(180\sqrt{3})$ |

Three parameters, $C_{\text{diff}}$, $R_s$ and $R_d$, are characterized by EIS measurement. There are four measurands measured by EIS: current $I$, voltage $V$, frequency $f$ and phase $\varphi$. Their uncertainty specified by the VMP 3 manufacturer is shown in Table 1.5. The uncertainty of the differential capacitance defined in Eq. 1.13 is obtained by:

$$u(C_{\text{diff}})^2 = (\frac{\partial C_{\text{diff}}}{\partial I})^2 u(I)^2 + (\frac{\partial C_{\text{diff}}}{\partial V})^2 u(V)^2 + (\frac{\partial C_{\text{diff}}}{\partial \varphi})^2 u(\varphi)^2 + (\frac{\partial C_{\text{diff}}}{\partial f})^2 u(f)^2 \tag{1.46}$$

$$\text{with} \quad \frac{\partial C_{\text{diff}}}{\partial I} = \frac{-1}{2\pi f V \sin\varphi}, \quad \frac{\partial C_{\text{diff}}}{\partial V} = \frac{I}{2\pi f V^2 \sin\varphi}$$
$$\frac{\partial C_{\text{diff}}}{\partial \varphi} = \frac{I\cos\varphi}{2\pi f V (\sin\varphi)^2}, \quad \frac{\partial C_{\text{diff}}}{\partial f} = \frac{I}{2\pi f^2 V \sin\varphi} \tag{1.47}$$

Finally, $u(C_{\text{diff}})$ can be obtained by:

$$u(C_{\text{diff}})^2 = C_{\text{diff}}^2 \left( \frac{u(I)^2}{I^2} + \frac{u(V)^2}{V^2} + \frac{u(f)^2}{f^2} + \cot(\varphi)^2\, u(\varphi)^2 \right) \tag{1.48}$$

– *Uncertainty of the series resistance* - $u(R_s)$

From the expression of $R_s$ in Eq. 1.18, its uncertainty $u(R_s)$ can be obtained from:

$$u(R_s)^2 = 4u(Z_{rA})^2 + u(R_0)^2 \tag{1.49}$$

The uncertainty of $R_0$, $u(R_0)$, is derived from Eqs. 1.16 and 1.39:

$$u(R_0)^2 = (\frac{\partial R_0}{\partial Z_{r1}})^2 u(Z_{r1})^2 + (\frac{\partial R_0}{\partial Z_{r2}})^2 u(Z_{r2})^2 + (\frac{\partial R_0}{\partial \varphi_1})^2 u(\varphi)^2 + (\frac{\partial R_0}{\partial \varphi_2})^2 u(\varphi)^2 \tag{1.50}$$

$$\text{with} \quad \frac{\partial R_0}{\partial Z_{r1}} = \frac{\varphi_2}{\varphi_2 - \varphi_1}, \quad \frac{\partial R_0}{\partial Z_{r2}} = -\frac{\varphi_1}{\varphi_2 - \varphi_1}$$
$$\frac{\partial R_0}{\partial \varphi_1} = \frac{\varphi_2 (Z_{r1} - Z_{r2})}{(\varphi_2 - \varphi_1)^2}, \quad \frac{\partial R_0}{\partial \varphi_2} = \frac{\varphi_1 (Z_{r2} - Z_{r1})}{(\varphi_2 - \varphi_1)^2} \tag{1.51}$$

$$\begin{aligned} \text{and } u(Z_{rk})^2 &= \frac{\cos(\varphi_k)^2}{I_k^2} \cdot u(V)^2 + \frac{V_k^2 \cos(\varphi_k)^2}{I_k^4} \cdot u(I)^2 + \frac{V_k^2 \sin(\varphi_k)^2}{I_k^2} \cdot u(\varphi)^2 \\ &= \frac{V_k^2 \cos(\varphi_k)^2}{I_k^2} \cdot \left( \frac{u(V)^2}{V_k^2} + \frac{u(I)^2}{I_k^2} + \frac{\sin(\varphi_k)^2}{cos(\varphi_k)^2} u(\varphi)^2 \right) \\ &= Z_{rk}^2 \left( \frac{u(V)^2}{V_k^2} + \frac{u(I)^2}{I_k^2} + \tan(\varphi_k)^2 u(\varphi)^2 \right) \quad (k = 1, 2) \end{aligned} \tag{1.52}$$

The uncertainty $u(Z_{rA})$ can be calculated from:

$$\begin{aligned} u(Z_{rA})^2 =& (\frac{\partial Z_{rA}}{\partial Z_{rl}})^2 u(Z_{rl})^2 + (\frac{\partial Z_{rA}}{\partial Z_{rc}})^2 u(Z_{rc})^2 + (\frac{\partial Z_{rA}}{\partial Z_{rr}})^2 u(Z_{rr})^2 + \\ & (\frac{\partial Z_{rA}}{\partial Z_{il}})^2 u(Z_{il})^2 + (\frac{\partial Z_{rA}}{\partial Z_{ic}})^2 u(Z_{ic})^2 + (\frac{\partial Z_{rA}}{\partial Z_{ir}})^2 u(Z_{ir})^2 \end{aligned} \tag{1.53}$$

$$\text{with} \quad u(Z_{rk})^2 = Z_{rk}^2 \left( \tfrac{u(V)^2}{V_k^2} + \tfrac{u(I)^2}{I_k^2} + \tan(\varphi_k)^2 u(\varphi)^2 \right), \ (k = l, c, r)$$
$$u(Z_{ik})^2 = Z_{ik}^2 \left( \tfrac{u(V)^2}{V_k^2} + \tfrac{u(I)^2}{I_k^2} + \cot(\varphi_k)^2 u(\varphi)^2 \right), \ (k = l, c, r)$$

– *Uncertainty of the dynamic resistance* - $u(R_d)$
Since the dynamic resistance is expressed as $R_d = 3(R_{\text{knee}} - R_s)$, its uncertainty is calculated as:

$$u(R_d)^2 = 9\left(u(R_{\text{knee}})^2 + u(R_s)^2\right) \tag{1.54}$$

As shown by Eq. 1.26, the parameter $R_{\text{knee}}$ is calculated by linear interpolation, as $R_0$. Thus, its uncertainty is calculated the same way as $u(R_0)$:

$$u(R_{\text{knee}})^2 = \frac{a_2^2 u(Z'_{r1})^2 + a_1^2 u(Z'_{r2})^2}{(a_2 - a_1)^2} + \frac{(Z'_{r1} - Z'_{r2})^2\left(a_2^2 u(a_1)^2 + a_1^2 u(a_2)^2\right)}{(a_2 - a_1)^4} \tag{1.55}$$

$$\text{where} \quad u(a_k)^2 = u(Z'_{rk})^2 + u(Z'_{ik})^2 + u(R_s)^2\ ; \ \ (k = 1, 2)$$

$$\text{and} \quad u(Z'_{rk})^2 = {Z'_{rk}}^2\left(\frac{u(V)^2}{{V'_k}^2} + \frac{u(I)^2}{{I'_k}^2} + \tan(\varphi'_k)^2 u(\varphi)^2\right) \tag{1.56}$$

$$u(Z'_{ik})^2 = {Z'_{ik}}^2\left(\frac{u(V)^2}{{V'_k}^2} + \frac{u(I)^2}{{I'_k}^2} + \cot(\varphi'_k)^2 u(\varphi)^2\right)$$

– *Uncertainty of the leakage resistance* - $u(R_{\text{leak}})$
The uncertainty of the leakage resistance $u(R_{\text{leak}})$ is simply expressed as:

$$u(R_{\text{leak}})^2 = R_{\text{leak}}^2\left(\frac{u(v)^2}{v^2} + \frac{u(i)^2}{i^2}\right) \tag{1.57}$$

– *Uncertainty of self-discharge resistance* - $u(R_{\text{sd}})$
The uncertainty of self-discharge resistance $u(R_{\text{sd}})$ can be deduced from:

$$u(R_{\text{sd}})^2 = R_{\text{sd}}^2\left(\frac{u(\tau)^2}{\tau^2} + \frac{u(C_{\text{diff}})^2}{C_{\text{diff}}^2}\right) \tag{1.58}$$

To calculate $u(\tau)$, the following equations are derived from Eqs. 1.31 and 1.39:

$$u(\tau)^2 = (\frac{\partial\tau}{\partial t_1})^2 u(t)^2 + \left((\frac{\partial\tau}{\partial v_0})^2 + (\frac{\partial\tau}{\partial v_1})^2 + (\frac{\partial\tau}{\partial v_2})^2\right) u(v)^2 \tag{1.59}$$

with $v_0 = v(0)$, $v_1 = v(t_1)$, $v_2 = v(2t_1)$ and

$$\begin{aligned}
\frac{\partial\tau}{\partial t_1} &= \frac{1}{\ln(x)}; \quad x = \frac{v_0 - v_1}{v_1 - v_2} = e^{t_1/\tau} \\
\frac{\partial\tau}{\partial v_0} &= \frac{-t_1}{\ln(x)^2(v_0 - v_1)} \\
\frac{\partial\tau}{\partial v_1} &= \frac{t_1(v_0 - v_2)}{\ln(x)^2(v_0 - v_1)(v_1 - v_2)} \\
\frac{\partial\tau}{\partial v_2} &= \frac{-t_1}{\ln(x)^2(v_1 - v_2)}
\end{aligned} \tag{1.60}$$

Therefore,

$$u(\tau)^2 = \tau^2 \left( \frac{u(t)^2}{t_1^2} + J u(v)^2 \right) \tag{1.61}$$

$$\text{with} \quad J = \frac{(v_1 - v_2)^2 + (v_2 - v_0)^2 + (v_0 - v_1)^2}{(v_0 - v_1)^2 (v_1 - v_2)^2 \ln\left(\frac{v_0 - v_1}{v_1 - v_2}\right)^2} \tag{1.62}$$

Combining with Eq. 1.30, $J$ can be written as a function of $x$:

$$J(x) = \frac{x^2(1 + x^2 + (1 + x)^2)}{V_1^2 (x - 1)^2 \ln(x)^2} \tag{1.63}$$

which has a minimum value when $\ln(x) \approx 1.59$ (see Fig. 1.18). Therefore, the uncertainty of $R_{\text{sd}}$ is minimum when $t_1$ is chosen close to $1.59\tau$.

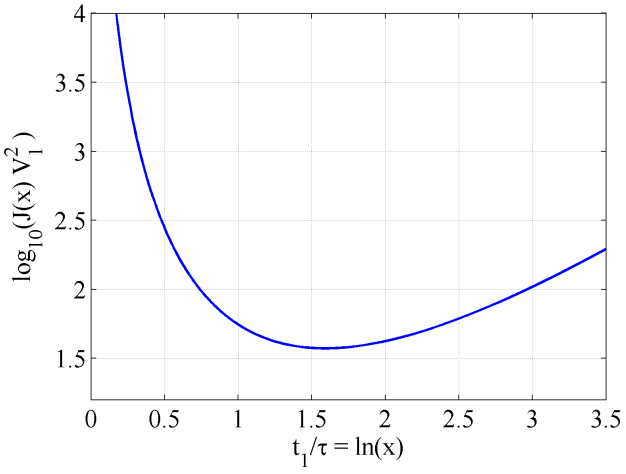


Figure 1.18: Plot of $\log_{10}(J(x)V_1^2)$ in function of $t_1/\tau$.

– *Uncertainty of the charge efficiency - $\eta_c$*

The uncertainty of the charge efficiency $\eta_c$ defined by Eq. 1.34 can be calculated from:

$$\frac{u(\eta_c)^2}{\eta_c^2} = \frac{u(\widehat{\Delta Q}_{bc})^2}{\widehat{\Delta Q}_{bc}^2} + \frac{u(\widehat{\Delta Q}_{ab})^2}{\widehat{\Delta Q}_{ab}^2} \tag{1.64}$$

$$\text{with} \quad u(\widehat{\Delta Q}_{bc})^2 = T_s^2 \left( k_c - k_b - \frac{1}{2} \right) u(i)^2 + \left( i[k_b]^2 + i[k_c]^2 \right) u(t)^2 \tag{1.65}$$

$$u(\widehat{\Delta Q}_{ab})^2 = T_s^2 \left( k_b - k_a - \frac{1}{2} \right) u(i)^2 + \left( i[k_a]^2 + i[k_b]^2 \right) u(t)^2 \tag{1.66}$$

The last term in Eq. 1.65 and 1.66 is added to take the uncertainties of the exact values of $t_a$, $t_b$ and $t_c$ into account. $t_a$, $t_b$ and $t_c$ are the beginning/terminal instants of charging/discharge phases and could have uncertainties due to the sampling issue. The sampling period $T_s$ used to determine the uncertainty of the efficiency parameters is 5 ms. The uncertainty of the time instants $t_a$, $t_b$

and $t_c$ caused by the sampling are considered as a random variable uniformly distributed on an interval with a width $T_s$. Thus, the time instant uncertainty is expressed as $u(t) = T_s/(2\sqrt{3})$.

– *Uncertainty of the energy efficiency - $\eta_e$*
The uncertainty of the energy efficiency $\eta_e$ defined by Eq. 1.34 can be calculated from:

$$\frac{u(\eta_e)^2}{\eta_e^2} = \frac{u(\widehat{E}_{bc})^2}{\widehat{E}_{bc}^2} + \frac{u(\widehat{E}_{ab})^2}{\widehat{E}_{ab}^2} \tag{1.67}$$

$$\begin{aligned} \text{with} \quad u(\widehat{E}_{bc})^2 = {} & T_s^2 u(v)^2 \left( \frac{i[k_b]^2 + i[k_c]^2}{4} + \sum_{k=k_b+1}^{k_c-1} i[k]^2 \right) \\ & + T_s^2 u(i)^2 \left( \frac{v[k_b]^2 + v[k_c]^2}{4} + \sum_{k=k_b+1}^{k_c-1} v[k]^2 \right) \\ & + \left( v[k_b]^2 i[k_b]^2 + v[k_c]^2 i[k_c]^2 \right) u(t)^2 \end{aligned} \tag{1.68}$$

$$\begin{aligned} u(\widehat{E}_{ab})^2 = {} & T_s^2 u(v)^2 \left( \frac{i[k_a]^2 + i[k_b]^2}{4} + \sum_{k=k_a+1}^{k_b-1} i[k]^2 \right) \\ & + T_s^2 u(i)^2 \left( \frac{v[k_a]^2 + v[k_b]^2}{4} + \sum_{k=k_a+1}^{k_b-1} v[k]^2 \right) \\ & + \left( v[k_a]^2 i[k_a]^2 + v[k_b]^2 i[k_b]^2 \right) u(t)^2 \end{aligned} \tag{1.69}$$

The last term in 1.68 and 1.69 is added for the same reason as that for the charge efficiency explained before. For the last presented four parameters $R_{\text{leak}}$, $R_{\text{sd}}$, $\eta_c$ and $\eta_e$, three measurands (voltage $u$, current $i$ and time $t$) are needed to determine $u(R_{\text{leak}})$, $u(R_{\text{sd}})$, $u(\eta_c)$ and $u(\eta_e)$. The uncertainty values of these three measurands are shown in Table 1.6.

Table 1.6: $u(t)$, $u(i)$ and $u(v)$ to determine $u(R_{\text{leak}})$, $u(R_{\text{sd}})$, $u(\eta_c)$ and $u(\eta_e)$.

| $u(t)$ [s] | $u(i)$ [A] | $u(v)$ [V] |
|---|---|---|
| $T_s/(\sqrt{12})$ | $0.1\% \times 0.01/\sqrt{3}$ | $0.1\% \times 3/\sqrt{3}$ |

## 1.4 Experimental results

### 1.4.1 Characterization of fresh EDLCs

The EDLCs studied and tested in the experiments are manufactured by Nichicon (type UM105) with a nominal capacitance of 1 F and a nominal maximum voltage

Table 1.7: Values of $C_{\text{int1}}$ and $C_{\text{int2}}$ obtained for 5 EDLCs and for two voltage scanning rates.

| | $C_{\text{int1}}$ $(F)$ | | $C_{\text{int2}}$ $(F)$ | |
|---|---|---|---|---|
| | 100 mV/s | 10 mV/s | 100 mV/s | 10 mV/s |
| $N°1$ | 0,7248 | 0,9421 | 0,7241 | 0,9390 |
| $N°2$ | 0,7204 | 0,9276 | 0,7191 | 0,9249 |
| $N°3$ | 0,7323 | 0,9425 | 0,7326 | 0,9406 |
| $N°4$ | 0,7206 | 0,9374 | 0,7195 | 0,9340 |
| $N°5$ | 0,7206 | 0,9355 | 0,7195 | 0,9334 |

of 2.7 V. Table 1.8 to 1.14 present the estimated parameters of 5 fresh EDLCs obtained by the proposed characterization methods in previous sections. The characterizations carried out on 5 new EDLCs allow to assess the repeatability of each measurement.

The integral capacitance is considered as the average value of $C_{\text{int1}}$ and $C_{\text{int2}}$, which are the capacitances calculated from the charging and discharging phases respectively. The values of these two capacitances obtained by different voltage scanning rates are shown in Table 1.7. The capacitance calculated from the discharging phase is slightly smaller than that from the charging phase and it is due to the inequality of the charges released during the discharging period and the charges accumulated during the charging period. The final integral capacitance, $C_{\text{int}}$, presented in Table 1.8, has a value approaching to 1 F, which is the nominal value indicated by Nichicon, when the voltage scanning rate is 10 mV/s. Under this scanning rate, a complete charging process from 0 V to 2.7 V lasts 4 min 30. With a scanning rate of 100 mV/s, it needs only 27 s to finish a charging process, but there is not enough time for the ions in the electrolyte to spread in all the pores, which leads to a lower capacitance. The uncertainty of the integral capacitance, $u(C_{\text{int}})$, of each EDLC is less than 1 mF and less than the standard deviation of the 5 samples $S_{\overline{C_{\text{int}}}}$, which shows that the proposed method achieves a fairly good determination of the integral capacitance values. Therefore, this parameter obtained by a CV characterization method provides reliable values that can be used to monitor the aging of EDLCs.

The differential capacitance (Table 1.9) clearly shows its dependency on the polarization DC potential $v_0$, between 0 V and 2.7 V. Fig. 1.19 shows that the differential capacitance (average values of the 5 EDLC with their dispersions) has a nearly linear relationship with its DC voltage. The measurement uncertainty of this parameter is of the order of 150 mF and the parameter dispersion of the 5 simples is around 5 mF. As a result, the uncertainty of the average of the measurements, $u(\overline{C_{\text{diff}}})$, is

Table 1.8: Values of $C_{\text{int}}$ with their absolute and relative uncertainty, obtained for 5 EDLCs and for two voltage scanning rates.

| | $C_{\text{int}}$ $(F)$ | | $u(C_{\text{int}})$ $(mF)$ | | $u(C_{\text{int}})/C_{\text{int}}$ $(\times 10^{-3})$ | |
|---|---|---|---|---|---|---|
| | 100 mV/s | 10 mV/s | 100 mV/s | 10 mV/s | 100 mV/s | 10 mV/s |
| $N°1$ | 0,7244 | 0,9405 | 0,465 | 0,604 | 0,642 | 0,642 |
| $N°2$ | 0,7197 | 0,9263 | 0,462 | 0,594 | 0,641 | 0,642 |
| $N°3$ | 0,7325 | 0,9416 | 0,470 | 0,604 | 0,642 | 0,642 |
| $N°4$ | 0,7200 | 0,9357 | 0,462 | 0,600 | 0,642 | 0,641 |
| $N°5$ | 0,7200 | 0,9344 | 0,462 | 0,600 | 0,642 | 0,642 |
| $\overline{C_{\text{int}}}$ $(F)$ | 0,7233 | 0,9357 | $u(\overline{C_{\text{int}}})$ $(mF)$ | | $u(\overline{C_{\text{int}}})/\overline{C_{\text{int}}}$ $(\times 10^{-3})$ | |
| $S_{\overline{C_{\text{int}}}}$ $(mF)$ | 5,468 | 6,084 | 5,488 | 6,114 | 7,588 | 6,534 |

Table 1.9: Values of $C_{\text{diff}}$ with their absolute and relative uncertainty, obtained for 5 EDLCs and for different polarized DC potential values $v_0$.

| | $C_{\text{diff}}$ $(F)$ | | | | $u(C_{\text{diff}})$ $(F)$ | | | | $u(C_{\text{diff}})/C_{\text{diff}}$ | | | |
|---|---|---|---|---|---|---|---|---|---|---|---|---|
| $v_0$ | 0 V | 1 V | 2 V | 2,7 V | 0 V | 1 V | 2 V | 2,7 V | 0 V | 1 V | 2 V | 2,7 V |
| $N°1$ | 0,749 | 0,835 | 1,010 | 1,136 | 0,123 | 0,137 | 0,167 | 0,196 | 0,164 | 0,164 | 0,165 | 0,172 |
| $N°2$ | 0,745 | 0,820 | 0,997 | 1,124 | 0,122 | 0,134 | 0,165 | 0,193 | 0,164 | 0,164 | 0,165 | 0,171 |
| $N°3$ | 0,753 | 0,836 | 1,018 | 1,144 | 0,122 | 0,135 | 0,166 | 0,196 | 0,162 | 0,162 | 0,164 | 0,171 |
| $N°4$ | 0,756 | 0,828 | 1,009 | 1,132 | 0,129 | 0,140 | 0,172 | 0,195 | 0,171 | 0,169 | 0,171 | 0,173 |
| $N°5$ | 0,753 | 0,827 | 1,008 | 1,130 | 0,124 | 0,136 | 0,167 | 0,194 | 0,164 | 0,164 | 0,166 | 0,172 |
| $\overline{C_{\text{diff}}}$ $(F)$ | 0,751 | 0,829 | 1,008 | 1,133 | $u(\overline{C_{\text{diff}}})$ $(F)$ | | | | $u(\overline{C_{\text{diff}}})/\overline{C_{\text{diff}}}$ | | | |
| $S_{\overline{C_{\text{diff}}}}$ $(mF)$ | 4,292 | 6,526 | 7,455 | 7,492 | 0,129 | 0,140 | 0,172 | 0,196 | 0,172 | 0,169 | 0,171 | 0,173 |

mainly due to the measurement uncertainty. Compared to $C_{\text{int}}$, the uncertainty of $C_{\text{diff}}$ is much larger, around $17\%$. Thus, when determining the capacitance of an EDLC, $C_{\text{int}}$ should be preferred to $C_{\text{diff}}$.

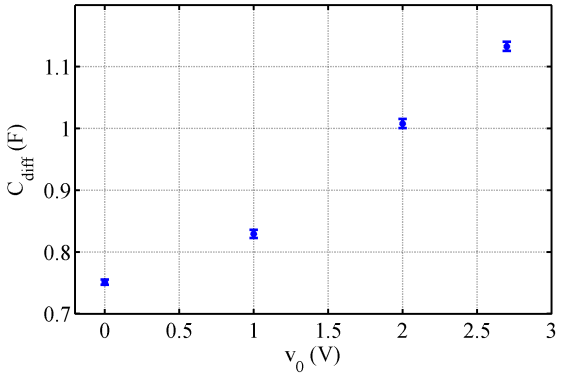


Figure 1.19: Voltage dependent differential capacitance.

Table 1.10: Values of $R_s$ with their absolute and relative uncertainty, obtained for $5$ EDLCs and for different polarized DC potential values $v_0$.

| | $R_s$ ($\Omega$) | | | | $u(R_s)$ ($\Omega$) | | | | $u(R_s)/R_s$ | | | |
|---|---|---|---|---|---|---|---|---|---|---|---|---|
| $v_0$ | 0 V | 1 V | 2 V | 2,7 V | 0 V | 1 V | 2 V | 2,7 V | 0 V | 1 V | 2 V | 2,7 V |
| $N°1$ | 0,982 | 0,995 | 1,026 | 1,142 | 0,411 | 0,415 | 0,432 | 0,533 | 0,419 | 0,418 | 0,421 | 0,467 |
| $N°2$ | 1,009 | 1,030 | 1,051 | 1,135 | 0,443 | 0,449 | 0,438 | 0,445 | 0,439 | 0,436 | 0,417 | 0,392 |
| $N°3$ | 0,968 | 0,984 | 1,005 | 1,118 | 0,412 | 0,420 | 0,432 | 0,518 | 0,426 | 0,427 | 0,430 | 0,463 |
| $N°4$ | 1,098 | 1,116 | 1,133 | 1,238 | 0,635 | 0,631 | 0,631 | 0,631 | 0,579 | 0,565 | 0,558 | 0,510 |
| $N°5$ | 1,003 | 1,025 | 1,049 | 1,167 | 0,411 | 0,410 | 0,429 | 0,526 | 0,409 | 0,400 | 0,409 | 0,451 |
| $\overline{R_s}$ ($\Omega$) | 1,012 | 1,030 | 1,053 | 1,160 | $u(\overline{R_s})$ ($\Omega$) | | | | $u(\overline{R_s})/\overline{R_s}$ | | | |
| $S_{\overline{R_s}}$ ($\Omega$) | 0,051 | 0,052 | 0,049 | 0,047 | 0,637 | 0,633 | 0,633 | 0,633 | 0,629 | 0,615 | 0,602 | 0,545 |

The series resistance $R_s$ presented in Table 1.10 slightly increases with the increase of the polarized DC voltage. For this parameter, the relative uncertainty is quite large, around $50$ % of the parameter value. The measurement uncertainty of $R_s$, around $0.45$ $\Omega$, is much larger than the parameter dispersion of 5 EDLCs which is around $0.05$ $\Omega$. Thus, the majority of the average parameter uncertainty comes from the measurement uncertainty.

The measured values of the dynamic resistance (see Table 1.11) are significantly larger than those of the series resistance, showing that the resistivity of the electrolyte ions in the pores is mainly responsible for the energy dissipation. When the polarized DC voltage increases, the charge density in the pores becomes larger, so the resistivity of the electrolyte in the pores increases, as is clearly shown by the measurements. The measurement uncertainty is about $40$ %. The uncertainty of the measurements is more than twice the standard deviation of the 5 EDLCs samples. This measurement uncertainty constitutes the main part of the uncertainty of the average value.

The obtained value of the leakage resistance corresponds to a leakage current independent of the voltage (about $0.3$ mA after 30 minutes of stabilization of the potential). This phenomenon may be due to the reorganization of the charges inside the pores of the electrodes. The measurement uncertainty and the dispersion of the samples are both quite small (about $2$ %).

The values of the self-discharge resistance (Table 1.13) are quite large and result in a time constant of about one hour, thus confirming that the SC cannot be used to store electricity over long periods. Furthermore, the measurement uncertainty and the dispersion of results are both very large.

The values of charge and energy efficiencies confirm the good behavior of the SC: the charge efficiency is very close to 1 and the energy efficiency is higher than

Table 1.11: Values of $R_d$ with their absolute and relative uncertainty, obtained for 5 EDLCs and for different polarized DC potential values $v_0$.

| | $R_d$ ($\Omega$) | | | | $u(R_d)$ ($\Omega$) | | | | $u(R_d)/R_d$ | | | |
|---|---|---|---|---|---|---|---|---|---|---|---|---|
| $v_0$ | 0 V | 1 V | 2 V | 2,7 V | 0 V | 1 V | 2 V | 2,7 V | 0 V | 1 V | 2 V | 2,7 V |
| $N°1$ | 4,646 | 4,847 | 5,893 | 7,599 | 1,698 | 2,212 | 2,236 | 3,081 | 0,365 | 0,456 | 0,380 | 0,406 |
| $N°2$ | 4,251 | 4,530 | 5,331 | 7,003 | 1,985 | 1,987 | 2,018 | 2,243 | 0,467 | 0,439 | 0,379 | 0,320 |
| $N°3$ | 4,369 | 4,660 | 5,506 | 7,079 | 1,848 | 1,836 | 1,846 | 2,332 | 0,423 | 0,394 | 0,335 | 0,330 |
| $N°4$ | 4,403 | 4,650 | 5,592 | 7,286 | 2,373 | 2,727 | 2,614 | 2,987 | 0,539 | 0,586 | 0,467 | 0,410 |
| $N°5$ | 4,554 | 4,698 | 5,693 | 7,547 | 1,758 | 1,780 | 1,963 | 2,741 | 0,386 | 0,379 | 0,345 | 0,363 |
| $\overline{R_d}$ ($\Omega$) | 4,445 | 4,677 | 5,603 | 7,303 | $u(\overline{R_d})$ ($\Omega$) | | | | $u(\overline{R_d})/\overline{R_d}$ | | | |
| $S_{\overline{R_d}}$ ($\Omega$) | 0,156 | 0,114 | 0,210 | 0,270 | 2,378 | 2,729 | 2,621 | 3,093 | 0,535 | 0,584 | 0,468 | 0,424 |

Table 1.12: Values of $R_{\text{leak}}$ with their absolute and relative uncertainty, obtained for 5 EDLCs and for different voltage levels $v$.

| | $R_{\text{leak}}$ ($k\Omega$) | | | $u(R_{\text{leak}})$ ($\Omega$) | | | $u(R_{\text{leak}})/R_{\text{leak}}$ | | |
|---|---|---|---|---|---|---|---|---|---|
| $v$ | 1 V | 2 V | 2,7 V | 1 V | 2 V | 2,7 V | 1 V | 2 V | 2,7 V |
| $N°1$ | 4,218 | 6,466 | 9,153 | 102,97 | 120,80 | 179,24 | 0,024 | 0,019 | 0,020 |
| $N°2$ | 4,318 | 6,703 | 9,883 | 107,89 | 129,83 | 208,92 | 0,025 | 0,019 | 0,021 |
| $N°3$ | 4,318 | 6,655 | 9,443 | 107,97 | 128,01 | 190,80 | 0,025 | 0,019 | 0,020 |
| $N°4$ | 4,347 | 6,604 | 9,558 | 109,38 | 126,04 | 195,47 | 0,025 | 0,019 | 0,020 |
| $N°5$ | 4,268 | 6,539 | 9,634 | 105,39 | 123,56 | 198,54 | 0,025 | 0,019 | 0,021 |
| $\overline{R_{\text{leak}}}$ ($k\Omega$) | 4,294 | 6,593 | 9,534 | $u(\overline{R_{\text{leak}}})$ ($\Omega$) | | | $u(\overline{R_{\text{leak}}})/\overline{R_{\text{leak}}}$ | | |
| $S_{\overline{R_{\text{leak}}}}$ ($\Omega$) | 51,32 | 93,83 | 267,19 | 120,82 | 160,19 | 339,18 | 0,028 | 0,024 | 0,036 |

Table 1.13: Values of $R_{\text{sd}}$ with their absolute and relative uncertainty, obtained for 5 EDLCs.

| | $R_{\text{sd}}$ ($k\Omega$) | $u(R_{\text{sd}})$ ($k\Omega$) | $u(R_{\text{sd}})/R_{\text{sd}}$ |
|---|---|---|---|
| $N°1$ | 3,671 | 2,397 | 0,653 |
| $N°2$ | 2,934 | 1,644 | 0,560 |
| $N°3$ | 2,868 | 1,413 | 0,493 |
| $N°4$ | 4,003 | 3,109 | 0,777 |
| $N°5$ | 4,449 | 4,470 | 1,005 |
| $\overline{R_{\text{sd}}}$ ($k\Omega$) | 3,585 | $u(\overline{R_{\text{sd}}})$ ($k\Omega$) | $u(\overline{R_{\text{sd}}})/\overline{R_{\text{sd}}}$ |
| $S_{\overline{R_{\text{sd}}}}$ ($k\Omega$) | 0,683 | 4,522 | 1,261 |

Table 1.14: Values of $\eta_c$ et $\eta_e$ with their absolute and relative uncertainty, obtained for 5 EDLCs.

| | $\eta_c$ | $\eta_e$ | $u(\eta_c)$ | $u(\eta_e)$ | $u(\eta_c)/\eta_c$ | $u(\eta_e)/\eta_e$ |
|---|---|---|---|---|---|---|
| $N°1$ | 0,9976 | 0,8818 | $2,30\ 10^{-5}$ | $2,84\ 10^{-5}$ | $2,31\ 10^{-5}$ | $3,23\ 10^{-5}$ |
| $N°2$ | 0,9980 | 0,8849 | $2,38\ 10^{-5}$ | $2,94\ 10^{-5}$ | $2,39\ 10^{-5}$ | $3,32\ 10^{-5}$ |
| $N°3$ | 0,9983 | 0,8872 | $2,34\ 10^{-5}$ | $2,89\ 10^{-5}$ | $2,34\ 10^{-5}$ | $3,26\ 10^{-5}$ |
| $N°4$ | 0,9973 | 0,8820 | $2,35\ 10^{-5}$ | $2,90\ 10^{-5}$ | $2,35\ 10^{-5}$ | $3,28\ 10^{-5}$ |
| $N°5$ | 0,9977 | 0,8819 | $2,36\ 10^{-5}$ | $2,91\ 10^{-5}$ | $2,36\ 10^{-5}$ | $3,30\ 10^{-5}$ |
| $\overline{\eta}$ | 0,998 | 0.884 | $u(\overline{\eta_c})$ | $u(\overline{\eta_e})$ | $u(\overline{\eta_c})/\overline{\eta_c}$ | $u(\overline{\eta_c})/\overline{\eta_c}$ |
| $S_{\overline{\eta}}$ | $3,76\ 10^{-4}$ | $2,40\ 10^{-4}$ | $3,77\ 10^{-4}$ | $2,40\ 10^{-4}$ | $3,78\ 10^{-4}$ | $2,72\ 10^{-4}$ |

what is usually obtained with a battery (about 75%), due to the electrostatic and non electrochemical charge storage mechanism of EDLCs. The measurement uncertainty and the dispersion of results are very small, which shows the quality of both parameters and the possibility to provide a reliable EDLC diagnosis based on these characteristics.

### 1.4.2 Parameters evolution resulting from the EDLCs aging

#### Aging experiment

The accelerated calendar aging test bench consists of five main parts (see Fig. 1.20): 100 independent EverCAP EDLCs manufactured by Nichicon with a nominal capacitance of 1 F and a nominal maximum voltage of 2.7 V, two thermostatic chambers (one providing the desired aging temperature, another providing a constant room temperature for EDLCs analysis), a DC constant voltage power supply and a multipotentiostat (Biologic VMP3). To generate an accelerated aging process, the EDLCs were placed up to 10 weeks in the heating chamber at 60° C with the floating voltages of 0 V and 2.5 V provided by the voltage source. Each week, 5 EDLCs aged at 0 V and another 5 aged at 2.5 V are taken out from the heating chamber and characterized with the VMP3 at 25° C. After the characterization, these EDLCs are stored at constant room temperature to avoid their aging for later use and characterization.

#### The parameters evolution

Fig. 1.21 illustrates the impedance plots of EDLCs at different aging phases during the accelerated calendar aging process at 60° C and 2.5 V. It is clear to see from the figure the obvious aging of EDLC: the impedance spectrum moves towards right.

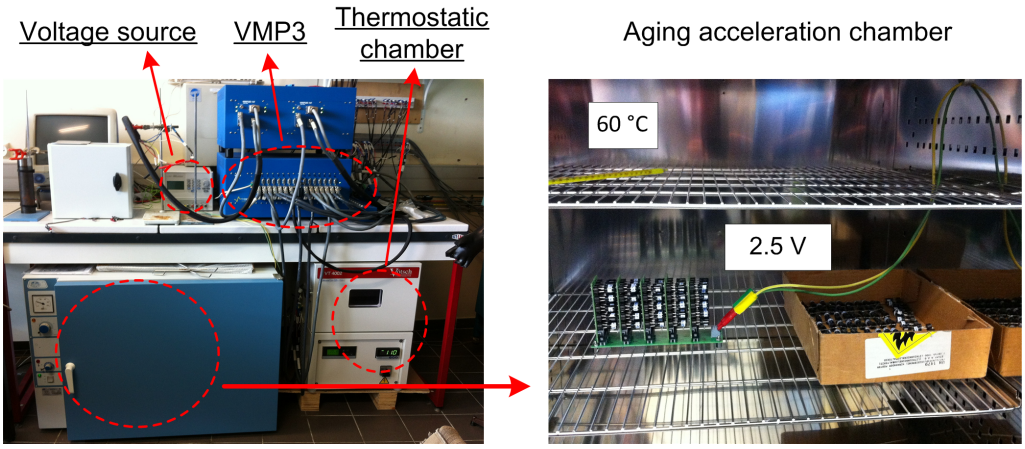


Figure 1.20: Accelerated aging test bench.

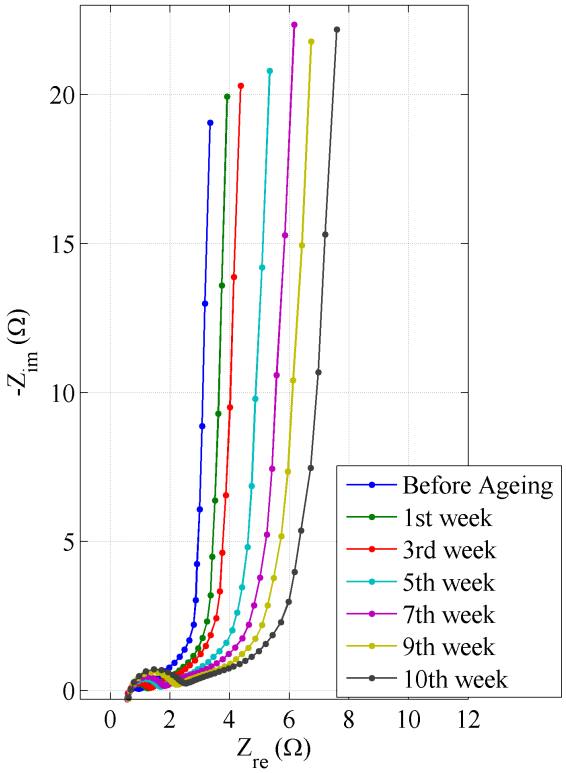


Figure 1.21: Impedance spectrum of differently aged EDLCs in the accelerated calendar aging test.

Figs. 1.22 to 1.30 present the evolution of the characteristic parameters resulting from the EDLCs' aging by showing the average parameter value of 5 EDLCs and their dispersion. Since the EDLCs have a more complete charge/discharge process in a CV test at a smaller scanning rate, i.e. 10 mV/s, the integral capacitance computed at this rate is used each week to observe the EDLCs' aging. This capacitance and the differential capacitance stay almost the same when the EDLCs are aged at 0 V, while when the EDLCs are aged at 2.5 V, they decrease by around 10%. These evolutions show that the degradation of capacitance of this kind of EDLC occurs when the EDLCs are always performed at a high voltage. This characteristic leads to recommend the user to avoid to keep using EDLCs at a high voltage range during a long period in order to extend their lifetime. Fig. 1.24 clearly shows that the differential capacitance depends on the terminal DC voltage $v_0$. This dependency can be approximated as linear which can be described by the following equation:

$$C_{\text{diff}} = C_0(1 + \alpha v_0) \tag{1.70}$$

where $C_0$ is the no load capacitance and $\alpha$ is a voltage sensitivity coefficient. The variation of voltage dependency degree resulting from the EDLC aging can be revealed from the coefficient $\alpha$. By a linear fitting of $C_{\text{diff}}$ vs. $v_0$ curve shown in Fig. 1.24, the evolutions of $\alpha$ for the EDLCs respectively aged at 0 V and at 2.5 V are obtained and shown in Fig. 1.25. For the EDLCs aged at 0 V, the voltage sensitivity coefficient $\alpha$ has increased around 18 % at the end of aging experiment while for the EDLCs aged at 2.5 V, $\alpha$ has an significant decrease about 27 %. It implies that the voltage dependency of capacitance gets more serious in the aging process where the EDLCs are always under a low voltage. In the opposite, the voltage dependency feature becomes less important during the aging under a high voltage.

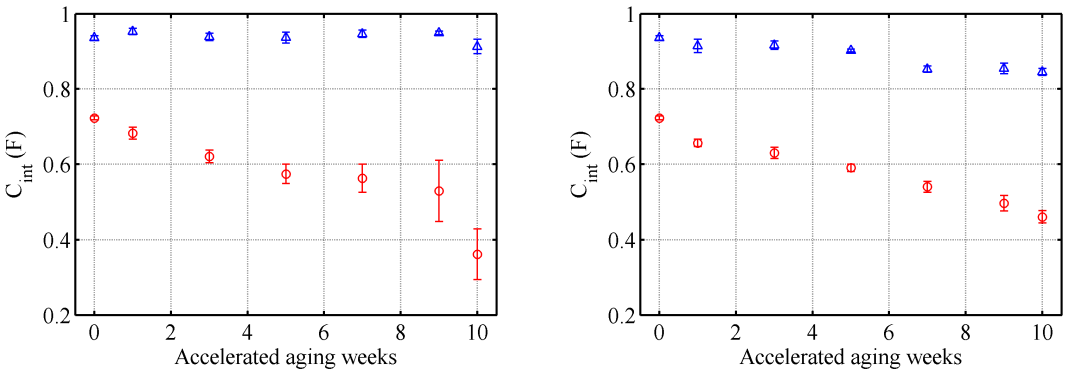


(a) EDLCs aged at 0 V (b) EDLCs aged at 2.5 V

Figure 1.22: Evolution of integral capacitance $C_{\text{int}}$ with EDLC aging (red circle: 100 mV/s, blue up-triangle: 10 mV/s).

It is obvious to see from Figs. 1.26 and 1.27 that the series resistance $R_s$ and

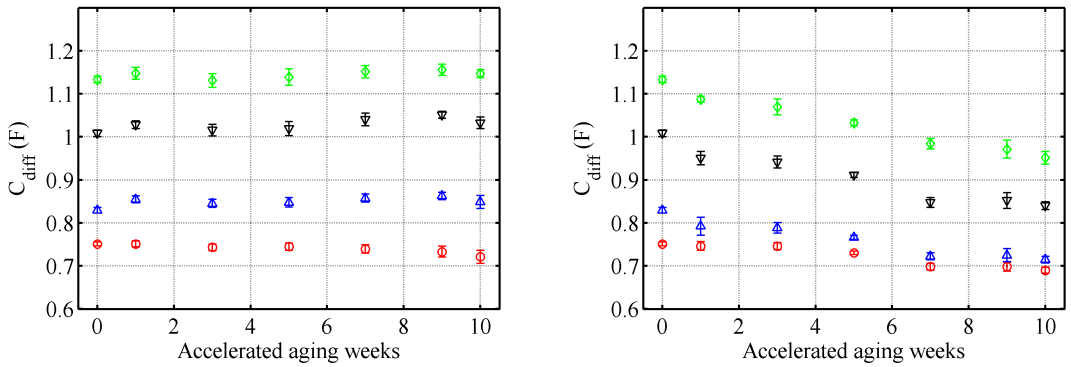


(a) EDLCs aged at 0 V (b) EDLCs aged at 2.5 V

Figure 1.23: Evolution of differential capacitance $C_{\text{diff}}$ with EDLC aging (red circle: 0 V, blue up-triangle: 1 V, black down-triangle: 2 V, green diamond: 2.7 V).

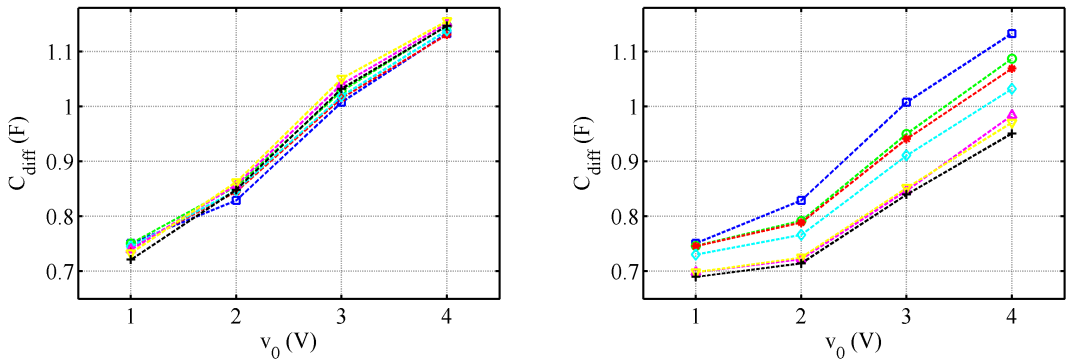


(a) EDLCs aged at 0 V (b) EDLCs aged at 2.5 V

Figure 1.24: Voltage dependent differential capacitance in different EDLC aging phases (blue square: before aging, green circle: 1st week, red star: 3rd week, cyan diamond: 5th week, m up-triangle: 7th week, yellow down-triangle: 9th week, black plus: 10th week).

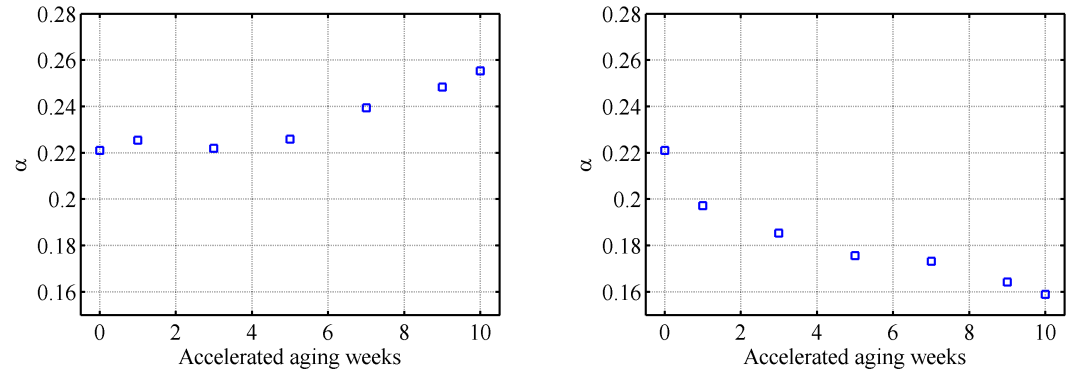


(a) EDLCs aged at 0 V (b) EDLCs aged at 2.5 V

Figure 1.25: Evolution of voltage sensitivity coefficient $\alpha$ with EDLC aging.

the dynamic resistance $R_d$ significantly increase with EDLCs' aging. The increase of $R_s$ can be explained by the expanded semi-circle in the impedance spectrum (Fig. 1.21) which is mainly caused by the degradation of the interface between the electrode and electrolyte. The series resistance $R_s$ of the EDLCs aged at $0$ V has increased by around $400\%$ at the end of the aging experiments with an increasing parameter dispersion. For the EDLCs aged at $2.5$ V, $R_s$ has increased by about $150\%$. It indicates that the lower the working voltage is during aging, the faster the series resistance increases. This is the opposite for the capacitance and dynamic resistance. The dynamic resistance of the EDLCs aged at a higher voltage has a much higher growth rate than that of the EDLCs aged at a lower voltage. It means that the resistivity of the ions of the electrolyte in the pores increases with aging, especially under high voltage. Since $R_s$ and $R_d$ evolve significantly with time, they can be considered as good indicators of EDLCs' aging.

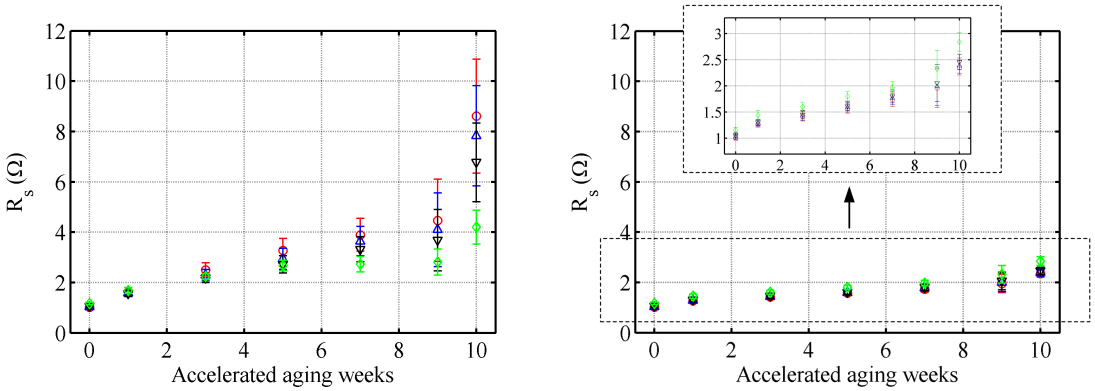


(a) EDLCs aged at 0 V (b) EDLCs aged at 2.5 V

Figure 1.26: Evolution of the series resistance $R_s$ with EDLC aging (red circle: $0$ V, blue up-triangle: $1$ V, black down-triangle: $2$ V, green diamond: $2.7$ V).

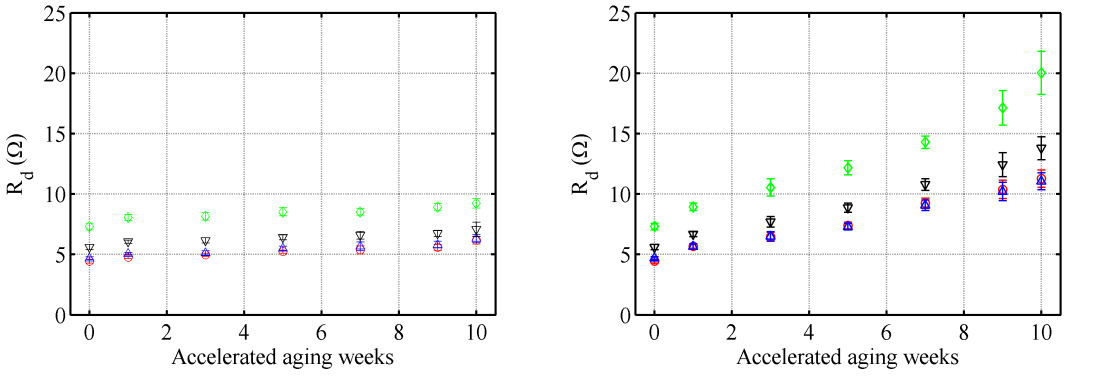


(a) EDLCs aged at 0 V (b) EDLCs aged at 2.5 V

Figure 1.27: Evolution of the dynamic resistance $R_d$ with EDLC aging (red circle: $0$ V, blue up-triangle: $1$ V, black down-triangle: $2$ V, green diamond: $2.7$ V).

For the leakage resistance $R_{\text{leak}}$, the variation with aging is not very obvious.

The self-discharge $R_{\text{sd}}$ decreases slightly with aging, but with a very large dispersion. Thus, it is not suggested to use these parameters as indicators of the EDLCs aging.

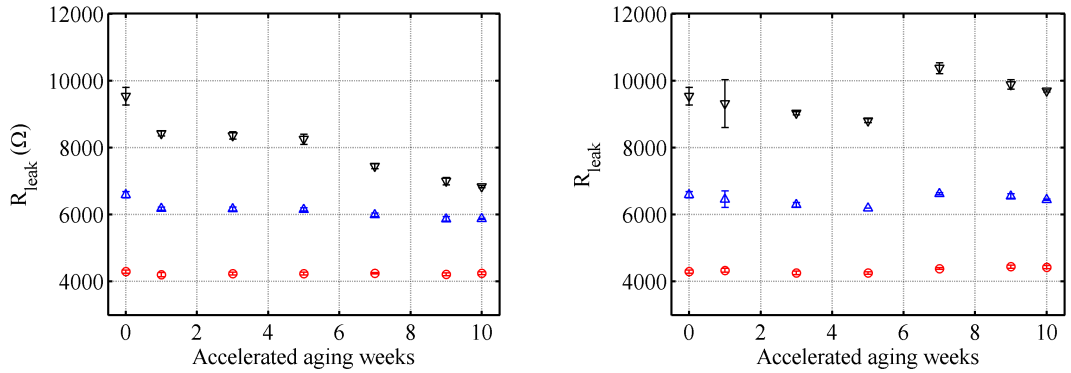


(a) EDLCs aged at 0 V (b) EDLCs aged at 2.5 V

Figure 1.28: Evolution of the leakage resistance $R_{\text{leak}}$ with EDLC aging (red circle: 1 V, blue up-triangle: 2 V, black down-triangle: 2.7 V).

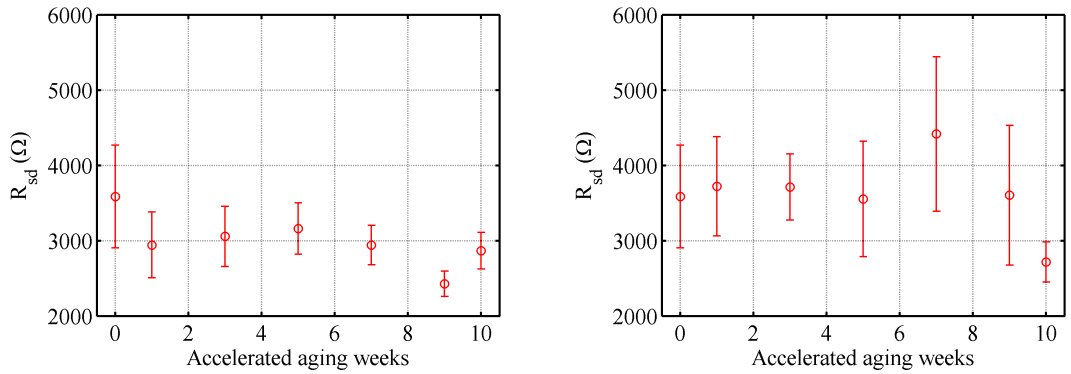


(a) EDLCs aged at 0 V (b) EDLCs aged at 2.5 V

Figure 1.29: Evolution of self-discharge resistance $R_{\text{sd}}$ with EDLC aging.

As is shown in Fig. 1.30, the charge efficiency has stayed almost the same during all the aging process. While the energy efficiency $\eta_e$ has a significant decrease of about $15\%$ at the end of the aging experiment, which manifests that the aged EDLCs will lose more energy during their usage. This is due to the increase of the series resistance during the EDLCs' aging (see Fig. 1.26) which aggravates the energy dissipation. The significant decrease of the energy efficiency during EDLCs aging happened for both low and high aging voltage. Thus, the energy efficiency could be considered as a very interesting aging indicator thanks to its voltage independent feature.

To determine which parameters are reliable offline aging indicators, both the estimation quality and the aging sensitivity of the parameters should be considered. The estimation quality of each paramter has been assessed from their uncertainties

(Table 1.8 - 1.14), while the aging sensitivity has been obtained from the evolution of the parameters estimation (Fig. 1.22 - 1.30). They are summarized in Fig. 1.31. It reveals that the three parameters, $R_s$, $R_d$ and $\eta_e$, can be considered as reliable offline aging indicators for the tested EDLC.

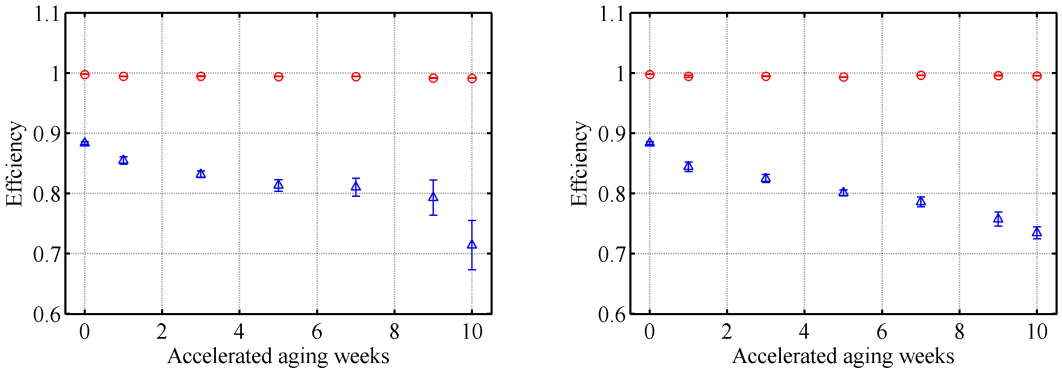


(a) EDLCs aged at 0 V (b) EDLCs aged at 2.5 V

Figure 1.30: Evolution of the charge efficiency $\eta_c$ and energy efficiency $\eta_e$ with EDLC aging (red circle: charge efficiency, blue up-triangle: energy efficiency).

| | Estimation quality (uncertainty study) | Aging sensitivity (aging study) |
|---|---|---|
| $C_{int}$ | ★ ★ ★ | ★ ☆ ☆ |
| $C_{diff}$ | ★ ★ ☆ | ★ ☆ ☆ |
| $R_s$ | ★ ☆ ☆ | ★ ★ ★ |
| $R_d$ | ★ ☆ ☆ | ★ ★ ★ |
| $R_{sd}$ | ★ ☆ ☆ | ★ ☆ ☆ |
| $R_{leak}$ | ★ ★ ★ | ★ ☆ ☆ |
| $\eta_c$ | ★ ★ ★ | ★ ☆ ☆ |
| $\eta_e$ | ★ ★ ★ | ★ ★ ★ |

Figure 1.31: Parameters assessment for reliable offline aging indicators.

# Conclusion

In this chapter, a state of the art about the existing offline characterization for EDLCs has been done. Based on that, we have defined some physical parameters of EDLCs for their aging monitoring. Several characterization techniques, such as cyclic voltammetry and electrochemical impedance spectroscopy, are used and the calculation of these parameters are given. In order to assess the quality of the proposed characterization techniques, the uncertainty of each parameter has been computed, so as to know if they can be used for aging monitoring purposes.

In the last part, experimental results are given and analyzed. First of all, the parameter values of a fresh EDLC with their uncertainties are presented. The integral capacitance obtained at a low voltage scanning rate in a CV test has very small uncertainty and thus can be considered as a good variable to minitor the EDLCs aging. The differential capacitance clearly shows a voltage dependent feature and that is why the capacitance is often called SoC (state of charge)-dependent. Since the differential capacitance depends on voltage, the integral capacitance is preferred to determine the EDLCs' capacitance. Compared to the capacitive parameters, the series resistance, the dynamic resistance and the self-discharge resistance have higher uncertainty which is mainly due to the measurement. The leakage resistance which also depends on the terminal voltage has a quite small uncertainty. It is confirmed from the high values of charge and energy efficiencies that the EDLCs have better performance than some other storage device such as the batteries. In the second place, the parameters evolution together with their five-samples dispersion during a 10 weeks accelerated aging process are presented. The results show that for the used Nichicon EDLCs, the capacitance has only slightly decreased while the series resistance and the dynamic resistance have increased significantly with EDLCs' aging and thus could be good indicators for the aging monitoring. The leakage resistance and self-discharge resistance are not suggested to monitor the EDLCs' aging due to the unclear evolution or large dispersion. Compared to the quite constant charge efficiency evolution, the energy efficiency of EDLCs has a significant decrease with a quite small dispersion during the aging process. Furthermore, the decrease of the energy efficiency seems to be independent of the aging voltage. For this, the energy efficiency could be considered as a good indicator for the offline monitoring of EDLCs' aging.

The following chapters are dedicated to the design of an online method to monitor the EDLCs' aging in an industrial application. The second chapter will present how to choose the appropriate model for the online aging monitoring. The third chapter will present the design of state estimators based on state observer theory. The offline characterization results obtained in this chapter will be considered as a reference when analyzing the online aging monitoring results in the third chapter.

# 2

# Modeling of supercapacitors

## Introduction

The objective of this thesis is to propose an in-situ online low-cost aging monitoring system for EDLCs, through the observation of the parameter estimators during their life. There exists a wide range of methods for model identification, each one with its own advantages and disadvantages [62]. For example, the discrete recurrence equations and identification algorithms derived from the least square framework are often used for the synthesis of control laws [63]. But if the goal is to deeply understand the system behavior, then the identification of continuous-time knowledge models presents more attractive features, particularly because their parameters have a physical meaning and thus can be more simply related to the physical phenomena occurring in the monitored system [64] [65]. For the user, the choice of the system identification method depends on the industrial context concerning the available signals, the available system excitation in operating condition, the dynamic behavior of the aging process, the noise characteristics, the modeling non-linearities, the acceptable computational cost of the identification algorithm, and also the designer's experience.

As explained in the introduction of the thesis, in order to design an online aging monitoring system for EDLCs, we intend to use model based real-time observers, such as Kalman filters, particularly because they offer a very low computational cost which deals with our industrial problematics, and because of our knowledge of this algorithm. Concerning the model of EDLCs used in this aging monitoring

system, we considered continuous-time knowledge models in the form of electrical circuits, because the parameters of such models can be directly related to physical phenomenas and thus may allow to explain the aging of the EDLCs. Accordingly, the problem becomes to select an appropriate model structure of the EDLCs for the online aging monitoring system.

The optimal experimental design and the selection of linear models have been widely used by the statisticians since 1930s [62] [66]. But these studies have been seldom applied in the electrical engineering domain, probably due to the difficulty caused by the nonlinearity of the systems. In this chapter, we propose to use three comprehensive criteria mainly based on the geometric study of the hyper-surface of the output error energy in the relative parametric space. This approach, derived from the system identification by the output error method (also called "Méthode du modèle" in french), allows to use comprehensive comparison criteria without any assumption about the statistical characteristics of the system disturbances (for instance, the noises) [67]. This is specially interesting when the modeling noise is far more important than the measurement noise, which is particularly the case for EDLCs, because the behavior of an EDLC is too complicated to be accurately modeled.

In this chapter, an overview of the popular EDLCs model structures proposed in relevant publications is firstly presented. In the second part, three criteria (the output error energy, the uncertainty of parameter estimation and the aging diagnosis ability) are proposed to select an appropriate model for online EDLCs aging monitoring. The details about how the study of output error energy in the parametric space allows to evaluate the uncertainties of the estimated parameters for a given input signal protocol by using the relative sensitivity functions are presented. In the last section, several model structures are compared by applying the proposed methodology using the experimental data presented in the previous chapter so as to determine the best model.

## 2.1 State of the art

### 2.1.1 Classical models

To study the physical behavior of EDLCs and to characterize them, a lot of studies have been devoted to the modeling of EDLCs. Most of these models can be derived from two main classical EDLC models: one is the simple first-order RRC model and the other one is the transmission line model.

### Classical simple RRC model

Fig. 2.1 shows a first-order RRC model including a capacitance $C$, an equivalent series resistance $R_s$ and a parallel resistance $R_p$ [1] [68] [51]. $C$ is the charge storage capability of the EDLC. $R_s$ is responsible for the energy lost by internal heating of the EDLC. $R_p$ corresponds to the self-discharge phenomenon of the EDLC which deteriorates the long-term energy storage performance. Normally, $R_p$ has a much higher value than $R_s$ (thousands of Ohms compared to several Ohms for the series resistance for the tested Nichicon EDLC). The impedance of this RRC model is expressed as:

$$Z(\jmath\omega) = R_s + \frac{R_p}{1 + \jmath\omega R_p C} \tag{2.1}$$

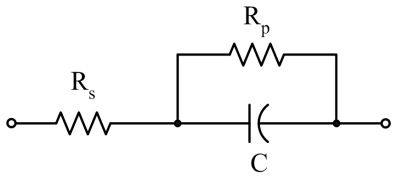


Figure 2.1: First-order RRC model.

This model is suitable for describing the simple charge and discharge of EDLCs without high requirement of an accurate physical behavior description. In [69], the authors used this model in simulations in order to design and evaluate the charge-balancing circuits of supercapacitor systems. This EDLC model is also used in [25] for the dynamic modeling of a wind/fuel cell/supercapacitor hybrid power generation system.

The parallel resistance $R_p$ is often neglected when the long-term performance of EDLCs is not considered in the study. For example, in [70], the authors have developed an automated high current cycling test system for supercapacitor characterization, where a simple RC model neglecting $R_p$ is used because the supercapacitors are charged or discharged with a high current within a very short duration. The simplified RC model with only a resistor in series with a capacitor is often used by manufacturers to characterize their products. It is also frequently used to represent the energy storage capacity for global management of a power system using EDLCs as energy storage devices.

Since the EDLC's behavior is very complex due to its physical construction, for example the porous electrodes, this model is just a simplified model which cannot accurately fit the EDLC's behavior over a wide frequency range.

### Transmission line model

The EDLCs have a high capacitance thanks to the high surface area of the electrodes made by large area powders, fibrous or porous materials. These materials

have complex physical structures which can be formed by plenty of irregularly distributed pores [1] as shown in Fig. 3. Therefore, the crucial part to obtain an accurate EDLC model is the modeling of the electrochemical behavior of the electrode pores.

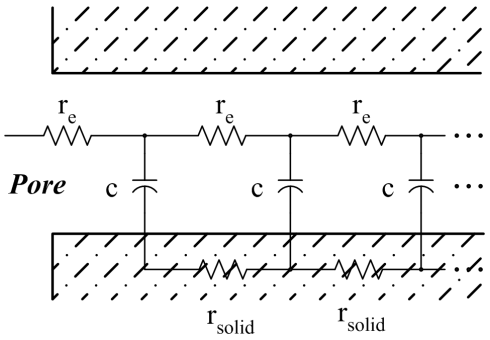


Figure 2.2: Equivalent circuit model of a pore [1].

The porous electrode was firstly described by a RC transmission line net by de Levie in 1963 [71]. The pores of the electrodes are assumed to be circular cylinders of uniform diameter and to be homogeneously filled with electrolyte. The main current existing in the pore consists of an ionic current through the electrolyte, an electronic current through the electrode and a displacement current at the electrode-electrolyte interface. The ionic and electronic currents are caused by the movement of the ions in the electrolyte and of the electrons in the electrodes. The displacement current is a result of the rearrangement of the charges at electrode-electrolyte interface. Fig. 2.2 shows the electrical circuit model of a pore, where $r_e$ and $r_{\text{solid}}$ are electrolyte and electrode resistances per unit length and $c$ represents the capacitance per unit length at electrode-electrolyte interface. Since the electrode conductivity is much higher than the electrolyte conductivity, the resistance of the electrode material is often neglected when modeling a pore behavior. Then, the simplified ideal model of pore is shown in Fig. 2.3.

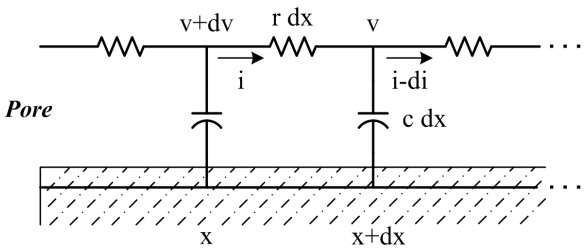


Figure 2.3: Equivalent ideal circuit model of a pore [1].

With the notations specified in Fig. 2.3, the differential system governing volt-

age and current evolution along the transmission line is expressed by [1] [72]:

$$\begin{cases} \frac{\partial v}{\partial x}(x,t) = -ri(x,t) \\ \frac{\partial i}{\partial x}(x,t) = -c\frac{\partial v}{\partial t}(x,t) \end{cases} \tag{2.2}$$

The following equations are obtained by differentiating Eq. 2.2:

$$\begin{cases} \frac{\partial^2 v}{\partial x^2}(x,t) = rc\frac{\partial v}{\partial t}(x,t) \\ \frac{\partial^2 i}{\partial x^2}(x,t) = rc\frac{\partial i}{\partial t}(x,t) \end{cases} \tag{2.3}$$

Applying a Laplace transformation to Eq. 2.3, and then the general solutions of these two differential equations in the frequency domain can be obtained:

$$\begin{cases} V(x,s) = Ae^{-x\sqrt{src}} + Be^{x\sqrt{src}} \\ I(x,s) = \frac{\sqrt{src}}{r}\left(Ae^{-x\sqrt{src}} - Be^{x\sqrt{src}}\right) \end{cases} \tag{2.4}$$

Supposing that $l$ is the maximum length of the pore, then $I(l,s) = 0$ and it is obtained that $Ae^{-l\sqrt{src}} = Be^{l\sqrt{src}}$. Combining this obtained equation with Eq.2.4, the simplified voltage and current expressions are obtained:

$$\begin{cases} V(x,s) = 2Be^{l\sqrt{src}}\cosh(\sqrt{src}(l-x)) \\ I(x,s) = 2B\frac{\sqrt{src}}{r}e^{l\sqrt{src}}\sinh(\sqrt{src}(l-x)) \end{cases} \tag{2.5}$$

Then the impedance is determined at $x = 0$:

$$Z(\jmath\omega) = \frac{V(0,\jmath\omega)}{I(0,\jmath\omega)} = \frac{r}{\sqrt{\jmath\omega rc}}\coth(l\sqrt{\jmath\omega rc}) \tag{2.6}$$

Replacing the local parameters $r$ and $c$ by the pore total resistance $R$ and the pore total capacitance $C$: $R = rl,\ C = cl$. Therefore, a final analytical expression of the pore impedance can be obtained [2] [44]:

$$Z_p = \sqrt{\frac{R}{\jmath\omega C}}\coth\left(\sqrt{\jmath\omega RC}\right) \tag{2.7}$$

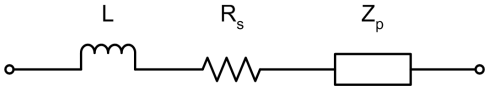


Figure 2.4: The EDLC equivalent circuit model [43].

Finally, the impedance of the whole EDLC equivalent circuit model (shown in

Figure 2.4) is obtained by adding a series resistance $R_s$ and an inductance $L$ which explains the high frequency behavior of an EDLC [73] [43].

$$Z = R_s + \jmath\omega L + \sqrt{\frac{R}{\jmath\omega C}} \coth\left(\sqrt{\jmath\omega RC}\right) \tag{2.8}$$

Here, the inductance $L$ is often neglected because it is insignificant except at very high frequencies which is often out of the current/voltage frequency bandwidth in most industrial applications.

At very low frequency, this impedance model provides an impedance spectrum as a vertical line while for a real EDLC, the impedance spectrum presents a small slope [2] [74]. This difference comes from the assumption of an uniform pore distribution, without considering the charge redistribution and self-discharge phenomenons. In order to include these phenomenons in the model, R. Kotz has proposed to add a Constant Phase Element (CPE) to the pore impedance expression (Eq. 2.7) [2]. The improved impedance pore model replaces every $\jmath\omega$ in Eq. 2.8 by $(\jmath\omega)^\gamma$, where $0 < \gamma < 1$. The analytical expression of the EDLCs' impedance neglecting the inductance thus becomes:

$$Z = R_s + \sqrt{\frac{R}{(\jmath\omega)^\gamma C}} \coth\left(\sqrt{(\jmath\omega)^\gamma RC}\right) \tag{2.9}$$

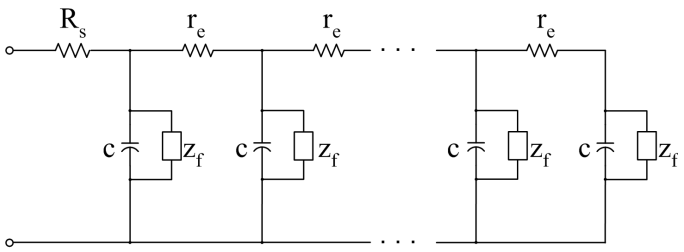


Figure 2.5: Equivalent electrical transmission line model of an EDLC [71].

This model with CPE provides a very satisfying fitting of the impedance between the model and the experimental spectrum in a wide frequency range. But it is necessary to make impedance measurements before to fit this frequency domain model. Furthermore, it is not always easy to find a physical meaning of this parameter $\gamma$. Therefore, in order to get an equivalent RC electrical circuit model in time domain instead of the mathematical expression above, a transmission line electrical model (Fig. 2.5) with a Faradaic impedance $Z_f$ across the capacitor in each branch was proposed by de Levie [71] [1]. The added $Z_f$ has the same role as the constant phase element in Eq. 2.9, and represents the long-term phenomenons such as charge redistribution and self-discharge. When simulating the EDLC by this circuit, the Faradaic impedance is usually simplified as a leakage resistance.

Because the value of the leakage resistance is much larger than the series resistance and electrolyte resistance, many researchers have replaced the $n$ leakage resistors by one resistor in parallel with the transmission line to simplify the circuit [75] [76]. The transmission line model has a dynamic behavior very close to a real EDLC but apparently it has a fairly complex structure.

After the mathematical expression with CPE and the transmission line circuit have been proposed, a large number of research works on the EDLCs' behavior based on the transmission line model have been carried out. In [74] and [77], the authors characterized the parameters of this model during the EDLCs aging and finally derived an aging model of the EDLCs which allows to predict the EDLCs' aging. To go further, the authors in [55] used voltage dependent capacitors in the transmission line model proposed by Levie for the modeling of EDLCs used as peak power sources. In [78], an approximative rational fractional model of EDLC obtained from the analytical impedance expression contributed to the success of an online EDLC parameter estimation.

### 2.1.2 Recent variant models

According to the different requirements of the applications, several models have been recently proposed and developed. There are mainly three groups of models, based on which studies have been carried out for the different applications of EDLCs.

#### Three-branch model

L. Zubieta has proposed an equivalent electrical model of an EDLC for applications in power electronics [79]. The proposed model shown in Fig. 2.6 consists of a leakage resistance and three RC branches with different time constants in parallel. The first branch, called immediate branch, is made of a resistor $R_i$ in series with a voltage dependent capacitor consisting of a fixed capacitance $C_{i0}$ and a voltage dependent capacitor $C_{i1}V_i$. This first branch manifests for the immediate behavior in the time range of seconds. The second branch, called delayed branch, consisting of $R_d$ and $C_d$ in series, is mainly responsible for the EDLCs' behavior in the time range of minutes. The third branch, called long term branch, with $R_l$ and $C_l$ in series, has a time constant of more than $10$ minutes. The last two branches represent the charge redistribution phenomenon and the leakage resistance represents the self-discharge phenomenon in a long-term period. This model simulates the dynamic behavior of the EDLC below $1$ mHz very well but not for the frequencies higher than $10$ mHz. Furthermore, at low voltages, the error between the simulated voltage based on the proposed model and the experimental voltage is quite large because of the assumption that only the capacitance of the first branch is voltage

dependent. Another disadvantage of this model is the large number of parameters, 8 in this case, which may cause difficulty in the context of online identification.

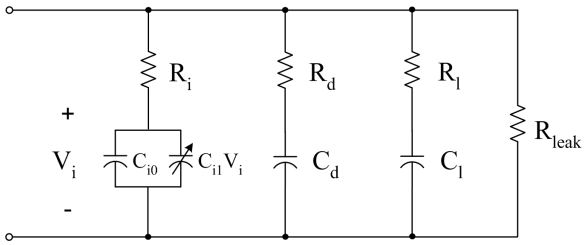


Figure 2.6: Three-branch model [79].

### Series RC branch model

Fig. 2.7 shows a model with RC branches in series. This model was firstly proposed by S. Buller in 2002 [43] and then became very popular in many other modeling studies of EDLCs. This electrical model is derived from the impedance model of EDLCs expressed by Eq. 2.8. This impedance model in the frequency domain has been transformed into the time domain, leading to the so called series RC branch model. This proposed model consists of a series resistor $R_s$ , a capacitor $C$ and $n$ RC elements in series. The values of the capacitor $C_n$ and the resistor $R_n$ in the RC branches are given by [43]:

$$C_n = \frac{C}{2}\ , \quad R_n = \frac{2R}{n^2\pi^2} \tag{2.10}$$

where $C$ and $R$ are the capacitance and the electrolyte resistance in Eq. 2.8.

Since this model is derived from the impedance model in the frequency domain, it is able to simulate the EDLCs' behavior in a wide frequency range between 10 mHz and several hundred Hz [80]. Another important advantage of this model is that there are only three parameters to determine, $R_s$, $C$ and $R$. This feature makes the characterization of an EDLC much easier. The drawback of this model is that it is not able to represent the charge redistribution or self-discharge phenomenon of the EDLC, which takes place at very low frequencies.

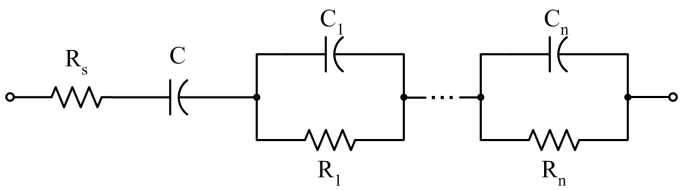


Figure 2.7: Series RC branch model [43].

In fact, this model and the de Levie transmission line model (described by Fig. 2.5) ignoring $Z_F$ are formally very similar because both models lead to the

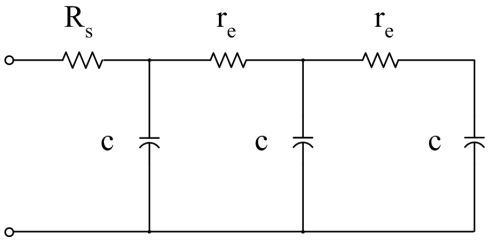


Figure 2.8: Third-order transmission line model of an EDLC.

same impedance expression if one takes special values of the resistances and capacitances. For example, the impedance of the third-order transmission line model shown in Fig. 2.8 is:

$$Z = R_s + \frac{1 + 3j\omega r_e c - \omega^2 r_e^2 c^2}{3j\omega c - 4\omega^2 r_e c^2 - j\omega^3 r_e^2 c^3} \tag{2.11}$$

For a series RC branch model as shown in Fig. 2.7 with two RC branches in series ($n = 2$), if their parameters are chosen as, for example, $R_1 = \frac{1}{2}r_e$, $R_2 = \frac{1}{18}r_e$, $C_1 = 2c$, $C_2 = 6c$ and $C = 3c$, then the impedance of this series RC branch model becomes the same as that of the third-order transmission line model shown in Eq. 2.11. Therefore, this series RC branch model just uses another circuit connection instead of transmission line net to simulate the behavior of an EDLC.

### Modified series RC branch model

After the proposition of the series RC branch model, some researchers have developed and proposed improved models. Considering that the limit of the series RC branch model is that it does not take into account the charge redistribution in the pores with irregular sizes, A. Hammar has proposed a model called multipore model [34] (see Fig. 2.9). The authors consider that the series RC branch model proposed by S. Buller can only describe a single pore behavior. Thus, they proposed to parallel several series RC branches to describe the behavior of the pores with different sizes. The number of the paralleled branches are chosen at least equal to three to acquire an adequate simulated behavior of the EDLC. This model is used in [81] to observe the evolution of the parameters of the EDLCs during their aging. The problem of this model is its large number of parameters and the complex electrical structure.

The authors of [82] have proposed a modified model based on the series RC branch model. In order to include the redistribution and self-discharge phenomenons, they added another two RC branches and a leakage resistance in parallel with the series RC branch model as shown in Fig. 2.10. The proposed model was used to determine the effect of parameter variations on the dynamic response of supercapacitors [82].

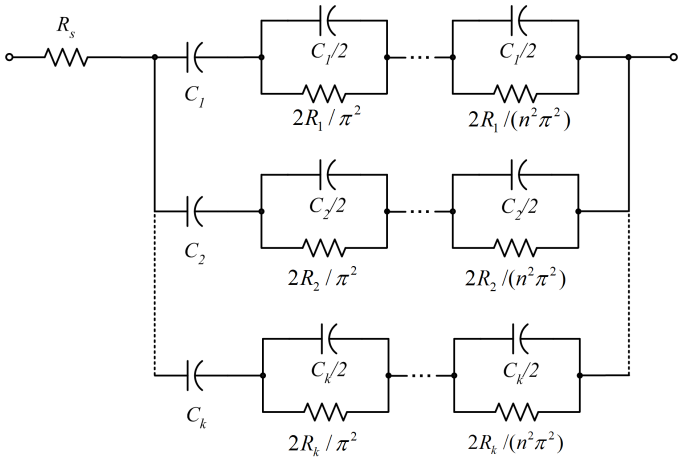


Figure 2.9: Multi-pore model [34].

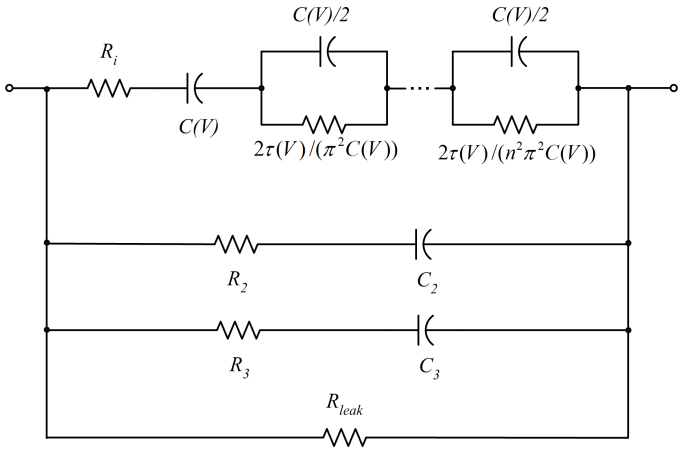


Figure 2.10: Modified series RC branch model in [82].

These modified models have indeed improved the accuracy of the supercapacitors model in a wide frequency range. However, the price to pay is the more complex electrical structure and the large number of parameters. So it seems that, no matter simple or complicated models, they have their own advantages and shortcomings and should be chosen according to the requirement of their application. For our objective of EDLCs aging monitoring by online parametric identification, what kind of model should be used? Can we be satisfied with the very simple RC model or is it necessary to use more complex model and if yes, how complex it should be? The following sections will propose some answers.

## 2.2 Model structure selection using the output error method

### 2.2.1 Introduction

The flowchart in Fig. 2.11 resumes the usual process for the research of a dedicated model structure from experimental data [65] [67] [62]. The term "structure" refers to a set of mathematical equations that links the outputs to the inputs of a system, whereas "model" refers to the association of a given structure and its estimated parameters, for a given input-output data set.

As explained in the introduction of this chapter, we initially decided to explore the opportunity of using real-time state observers for online aging monitoring of the EDLCs. Accordingly, the problem becomes to select a model structure which well suits its practical implementation constraints, and which represents the best trade-off between the complexity and the performance of the model:

– *Performance*

  The performance of a model refers to the adequacy of the model to the system and the ability of the model to explain the relationship between the physical parameter changes and the state of health of an EDLC. More precisely, a model with a good performance should be able to simulate the EDLCs' behavior as close as that of a real system. It should also be able to help the user to build an aging diagnosis indicator. For example, it is well-known that the estimated series resistance of many usual EDLC models evolves in the same range with aging as well as with temperature, and thus it becomes difficult without the temperature measurement to determine if the evolution of the resistance is due to the aging or due to a change of the environmental temperature. From this point of view, a structure based on which a reliable state of health indicator independent of temperature can be built, is considered to have good performance.

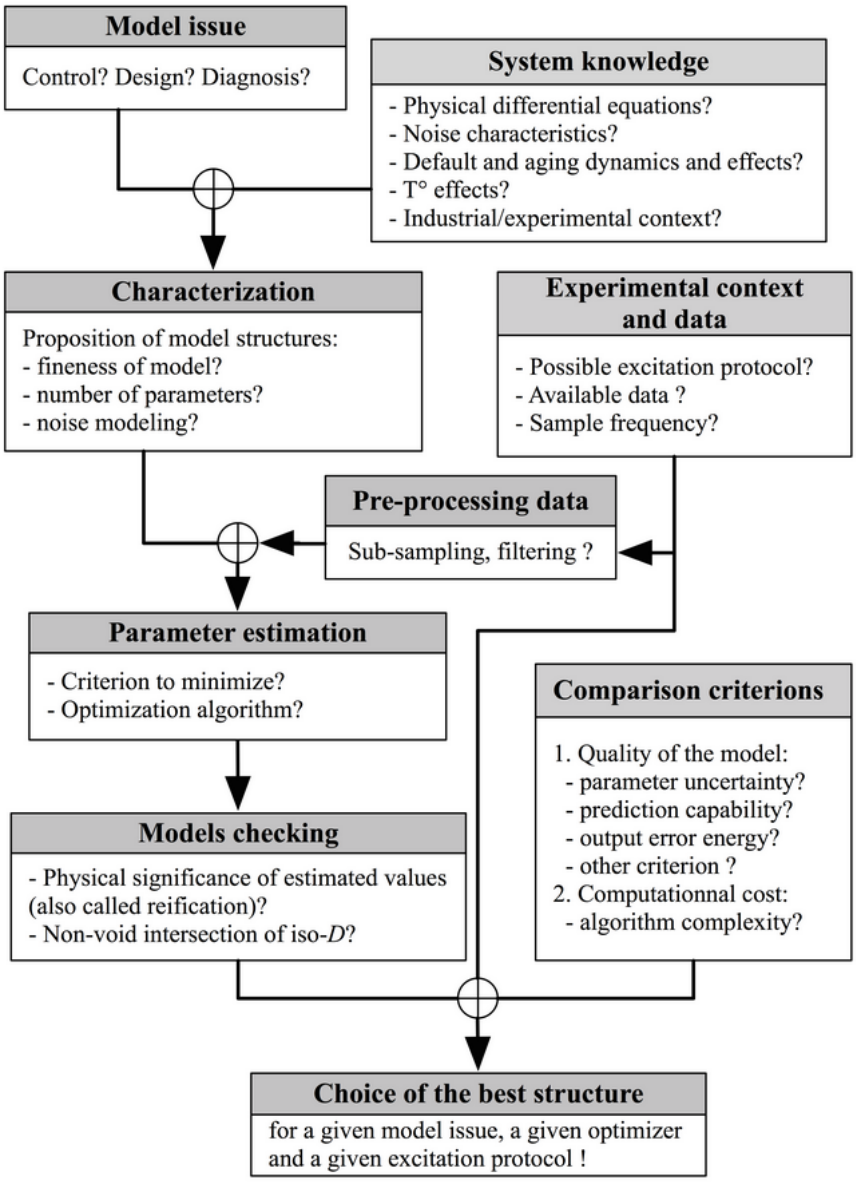


Figure 2.11: Process of choosing a dedicated model structure.

– *Complexity*

A continuous-time model of an EDLC is often expressed by a state-space representation with physical ordinary differential equations. The model complexity refers to the degree of difficulty to solve and to simulate these differential equations and to the computational cost of the parametric identification algorithm. In detail, this model complexity is related to the dimension of the state space vector, thus to the number of the differential equations, and to the number of parameters to identify. Increasing the number of differential equations implies a slight rise of the computational cost of the model simulation, but it generally leads to a better simulation of the system behavior, in a wider valid frequency bandwidth. On the other hand, increasing the number of parameters provides a structure with more degrees of freedom that can better fit the measured system output, but it generally greatly increases the computational cost of the optimization algorithm used for the parameter estimation. Moreover, an over-parametrization may result in modeling the noises for a given input-output record. The over-parameterized model can well fit the given recorded data but will be no longer be accurate when the input-output data is changed.

With a chosen model, the parameter estimation can be obtained by some identification algorithms, such as the minimization of the output error energy or by real-time state observers such as the ones presented in the next chapter. The parameter estimation depends on the parameter sensibilization by the input excitation available in operating conditions. This means that, the more parameters to estimate, the more information the input signals of the systems should provide to obtain an accurate estimation and to ensure the convergence of the algorithm. One reliable solution is to design an optimally exciting input of the model but it is not always applicable in operating conditions. Therefore, in this work, we try to find a general method which allows to compare the potentialities of any model structure for any given excitation signal, in a simple and quick manner.

### 2.2.2 Selection criteria

As is introduced before, the choice of a "good" model for the online identification of EDLCs requires to set some criteria for the comparison of different model structures. In our work, we propose the following three criteria which can be weighted by the user:

– *Output error energy*

A model used to simulate a system should ideally correctly explain its behavior. So for the same input (for example, a current) signal, the simulated output of the model (EDLC voltage in the case of a current input) should be as close

as possible to the measured output of the system. From this point of view, the energy of the output error between the model and the system for a given input can be considered as a reliable model selection criterion. The smaller the output error energy is, the better the model fits the system.

– *Parameters uncertainty*
In the context of aging monitoring of EDLCs, determining the aging level through the parameter evolution requires to have accurate parameters estimations. The parameters uncertainty can be an important criterion for models comparison because it provides the information on how much we can trust on the parameters obtained by identification methods. The model structures with lower parameters uncertainty are clearly preferred to other structures. This criterion allows to make the right aging diagnosis.

– *Aging diagnosis ability*
The parameters evolution of the EDLCs during their use may evolve with the operating conditions as well as with their aging. For example, the resistance of a model may increase because of either the aging or the temperature. Thus, temperature can prevent a state of health indicator to give correct aging diagnostic information. This criteria deals with the ability to design a state of health indicator which is independent of operation conditions.

The first two criteria can be numerically quantified thanks to a geometric study of the hyper surface of output error energy. The following sections will explain in detail how these two criteria can be derived from such a study. The last criterion needs to check if the model has the aging diagnostic ability according to the given experimental information. There is no requirement on theoretical or mathematical analysis. An application of this criteria on a given kind of EDLCs will be presented at §2.4.4.

### 2.2.3 Study of the output error energy

For an EDLC, a continuous-time parametric state space model $M(\boldsymbol{\theta})$ can be built according to the equations of their dynamic physical behavior (the bold terms represent vectors):

$$M(\boldsymbol{\theta}) : \begin{cases} \dot{\boldsymbol{x}}(t, \boldsymbol{\theta}) = \boldsymbol{f}(\boldsymbol{x}(t, \boldsymbol{\theta}), \boldsymbol{\theta}, u(t)) \\ y_m(t, \boldsymbol{\theta}) = g(\boldsymbol{x}(t, \boldsymbol{\theta}), \boldsymbol{\theta}, u(t)) \end{cases} \tag{2.12}$$

where $\boldsymbol{\theta} = [\theta_1, \theta_2, ..., \theta_n]^T$ is the parameter vector and $\boldsymbol{x}$ is the state vector. The input and output of the EDLC model, $u(t)$ and $y_m(t, \boldsymbol{\theta})$, can be either current or voltage and they are clearly scalars. The functions $\boldsymbol{f}$ and $g$ are obtained from physical laws used to derive the EDLCs' electrical model, and they are generally non-linear

with respect to parameters. This general form allows to study linear systems as well as nonlinear systems. For different structures of EDLCs, the corresponding state space models are also different.

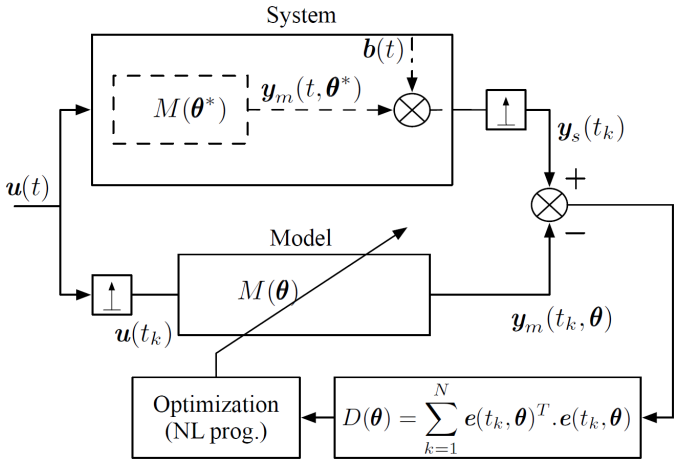


Figure 2.12: Principle of model identification by the minimization of the criterion $D(\boldsymbol{\theta})$ (the output error energy).

The aim of EDLCs' identification is to find the optimal numerical values of the parameters of the proposed EDLC model, so that for a given input, the output of the model can be as close as possible to that of the objective system (i.e. a real EDLC). Fig. 2.12 shows the principle of model identification by minimizing the output error energy. The output error between the objective system and the model for a given input signal at time $t_k$ is expressed as:

$$e(t_k, \boldsymbol{\theta}) = y_s(t_k) - y_m(t_k, \boldsymbol{\theta}) \tag{2.13}$$

where $y_s(t_k)$ is the measured output of the system and $y_m(t_k, \boldsymbol{\theta})$ is the simulated output of the model depending on parameters. The optimal estimated parameter vector $\boldsymbol{\theta}_o = \arg\min D(\boldsymbol{\theta})$ is obtained by the non-linear minimization of the following quadratic criterion $D(\boldsymbol{\theta})$ (usually called state-distance), which is the output error energy [67]:

$$D(\boldsymbol{\theta}) = \sum_{k=1}^{N} e(t_k, \boldsymbol{\theta})^T e(t_k, \boldsymbol{\theta}) = \sum_{k=1}^{N} [y_s(t_k) - y_m(t_k, \boldsymbol{\theta})]^2 \tag{2.14}$$

where $N$ is the number of output samples and the output error $e(t_k, \boldsymbol{\theta})$ at sample time $t_k$ is a scalar in our case.

The non-linear optimization algorithm consists in an iterative displacement of the parameter estimation in the parametric space in order to find the minimum of the quadratic criterion $D(\boldsymbol{\theta})$. The Levenberg-Marquardt algorithm is probably the most popular algorithm, because it provides a good trade-off between speed of convergence and immunity to bad initialization [83]. This minimization algorithm is

not in the scope of this chapter because we are only interested in the model comparison using some numerical optimal estimation provided by nonlinear minimization of the output error energy. In the following section, a geometric study of the output error energy $D(\boldsymbol{\theta})$ will be presented in order to explain why and how the parameter uncertainty is derived.

### 2.2.4 Parameter uncertainty

It is assumed that the system output is the sum of the model output with "true" values of parameters $\boldsymbol{\theta}^*$ and an additional term $b(t)$ which represents all measurement and modeling noises:

$$y_s(t) = y_m(t, \boldsymbol{\theta}^*) + b(t) \tag{2.15}$$

When replacing the system output term in Eq. 2.14 by its assumed expression given above, the output error energy for a scalar output structure can be re-arranged in the following form, which reveals the elliptic nature of the hyper-surface near the optimum (see Fig. 2.13):

$$\begin{aligned} D(\boldsymbol{\theta}) &= \sum_{k=1}^{N} [\, y_m(t_k, \boldsymbol{\theta}^*) + b(t_k) - y_m(t_k, \boldsymbol{\theta}) \,]^2 \\ &= \underbrace{\underbrace{\sum_{k=1}^{N} b(t_k)^2}_{E} + \sum_{k=1}^{N} [\, y_m(t_k, \boldsymbol{\theta}^*) - y_m(t_k, \boldsymbol{\theta}) \,]^2}_{\text{Elliptic paraboloid hyper-surface } S_{\boldsymbol{\theta}^*}} \\ &\quad + \underbrace{2 \sum_{k=1}^{N} b(t_k) \cdot (\, y_m(t_k, \boldsymbol{\theta}^*) - y_m(t_k, \boldsymbol{\theta}) \,)}_{\text{Deformation of } S_{\boldsymbol{\theta}^*}} \end{aligned} \tag{2.16}$$

The first term $E = D(\boldsymbol{\theta}^*) = \sum_{k=1}^{n} b(k)^2$ is the energy of noise. The first two terms of this equation can be considered as a quadratic elliptic paraboloidal hyper-surface $S_{\boldsymbol{\theta}^*}$ near the output error energy obtained with true parameters values, $D(\boldsymbol{\theta}^*)$. The third term is considered as the deformation of the hyper-surface $S_{\boldsymbol{\theta}^*}$. For the sake of clarity, an example of a two-dimensional parameter vector ($\boldsymbol{\theta} = [\theta_1, \theta_2]^T$) is illustrated. Fig. 2.13 shows the analytical surface of the output error energy $D(\boldsymbol{\theta})$ near the optimum for the two parameters case. The black dashed lines represent the elliptic surface $S_{\boldsymbol{\theta}^*}$ near the true parameter values. Due to the noise $b(t)$, the value of output error energy corresponding to the bottom of the paraboloidal surface $S_{\boldsymbol{\theta}^*}$ is the noise energy $E$. The optimization method used for EDLCs identification is expected to provide $\boldsymbol{\theta}^*$ as the optimal parameters. But unfortunately, the last term added to the first two terms in Eq. 2.16 leads to a distortion of the surface $S_{\boldsymbol{\theta}^*}$. As

a result, the optimal parameter vector, $\boldsymbol{\theta}_o$, obtained by the optimization algorithms for the real surface $S_{\boldsymbol{\theta}}$ of $D(\boldsymbol{\theta})$ is no longer the "true" parameter vector $\boldsymbol{\theta}^*$ (see Fig. 2.13). Therefore, when the optimal values of the parameters, $\boldsymbol{\theta}_o$, are determined by an optimization method, it is very important to know how much we can trust on these provided parameter estimations. For this purpose, the uncertainty of the parameters should be calculated.

In order to determine the parameters uncertainty, J. Richalet has proposed an iso-distance $\mathrm{ID}(\boldsymbol{\theta})$ in the parametric space (shown in Fig. 2.13) given by the implicit equation [67]:

$$D(\boldsymbol{\theta}) = (1+\alpha)D(\boldsymbol{\theta}_o) \tag{2.17}$$

where the coefficient $\alpha$ is chosen to ensure that the true parameter $\boldsymbol{\theta}^*$ is inside the iso-distance. If the output error can be modeled by a random noise with normal distribution $\mathcal{N}(0, \sigma^2)$, then taking $\alpha = 9/N$ allows to say that $\boldsymbol{\theta}_o$ has a probability of $95\%$ to be inside the iso-distance. In more general cases, one can simply determine the smallest value of $\alpha$ which ensures that the intersection of the iso-distances obtained for different input excitation protocols is not void [67].

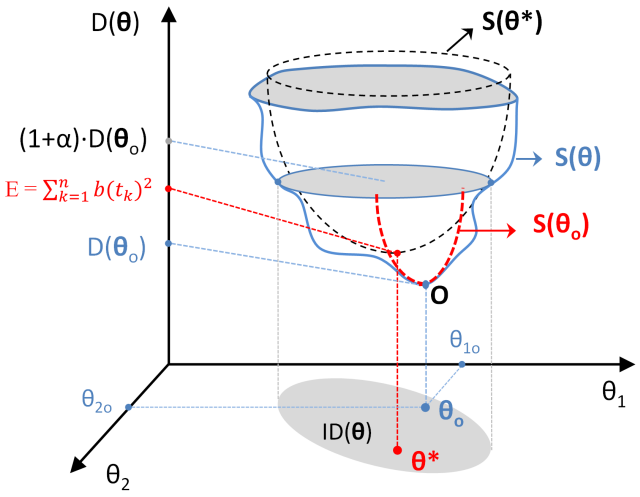


Figure 2.13: Analytical plot of the surface of $D(\boldsymbol{\theta})$.

In order to derive the expression of the uncertainty, we start from the second-order Taylor expansion of $D(\boldsymbol{\theta})$ around the optimal parameters $\boldsymbol{\theta}_o$:

$$D(\boldsymbol{\theta}) \approx D(\boldsymbol{\theta}_o) + \underbrace{\boldsymbol{G}(\boldsymbol{\theta}_o)^T(\boldsymbol{\theta}-\boldsymbol{\theta}_o)}_{0} + \underbrace{\frac{1}{2}(\boldsymbol{\theta}-\boldsymbol{\theta}_o)^T\boldsymbol{H}(\boldsymbol{\theta}_o)(\boldsymbol{\theta}-\boldsymbol{\theta}_o)}_{\text{Hyper-surface } S(\boldsymbol{\theta})} \tag{2.18}$$

where the gradient vector $\boldsymbol{G}$ is zero at $\boldsymbol{\theta}_o$ and $\boldsymbol{H}(\boldsymbol{\theta}_o)$ represents the Hessian matrix

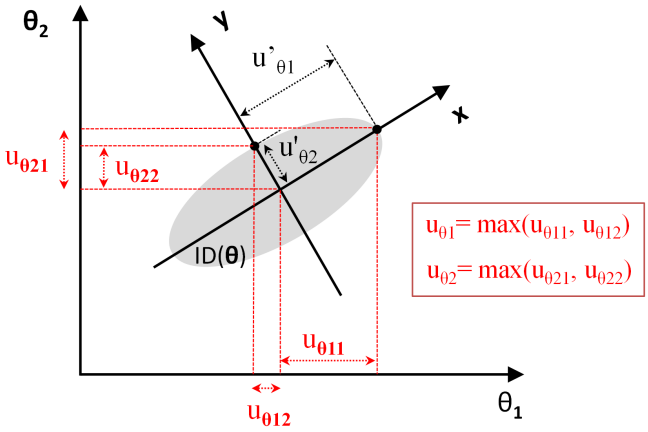


Figure 2.14: Parameter uncertainty analysis (example of two parameters)..

of $D(\boldsymbol{\theta})$ at point $\boldsymbol{\theta}_o$:

$$\boldsymbol{G}(\boldsymbol{\theta}_o) = \left[\frac{\partial D}{\partial \theta_1}(\boldsymbol{\theta}_o),\ \frac{\partial D}{\partial \theta_2}(\boldsymbol{\theta}_o), ..., \frac{\partial D}{\partial \theta_n}(\boldsymbol{\theta}_o)\right]^T = 0 \tag{2.19}$$

$$\boldsymbol{H}(\boldsymbol{\theta}_o) = \begin{bmatrix} \frac{\partial^2 D}{\partial \theta_1^2}(\boldsymbol{\theta}_o) & \frac{\partial^2 D}{\partial \theta_1 \partial \theta_2}(\boldsymbol{\theta}_o) & \dots & \frac{\partial^2 D}{\partial \theta_1 \partial \theta_n}(\boldsymbol{\theta}_o) \\ \vdots & \vdots & \vdots & \vdots \\ \frac{\partial^2 D}{\partial \theta_n \partial \theta_1}(\boldsymbol{\theta}_o) & \frac{\partial^2 D}{\partial \theta_n \partial \theta_2}(\boldsymbol{\theta}_o) & \dots & \frac{\partial^2 D}{\partial \theta_n^2}(\boldsymbol{\theta}_o) \end{bmatrix} \tag{2.20}$$

For simplicity, the following derivation of the parameter uncertainty is based on a two-dimensional parameter case. To determine the iso-distance $\mathrm{ID}(\boldsymbol{\theta})$, Eq. 2.17 is substituted into Eq. 2.18:

$$(1+\alpha)\cdot D(\boldsymbol{\theta}_o) = D(\boldsymbol{\theta}_o) + \frac{1}{2}(\boldsymbol{\theta}-\boldsymbol{\theta}_o)^T \cdot \boldsymbol{H}(\boldsymbol{\theta}_o)\cdot(\boldsymbol{\theta}-\boldsymbol{\theta}_o) \tag{2.21}$$

where $\boldsymbol{\theta}-\boldsymbol{\theta}_o = [\theta_1-\theta_{1o},\ \theta_2-\theta_{2o}]^T$ and $\theta_{1o}$ and $\theta_{2o}$ are the optimal values of parameters $\theta_1$ and $\theta_2$ obtained by parameter optimization algorithm. Simplifying this equation leads to:

$$2\alpha D(\boldsymbol{\theta}_o) = (\boldsymbol{\theta}-\boldsymbol{\theta}_o)^T \cdot \boldsymbol{H}(\boldsymbol{\theta}_o)\cdot(\boldsymbol{\theta}-\boldsymbol{\theta}_o) \tag{2.22}$$

The symmetric Hessian matrix $\boldsymbol{H}(\boldsymbol{\theta}_o)$ can be diagonalized thanks to its eigen-decomposition:

$$\boldsymbol{H}(\boldsymbol{\theta}_o) = \boldsymbol{S}\begin{bmatrix}\lambda_1 & 0\\ 0 & \lambda_2\end{bmatrix}\boldsymbol{S}^T \tag{2.23}$$

where $\lambda_1$, $\lambda_2$ are the eigenvalues of matrix $\boldsymbol{H}(\boldsymbol{\theta}_o)$ and $\boldsymbol{S}$ is a square matrix whose

columns corresponds to the eigenvectors of $\boldsymbol{H}(\boldsymbol{\theta}_o)$. Eq. 2.21 is then simplified as

$$2\alpha D(\boldsymbol{\theta}_o) = (\boldsymbol{\theta} - \boldsymbol{\theta}_o)^T \cdot \boldsymbol{S} \cdot \begin{bmatrix} \lambda_1 & 0 \\ 0 & \lambda_2 \end{bmatrix} \cdot \boldsymbol{S}^T \cdot (\boldsymbol{\theta} - \boldsymbol{\theta}_o) \tag{2.24}$$

Let's note the coordinates of the parameter vector in the eigenbase coordinates:

$$[x, y] = (\boldsymbol{\theta} - \boldsymbol{\theta}_o)^T \cdot \boldsymbol{S} \tag{2.25}$$

then the algebraic form of the equation above in a new $x$-$y$ coordinate is written as

$$\frac{x^2}{2\alpha D(\boldsymbol{\theta}_o)/\lambda_1} + \frac{y^2}{2\alpha D(\boldsymbol{\theta}_o)/\lambda_2} = 1 \tag{2.26}$$

This equation shows that the boundary of the area $\mathrm{ID}(\boldsymbol{\theta})$ shown in Fig. 2.14 is an ellipse. The parameters uncertainty in $x$-$y$ coordinate, $u'_{\theta 1}$ and $u'_{\theta 2}$, are respectively considered as the major axis and minor axis of the ellipse.

$$u'_{\theta 1} = \sqrt{2\alpha D(\boldsymbol{\theta}_o)/\lambda_1}; \quad u'_{\theta 2} = \sqrt{2\alpha D(\boldsymbol{\theta}_o)/\lambda_2} \tag{2.27}$$

These calculations are based on the two-dimensional parameter case, but they are also appropriate for the case of a $N$-dimensional parameter space:

$$u'_{\theta i} = \sqrt{2\alpha D(\boldsymbol{\theta}_o)/\lambda_i}, \quad (i = 1, 2, ..., N) \tag{2.28}$$

Inverting Eq. 2.25 allows to project the major axis $u'_{\theta 1}$ and minor axis $u'_{\theta 2}$ of the ellipse to the parametric axis:

$$\begin{cases} [u_{\theta_{11}}, u_{\theta_{21}}] = [u'_{\theta_1}, 0] \cdot \boldsymbol{S}^{-1} \\ [u_{\theta_{12}}, u_{\theta_{22}}] = [0, u'_{\theta_2}] \cdot \boldsymbol{S}^{-1} \end{cases} \tag{2.29}$$

where $u_{\theta_{11}}$ and $u_{\theta_{21}}$ are respectively the projection of $u'_{\theta 1}$ on $\theta_1$ axis and $\theta_2$ axis, and $u_{\theta_{12}}$ and $u_{\theta_{22}}$ are respectively the projection of $u'_{\theta 2}$ on $\theta_1$ axis and $\theta_2$ axis (see Fig. 2.14). Then the final parameters uncertainty, $u_{\theta i}$, in the parametric space can be conservatively determined as:

$$u_{\theta 1} = \max(u_{\theta_{11}}, u_{\theta_{12}}); \quad u_{\theta 2} = \max(u_{\theta_{21}}, u_{\theta_{22}}) \tag{2.30}$$

One can also use the same approach for N-dimensional parameter case. With this approach, the parameter uncertainty can be simply derived from their corresponding Hessian matrix. When comparing different model structures, the one with the smallest parameter uncertainties is better than the others because with this structure, more accurate parameter estimations can be obtained with the same input ex-

citation signal.

According to the analysis above, it is very clear to see that the uncertainty of one parameter as well as the shape of the ellipse in Fig. 2.14 is closely related to the corresponding eigenvalue of the Hessian matrix. It should be noticed that, if the eigenvalues corresponding to different parameters have a very large difference, some parameters may be very badly estimated. For example, in the 2-dimensional case, if one eigenvalue is much larger than the other one ($\lambda_2 \gg \lambda_1$), the surface of $D(\boldsymbol{\theta})$, $S(\boldsymbol{\theta}_o)$, near the optimal parameters $\boldsymbol{\theta}_o$ presents a valley (see Fig. 2.15) in the direction closely parallel to the $\boldsymbol{\theta}_1$ axis. As a result, $\boldsymbol{\theta}_1$ is much more badly sensibilized than the other parameters because a small variation of this parameter around its nominal value has a small influence on the model output, and therefore on the output error energy. In this case, any identification algorithm will be confronted to a slow convergence towards the objective parameter vector and the resulting estimation of the badly sensibilized parameter may be not accurate. This is also the case for multidimensional parameter spaces. Therefore, it is important to know the difference of the eigenvalues of $H(\boldsymbol{\theta})$. To measure this difference, we define the condition number $\rho$ of $H(\boldsymbol{\theta})$ as

$$\rho = \lambda_{\max}/\lambda_{\min} \tag{2.31}$$

where $\lambda_{\min}$ and $\lambda_{\max}$ represent the minimum and maximum eigenvalues in the parametric space. The lower the condition number $\rho$, the more accurate the estimated parameters. Thus, the condition number can also be used to compare different EDLC model structures and the one with lower condition number will be preferred.

This section has analytically studied the hyper-surface of the output error energy and has explained how this allows to derive the parameters uncertainty. The next section will present how to numerically implement these analytical expressions in practice .

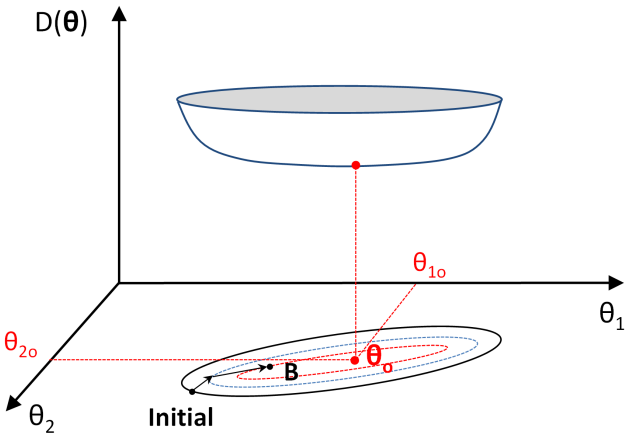


Figure 2.15: Surface of $D(\boldsymbol{\theta})$ as a valley.

## 2.3 Practical implementation

The minimal output error energy can be simply calculated from the measured system output and from the simulated model output (Eq. 2.12). But it is more complicated for the numerical calculation of the parameter uncertainty. As is explained before, the parameter uncertainty depends on the eigenvalues of the Hessian matrix of $D(\boldsymbol{\theta}_o)$. Once the Hessian matrix is known, its eigenvalues can be computed as well as the parameters uncertainty and the condition number. In practice, the numerical derivation of $D(\boldsymbol{\theta})$ could induce dramatic computational problems. A better solution consists in using the numerical integration of the sensitivity functions.

### 2.3.1 Gauss-Newton approximation of the Hessian matrix

Based on Eq. 2.14, the gradient of the output error energy $D(\boldsymbol{\theta})$ with respect to each parameter can be obtained as:

$$\begin{cases} \frac{\partial D}{\partial \theta_1}(\boldsymbol{\theta}) = -2\sum_{k=1}^{N} \frac{\partial y_m}{\partial \theta_1}(t_k,\boldsymbol{\theta}) \cdot [\, y_s(t_k) - y_m(t_k,\boldsymbol{\theta}) \,] \\ \quad \vdots \\ \frac{\partial D}{\partial \theta_n}(\boldsymbol{\theta}) = -2\sum_{k=1}^{N} \frac{\partial y_m}{\partial \theta_n}(t_k,\boldsymbol{\theta}) \cdot [\, y_s(t_k) - y_m(t_k,\boldsymbol{\theta}) \,] \end{cases} \tag{2.32}$$

The matrix form of these equations leads to:

$$\boldsymbol{G}(\boldsymbol{\theta}) = -2\sum_{k=1}^{N} \Psi(t_k,\boldsymbol{\theta})^T \cdot e(t_k,\boldsymbol{\theta}) \tag{2.33}$$

where $\Psi(t_k,\boldsymbol{\theta}) = \left[\frac{\partial y_m}{\partial \theta_1}(t_k,\boldsymbol{\theta}), \frac{\partial y_m}{\partial \theta_2}(t_k,\boldsymbol{\theta}), ..., \frac{\partial y_m}{\partial \theta_n}(t_k,\boldsymbol{\theta})\right]$ is the transpose of the gradient of $y_m(t_k,\boldsymbol{\theta})$ and $\frac{\partial y_m}{\partial \theta_i}(t_k,\boldsymbol{\theta})$ is the output sensitivity function of the parameter $\theta_i$. An output sensitivity function evaluates the sensitivity of the model output with respect to a parameter: the higher its absolute value, the more an elementary variation of the parameter brings an important output variation, and thus the more accurate parameter estimations can be obtained.

The Hessian matrix is the derivative of the gradient vector, $\boldsymbol{H}(\boldsymbol{\theta}) = \frac{\partial \boldsymbol{G}}{\partial \boldsymbol{\theta}}(\boldsymbol{\theta})$:

$$\boldsymbol{H}(\boldsymbol{\theta}) = -2\sum_{k=1}^{N} \frac{\partial \Psi}{\partial \boldsymbol{\theta}}(t_k,\boldsymbol{\theta})^T \cdot e(t_k,\boldsymbol{\theta}) - 2\sum_{k=1}^{N} \Psi(t_k,\boldsymbol{\theta})^T \cdot \frac{\partial e}{\partial \boldsymbol{\theta}}(t_k,\boldsymbol{\theta}) \tag{2.34}$$

$$\text{with} \quad \frac{\partial e}{\partial \boldsymbol{\theta}}(t_k,\boldsymbol{\theta}) = -\frac{\partial y_m}{\partial \boldsymbol{\theta}}(t_k,\boldsymbol{\theta}) = -\Psi(t_k,\boldsymbol{\theta})$$

Since the first term of this expression usually tends to zero near the optimum $\boldsymbol{\theta}_o$,

the Hessian matrix can be approximated as:

$$\boldsymbol{H}(\boldsymbol{\theta}) \approx 2\sum_{k=1}^{N} \Psi(t_k, \boldsymbol{\theta})^T \cdot \Psi(t_k, \boldsymbol{\theta}) \tag{2.35}$$

and then the hyper-surface $D(\boldsymbol{\theta}_o)+\frac{1}{2}(\boldsymbol{\theta}-\boldsymbol{\theta}_o)^T\boldsymbol{H}(\boldsymbol{\theta}_o)(\boldsymbol{\theta}-\boldsymbol{\theta}_o)$ deals with the elliptic paraboloidal $S(\boldsymbol{\theta}_o)$ defined by Fig. 2.13. This approximation allows to calculate the Hessian matrix only from the output sensitivity function. The next section will present how to calculate these sensitivity functions $\frac{\partial y_m}{\partial \theta_i}$ in practice.

### 2.3.2 Calculation of the sensitivity function

Since the output is a function of $\boldsymbol{\theta}$, $\boldsymbol{x}(t, \boldsymbol{\theta})$ and input $u(t)$ as expressed by Eq. 2.12, the output sensitivity function can then be calculated as the total derivative of $g$ with respect to parameters ($g(\boldsymbol{x}(t, \boldsymbol{\theta}), \boldsymbol{\theta}, u(t))$ and $\boldsymbol{f}(\boldsymbol{x}(t, \boldsymbol{\theta}), \boldsymbol{\theta}, u(t))$ will be denoted by $g$ and $\boldsymbol{f}$ for the simplicity.):

$$\Psi(t, \boldsymbol{\theta}) = \frac{dg}{d\boldsymbol{\theta}} = \frac{\partial g}{\partial \boldsymbol{\theta}} + \frac{\partial g}{\partial \boldsymbol{x}} \cdot \frac{d\boldsymbol{x}}{d\boldsymbol{\theta}} \tag{2.36}$$

In this equation, $\frac{d\boldsymbol{x}}{d\boldsymbol{\theta}}$ cannot be derived directly from the differential state equation $\dot{\boldsymbol{x}}(t, \boldsymbol{\theta}) = \boldsymbol{f}(\boldsymbol{x}(t, \boldsymbol{\theta}), \boldsymbol{\theta}, u(t))$. In order to solve this problem, the derivation of another state equation with respect to $\boldsymbol{\theta}$ is calculated:

$$\frac{d}{dt}\left(\frac{dx}{d\boldsymbol{\theta}}\right) = \frac{d}{d\boldsymbol{\theta}}(\frac{dx}{dt}) = \frac{\partial \boldsymbol{f}}{\partial \boldsymbol{\theta}} + \frac{\partial \boldsymbol{f}}{\partial \boldsymbol{x}} \cdot \frac{d\boldsymbol{x}}{d\boldsymbol{\theta}} \tag{2.37}$$

Combining Eqs. 2.36 and 2.37, a new continuous-time state space representation of the sensitivity function is obtained:

$$SF(\boldsymbol{\theta}) : \begin{cases} \dot{\Phi}(t, \boldsymbol{\theta}) = \mathcal{J}_{f\theta}(t, \boldsymbol{\theta}) + \mathcal{J}_{fx}(t, \boldsymbol{\theta}) \cdot \Phi(t, \boldsymbol{\theta}) \\ \Psi(t, \boldsymbol{\theta}) = \mathcal{J}_{f\theta}(t, \boldsymbol{\theta}) + \mathcal{J}_{gx}(t, \boldsymbol{\theta}) \cdot \Phi(t, \boldsymbol{\theta}) \end{cases} \tag{2.38}$$

where the state matrix $\Phi(t, \boldsymbol{\theta}) = \frac{d\boldsymbol{x}}{d\boldsymbol{\theta}}$ is called state sensitivity function, $\mathcal{J}_{f\theta} = \frac{\partial \boldsymbol{f}}{\partial \boldsymbol{\theta}}$ and $\mathcal{J}_{fx} = \frac{\partial \boldsymbol{f}}{\partial \boldsymbol{x}}$ are the Jacobian matrices of $\boldsymbol{f}$ with respect to $\boldsymbol{\theta}$ and $\boldsymbol{x}$, and $\mathcal{J}_{g\theta} = \frac{\partial \boldsymbol{g}}{\partial \boldsymbol{\theta}}$ and $\mathcal{J}_{gx} = \frac{\partial \boldsymbol{g}}{\partial \boldsymbol{x}}$ are the Jacobian matrices of $\boldsymbol{g}$ with respect to $\boldsymbol{\theta}$ and $\boldsymbol{x}$. The state sensitivity explores the influence of changes in parameters on the states of the EDLC model.

In conclusion, the study of the output error energy of any input/output model structure, for any input excitation protocol, only requires the user to provide the analytical expressions of the state-space functions $\boldsymbol{f}$ and $\boldsymbol{g}$ and their respective Jacobian matrices $\mathcal{J}_{f\theta}$, $\mathcal{J}_{fx}$, $\mathcal{J}_{g\theta}$ and $\mathcal{J}_{gx}$. By solving these continuous-time differential

systems $M(\boldsymbol{\theta})$ (Eq. 2.12) and $SF(\boldsymbol{\theta})$ (Eq. 2.38) with some numerical integration method such as the Runge-Kutta method, the elliptic hyperboloidal approximation of the hyper-surface $D(\boldsymbol{\theta})$ near the optimum is numerically obtained thanks to the Hessian matrix information given by Eq. 2.35. Thus, the numerical values of the parameters uncertainty and the condition number of $\boldsymbol{H}(\boldsymbol{\theta}_o)$ can be obtained for any model structure in a simple and quick way.

### 2.3.3 Practical implementation by normalization

It should be noticed that when calculating the values of the proposed criteria, different input signals may lead to different outputs and thus one value of $|e(t_k, \boldsymbol{\theta})|$ has not the same meaning for a small or a large output value $|y_m(t_k, \boldsymbol{\theta})|$. Therefore, it is proposed to use a normalized output error energy defined as:

$$D_n(\boldsymbol{\theta}) = \frac{\sum_{k=1}^{N} e(t_k, \boldsymbol{\theta})^2}{Y^2} \tag{2.39}$$

where $Y = \sqrt{\sum_{k=1}^{N} y_s(t_k)^2}$ and $Y^2$ represents the energy of the measured output. The normalized expression of the output error energy is a general equation which in particular allows to compare one model structure for several excitation protocols. This comparison is not discussed in this chapter. In our case, when comparing the model structures of EDLCs, the values of $D_n(\boldsymbol{\theta})$ for different models are obtained with the same input current protocol.

As presented before, the Hessian matrix can be obtained by calculating the output sensitivity function (see Eq. 2.35). However, the values of the parameters of an EDLC model can be quite different, for example, the nominal series resistance of a tested Nichicon EDLC is 1 Ω while the resistance representing the self-discharge or the charge redistribution may reach hundreds or thousands of ohms. In this case, the values of sensitivity functions $\frac{\partial y_m}{\partial \theta_i}(t_k, \boldsymbol{\theta})$ of different parameters $\theta_i$ may have large differences. As a result, the elements of the Hessian matrix are not in the same order which may lead to numerical problems when diagonalizing the Hessian matrix in order to calculate the parameter uncertainty. Therefore, it is proposed to study the Hessian matrix and hence the parameter uncertainty in the relative parametric space. Taking two-dimensional parameter case as an example, let's first express the parameter vector $\boldsymbol{\theta}$ in a relative way:

$$\boldsymbol{\theta} = \begin{bmatrix} \theta_1 \\ \theta_2 \end{bmatrix} = \begin{bmatrix} \theta_{1o}(1+\gamma_1) \\ \theta_{2o}(1+\gamma_2) \end{bmatrix} = \mathbf{I}_{\boldsymbol{\theta}_o}(1+\boldsymbol{\gamma}) \tag{2.40}$$

where $\mathbf{I}_{\boldsymbol{\theta}_o} = \text{diag}(\boldsymbol{\theta}_o)$ and $\boldsymbol{\gamma} = [\gamma_1, \gamma_2]^T$. $\boldsymbol{\theta}_o$ is the optimal parameter vector obtained by the parameter optimization algorithm, and the coefficient vector $\boldsymbol{\gamma}$ deals

with the relative variation of $\boldsymbol{\theta}$ near the optimum $\boldsymbol{\theta}_o$:

$$\gamma_1 = \frac{\theta_1 - \theta_{1o}}{\theta_{1o}},\ \gamma_2 = \frac{\theta_2 - \theta_{2o}}{\theta_{2o}} \tag{2.41}$$

And thus, the difference between the parameter vector and its optimum is derived:

$$\boldsymbol{\theta} - \boldsymbol{\theta}_o = \begin{bmatrix} \theta_{1o}\gamma_1 \\ \theta_{2o}\gamma_2 \end{bmatrix} = \mathbf{I}_{\boldsymbol{\theta}_o}\boldsymbol{\gamma} \tag{2.42}$$

In order to derive the parameter uncertainty in the relative space, Eq. 2.42 is substituted into Eq. 2.22 which leads to:

$$2\alpha D(\boldsymbol{\theta}_o) = \boldsymbol{\gamma}^T \mathbf{I}_{\boldsymbol{\theta}_o}^T \cdot \boldsymbol{H}(\boldsymbol{\theta}_o) \cdot \mathbf{I}_{\boldsymbol{\theta}_o}\boldsymbol{\gamma} \tag{2.43}$$

Dividing this equation by the measured output energy $Y^2$ leads to a normalized equation:

$$2\alpha D_n(\boldsymbol{\theta}_o) = \boldsymbol{\gamma}^T \cdot \underbrace{\frac{\mathbf{I}_{\boldsymbol{\theta}_o}^T \cdot \boldsymbol{H}(\boldsymbol{\theta}_o) \cdot \mathbf{I}_{\boldsymbol{\theta}_o}}{Y^2}}_{\boldsymbol{H}_{nr}(\boldsymbol{\theta}_o)} \cdot \boldsymbol{\gamma} \tag{2.44}$$

where $\boldsymbol{H}_{nr}(\boldsymbol{\theta}_o) = \frac{\mathbf{I}_{\boldsymbol{\theta}_o}^T \cdot \boldsymbol{H}(\boldsymbol{\theta}_o) \cdot \mathbf{I}_{\boldsymbol{\theta}_o}}{Y^2}$ is the normalized relative Hessian matrix. It is clear that this equation is a normalized equation of Eq. 2.22 in the relative parametric space. The parameter variation $\boldsymbol{\theta} - \boldsymbol{\theta}_o$ is replaced by the relative coefficient vector $\gamma$. Therefore, studying the eigenvalues of the normalized relative Hessian matrix $\boldsymbol{H}_{nr}(\boldsymbol{\theta}_o)$ allows to obtain the relative parameter uncertainty. The approach to derive the relative parameter uncertainty is the same as the one presented in §2.2.4 by using the eigenvalues of $\boldsymbol{H}_{nr}(\boldsymbol{\theta}_o)$. Substituting the Gauss-Newton approximation of the Hessian matrix (Eq. 2.35) into expression $\boldsymbol{H}_{nr}(\boldsymbol{\theta}_o)$, the normalized relative Hessian matrix can be practically calculated as:

$$\begin{aligned} &\boldsymbol{H}_{nr}(\boldsymbol{\theta}_o) \approx 2\sum_{k=1}^{N} \Psi_{rn}(t_k, \boldsymbol{\theta}_o)^T \cdot \Psi_{rn}(t_k, \boldsymbol{\theta}_o) \\ &\text{with} \quad \Psi_{rn}(t_k, \boldsymbol{\theta}_o) = \frac{1}{Y}\mathbf{I}_{\boldsymbol{\theta}_o}\Psi(t_k, \boldsymbol{\theta}_o) \end{aligned} \tag{2.45}$$

These normalized relative sensitivity functions are now in the same order of magnitude, and the normalized relative Hessian matrix $\boldsymbol{H}_{nr}(\boldsymbol{\theta}_o)$ is much better conditioned than $\boldsymbol{H}(\boldsymbol{\theta}_o)$. Moreover, the use of this approach for N-dimensional parameter case allows to compare different model structures. The next section will present the numerical values of these variables obtained with the same input protocol for several model structures.

## 2.4 Comparative analysis of different model structures

### 2.4.1 Current and voltage signals

The proposed criteria are all based on the state-space representation defined by Eq. 2.12, which describes the relationship between the input and output signals. In our case, the current is chosen as the input excitation signal. An industrially realistic input current waveform has been designed and the corresponding voltage signal is recorded. Fig. 2.16 shows the current and voltage signals of a real fresh Nichicon EDLC with a nominal capacitance of 1 F and a maximal voltage of 2.7 V during one charging/discharging cycle. These resulting current and voltage signals are typical signals of EDLCs used in an energy storage application. During the charging period ($0 - 30$ s), we charge the EDLC with a constant current of 50 mA. This value conforms with the current density in the porous electrodes of the EDLCs used in industrial applications. Right after the charging period, an open circuit phase is added to simulate the case where the EDLC is not immediately discharged. After that, three successive constant current discharging periods form an approximately constant power discharging phase until the EDLC is nearly empty. Before the next charging, an open circuit phase is added again to consider the case where the power supply cannot charge the EDLC immediately. The measured voltage and current signals during such a cycle are used for optimizing the structure fitting criteria.

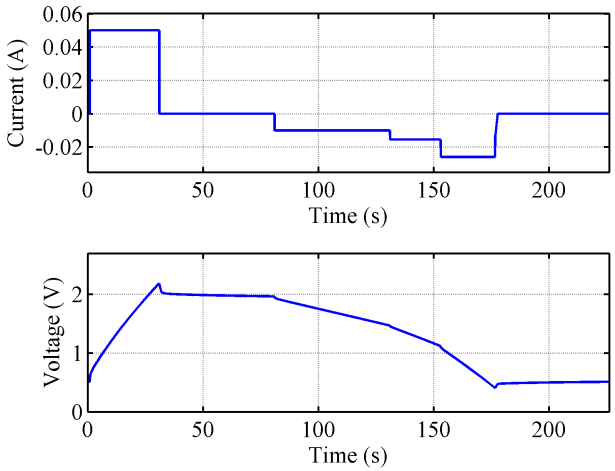


Figure 2.16: Current and voltage signals of a Nichicon 1 F/2.7 V EDLC.

Before choosing the model structures to compare, the voltage curve during a constant current charging phase (1 s to 31 s) and an open circuit phase (31 s to 80 s) (shown in Fig. 2.17) should be more precisely considered. At the beginning of the charging period shown in the enlarged plot No. 1, the voltage has an instantaneous increase caused by the series resistance and then starts to increase slowly. It is

noticed that during 0.02 s after the voltage increase, the voltage shape is an arc instead of a straight line shown by the red dashed line. This may be caused by the electrolyte resistance in the pores and this phenomenon can be represented by a transmission line structure when modeling the EDLC. During the constant current charging phase, the voltage doesn't increase quite linearly with time as shown in the enlarged plot No. 2. If the capacitance is independent of voltage, the EDLC voltage corresponding to a constant charging current should increase linearly with time as the red dashed line in plot No. 2. This phenomenon reveals the voltage dependent feature of the capacitance. The enlarged plot No. 3 shows that the terminal voltage decreases during an open circuit period where the current is null. This might be due to the charge redistribution occurring in the depth of the pores or to a self-discharge phenomenon. Because the open circuit period in our charging/discharging cycle is quite short (around 50 s), it is considered that the charge redistribution is mainly responsible for the voltage decay.

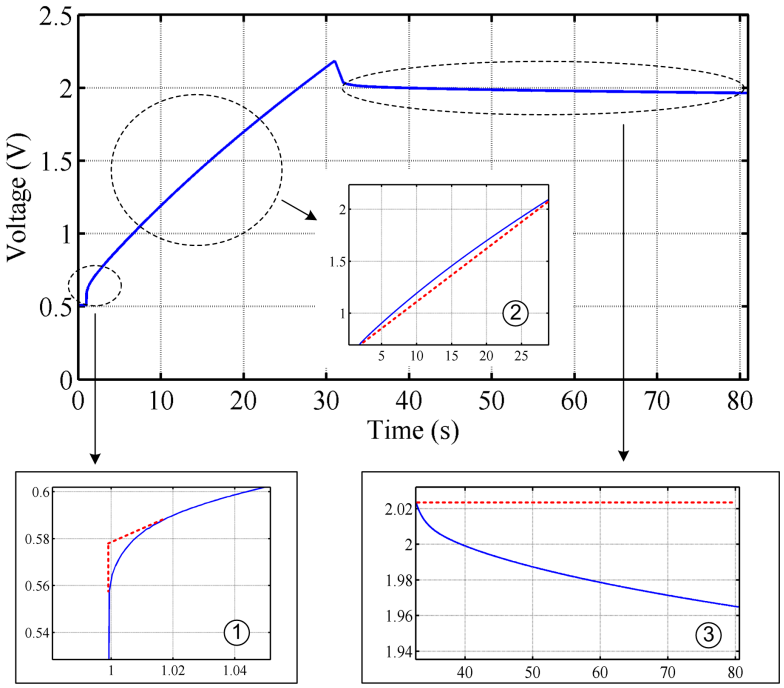


Figure 2.17: Voltage curve at charging phase and OCV phase of a Nichicon 1 F/2.7 V EDLC.

### 2.4.2 Considered model structures for an EDLC

According to the analysis above, we propose to compare the following 5 structures shown in Fig. 2.18.

– *Structure S1:* $R_s - C$

The first proposed structure is a standard "industrial" model with a series resistance and a capacitance in series. Its state space model is simply written

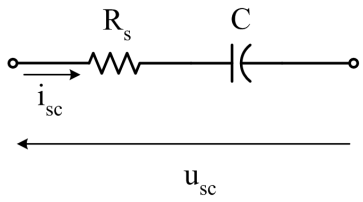


(a) Structure S1

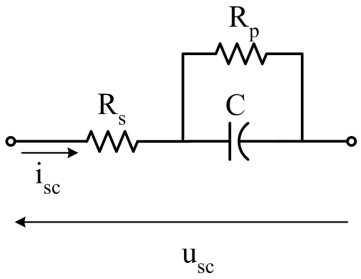


(b) Structure S1'

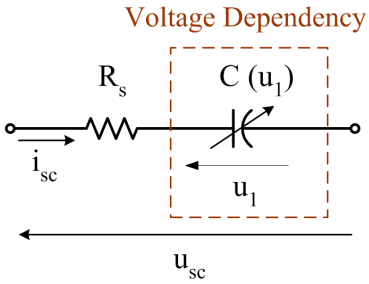


(c) Structure S2

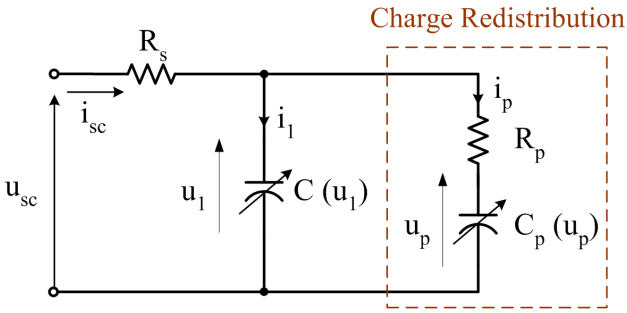


(d) Structure S3

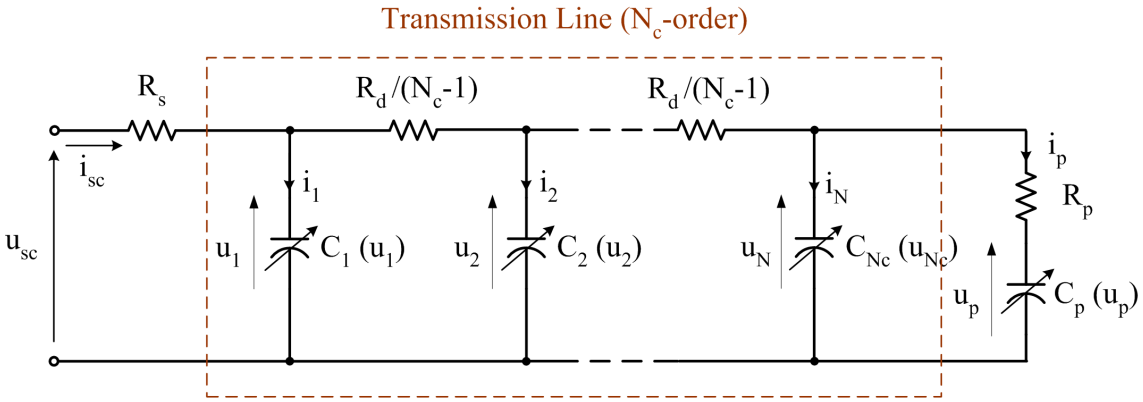


(e) Structure S4 ($N_c$=2, 3, 4)

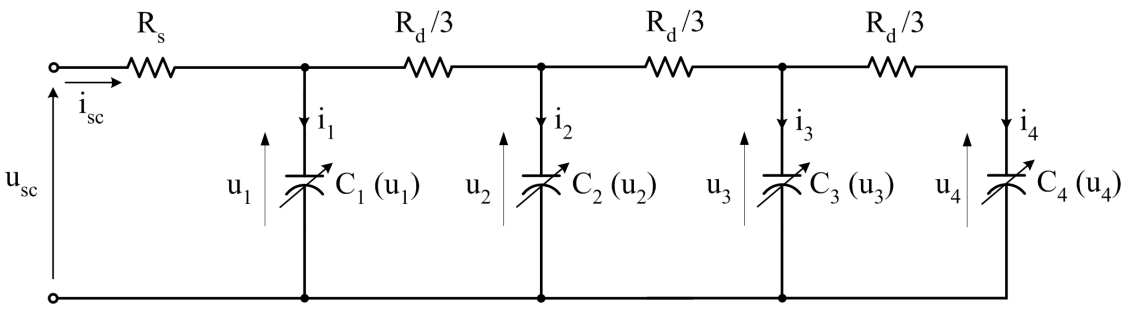


(f) Structure S5

Figure 2.18: Studied model structures.

as

$$\dot{u}_1 = \frac{1}{C} i_{sc} \tag{2.46}$$

$$u_{sc} = u_1 + R_s i_{sc} \tag{2.47}$$

This model has only 1 state $u_1$ and 2 parameters, $R_s$ and $C$. The current $i_{sc}$ and voltage $u_{sc}$ are respectively considered as the input and output of the model as for the following three structures.

– *Structure S1': $R_s$ − $C$ − $R_p$*
Based on the previous structure, the structure S1' adds a resistance $R_p$ parallel to the capacitance, simulating the long-term behavior of the EDLC. Its state space model is written as

$$\dot{u}_1 = -\frac{1}{R_p C} u_1 + \frac{1}{C} i_{sc} \tag{2.48}$$

$$u_{sc} = u_1 + R_s i_{sc} \tag{2.49}$$

This model has one state $u_1$ and 3 parameters, $R_s$, $C$ and $R_p$.

– *Structure S2: $R_s$ − $C(u_1)$*
Considering the voltage dependency of the capacitance, the structure S2 uses a voltage dependent capacitance $C(u_1) = C_0(1 + \alpha u_1)$ where $C_0$ is the no load capacitance and $\alpha$ is the voltage sensitivity coefficient. The reason to use this capacitance equation was presented in section 1.4.2 of Chapter 1. The current through the capacitor can be expressed as

$$i_{sc} = \frac{dQ}{dt} = \frac{d}{dt}(C_0(1 + \alpha u_1) \cdot u_1) = C_0(1 + 2\alpha u_1) \cdot \frac{du_1}{dt} \tag{2.50}$$

Then the state space representation of this model is:

$$\dot{u}_1 = \frac{1}{C_0(1 + 2\alpha u_1)} i_{sc} \tag{2.51}$$

$$u_{sc} = u_1 + R_s i_{sc} \tag{2.52}$$

This model has 1 state $u_1$ and 3 parameters, $R_s$, $C_0$ and $\alpha$.

– *Structure S3: $R_s$ − $[C(u_1)//(R_p$ − $C_p(u_p))]$*

This structure includes the charge redistribution phenomenon by adding a branch in parallel with the main capacitor $C(u_1)$. The added branch consists

of a resistance $R_p$ in series with a voltage dependent capacitance $C_p(u_p) = C_{p0}(1+\alpha u_p)$. The voltage sensitivity of both capacitances are assumed to be the same in our study. The currents through each capacitor are expressed by

$$i_1 = \frac{dQ_C}{dt} = \frac{d}{dt}(C(u_1)\cdot u_1) = C_0(1+2\alpha u_1)\cdot\frac{du_1}{dt} \tag{2.53}$$

$$i_p = \frac{dQ_{C_p}}{dt} = \frac{d}{dt}(C_p(u_p)\cdot u_p) = C_{p0}(1+2\alpha u_p)\cdot\frac{du_p}{dt} \tag{2.54}$$

In addition, $i_1 = i_{sc} - i_p$ and $i_p = (u_1 - u_p)/R_p$, according to Kirchhoff's current law and Ohm's law. Combining these two equations with Eqs. 2.53 and 2.54, the state space model of this structure can be obtained as

$$\begin{cases} \dot{u}_1 = \frac{1}{C_0(1+2\alpha u_1)}(-\frac{1}{R_p}(u_1-u_p)+i_{sc}) \\ \dot{u}_p = \frac{1}{C_{p0}(1+2\alpha u_p)R_p}(u_1-u_p) \end{cases} \tag{2.55}$$

$$u_{sc} = u_1 + R_s i_{sc} \tag{2.56}$$

This third structure includes 2 states, $u_1$ and $u_p$, 5 parameters, $R_s$, $C_0$, $\alpha$, $R_p$ and $C_{p0}$.

– *Structure S4:* $R_s - [\mathrm{TL}(R_d, C_k(u_k))//(R_p - C_p(u_p))]$; $(k = 1, 2, ..., N_c)$
To better describe the EDLCs' behavior, the fourth proposed structure S4 adds a transmission line cell as the one shown in Fig. 2.3 to the third structure. Generally speaking, the higher the order of the transmission line $N_c (N_c \geq 2)$, the more accurate but also the more complex the model is. It is hence important to find a compromise between the accuracy and complexity of the model. It is assumed that all the capacitances in the transmission line cell are voltage dependent with the same voltage sensitivity coefficient: $C_k(u_k) = \frac{C_0}{N_c}(1+\alpha u_k)$; $(k = 1, 2, ..., N_c)$ and the same for the charge redistribution capacitance: $C_p(u_p) = C_{p0}(1+\alpha u_p)$. In this section, the second to fourth order ($N_c = 2, 3, 4$) transmission line cases are studied. The currents through each capacitors are expressed as

$$i_k = \frac{dQ_{c_k}}{dt} = \frac{d}{dt}(C_k(u_k)\cdot u_k) = \frac{C_0}{N_c}(1+2\alpha u_k)\cdot\frac{du_k}{dt} \tag{2.57}$$

$$i_p = \frac{dQ_{C_p}}{dt} = \frac{d}{dt}(C_p(u_p)\cdot u_p) = C_{p0}(1+2\alpha u_p)\cdot\frac{du_p}{dt} \tag{2.58}$$

According to the Ohm's law and Kirchhoff's current law, the following cur-

rent equations can be obtained for different orders of the transmission line:

$$(N_c = 2): \begin{cases} i_p &= \frac{u_2 - u_p}{R_p} \\ i_2 &= \frac{u_1 - u_2}{R_d} - i_p \\ i_1 &= i_{sc} - (i_2 + i_p) \end{cases} \tag{2.59}$$

$$(N_c = 3): \begin{cases} i_p &= \frac{u_3 - u_p}{R_p} \\ i_3 &= \frac{u_2 - u_3}{R_d/2} - i_p \\ i_2 &= \frac{u_1 - u_2}{R_d/2} - (i_3 + i_p) \\ i_1 &= i_{sc} - (i_2 + i_3 + i_p) \end{cases} \tag{2.60}$$

$$(N_c = 4): \begin{cases} i_p &= \frac{u_4 - u_p}{R_p} \\ i_4 &= \frac{u_3 - u_4}{R_d/3} - i_p \\ i_3 &= \frac{u_2 - u_3}{R_d/3} - (i_4 + i_p) \\ i_2 &= \frac{u_1 - u_2}{R_d/3} - (i_3 + i_4 + i_p) \\ i_1 &= i_{sc} - (i_2 + i_3 + i_4 + i_p) \end{cases} \tag{2.61}$$

Combining these equations with Eqs. 2.57 and 2.58, the state space models of the model structure S4 with $N_c = 2, 3, 4$ are then derived:

$$(N_c = 2): \begin{cases} \dot{u}_1 &= \frac{2}{C_0(1+2\alpha u_1)}(-\frac{1}{R_d}(u_1 - u_2) + i_{sc}) \\ \dot{u}_2 &= \frac{2}{C_0(1+2\alpha u_2)}(\frac{1}{R_d}u_1 - (\frac{1}{R_d} + \frac{1}{R_p})u_2 + \frac{1}{R_p}u_p) \\ \dot{u}_p &= \frac{1}{C_{p0}(1+2\alpha u_p)R_p}(u_2 - u_p) \end{cases} \tag{2.62}$$

The second-order transmission line model has 3 states, $u_1$, $u_2$ and $u_p$.

$$(N_c = 3): \begin{cases} \dot{u}_1 &= \frac{3}{C_0(1+2\alpha u_1)}(-\frac{1}{R_d/2}(u_1 - u_2) + i_{sc}) \\ \dot{u}_2 &= \frac{3}{C_0(1+2\alpha u_2)(R_d/2)}(u_1 - 2u_2 + u_3) \\ \dot{u}_3 &= \frac{3}{C_0(1+2\alpha u_3)}(\frac{1}{R_d/2}u_2 - (\frac{1}{R_d/2} + \frac{1}{R_p})u_3 + \frac{1}{R_p}u_p) \\ \dot{u}_p &= \frac{1}{C_{p0}(1+2\alpha u_p)R_p}(u_3 - u_p) \end{cases} \tag{2.63}$$

The third-order transmission line model has 4 states, $u_1$, $u_2$, $u_3$ and $u_p$.

$$(N_c=4):\begin{cases}\dot{u}_1 &= \frac{4}{C_0(1+2\alpha u_1)}(-\frac{1}{R_d/3}(u_1-u_2)+i_{sc})\\ \dot{u}_2 &= \frac{4}{C_0(1+2\alpha u_2)(R_d/3)}(u_1-2u_2+u_3)\\ \dot{u}_3 &= \frac{4}{C_0(1+2\alpha u_3)(R_d/3)}(u_2-2u_3+u_4)\\ \dot{u}_4 &= \frac{4}{C_0(1+2\alpha u_4)}(\frac{1}{R_d/3}u_3-(\frac{1}{R_d/3}+\frac{1}{R_p})u_4+\frac{1}{R_p}u_p)\\ \dot{u}_p &= \frac{1}{C_{p0}(1+2\alpha u_p)R_p}(u_4-u_p)\end{cases} \tag{2.64}$$

The fourth-order transmission line model has 5 states, $u_1$, $u_2$, $u_3$, $u_4$ and $u_p$. The expression of the output voltage for these three cases is always the same: $u_{sc} = u_1 + R_s i_{sc}$. No matter the order of the transmission line, the model structure S4 has always 6 parameters: $R_s$, $C_0$, $\alpha$, $R_p$, $C_{p0}$ and $R_d$.

– *Structure S5 :* $R_s - \mathrm{TL}(R_d, C_k(u_k))$;
This structure is a simplified model structure of S4 ($N_c = 4$) without charge redistribution branch. The purpose of the proposition of this model is to see how accurate the model could be when neglecting the charge redistribution phenomenon. This simplification could be interesting because the parameters of this model are reduced from 6 to 4. For this model, the current through each capacitor is expressed as

$$i_k = \frac{dQ_{c_k}}{dt} = \frac{d}{dt}(C_k(u_k)\cdot u_k) = \frac{C_0}{4}(1+2\alpha u_k)\frac{du_k}{dt}, (k=1,2,3,4) \tag{2.65}$$

These currents can be also written as the following equations according to Ohm's law and Kirchhoff's law:

$$\begin{cases} i_4 &= \frac{u_3-u_4}{R_d/4}\\ i_3 &= \frac{u_2-u_3}{R_d/4} - i_4\\ i_2 &= \frac{u_1-u_2}{R_d/4} - (i_3+i_4)\\ i_1 &= i_{sc} - (i_2+i_3+i_4)\end{cases} \tag{2.66}$$

Combining Eqs. 2.65 and 2.66, the differential equations of the voltages across each capacitors are:

$$(N=4):\begin{cases}\dot{u}_1 &= \frac{4}{C_0(1+2\alpha u_1)}(-\frac{1}{R_d/4}(u_1-u_2)+i_{sc})\\ \dot{u}_2 &= \frac{4}{C_0(1+2\alpha u_2)(R_d/4)}(u_1-2u_2+u_3)\\ \dot{u}_3 &= \frac{4}{C_0(1+2\alpha u_3)(R_d/4)}(u_2-2u_3+u_4)\\ \dot{u}_4 &= \frac{4}{C_0(1+2\alpha u_4)(R_d/4)}(u_3-u_4)\end{cases} \tag{2.67}$$

Table 2.1: Numerical comparison of different structures (mean values of five new EDLCs).

| | S1 | S1' | S2 | S3 | S4 | | | S5 |
|---|---|---|---|---|---|---|---|---|
| $\alpha = 1\%$ | | | | | $N_c = 2$ | $N_c = 3$ | $N_c = 4$ | |
| $D_n(\boldsymbol{\theta}_o)$ | $3.05\ 10^{-3}$ | $2.5\ 10^{-3}$ | $2.66\ 10^{-3}$ | $2.70\ 10^{-4}$ | $1.15\ 10^{-4}$ | $9.81\ 10^{-5}$ | $9.21\ 10^{-5}$ | $1.70\ 10^{-3}$ |
| $\rho(H_{nr}(\boldsymbol{\theta}_o))$ | $1.17\ 10^{2}$ | $7.55\ 10^{3}$ | $1.22\ 10^{4}$ | $9.96\ 10^{3}$ | $4.22\ 10^{4}$ | $3.32\ 10^{4}$ | $3.68\ 10^{4}$ | $7.76\ 10^{4}$ |
| $u_r(R_s)$ | 0.031 | 0.030 | 0.029 | 0.022 | 0.041 | 0.058 | 0.078 | 0.593 |
| $u_r(C)$ | 0.003 | 0.003 | - | - | - | - | - | - |
| $u_r(C_0)$ | - | - | 0.029 | 0.020 | 0.014 | 0.011 | 0.011 | 0.025 |
| $u_r(\alpha)$ | - | - | 0.305 | 0.044 | 0.032 | 0.026 | 0.025 | 0.212 |
| $u_r(R_p)$ | - | 0.225 | - | 0.087 | 0.105 | 0.083 | 0.070 | - |
| $u_r(C_{p0})$ | - | - | - | 0.025 | 0.053 | 0.036 | 0.034 | - |
| $u_r(R_d)$ | - | - | - | - | 0.053 | 0.047 | 0.049 | 0.074 |

Table 2.2: Numerical comparison of different structures (mean values of five EDLCs after 10 weeks of accelerated aging).

| | S1 | S1' | S2 | S3 | S4 | | | S5 |
|---|---|---|---|---|---|---|---|---|
| $\alpha = 1\%$ | | | | | $N_c = 2$ | $N_c = 3$ | $N_c = 4$ | |
| $D_n(\boldsymbol{\theta}_o)$ | $6.70\ 10^{-3}$ | $3.20\ 10^{-3}$ | $6.45\ 10^{-3}$ | $1.13\ 10^{-3}$ | $4.94\ 10^{-4}$ | $4.11\ 10^{-4}$ | $3.77\ 10^{-4}$ | $1.99\ 10^{-3}$ |
| $\rho(H_{nr}(\boldsymbol{\theta}_o))$ | $2.90\ 10^{1}$ | $8.89\ 10^{2}$ | $1.46\ 10^{4}$ | $4.53\ 10^{3}$ | $4.09\ 10^{4}$ | $2.22\ 10^{4}$ | $1.92\ 10^{4}$ | $2.69\ 10^{3}$ |
| $u_r(R_s)$ | 0.024 | 0.018 | 0.023 | 0.021 | 0.017 | 0.027 | 0.037 | 0.053 |
| $u_r(C)$ | 0.005 | 0.003 | - | - | - | - | - | - |
| $u_r(C_0)$ | - | - | 0.042 | 0.054 | 0.040 | 0.034 | 0.032 | 0.032 |
| $u_r(\alpha)$ | - | - | 0.493 | 0.120 | 0.107 | 0.089 | 0.084 | 0.100 |
| $u_r(R_p)$ | - | 0.093 | - | 0.085 | 0.241 | 0.164 | 0.145 | - |
| $u_r(C_{p0})$ | - | - | - | 0.031 | 0.101 | 0.036 | 0.030 | - |
| $u_r(R_d)$ | - | - | - | - | 0.063 | 0.044 | 0.038 | 0.057 |

This model has 4 states, $u_k$, $(k = 1, 2, 3, 4)$, and 4 parameters $R_s$, $R_d$, $C_0$ and $\alpha$. The output voltage is expressed as: $u_{sc} = u_1 + R_s i_{sc}$.

Once the state space representations of these five model structures are obtained, they can be compared by calculating the proposed criteria presented in section 1.3. The comparison results are shown in the following section.

### 2.4.3 Analysis of the experimental results

To compare the proposed models, the output error energy, the condition number of the Hessian matrix and the uncertainties of the model parameters are calculated and illustrated in Table 2.1. All these results are normalized relative values as explained in §2.3.3 and they are the mean values of five fresh EDLCs.

As expected, the output error energy of the simple structure S1 is the largest compared to the other structures. By adding more degrees of freedom to the model structure to take into account the long term behavior (S1'), the voltage dependency (S2), the charge redistribution (S3) and the transmission line effect (S4), the simulated output voltage becomes closer to the measured voltage. This is especially obvious when the charge redistribution component is included in the EDLC model structure because the output error energy of S3 and S4 are around $10\%$ less than that of S1 and S2. The condition number of S1 is quite small compared to the other structures. This is due to its very simple structure with only two parameters, $R_s$ and $C$, which are almost of the same order of magnitude. For the other structures, S3 has the smallest condition number of its normalized relative Hessian matrix. S3 also has the smallest relative parameter uncertainty of the series resistance. It is noticed that, when the charge redistribution and the transmission line components are added to S2, the uncertainties of $C_0$ and $\alpha$ based on S3 and S4 are getting smaller. It implies that adding these two components not only improves the accuracy of the model (smaller output error), but also provides a more accurate parameter estimation of the capacitance which is responsible of the energy storage of an EDLC.

To investigate the influence of the order $N_c$ of the transmission line, the cases $N_c = 2,\ 3,\ 4$ have been considered. As expected, the higher the order of the transmission line, the smaller the output error energy and thus the more accurate the model. Moreover, the condition number of the normalized relative Hessian matrix and most of the parameter uncertainties decrease when increasing the transmission line order. This is quite normal because the transmission line model simulates the behavior of electrodes pores and the EDLC model with a higher transmission line order explains better the pores behavior.

But it is also noticed that these improvements are very slight. At last, the model structure S5 which is a simplified model baseds on S4 ($N_c = 4$) neglecting the charge redistribution phenomenon is shown in the last column of Table 2.1. This model is also an improvement of S2 using a transmission line instead of a simple voltage dependent capacitance. This improvement of S2 leads to a lower output error energy and smaller uncertainties for most parameters except $R_s$. Because the charge redistribution effect is ignored, all the criteria values of this model are worse than that of structure S4. This shows the importance of the long-term phenomenon such as the charge redistribution to the accuracy of the EDLC model.

Globally speaking, according to this table, S3 and S4 are much better than S1, S2 and S5 because of the much lower output error energy and the the smaller parameter uncertainties, especially for $\alpha$. The structure S4 ($N_c = 2,\ 3,\ 4$) has an output error energy slightly lower than S3, while the condition number of S4 is larger than that of S3 because the number of parameters is increased. Some parameter uncertainties of S4 are smaller than that of S3 while others are larger, but overall,

the differences are not very large. Now, considering the model complexity, S4 has a higher dimension of state space vector and more parameters compared to S3, and hence more degrees of difficulty to solve and simulate the differential equations. For structure S4, the increase of the transmission line order only slightly improves the model performance, but increases the order of differential equations and thus increases its computational cost.

The results obtained above show that S3 and S4 seem to be good models for the fresh EDLCs. One may doubt if these model structures are still good once the EDLCs are aged. Table 2.2 shows the criteria values of different structures for aged EDLCs. The data in this table are the average values of five EDLCs aged at $60°C$ under a floating voltage of $2.5$ V during $10$ weeks. The comparison results obtained for the aged EDLCs are similar to those for fresh EDLCs. This table allows to check that the criteria values are not greatly influenced by aging.

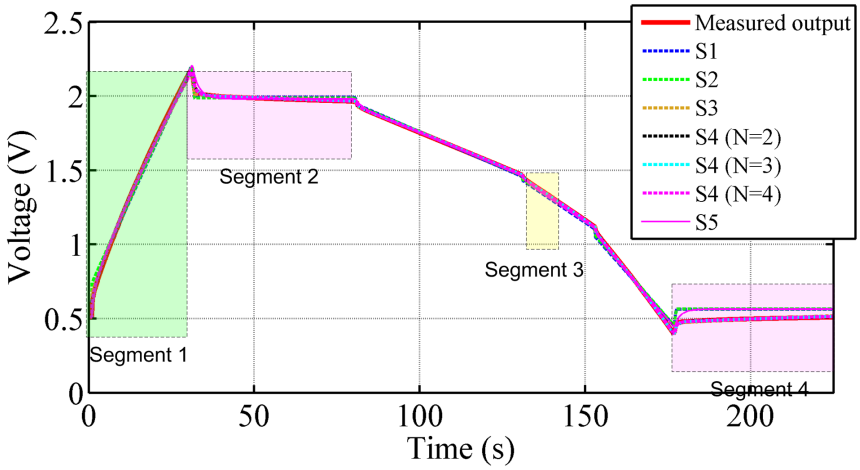


Figure 2.19: Measured and simulated output voltage.

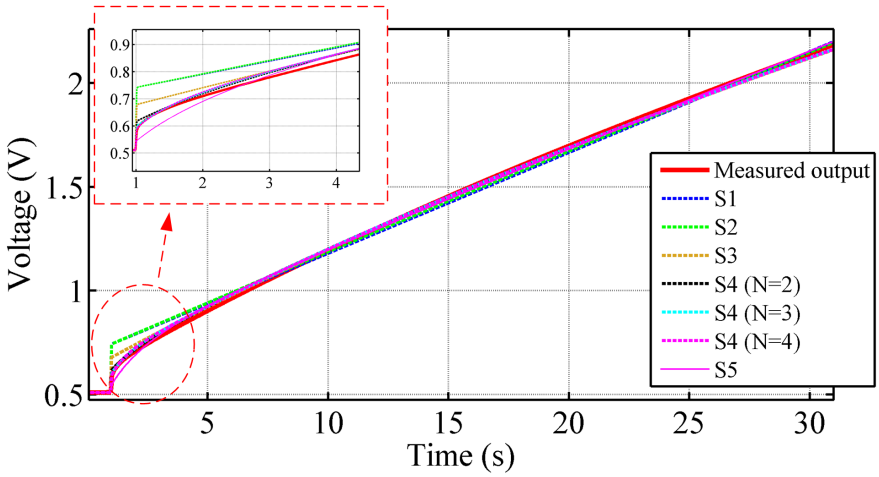


Figure 2.20: Enlarged plot of segment 1.

Besides the numerical comparison of the criteria, the measured voltage and the simulated voltages obtained during one charging/discharging cycle are shown in

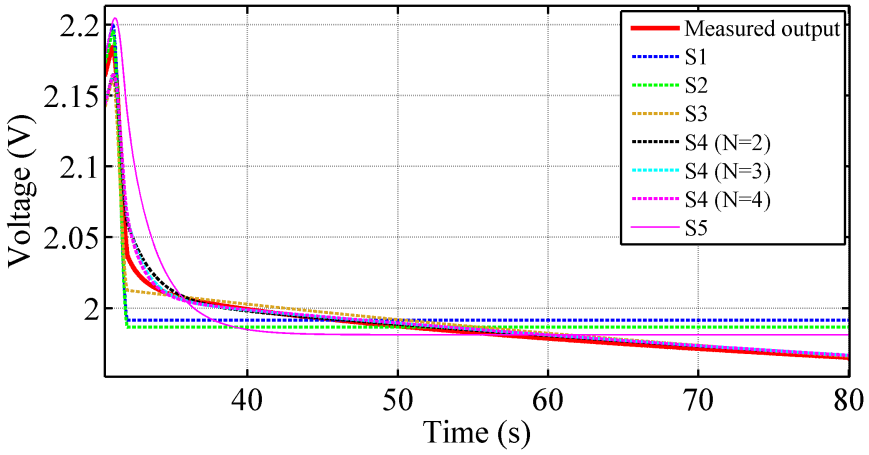


Figure 2.21: Enlarged plot of segment 2.

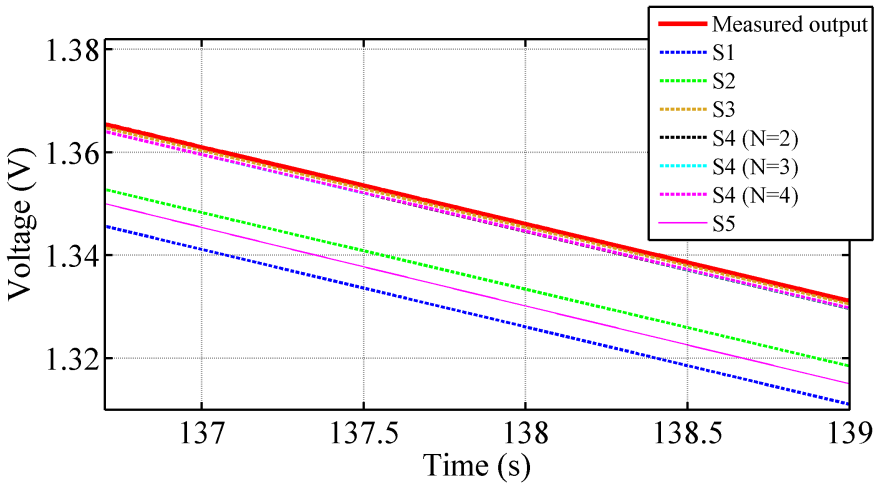


Figure 2.22: Enlarged plot of segment 3.

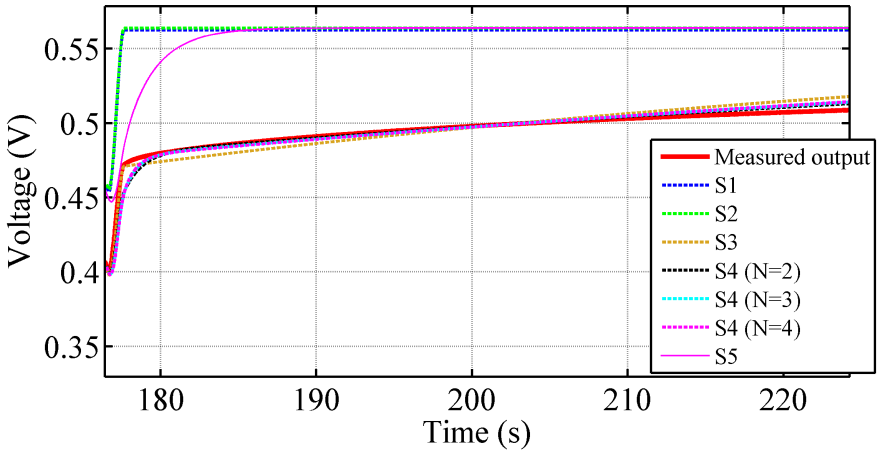


Figure 2.23: Enlarged plot of segment 4.

Fig. 2.19. Fig. 2.20 shows the enlarged segment of the constant current charging phase. As expected, the simulated voltage of S1 increases linearly with time, since this model does not take into account the voltage dependent feature of the capacitance. The simulated voltage curves get more closer to the measured data from S2 to S4, especially at the beginning of the charging phase which reveals a good model accuracy of structure S4. The segments 2 and 4 in Figs. 2.21 and 2.23 show the measured voltage and simulated voltage curves during open circuit phases after charging and discharging phases. It can be seen clearly from these two figures that the simulated voltages based on S1, S2 and S5 remain constant after their transitional periods and this is of course due to the lack of charge redistribution component in their models. Using structure S3 seems to give better voltage curves but not as well as structure S4. There are no obvious differences between the different orders of structure S4 revealed from the simulated voltage curves. Fig. 2.22 is an enlarged segment in the discharging period. The simulated voltage curves based on structures S3 and S4 (no matter which order) are much closer to the real data compared to S1, S2 and S5.

To summarize all the comparison analysis above, the model structure S3 and S4 are quite accurate. S4 is slightly more accurate than S3 but increases the model complexity. But the third criterion (the diagnosis ability) must also be taken into account. This will be explained in the next section.

### 2.4.4 Diagnosis ability

A good model structure used for the aging diagnosis of the EDLCs should provide enough information to diagnose their aging. As presented in the previous chapter, the series resistance and the dynamic resistance increase significantly with the aging which makes them reliable aging indicators. However, existing studies proved that the resistive parameters of the EDLCs may also increase with the decrease of the operating temperature. In this case, it could be very difficult to determine the aging level from the increase of these resistive parameters if the ambient temperature is not measured. Then, a good diagnosis model should be able to provide a temperature independent diagnosis indicator.

To check if the proposed models can provide temperature independent diagnosis indicators, the influence of the temperature to the EDLCs parameters is firstly studied. Fig. 2.24 shows the parameter relative evolution of different structures estimated by the output error method under different temperatures. At each temperature, the ratio $\boldsymbol{\theta}_o(T_k)/\boldsymbol{\theta}(-20°C)$ is calculated by means of $5$ records performed with $5$ fresh EDLCs. Compared to other structures, the structure S$4$ presents an outstanding result: the estimated $C_0$ is independent of temperature and the series resistance and dynamic resistance evolve with the temperature with a very similar

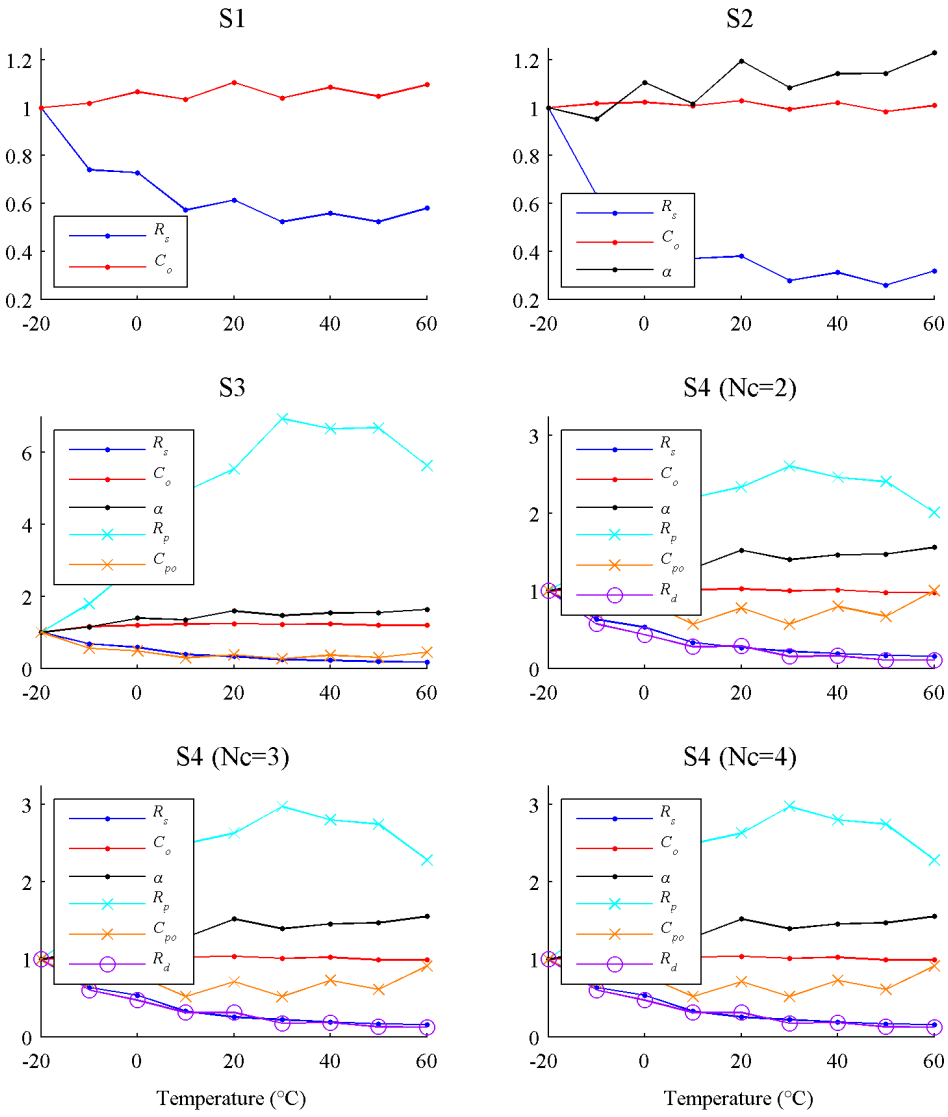


Figure 2.24: Parameters estimation at different temperatures.

rate. Therefore, the ratio between these resistances $R_s/R_d$ is independent of temperature, and therefore can be considered as a potential aging indicator. From this point of view, the structure S4 has a better diagnosis ability compared to S3. Therefore, with the given signals, the structure S4 seems to be a good choice for the online aging monitoring for the tested EDLCs. As for the order of the transmission line in structure S4, $N_c = 2$ is suggested to be chosen in our case, since the proposed criteria are already quite satisfying with such a small order of the transmission line network.

# Conclusion

This chapter was dedicated to look for the "best" EDLC model structure for aging monitoring. At first, a state of the art about the existing EDLC models was made and some popular EDLC models have been illustrated and analyzed. In order to comprehensively compare different structures of EDLCs and to find a best compromise between performance and complexity, three criteria, namely the output error energy, the parameter uncertainty and the aging diagnosis ability, are proposed. The geometric study of the hyper-surface of the output error energy in the parametric space was carried out in order to evaluate the uncertainties of the estimated parameters. The Hessian matrix obtained by using the numerical integration of the relative sensitivity functions allowed to practically determine the parameters uncertainty and the condition number. At last, five different model structures of EDLC including different physical features, such as voltage dependency of the capacitance, charge redistribution phenomenon and transmission line effect, were proposed and their state space representations were derived.

The numerical values of the first two criteria were presented and the aging diagnosis ability of different models was analyzed. The results showed that adding the charge redistribution and transmission line components in the EDLC model greatly improves the accuracy of the model. The model structures S3 and S4 showed a better performance compared to the other proposed structures. The influence of the transmission line order of structure S4 was investigated and the results showed that for the tested EDLCs, the model performance has only slightly increased with the increase of the transmission line order, whereas the complexity of the model has greatly increased. These results are then confirmed by comparing the output voltage curves of different models with the measured voltage.

The study of the parameter estimations at different temperatures of the tested EDLCs showed that the model structure S4 presents a good aging diagnosis ability, because it may provide a temperature independent aging indicator. A good model is not necessarily required to be very complicated, for example, the second-

order transmission line model with a charge redistribution branch was considered as a satisfying model for online aging monitoring of the studied Nichicon EDLCs. The proposed model comparison criteria and implementation approaches provide an idea of how to compare different EDLC models comprehensively and are also applicable for other kinds of EDLCs.

# 3

# Online monitoring of the supercapacitors aging

## Introduction

The aim of this chapter is to design model-based state observers to monitor the aging of the supercapacitors in-situ and online. Unlike the offline aging monitoring of EDLCs, the online observers designed in this chapter can be embedded into energy storage applications and provide the parameters of EDLCs in real time without interrupting the function of the applications.

The first section of this chapter reviews some existing online monitoring methods for EDLCs' aging. In the second section, a strategy for online aging monitoring is proposed, followed by the definition of state of health (SoH) and state of charge (SoC) estimators for an EDLC. After that, the basis of linear and nonlinear observers design based on Kalman filtering and Luenberger observers design are recalled. In the fourth section, two kinds of observers, an extended Kalman filter and interconnected observers are firstly designed based on the simple classical RRC model of an EDLC. In the following section, two kinds of observers, an extended Kalman filter and braided Kalman filters are designed based on a more sophisticated and accurate fourth-order transmission line (TL) model. The performance of the designed observers for both models are verified through simulated experiments. Then, these observers are applied to a real fresh EDLC and the parameter estimation results obtained by different observers for both models are presented and compared. At last, the designed observers based on different models are applied to differently aged EDLCs in an accelerated calendar aging experiment, in order to perceive their

parameters evolutions during the aging. An example of the calculation of the state of health is given, allowing the SoH of EDLCs embedded in industrial applications to be perceived at any time.

## 3.1 State of the art

A great amount of research work has been done for the monitoring of the supercapacitors aging based on different characterization methods. A lot of them are offline methods realized in laboratories as presented in the first chapter. In contrast, very few work is dedicated to the online monitoring of the supercapacitors aging.

The authors of [84] [85] [47] proposed "online" characterization of EDLCs during power cycling aging. The proposed method allows to characterize the EDLCs during the aging experiments without requiring a break off for characteriztion. For the similar purpose, N. Rizoug has proposed a hybrid characterization method [9] [86] combining both time and frequency domain characterizations and applied directly to constant current charging/discharging aging cycles. In [78], the authors have developed a nonlinear model of an EDLC in frequency domain and proposed a so-called online identification method. The model has been identified in time domain instead of frequency domain by using some specific procedures to determine different parameters of EDLCs.

In [87], the authors proposed a new aging indicator, the stored energy, in order to realize supercapacitors diagnosis online. The stored energy in a fixed voltage interval was calculated and compared before and after aging and thus, the energy loss during the supercapacitors aging was then observed. This proposition could be considered as a quite simple way to diagnose supercapacitors aging online. However, to compare energy loss of the supercapacitors at different aging stages, the stored energy calculation need to be obtained in the same fixed interval which may not easy to be realized during the function of supercapacitors in an application.

Very few people have considered to use real-time optimal estimators to identify the EDLCs' parameters. The authors of [88] used a real-time recursive least square algorithm to estimate the internal resistance of EDLCs during their aging. The proposed algorithm has provided a quite accurate internal resistance evolution with aging. But other parameters of EDLCs, for example, the capacitance, are not estimated by the method proposed in this paper. Chia-jui Chiang et al. in [89] have achieved to estimate simultaneously the State of Charge (SoC) and temperature of supercapacitor by applying a real-time algorithm, an Extended Kalman Filter (EKF), with only the voltage and current measurements. In this paper, the parameters of the EDLC model are determined from EIS measurement by least square method. The experimental results proved that the EKF based estimator provided a

satisfying prediction of the state of charge and temperature. They have prospected that the EKF algorithm can also allow to estimate other states and parameters with an extended model. This prospective is precisely one important part of this thesis. Artificial intelligence techniques such as ANN (Artificial Neural Networks) have been used recently to understand and model the nonlinear complicated behaviors of EDLCs [90] [91]. For example, the authors in [91] have developed an artifical neural network simulator for supercapacitor performance prediction and a three-layer artifical neural network was used in [90] to generate the highly nonlinear relationships between the temperature, voltage and the unknown parameters based on which the online supercapacitor dynamic models are built for energy conversion and management. But because of some drawbacks, these artificial intelligence techniques are still impractical for real-time execution, as commented in [88].

The online monitoring of EDLCs proposed in this thesis uses the real-time state observers to estimate the parameters of the EDLCs during their aging life. One outstanding advantage of the proposed method is that it can be implemented for the EDLCs embedded in the application without interrupting the EDLCs' functioning. Furthermore, the EDLCs parameters identification does not require any specific charging/discharging procedure but only with the current and terminal voltage measurements during their functioning.

## 3.2 Strategy of online monitoring of EDLCs' aging

### 3.2.1 State of Health (SoH) and State of Charge (SoC)

As presented in the first chapter, some of the EDLCs parameters evolve with aging. Therefore, the state of health of the EDLCs can be determined from the evolution of their parameters. The end of life criterion of EDLCs is normally given by their manufacturers. For example, Maxwell has defined the life criteria of their products as a reduction of the capacitance of $20\%$ or an increase of the equivalent series resistance of $100\%$. When there are more than two parameters considered as aging indicators, as illustrated in the first chapter, some of them have a large variation during aging, such as the dynamic and series resistances, while some others, for example the capacitance, evolve slightly with aging. Different parameters may have different contributions when determining the SoH. Supposing $N$ parameters can be considered as indicators of the EDLC aging, the SoH can be defined as [92] [93]:

$$\mathrm{SoH}_1(\%) = 100 \times \sum_{j=1}^{N} \beta_j \left| \frac{D_j - D_j^{\mathrm{end}}}{D_j^{\mathrm{init}} - D_j^{\mathrm{end}}} \right|, \text{ with } \sum_{\mathrm{j}=1}^{\mathrm{N}} \beta_{\mathrm{j}} = 1 \tag{3.1}$$

where $D_j$ is a current parameter value in the aging process, $D_j^{\text{init}}$ is the value of a fresh EDLC, $D_j^{\text{end}}$ is the parameter value of a fully aged EDLC which is often specified by the manufacturer and $\beta_j$ is the weight for each parameter. For the parameters whose evolutions during the aging are much closely related to the performance degradation of the EDLCs, or whose estimations are more reliable, their aging weights are relatively larger.

Since some parameters may reach their end of life criterion before the others, another possible SoH indicator can be defined as:

$$\text{SoH}_2(\%) = 100 \times \underset{j=1\ldots N}{\text{Min}} \left| \frac{D_j - D_j^{\text{end}}}{D_j^{\text{init}} - D_j^{\text{end}}} \right| \tag{3.2}$$

Another essential variable is called the state of charge. During the use of an EDLC in an application, it is very important for the user to know the level of remanent energy. For an ideal EDLC model with only one capacitance, the stored energy of the capacitor can be calculated by [2]

$$E = \int P dt = \int \left( V \cdot C \frac{dV}{dt} \right) dt = \frac{1}{2} C V^2 \tag{3.3}$$

where $C$ is the capacitance of the voltage and $V$ is the open circuit voltage of an EDLC. The state of charge can be defined as the percentage of the remanent energy and the total energy:

$$\text{SoC}(\%) = 100 \times \frac{E_{\text{remanent}}}{E_{\text{total}}} \tag{3.4}$$

The total energy is the energy stored in the EDLC when it is fully charged. It seems that if the capacitance $C$ is constant, the SoC can be obtained only from the open circuit voltage measurement. However, it should be noticed that a real EDLC is not an ideal capacitor and it is often modeled with some resistances which explain Joule losses. In this case, the energy calculated by Eq. 3.3 cannot provide an accurate estimation of the SoC. Therefore, a better estimation of SoC is based on an appropriate EDLC model. An EDLC model often has several capacitors in parallel or series, for example, the three-branch model or transmission line model presented in the previous chapter. Thus, the energy stored in the EDLC is expressed as the sum of the energy stored in each capacitor:

$$E = \sum_{j=1}^{N} \left( \int P_j \, dt \right) = \sum_{j=1}^{N} \left( \int u_j i_j \, dt \right) \tag{3.5}$$

where $N$ is the number of the capacitors, $u_j$ is the voltage across each capacitor and $i_j$ is the current through each capacitor. As far as the internal voltage and current of each capacitor in the EDLC model can be estimated, a correct value of the state of

charge of the EDLC can be obtained.

### 3.2.2 Online identification

In an EDLCs energy storage system, the discharging of EDLCs is seldom perfectly deterministic and always depends on the energy consumer. On the other hand, during the charging phase, the EDLCs are often charged with a known constant current or a constant power supply and the charging process is thus quite simple and easy to control. The signals (i.e. voltage and current) obtained from charging phase are also quite regular and very easy to process. For this reason, the online monitoring strategy proposed in this thesis is to apply an observer-based monitoring system to the EDLCs during their charging period only. This way, the monitoring system does not disturb the function of the load and the current and voltage signals can be made sufficiently exciting for the states and parameters to be observed.

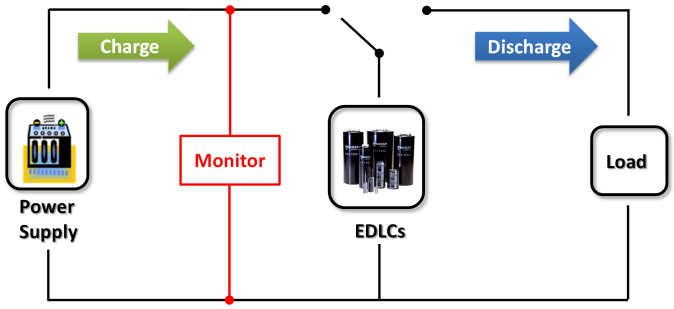


Figure 3.1: EDLCs aging monitoring system.

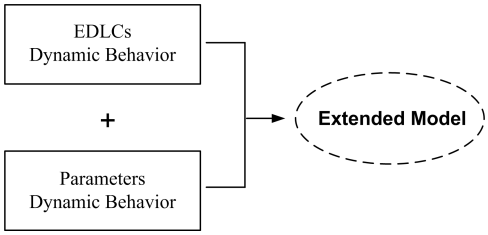


Figure 3.2: Schematic diagram of the extended model.

Supposing that the EDLCs can be represented by a state space model as follows:

$$\Sigma_{\text{sys}}: \begin{cases} \dot{x}_s = f(x_s, u) \\ y \quad = h(x_s, u) \end{cases} \tag{3.6}$$

where $x_s \in \boldsymbol{R}^n$ is the state of the EDLC model, $u$ and $y$ are the input and output of the system. The EDLC parametric model can be linear or nonlinear according to the circuit diagram behind. Supposing that the parameters of this system are known and thus with the input and output information of the system, an appropriate real-time observer, such as an Kalman filter, can provide an estimation of the system internal

states, which are often current or voltage variables. But during the aging of EDLCs, the physical parameters of EDLCs, such as the series resistance or capacitance, may evolve with time. The purpose of this work is to estimate not only the internal states of the EDLCs system but also their physical parameters in real time. One possible solution is to extend the states of EDLC system by adding the parameters as new states. Thus, the extended states $x_e$ includes the original states $x_s$ (i.e. internal current or voltage variables) and additional parametric states $x_p \in \boldsymbol{R}^p$.

$$x_e = \begin{bmatrix} x_s \\ --- \\ x_p \end{bmatrix}, \quad (x_e \in \boldsymbol{R}^{n+p}) \tag{3.7}$$

As said previously, the parameters of EDLCs vary with aging. But with respect to the current or voltage variables, the variation of these parameters is very slow and can be approximated as constant during a small piece of time. Therefore, the dynamic behavior of the parameters are approximated by

$$\dot{x}_p = 0 \tag{3.8}$$

Then, an extended EDLCs model $\Sigma_{\text{ext}}$ can be obtained by adjoining the parameters dynamic behavior to the EDLCs system (Fig. 3.2):

$$\Sigma_{\text{ext}} : \begin{cases} \dot{x}_e = f'(x_e, u) = \begin{bmatrix} f(x_s, u) \\ 0 \end{bmatrix} \\ y \ = h'(x_e, u) \end{cases} \tag{3.9}$$

Once the extended EDLC model is obtained, a real-time observer can be designed to estimate both the parameters and the internal states of the EDLC with the input and output signals which can be either terminal voltage or current measurement. It allows to estimate the state of charge during the usage of the EDLC and to determinate the state of health during its aging life (see Fig. 3.3).

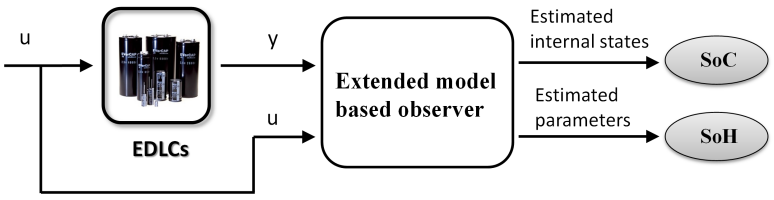


Figure 3.3: Online observation of SoC and SoH.

## 3.3 Review of observer theory

### 3.3.1 Observability

The goal of this chapter is to estimate the EDLC parameters using a state observer based on a specific EDLC model. Before to design the observer, it is necessary to check the observability of the system. A system is said observable if its initial states can be uniquely determined from the input and output signals measured on a finite time interval (see Fig. 3.4). The target system can be linear or non-linear leading to different ways to determine its observability.

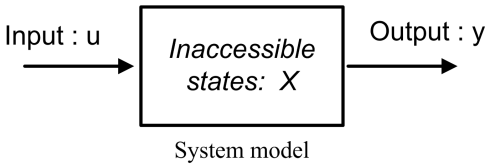


Figure 3.4: Target system model with unknown states.

#### Observability of a linear system

The following equation is a general expression of a linear time-invariant system [94] [95]:

$$\begin{cases} \dot{x} = Fx + Gu \\ y = Hx \end{cases} \tag{3.10}$$

where $u \in \boldsymbol{R}^r$ is the input, $y \in \boldsymbol{R}^m$ is the output and $x \in \boldsymbol{R}^n$ is the state vector. To determine the observability of such a linear system, the well-known criterion called Observability Rank Condition (ORC) [94] [95] is often used. The linear system is observable if the observability matrix $O$ has full rank $n$ [94] [40].

$$O = \begin{bmatrix} H \\ HF \\ \vdots \\ HF^{n-1} \end{bmatrix} \tag{3.11}$$

#### Observability of a nonlinear system

The observability of a nonlinear dynamic system defined as

$$\Sigma : \begin{cases} \dot{x} = f(x,u) \\ y = h(x,u) \end{cases} \tag{3.12}$$

where the input $u \in \boldsymbol{R}^r$, the output $y \in \boldsymbol{R}^m$ and the states $x \in M$ ($M$ is an open subset of $R^n$), was studied by R. Hermann and A. J. Krener in 1977 in [94]. First

of all, several definitions are specified [94]:

- *Definition 1: Indistinguishability*
  A pair of different points $x^0$ and $x^1$ is indistinguishable if the system realizes the same input-output map for the same input $u$, with state initialization at $x^0$ and $x^1$ respectively $x^0(0)$ and $x^1(0)$: $y(t) = h(x^0(t), u(t)) = h(x^1(t), u(t))$. We denote by the indistinguishability set $I(x^0)$ all points $x^1$ that are indistinguishable from $x^0$.
- *Definition 2: Observability*
  The nonlinear system $\Sigma$ is observable at $x^0$ if $I(x^0) = \{x^0\}$, and globally observable if $I(x^0) = \{x^0\}$ for any $x^0 \in M$.
- *Definition 3: Local observability*
  Local observability is a stronger concept compared to observability. The system $\Sigma$ is said locally observable at $x^0$, if for any neighborhood $U$ of $x^0$, $I(x^0) \cap U = \{x^0\}$ and is said locally observable if it is true for any $x^0 \in M$.

Once the definitions of the "Observability" and "Local observability" are given, their numerical determination will be explained as follows.

To determine if a system is observable, we need to know if there is enough information brought by the output to reconstruct the states. In other words, if the map $\boldsymbol{R}^n(x) \mapsto \boldsymbol{R}^n(y, \dot{y}, ..., y^{(n-1)})$ is invertible, the states of the system can be observable [96]. Supposing that the output is a scalar, its first to $(n-1)$th-order derivatives are derived to form an equation set and thus to see if there exists a solution (i.e. states $x$) for this equation set.

The first-order derivative of $y$ is expressed as follows and is a function of $x$, the input $u$ and its derivative.

$$\begin{aligned} \dot{y} = \frac{dy}{dt} &= \frac{\partial h}{\partial x} f + \frac{\partial h}{\partial u} \dot{u} \\ &= h_1(x, u, \dot{u}) \end{aligned} \tag{3.13}$$

Similarly, the $i$ th-order derivative $(2 \leq i \leq n-1)$ of $y$ is calculated as the total differentiation of $h_{i-1}$ and is a function of $x$, the input $u$ and its derivatives.

$$\begin{aligned} y^{(i)} = \frac{dy^{(i-1)}}{dt} &= \frac{\partial h_{i-1}}{\partial x} f + \frac{\partial h_{i-1}}{\partial u} \dot{u} + \cdots + \frac{\partial h_{i-1}}{\partial u^{(i-1)}} u^{(i)} \\ &= h_i(x, u, \dot{u}, \cdots, u^{(i)}) \end{aligned} \tag{3.14}$$

For simplicity, the vectors $Y$ and $U$ are defined as (supposing that the output $y$ is a scalar): $\boldsymbol{Y} = [y,\ \dot{y},\ ...\ , y^{(n-1)}]^T$, $\boldsymbol{U} = [u,\ \dot{u},\ ...\ , u^{(n-1)}]^T$. A Lie operator $L_f(h)$ is defined as the total differentiation of $h$ and used to represent the $i$ th derivative of

output $y$ [97]:

$$y^{(i)} = L_f(h_{i-1})(x, \boldsymbol{U}) = \frac{\partial h_{i-1}}{\partial x}(x, \boldsymbol{U}) f(x, u) + \frac{\partial h_{i-1}}{\partial u}(x, \boldsymbol{U}) \frac{d\boldsymbol{U}}{dt} \tag{3.15}$$

Therefore, the output and their derivatives equation set can be written as

$$\boldsymbol{Y} = \begin{bmatrix} h(x,u) \\ h_1(x, \boldsymbol{U}) \\ h_2(x, \boldsymbol{U}) \\ \vdots \\ h_{n-1}(x, \boldsymbol{U}) \end{bmatrix} = \begin{bmatrix} h(x,u) \\ L_f(h)(x, \boldsymbol{U}) \\ L_f(h_1)(x, \boldsymbol{U}) \\ \vdots \\ L_f(h_{n-2})(x, \boldsymbol{U}) \end{bmatrix} \tag{3.16}$$

If there exists a solution for the equation set 3.16, the nonlinear system is said globally observable for a given input $u$. The nonlinear system might be very complex, thus adding difficulty and even making this equation set impossible to solve. Therefore, the local observability is more often used to check if the nonlinear system is observable with the following theorem [94].

– *Theorem 1*

If the Jacobian matrix of vector $\boldsymbol{Y}$, defined by

$$J = \frac{\partial \boldsymbol{Y}}{\partial x} = \frac{\partial}{\partial x} \begin{bmatrix} h(x,u) \\ L_f(h)(x, \boldsymbol{U}) \\ L_f(h_1)(x, \boldsymbol{U}) \\ \vdots \\ L_f(h_{n-2})(x, \boldsymbol{U}) \end{bmatrix}, \tag{3.17}$$

has full rank $n$ at $x^0 \in M$, the nonlinear system is locally observable at $x^0$.

The observability study allows to know if it is possible to observe the states of a system. Once a system is determined as observable, its states can be estimated by using an appropriate observer which will be presented in the following section.

### 3.3.2 Real-time state observers

In a physical system, the states can be temperature, pressure, voltage and so on. Unfortunately sometimes, some states are internal variables of the system and may be not available for measurement or their measurement need costly sensors. The goal of using a real-time state observer is to provide an approximation of these states on the basis of available measurements. For example, the extended Kalman filter is frequently used in the permanent magnet synchronous machine sensorless drive to estimate the position and speed [98] [99]. In this section, two classical observers, Luenberger observers and Kalman filters will be firstly introduced. Both

observers employ a "prediction-correction" principle to realize the observation of the system states as shown in Fig. 3.5. The essential part of the state observation is the correction term composed of a correction gain $K$ multiplied by the error between the measured and predicted output of the system. In this way, even if the initial state estimation is not well set, the correction part will still allow the state estimation to converge to the correct value.

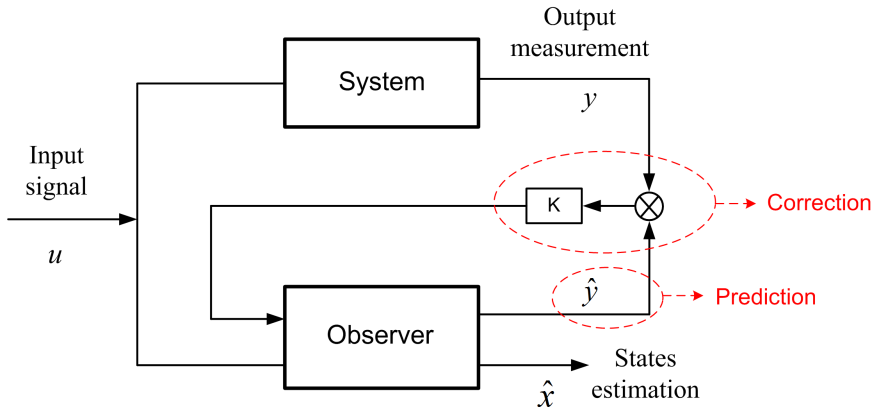


Figure 3.5: Principle of states observation.

### Observers for linear systems

Luenberger observer and Kalman filter are often used to estimate the states of linear time-invariant system with a general form given by

$$\begin{cases} \dot{x}(t) = Fx(t) + Gu(t) \\ y(t) = Hx(t) + Iu(t) \end{cases} \tag{3.18}$$

where $x$ is an $n \times 1$ state vector, $u$ is an $r \times 1$ input vector, $y$ is an $m \times 1$ output vector, $F$ is an $n \times n$ state transition matrix, $G$ is an $n \times r$ state distribution matrix, $H$ is an $m \times n$ output transition matrix and $I$ is an $m \times r$ output distribution matrix. It is assumed that only the input $u(t)$ and $y(t)$ can be measured and that the state variable $x(t)$ is observable.

The main observation principles of these observers are the same as shown in Fig. 3.5. The only difference is how the correction gain $K$ is determined.

– *Luenberger observer (LO)*

The Luengerber state observer was proposed by Luenberger in the early 1960s [100] [101]. The Luenberger observer reconstructs the states of the continuous-time system with a feedback from the estimation error $(y - \hat{y})$:

$$\begin{cases} \dot{\hat{x}}(t) = F\hat{x}(t) + Gu(t) + K(y(t) - \hat{y}(t)) \\ \hat{y}(t) = H\hat{x}(t) + Iu(t) \end{cases} \tag{3.19}$$

where the observer gain $K$ is a $n \times m$ matrix.
The state estimation error is the difference between the real state and the estimated state:

$$e(t) = x(t) - \hat{x}(t) \tag{3.20}$$

The aim of the Luenberger observer is to provide the state estimation as close as possible to the real state such that the error is minimal. To study the dynamic evolution of this state estimation, the derivative of the error is deduced:

$$\begin{aligned} \dot{e}(t) &= \dot{x}(t) - \dot{\hat{x}}(t) \\ &= (F - KH) \cdot e(t) \end{aligned} \tag{3.21}$$

This equation implies that the dynamic behavior of this observer depends on the observer gain $K$. Regardless of the initial conditions and input, as long as the eigenvalues of the matrix $(F - KH)$ are located on the left part of the complex plane, the equation above is asymptotically stable, which means that the estimated states will converge to the real states of the observed system [102]. The convergence rate can be adjusted by a proper choice of the observer gain.

– *Kalman filter (KF)*
The Luenberger observer is a deterministic state estimator which neglects the influence of noise on the model. In other words, LO can be a good estimator if the model based on which the observer is designed is very close to the real system. But if the model is not so accurate with a significant amount of noise, the estimation results provided by LO maybe not satisfying. On the other hand, Kalman filter is an optimal estimator based on a stochastic state model involving the modelization error and measurement noise. KF provides optimal state estimation by minimizing the mean square error of the estimated state. The KF in the continuous-time case is better known as the Kalman-Bucy filter. Compared to the model (Eq. 3.18) used by LO, the continuous-time linear stochastic dynamic model used by KF takes the noises into account [103]:

$$\begin{cases} \dot{x}(t) = Fx(t) + Gu(t) + v(t) \\ y(t) = Hx(t) + Iu(t) + w(t) \end{cases} \tag{3.22}$$

where the random variable $v(t)$ represents the process noise (i.e. the modelization error) which is assumed to be a zero-mean white noise with covariance matrix $Q \in \boldsymbol{R}^{n \times n}$ and the random variable $w(t)$ is a zero-mean white noise of covariance $R \in \boldsymbol{R}^{m \times m}$ produced by the output measurement. The

Kalman filter can be written as [103] [104]:

$$\dot{\hat{x}}(t) = F\hat{x}(t) + Gu(t) + K \cdot (y(t) - (H\hat{x}(t) + Iu(t))) \quad (3.23)$$

$$K(t) = P(t)H^T R^{-1} \quad (3.24)$$

$$\dot{P}(t) = FP(t) + P(t)F^T + Q - P(t)H^T R^{-1} HP(t) \quad (3.25)$$

where $K$ is the correction gain and $P(t) \in \boldsymbol{R}^{n\times n}$ is the covariance matrix of the state estimation error. The expression of $K$ is obtained by minimizing the covariance matrix $P$. The value of the correction gain is continuously updated and thus allows the state estimation to converge to the real state value. The covariance matrices $Q$, $R$ and $P$ are symmetric which gives $K^T = R^{-1}HP(t)$. Then Eq. 3.25 can be simplified to

$$\dot{P}(t) = FP(t) + P(t)F^T + Q - K(t)RK(t)^T \quad (3.26)$$

and thus the computational cost is reduced by avoiding the calculation of $P(t)H^T R^{-1}$ in Eq. 3.25.

In the case of one dimensional output, the covariance of measurement noise $R$ is a constant scalar. Then, $P$ can be defined as $P = RP_n$, where the normalized matrix $P_n = PR^{-1}$ is a positive definite symmetric matrix, and Eqs. 3.24 and 3.26 become [105]:

$$K(t) = P_n(t)H^T \quad (3.27)$$

$$\dot{P}_n(t) = FP_n(t) + P_n(t)F^T + QR^{-1} - K(t)K(t)^T \quad (3.28)$$

These equations clearly show that, by using a normalized matrix of $P$, the tuning parameters are reduced to only one matrix $QR^{-1}$.

**Observers for nonlinear systems**

The two observers introduced before are for a linear system and are not suitable for a nonlinear one. Consider the following nonlinear system

$$\begin{cases} \dot{x}(t) = f(x(t), u(t)) \\ y(t) = h(x(t), u(t)) \end{cases} \quad (3.29)$$

where $x$ is an $n \times 1$ state vector, $u$ is an $r \times 1$ input vector, $y$ is an $m \times 1$ output vector, $f$ and $h$ are continuously differentiable with respect to $x$ and $u$.

To observe the state of this nonlinear system, one possible solution is to linearize the nonlinear system and thus to use a Luenberger observer or a Kalman

filter on the linearized system. The functions $f(x(t), u(t))$ and $h(x(t), u(t))$ can be approximated by a first-order Taylor approximation at the state estimation $\hat{x}$:

$$\begin{cases} \dot{x} \simeq f(\hat{x}, u(t)) + \frac{\partial f}{\partial x}(\hat{x}, u(t))(x - \hat{x}) \\ y \simeq h(\hat{x}, u(t)) + \frac{\partial h}{\partial x}(\hat{x}, u(t))(x - \hat{x}) \end{cases} \tag{3.30}$$

Then the nonlinear system in Eq. 3.29 is linearized about the estimated state $\hat{x}$:

$$\begin{cases} \dot{x} \simeq Fx + g_f(\hat{x}, u(t)) \\ y \simeq Hx + g_h(\hat{x}, u(t)) \end{cases} \tag{3.31}$$

where $g_f(\hat{x}, u(t)) = f(\hat{x}, u(t)) - F\hat{x}$, $g_h(\hat{x}, u(t)) = h(\hat{x}, u(t)) - H\hat{x}$ and $F \in \boldsymbol{R}^{n \times n}$ and $H \in \boldsymbol{R}^{m \times n}$ are the Jacobian matrices of the system:

$$F = \frac{\partial f}{\partial x}(\hat{x}, u(t)), \; H = \frac{\partial h}{\partial x}(\hat{x}, u(t)) \tag{3.32}$$

Once the linearized system is obtained, the extended Luenberger observer (ELO) [106] and extended Kalman filter (EKF) [107] can be used for the state estimation.

– *Extended Luenberger observer (ELO)*
Similar to the Luenberger observer, the extended Luenberger observer is also realized by adding a correction term to the reconstructed model.

$$\begin{cases} \dot{\hat{x}}(t) = f(\hat{x}(t), u(t)) + K(y(t) - \hat{y}(t)) \\ \hat{y}(t) = h(\hat{x}(t), u(t)) \end{cases} \tag{3.33}$$

The derivative of the error between the real state $x$ and the estimated state $\hat{x}$ is obtained by

$$\begin{aligned} \dot{e}(t) =& f(x(t), u(t)) - f(\hat{x}(t), u(t)) \\ & - K\left(h(x(t), u(t)) - h(\hat{x}(t), u(t))\right) \end{aligned} \tag{3.34}$$

According the first order approximation of Eq. 3.31, the above equation is approximated as

$$\dot{e}(t) \simeq (F - KH) \cdot e(t) \tag{3.35}$$

For the estimated state to converge to the real state of the system, $K$ should be chosen appropriately to get eigenvalues of matrix $F - KH$ with negative real parts.

– *Extended Kalman filter (EKF)*

Based on the linearized model, the extended Kalman filter is expressed as [107]

$$\dot{\hat{x}}(t) = f(\hat{x}(t), u(t)) + K(y(t) - h(\hat{x}(t), u(t))) \quad (3.36)$$

$$K(t) = P(t)H^T R^{-1} \quad (3.37)$$

$$\dot{P}(t) = FP(t) + P(t)F^T + Q - K(t)RK(t)^T \quad (3.38)$$

It should be noticed that both observers, (E)LO and (E)KF, have the same structure of dynamic state estimation equation (see Eqs. 3.19 and 3.23 or Eqs. 3.33 and 3.36). The only difference is the way to calculate the correction gain. When choosing $K$, (E)LO uses a pole placement strategy [108], while (E)KF applies an optimization algorithm by minimizing the variance of the estimation error. Therefore, to some extend, (E)KF can be considered as an optimal version of (E)LO. It is clear to see that compared to (E)LO, (E)KF has higher computational cost because the correction gain is obtained by solving the differential equation of $P$ matrix. On the other side, (E)KF may provide more accurate estimation results with a high tolerance of modelization error and measurement noises. Therefore, which observer should be used for a system depends on the accuracy of the model and the data acquisition devices.

In the following two sections, the real-time observers will be designed based on two models. One is a quite simple model with three parameters and the other one is more complicated with more parameters which explains better the real EDLCs behavior. Afterwards, the state of health monitoring results based on these two models will allow to tell if the observers designed based on a simple model can be enough for online aging monitoring or it is better to observe with a more complicated model.

## 3.4 Parameter estimation for the RRC model of EDLCs

### 3.4.1 EDLC representation by a RRC model

#### State space representation

In this section, a simple RRC circuit, equivalent to a lumped first-order discrete transmission line model, is used for the supercapacitor modelization (see Fig. 3.6). The details of the physical representation for the components of this electrical circuit have been already discussed in Chapter 2 (see §2.1.1). The dynamic behavior of the EDLC modeled by the above electrical circuit is described by:

$$\begin{cases} \frac{du_1}{dt} = -\frac{1}{R_p C}u_1 + \frac{1}{C}i_{sc} \\ u_{sc} = u_1 + R_s i_{sc} \end{cases} \quad (3.39)$$

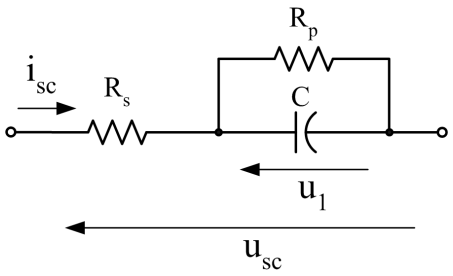


Figure 3.6: Simple RRC model of an EDLC.

where $u_1$ is the voltage across the capacitor, $i_{sc}$ and $u_{sc}$ are respectively the terminal current and voltage of the EDLC.

The State of Charge (SoC) of an EDLCs system can be determined by calculating the energy stored during the charging phase and the remaining energy during discharging phase, without the disturbance of measuring the open circuit voltage of EDLCs. The energy $E$ stored in the EDLC can be calculated by

$$E = \frac{1}{2} C u_1^2 \tag{3.40}$$

**Extended EDLC model**

It is assumed that the three parameters, $R_s$, $R_p$ and $C$ are slowly varying with respect to the electrical quantity $u_1$. Then the dynamic behavior of these parameters can be expressed as

$$\frac{d}{dt}\left[R_s\right](t) = 0, \quad \frac{d}{dt}\left[\frac{1}{C}\right](t) = 0, \quad \frac{d}{dt}\left[\frac{-1}{R_p C}\right](t) = 0 \tag{3.41}$$

Adjoining these three terms into the linear system Eq. 3.39, a parameterless extended state space model of an EDLC is obtained:

$$\begin{cases} \dot{x}_1 = x_1 x_4 + x_3 i_{sc} \\ \dot{x}_2 = 0 \\ \dot{x}_3 = 0 \\ \dot{x}_4 = 0 \end{cases} \tag{3.42}$$

$$u_{sc} = x_1 + x_2 i_{sc} \tag{3.43}$$

where $x_1 = u_1$, $x_2 = R_s$, $x_3 = 1/C$ and $x_4 = -1/(R_p C)$ are the state variables, the current $i_{sc}$ and voltage $u_{sc}$ are respectively the input and output of this system, corresponding to the known $u$ and measured $y$ of the general system representation (Eq. 3.29). This extended model is obviously nonlinear. Therefore, a nonlinear state observer is needed to estimate the states and it will allow to obtain the parameter

estimations.

### 3.4.2 Sensitivity and observability study

#### Sensitivity analysis

The main objective of this research is to realize the identification of the parametric model of EDLCs by online state observers. It should be noticed that not only the estimated parameters are important but also the confidence of these estimations. Therefore, the sensitivity analysis will be used to know the parameters uncertainty and to have an idea of how much frequency information of the signals is needed to obtain satisfying estimations.

The classical sensitivity analysis was introduced by Bode in 1945 [109] and extended by Horowitz [110]. It is a normalized measure of the change in some desired quantity $T$ with respect to the change in some system parameter $p$ [111]. The sensitivity of $T$ with respect to $p$ is defined as [111]:

$$S_p^T \equiv \frac{\Delta T/T}{\Delta p/p}, \tag{3.44}$$

where $\Delta T$ is the change of the quantity caused by the change of the parameter $\Delta p$. Classical sensitivity analysis explores the influence of parameters changes on the model output [112]. The sensitivity coefficient shows how much the quantity $T$ depends on the parameter $p$ : if $T$ depends on $p$ by a power law, $T = K\,p^n$, then $S_p^T = n$ and provides the degree of dependence of T on the $p$ parameter. Considering the simple EDLC model shown in Fig. 3.6, there are three unknown parameters ($R_s$, $R_p$, $C$) to estimate. The impedance of this model $Z$ depends on these three parameters: $Z(\jmath\omega) = R_s + R_p/(1 + \jmath R_p C\omega)$. The sensitivity of the impedance $Z$ with respect to the three parameters can be written as:

$$S_{R_s}^Z(\jmath\omega) \equiv \frac{R_s}{Z}\cdot\frac{\Delta Z}{\Delta R_s}, \quad S_{R_p}^Z(\jmath\omega) \equiv \frac{R_p}{Z}\cdot\frac{\Delta Z}{\Delta R_p}, \quad S_C^Z(\jmath\omega) \equiv \frac{C}{Z}\cdot\frac{\Delta Z}{\Delta C} \tag{3.45}$$

The sensitivities $S_{R_s}^Z$, $S_{R_p}^Z$ and $S_C^Z$ represent the influence of the changes in $R_s$, $R_p$ and $C$ on the impedance $Z$. If the sensitivity modulus with respect to one parameter is high, it means that a little variation of this parameter can bring a great change to the impedance, resulting in a large influence on the output of the system. So it is said that the output behavior of the model is very sensitive to this parameter and thus can help to estimate this parameter correctly. Apparently, the sensitivities given in Eq. 3.45 depends on frequency. In order to get a reliable parameter estimation, we need to find out the frequency range needed to obtain a high sensitivity modulus.

For the simple RRC model shown in Fig. 3.6, the sensitivity of the impedance

with respect to the three parameters can be analyzed and their modulus in function of frequency are shown in logarithmic coordinates in Fig. 3.7. In this study, the parameters are assumed as: $R_s = 1\ \Omega$, $R_p = 3000\ \Omega$, $C = 1$ F which are chosen according to the real Nichicon EDLC studied in this thesis. It is clear to see from this plot that the highest sensitivity of each parameter is obtained at different frequency ranges. The sensitivity modulus with respect to $R_s$ nearly equals one when the frequency is higher than 1 Hz. This is quite easy to understand because at high frequency, the impedance of the capacitor goes to zero, which leads to $Z \approx R_s$. Therefore, in order to obtain an accurate estimation of $R_s$, high frequency (at least 1 Hz) signals are required. When the frequency is very small ($f \rightarrow 0$), the impedance of the EDLCs goes to the sum of the series resistance and the parallel resistance ($Z = R_s + R_p$). It means that $R_p$ can be easy to estimate at very low frequencies. It is also revealed from Fig. 3.7 that at the frequencies lower than $10^{-4}$ Hz, the sensitivity modulus with respect to $R_p$ starts to be close to one. The sensitivity plot also shows that when the frequency is between $10^{-4}$ Hz and $10^{-1}$ Hz, the sensitivity modulus with respect to $C$ has maximum value.

It is concluded from this sensitivity study that, if we want to accurately estimate the three parameters of the simple RRC model with a small estimation uncertainty, different frequency ranges are required in the voltage and current signals.

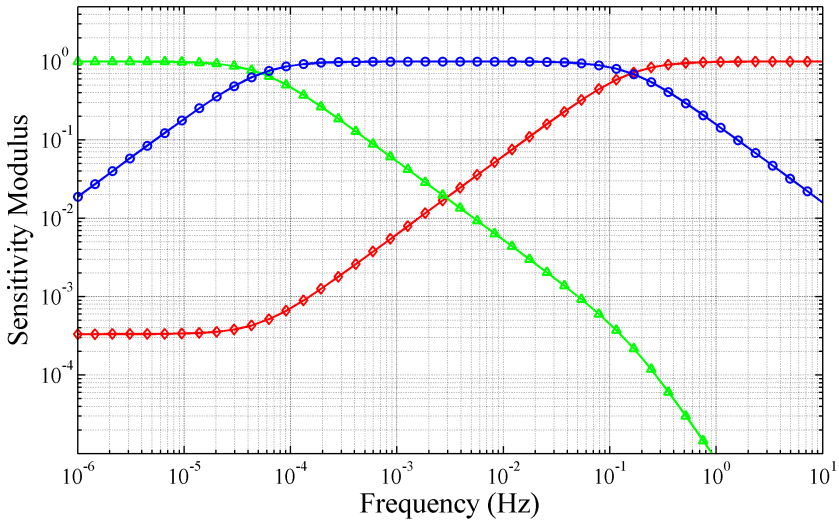


Figure 3.7: Sensitivity plot of the EDLC impedance $Z$ with respect to each parameter of the RRC model (red diamond: $R_s$, blue circle: $C$ and green triangle: $R_p$).

### Nonlinear observability study

The observability of this extended nonlinear EDLC model is studied in order to check the possibility to estimate the parameters with an observer. For our extended EDLC system represented by Eqs. 3.42 and 3.43, the output $u_{sc}$ and its first to third

derivatives, $\dot{u}_{sc}$, $\ddot{u}_{sc}$ and $\dddot{u}_{sc}$, are derived as

$$\begin{cases} u_{sc} = x_1 + x_2 i_{sc} \\ \dot{u}_{sc} = x_1 x_4 + x_3 i_{sc} + x_2 \dot{i}_{sc} \\ \ddot{u}_{sc} = x_1 x_4^2 + x_3 x_4 i_{sc} + x_3 \dot{i}_{sc} + x_2 \ddot{i}_{sc} \\ \dddot{u}_{sc} = x_1 x_4^3 + x_3 x_4^2 i_{sc} + x_3 x_4 \dot{i}_{sc} + x_3 \ddot{i}_{sc} + x_2 \dddot{i}_{sc} \end{cases} \tag{3.46}$$

where $\dot{i}_{sc}$, $\ddot{i}_{sc}$ and $\dddot{i}_{sc}$ are the first to third derivatives of the input current $i_{sc}$.

Solving the equation set 3.46 leads to:

$$\begin{cases} x_1 = u_{sc} - i_{sc} x_2 \\ x_2 = \frac{i_{sc}(\dot{u}_{sc}\dddot{u}_{sc} - \ddot{u}_{sc}^2) + \dot{i}_{sc}(\dot{u}_{sc}\ddot{u}_{sc} - u_{sc}\dddot{u}_{sc}) + \ddot{i}_{sc}(u_{sc}\ddot{u}_{sc} - \dot{u}_{sc}^2)}{u_{sc}(\ddot{i}_{sc}^2 - i_{sc}\dddot{i}_{sc}) + \dot{u}_{sc}(i_{sc}\dddot{i}_{sc} - \dot{i}_{sc}\ddot{i}_{sc}) + \ddot{u}_{sc}(\dot{i}_{sc}^2 - i_{sc}\ddot{i}_{sc})} \\ x_3 = (\dot{u}_{sc} - x_1 x_4 - x_2 \dot{i}_{sc})/i_{sc} \\ x_4 = \frac{\dot{u}_{sc}(\ddot{i}_{sc}^2 - \dot{i}_{sc}\dddot{i}_{sc}) + \ddot{u}_{sc}(i_{sc}\dddot{i}_{sc} - \dot{i}_{sc}\ddot{i}_{sc}) + \dddot{u}_{sc}(\dot{i}_{sc}^2 - i_{sc}\ddot{i}_{sc})}{u_{sc}(\ddot{i}_{sc}^2 - \dot{i}_{sc}\dddot{i}_{sc}) + \dot{u}_{sc}(i_{sc}\dddot{i}_{sc} - \dot{i}_{sc}\ddot{i}_{sc}) + \ddot{u}_{sc}(\dot{i}_{sc}^2 - i_{sc}\ddot{i}_{sc})} \end{cases} \tag{3.47}$$

The solution of the equation set only exists under the condition that the denominators of Eq. 3.47 are different from zero:

$$\begin{cases} u_{sc}(\ddot{i}_{sc}^2 - \dot{i}_{sc}\dddot{i}_{sc}) + \dot{u}_{sc}(i_{sc}\dddot{i}_{sc} - \dot{i}_{sc}\ddot{i}_{sc}) + \ddot{u}_{sc}(\dot{i}_{sc}^2 - i_{sc}\ddot{i}_{sc}) \neq 0 \\ i_{sc} \neq 0 \end{cases} \tag{3.48}$$

If the input current and output current of the system and their derivatives satisfy the condition presented in Eq. 3.48, this system is globally observable.

A globally unobservable system could be locally observable at some points. The theorem (Eq. 3.17) is used to determine the local observability by checking the rank of the Jacobian matrix. The Jacobian matrix of the extended system can be obtained:

$$\begin{aligned} J &= \frac{\partial(u_{sc}, \dot{u}_{sc}, \ddot{u}_{sc}, \dddot{u}_{sc})}{\partial(x_1, x_2, x_3, x_4)} \\ &= \begin{bmatrix} 1 & i_{sc} & 0 & 0 \\ x_4 & \dot{i}_{sc} & i_{sc} & x_1 \\ x_4^2 & \ddot{i}_{sc} & x_4 i_{sc} + \dot{i}_{sc} & 2x_1 x_4 + x_3 i_{sc} \\ x_4^3 & \dddot{i}_{sc} & x_4^2 i_{sc} + x_4 \dot{i}_{sc} + \ddot{i}_{sc} & 3x_1 x_4^2 + 2x_3 x_4 i_{sc} + x_3 \dot{i}_{sc} \end{bmatrix} \end{aligned} \tag{3.49}$$

To simplify the calculation of the determinant of matrix $J$, a new matrix $J'$ is

deduced from simple row operation of $J$.

$$J' = \begin{bmatrix} 1 & i_{sc} & 0 & 0 \\ 0 & \dot{i}_{sc} - x_4 i_{sc} & i_{sc} & x_1 \\ 0 & \ddot{i}_{sc} - x_4 \dot{i}_{sc} & \dot{i}_{sc} & x_1 x_4 + x_3 i_{sc} \\ 0 & \dddot{i}_{sc} - x_4 \ddot{i}_{sc} & \ddot{i}_{sc} & x_1 x_4^2 + x_3 x_4 i_{sc} + x_3 \dot{i}_{sc} \end{bmatrix} \tag{3.50}$$

The simplified matrix $J'$ has the same determinant and rank with $J$:

$$\begin{aligned} \det(J) &= \det(J') \\ &= x_1 x_4 (i_{sc} \dddot{i}_{sc} - \dot{i}_{sc} \ddot{i}_{sc}) + x_3 (\dot{i}_{sc}^3 + i_{sc}^2 \dddot{i}_{sc} - 2 i_{sc} \dot{i}_{sc} \ddot{i}_{sc}) + \\ &\quad x_1 (\ddot{i}_{sc}^2 - \dot{i}_{sc} \dddot{i}_{sc}) + (x_1 x_4^2 + x_3 x_4 i_{sc})(\dot{i}_{sc}^2 - i_{sc} \ddot{i}_{sc}) \end{aligned} \tag{3.51}$$

Therefore, the extended EDLC system will satisfy the sufficient local observability condition if $\det(J) \neq 0$:

$$\det(J) \neq 0 \Rightarrow \operatorname{rank}(J) = n \tag{3.52}$$

The condition to determine the global observability presented in Eq. 3.48 and the determinant of Jacobian matrix expressed by Eq. 3.51 has a complex form depending on the states, the input current $i_{sc}$, output voltage $u_{sc}$ and their derivatives. Therefore, it is rather difficult to tell if the system is observable or not. Here, several special cases of observability are studied.

– *Case 1: Constant input signal*
  Suppose that the input current of EDLC is a DC constant signal: $i_{sc} = \mathrm{Cst}$. The first, second and third order derivations of $i_{sc}$ are zero:

$$\dot{i}_{sc} = \ddot{i}_{sc} = \dddot{i}_{sc} = 0 \tag{3.53}$$

  In this case, both Eqs. 3.48 and 3.52 are obviously not satisfied. Therefore, the system is globally and locally unobservable when the input current is constant.

– *Case 2: Exponential input signal*
  Suppose that the input current of EDLC is an exponential signal: $i_{sc} = Ae^{Bt}$, where $A$ and $B$ are constants. The first to third order derivations of the input current are deduced:

$$\begin{cases} \dot{i}_{sc} = ABe^{Bt} = Bi_{sc} \\ \ddot{i}_{sc} = AB^2 e^{Bt} = B^2 i_{sc} \\ \dddot{i}_{sc} = AB^3 e^{Bt} = B^3 i_{sc} \end{cases} \tag{3.54}$$

which leads to

$$\begin{aligned} &u_{sc}(\ddot{i}_{sc}^2 - \dot{i}_{sc}\dddot{i}_{sc}) + \dot{u}_{sc}(i_{sc}\dddot{i}_{sc} - \dot{i}_{sc}\ddot{i}_{sc}) + \ddot{u}_{sc}(\dot{i}_{sc}^2 - i_{sc}\ddot{i}_{sc}) = 0 \\ &\text{and} \qquad\qquad \det(J) = 0 \end{aligned} \tag{3.55}$$

It clearly shows that the system is globally and locally unobservable when the input current is an exponential signal.

– *Case 3: Sinusoidal input signal*

Suppose that the input current of EDLC is an AC sinusoidal signal: $i_{sc} = I\sin(\omega t + \varphi)$, ($I \neq 0,\ \omega \neq 0$), where $I$ is the amplitude of the sinusoidal signal and $\omega$ is the angular frequency. The first to third order derivations of the input signal are deduced as follows:

$$\begin{cases} \dot{i}_{sc} = I\omega\cos(\omega t + \varphi) \\ \ddot{i}_{sc} = -I\omega^2\sin(\omega t + \varphi) \\ \dddot{i}_{sc} = -I\omega^3\cos(\omega t + \varphi) \end{cases} \tag{3.56}$$

The corresponding output voltage of the EDLC is also a sinusoidal signal with a phase shift $\varphi$: $u_{sc} = U\sin(\omega t + \varphi)$. Then its first to third order derivations are deduced as

$$\begin{cases} \dot{u}_{sc} = U\omega\cos(\omega t + \varphi) \\ \ddot{u}_{sc} = -U\omega^2\sin(\omega t + \varphi) \\ \dddot{u}_{sc} = -U\omega^3\cos(\omega t + \varphi) \end{cases} \tag{3.57}$$

It is obtained from Eqs. 3.56 and 3.57 that:

$$u_{sc}(\ddot{i}_{sc}^2 - \dot{i}_{sc}\dddot{i}_{sc}) + \dot{u}_{sc}(i_{sc}\dddot{i}_{sc} - \dot{i}_{sc}\ddot{i}_{sc}) + \ddot{u}_{sc}(\dot{i}_{sc}^2 - i_{sc}\ddot{i}_{sc}) = 0 \tag{3.58}$$

which obviously shows that the global observability condition is not satisfied. Therefore, the system is globally unobservable with a sinusoidal current.
To check the local observability of this system with sinusoidal current, the determinant of Jacobian matrix $J$ can be obtained:

$$\begin{aligned} det(J) &= \omega^2 I^2[x_1 x_4^2 + x_3 x_4 I\sin(\omega t) + x_3\omega I\cos(\omega t) + x_1\omega^2] \\ &= \omega^2 I^2[x_1 x_4^2 + x_3 x_4 i_{sc} + x_3\dot{i}_{sc} + x_1\omega^2] \end{aligned} \tag{3.59}$$

Substituting the first-order differential equation of $x_1$ presented in Eq. 3.42 into the equation of determinant of $J$ above, it is obtained that:

$$\begin{aligned} det(J) &= \omega^2 I^2[\dot{x}_1 x_4 + x_3\dot{i}_{sc} + x_1\omega^2] \\ &= \omega^2 I^2[\ddot{x}_1 + x_1\omega^2] = 0 \end{aligned} \tag{3.60}$$

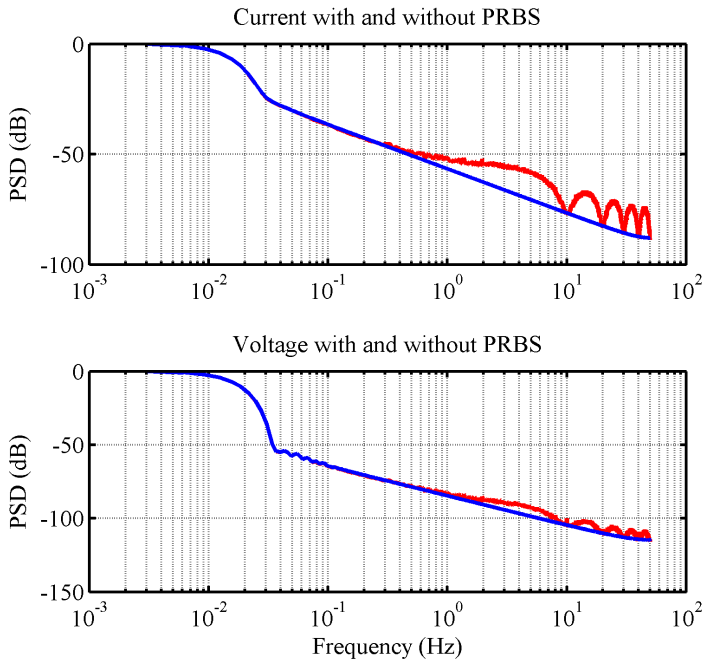


Figure 3.8: The power spectrum density of the current/voltage signals with (red line) and without PRBS (blue line).

Therefore, it is determined that the extended system is globally and locally unobservable when the input current is a sinusoidal signal.

In a real application, the EDLCs may be charged with a constant current, which is therefore not a persistently exciting signal ensuring the observability of the extended dynamic system. So as to estimate the model parameters while charging the supercapacitor, an additional Pseudo Random Binary Signal (PRBS) [63] is added to the constant reference of the charging current controller. The added PRBS provides persistently exciting signal which makes the extended system observable. In practice, the observability has been experimentally checked online as will be presented in §3.4.4.

As said already, $R_s$ is a very significant parameter for the aging monitoring of the EDLCs, but the sensitivity study shows that high frequencies are needed to correctly estimate this parameter. Therefore, the PRBS, injecting the required high frequencies to the original current signal, will help the estimation of $R_s$. For example, when a small pseudo random binary signal (2048-bit long, shortest time interval of $0.01$ s and amplitude of $2.5$ mA) is added to a constant charging current shown in Fig. 2.16, more high frequencies are included in the signals, as shown in Fig. 3.8.

### 3.4.3 Observers design

#### Extended Kalman filter design

The extended supercapacitor model represented by Eqs. 3.42 and 3.43 is a nonlinear system. An extended Luenberger observer or extended Kalman filter can be used for the state estimation. When designing an ELO, it is found that there exist two zero eigenvalues of the matrix $(F-KH)$ (see Eq. 3.35) which may result in an unstable observer. Therefore, the extended Kalman filter is chosen to estimate the states of this system. The extended EDLC model is an uncertain continuous-time nonlinear stochastic dynamic system that can be written as

$$\begin{cases} \dot{\mathbf{X}}_a = f(\mathbf{X}_a, i_{sc}) + v \\ u_{sc} = h(\mathbf{X}_a, i_{sc}) + w \end{cases} \tag{3.61}$$

where $\mathbf{X}_a = [x_1\ x_2\ x_3\ x_4]^T$ is the augmented state vector, $v$ and $w$ are respectively the zero mean process noise and the measurement noise, $f(\mathbf{X}_a, i_{sc})$ and $h(\mathbf{X}_a, i_{sc})$ are defined by Eqs. 3.42 and 3.43. The bold terms appearing here and in the following lines indicate vectors or matrices. To design an EKF for this nonlinear system, $f(\mathbf{X}_a, i_{sc})$ and $h(\mathbf{X}_a, i_{sc})$ are firstly approximated by the first-order Taylor expansion at the estimated state $\hat{\mathbf{X}}_a = [\hat{x}_1\ \hat{x}_2\ \hat{x}_3\ \hat{x}_4\ ]$:

$$\mathbf{F}(\hat{\mathbf{X}}_a, i_{sc}) = \frac{\partial f}{\partial \mathbf{X}_a}(\hat{\mathbf{X}}_a, i_{sc}) = \begin{bmatrix} \hat{x}_4 & 0 & i_{sc} & \hat{x}_1 \\ 0 & 0 & 0 & 0 \\ 0 & 0 & 0 & 0 \\ 0 & 0 & 0 & 0 \end{bmatrix} \tag{3.62}$$

$$\mathbf{H}(i_{sc}) = \frac{\partial h}{\partial \mathbf{X}_a}(\hat{\mathbf{X}}_a, i_{sc}) = [1\ \ i_{sc}\ \ 0\ \ 0] \tag{3.63}$$

Then, the EKF is designed as [103] [104]:

$$\dot{\hat{\mathbf{X}}}_a = f(\hat{\mathbf{X}}_a, i_{sc}) + \mathbf{K}(u_{sc} - h(\hat{\mathbf{X}}_a, i_{sc})) \tag{3.64}$$

$$\mathbf{K} = \mathbf{P}\mathbf{H}(i_{sc})^T R^{-1} \tag{3.65}$$

$$\dot{\mathbf{P}} = \mathbf{F}(\hat{\mathbf{X}}_a, i_{sc})\mathbf{P} + \mathbf{P}\mathbf{F}(\hat{\mathbf{X}}_a, i_{sc})^T + \mathbf{Q} - \mathbf{K}R\mathbf{K}^T \tag{3.66}$$

where the measurement noise variance $R$ is a scalar because there is only one measurement (i.e. terminal voltage) noise, the process noise covariance $\mathbf{Q}$ and the estimation error covariance $\mathbf{P}$ are both $4$ by $4$ symmetric matrices. The correction gain $\mathbf{K}$ is a $4$ by $1$ vector.

**Interconnected observers design**

– *Interconnected subsystems*

The extended supercapacitor model (Eqs. 3.42 and 3.43) can be seen as the interconnection between two subsystems $\Sigma_1$ and $\Sigma_2$ defined by

$$\Sigma_1 : \quad \begin{cases} \dot{\mathbf{X}}_1 = \mathbf{F}_1(\mathbf{X}_2, i_{sc})\mathbf{X}_1 \\ u_{sc} = \mathbf{H}_1(i_{sc})\mathbf{X}_1 \end{cases} \tag{3.67}$$

$$\Sigma_2 : \quad \begin{cases} \dot{\mathbf{X}}_2 = \mathbf{F}_2(\mathbf{X}_1)\mathbf{X}_2 + \mathbf{g}_1(\mathbf{X}_1, i_{sc}) \\ u_{sc} = \mathbf{H}_2(i_{sc})\mathbf{X}_2 + g_2(\mathbf{X}_1, i_{sc}) \end{cases} \tag{3.68}$$

$$\text{with} \quad \mathbf{X}_1 = [x_1 \ x_2 \ x_3]^T, \quad \mathbf{X}_2 = [x_1 \ x_4]^T \tag{3.69}$$

$$\mathbf{H}_1(i_c) = [1 \ i_{sc} \ 0], \quad \mathbf{H}_2 = [1 \ 0] \tag{3.70}$$

$$\mathbf{g}_1(X_1, i_{sc}) = [x_3 i_{sc} \ 0]^T, \quad g_2(X_1, i_{sc}) = x_2 i_{sc} \tag{3.71}$$

$$\mathbf{F}_1(X_2, i_{sc}) = \begin{bmatrix} x_4 & 0 & i_{sc} \\ 0 & 0 & 0 \\ 0 & 0 & 0 \end{bmatrix}, \quad \mathbf{F}_2(X_1) = \begin{bmatrix} 0 & x_1 \\ 0 & 0 \end{bmatrix} \tag{3.72}$$

This partition of the state vector can transform the nonlinear system into two almost linear subsystems (see Fig. 3.9), each subsystem using the state of the other subsystem as an input parameter. Different partitions have been considered and the proposed one is the only choice allowing that one of the subsystem is state affine and the other one can be order-reduced as explained later in the following parts. For these interconnected subsystems, interconnected observers (IOs) [113] [114] [115] have been designed (see Fig. 3.10).

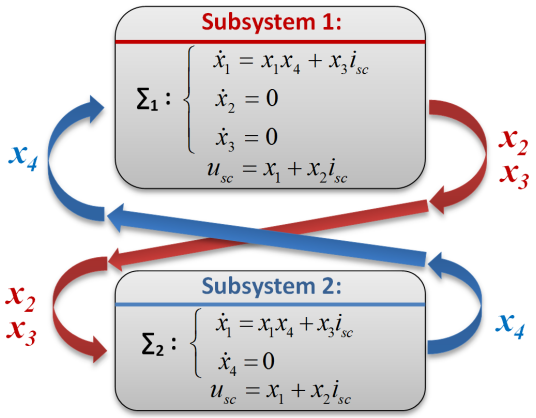


Figure 3.9: Structure of the interconnected subsystems.

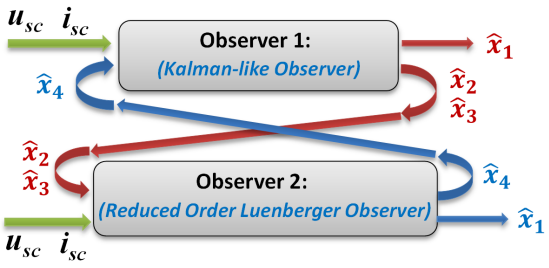


Figure 3.10: Structure of the interconnected observers.

– *Kalman-like observer (KLO)*

Since the first subsystem $\Sigma_1$ is state affine, a Kalman-like observer [116] can be used to estimate its states. This Kalman-like observer is defined as: [115] [117]:

$$\dot{\hat{\mathbf{X}}}_1 = \mathbf{F}_1(\hat{\mathbf{X}}_2, i_{sc})\hat{\mathbf{X}}_1 + \mathbf{K}_1(u_{sc} - \mathbf{H}_1(i_{sc})\hat{\mathbf{X}}_1) \tag{3.73}$$

$$\mathbf{K}_1 = \mathbf{S}^{-1}\mathbf{H}_1(i_{sc})^T \tag{3.74}$$

$$\dot{\mathbf{S}} = -\rho\mathbf{S} - \mathbf{S}\mathbf{F}_1(\hat{\mathbf{X}}_2, i_{sc}) - \mathbf{F}_1(\hat{\mathbf{X}}_2, i_{sc})^T\mathbf{S} + \mathbf{H}_1(i_{sc})^T\mathbf{H}_1(i_{sc}) \tag{3.75}$$

where $\hat{\mathbf{X}}_1 = [\hat{x}_1 \;\; \hat{x}_2 \;\; \hat{x}_3]^T$ is an estimation of $\mathbf{X}_1$, the correction gain $\mathbf{K}_1$ is a 3 by 1 vector, $\mathbf{S}$ is a 3 by 3 symmetric positive definite matrix and $\rho$ is a positive constant and the only tuning parameter of this state observer.
In fact, the Kalman-like observer can be considered as a modified Kalman filter. In order to compare the KLO with EKF, we intend to transform their expressions into a similar form. Therefore, the EKF expressions are equivalently transformed by using a normalized information matrix $\mathbf{S}_1 = R\mathbf{P}^{-1}$ instead of $\mathbf{P}$. Since $R$ is a constant, it is obtained that

$$\dot{\mathbf{S}}_1\mathbf{P} + \mathbf{S}_1\dot{\mathbf{P}} = 0 \tag{3.76}$$

Then the correction expression (Eq. 3.65) and differential equation of $\mathbf{P}$ (Eq. 3.66) of EKF become:

$$\mathbf{K} = \mathbf{S}_1^{-1}\mathbf{H}(i_{sc})^T \tag{3.77}$$

$$\dot{\mathbf{S}}_1 = -\mathbf{S}_1\mathbf{Q}R^{-1}\mathbf{S}_1 - \mathbf{S}_1\mathbf{F}(\hat{\mathbf{X}}_a, i_{sc}) - \mathbf{F}(\hat{\mathbf{X}}_a, i_{sc})^T\mathbf{S}_1 + \mathbf{H}(i_{sc})^T\mathbf{H}(i_{sc}) \tag{3.78}$$

When comparing Eqs. 3.77 and 3.78 of EKF with Eqs. 3.74 and 3.75 of KLO, one can see that KLO and standard EKF are very similar: the only difference is that KLO replaces the $-\mathbf{S}_1\mathbf{Q}R^{-1}\mathbf{S}_1$ term of Eq. 3.78 by $-\rho S$ in Eq. 3.75. As a consequence, the 10 tuning parameters of the $\mathbf{Q}R^{-1}$ symmetric matrix for our extended EDLC system with 4 states are reduced by only

one tuning parameter $\rho$. If the model of a system is ideal without modelization error ($v = 0$), the process noise covariance $\mathbf{Q}$ and parameter $\rho$ are null ($\mathbf{Q} = 0,\ \rho = 0$). In this case, a KLO is equivalent to an EKF. But the system model can not be ideal in a real application which is why non-zero $\mathbf{Q}$ and $\rho$ are needed in EKF and KLO in order to minimize the estimation error. Thus, EKF and KLO differ by the way they manage the modelization error.

– *Reduced order Luenberger observer (ROLO)*

For the second subsystem, it is noticed that the first state variable, $x_1$, can be estimated from the measurement:

$$x_1 = u_{sc} - x_2 i_{sc} \tag{3.79}$$

Substituting this equation into the differential equation of $x_1$, a new output equation is generated. Thus, the order of the subsystem $\Sigma_2$ can be reduced from two to one, and the reduced first-order state space model is

$$\Sigma_1^r : \begin{cases} \dot{x}_4 = 0 \\ y \ = \dot{x}_1 = x_4(u_{sc} - x_2 i_{sc}) + x_3 i_{sc} \end{cases} \tag{3.80}$$

where $y$ is the new output of this linear reduced order system and $x_4 = -1/(R_p C)$ becomes the only remaining state variable to estimate. To this aim, a reduced order Luenberger observer (ROLO) can be derived:

$$\dot{\hat{x}}_4 = K_2(\dot{x}_1 - \hat{y}) \tag{3.81}$$

$$\hat{y} = \hat{x}_4(u_{sc} - \hat{x}_2 i_{sc}) + \hat{x}_3 i_{sc} \tag{3.82}$$

where $\hat{x}_4$ is the estimation of $x_4$ and $K_2$ is the observer gain. It is noticed that there is a differential term, $\dot{x}_1$ in Eq. 3.81 which may add difficulty when solving this differential equation. To eliminate this differential part, a new state variable $x_5$ is defined as: $x_5 = \hat{x}_4 - K_2 x_1$ and its derivative is:

$$\dot{x}_5 = \dot{\hat{x}}_4 - K_2 \dot{x}_1 \tag{3.83}$$

Combining Eqs. 3.81 - 3.83, a new differential equation of $x_5$ instead of Eq. 3.81 is obtained:

$$\dot{x}_5 = -K_2(u_{sc} - \hat{x}_2 i_{sc})x_5 - K_2^2(u_{sc} - \hat{x}_2 i_{sc})^2 - K_2 \hat{x}_3 i_{sc} \tag{3.84}$$

Once the solution of this equation is obtained, the estimation of the state $x_4$ can therefore be obtained by:

$$\hat{x}_4 = x_5 + K_2(u_{sc} - \hat{x}_2 i_{sc}) \tag{3.85}$$

The positive gain $K_2$ determines the convergence speed of this reduced order Luenberger observer. One can show easily that its estimation error, defined as $e_{ROLO}(t) = x_4(t) - \hat{x}_4(t)$, satisfies the following ordinary differential equation:

$$\begin{aligned} \dot{e}_{ROLO}(t) &= \dot{x}_4(t) - \dot{\hat{x}}_4(t) \\ &= \delta(K_2) e_{ROLO}(t) + K_2 \hat{x}_4 (x_2 - \hat{x}_2) i_{sc} - K_2 (x_3 - \hat{x}_3) i_{sc} \end{aligned} \tag{3.86}$$

where $\delta(K_2) = -K_2 x_1$. Since $x_1 = u_1 \geq 0$, the convergence of this reduced Luenberger observer can be guaranteed by choosing a positive $K_2$.

**Practical implementation of the IOs**

Since the $\mathbf{S}$ matrix of the KLO is a symmetric positive matrix which can be written as

$$\mathbf{S} = \begin{bmatrix} S_{11} & S_{12} & S_{13} \\ S_{12} & S_{22} & S_{23} \\ S_{13} & S_{23} & S_{33} \end{bmatrix} \tag{3.87}$$

the $9$ th-order differential equations of $\mathbf{S}$ represented by Eq. 3.75 can be reduced to $6$ th-order differential equations:

$$\begin{cases} \dot{S}_{11} = -(\rho_1 + 2\hat{x}_4) S_{11} + 1 \\ \dot{S}_{12} = -(\rho_1 + \hat{x}_4) S_{12} + i_{sc} \\ \dot{S}_{13} = -(\rho_1 + \hat{x}_4) S_{13} - S_{11} i_{sc} \\ \dot{S}_{23} = -\rho_1 S_{23} - S_{12} i_{sc} \\ \dot{S}_{22} = -\rho_1 S_{22} + i_{sc}^2 \\ \dot{S}_{33} = -\rho_1 S_{33} - 2 S_{13} i_{sc} \end{cases} \tag{3.88}$$

Then, the differential equations developed from Eqs. 3.73 and 3.84 are expressed as

$$\begin{cases} \dot{\hat{x}}_1 = \hat{x}_1 \hat{x}_4 + \hat{x}_3 i_{sc} + k_1 (u_{sc} - \hat{x}_1 - \hat{x}_2 i_{sc}) \\ \dot{\hat{x}}_2 = k_2 (u_{sc} - \hat{x}_1 - \hat{x}_2 i_{sc}) \\ \dot{\hat{x}}_3 = k_3 (u_{sc} - \hat{x}_1 - \hat{x}_2 i_{sc}) \\ \dot{x}_5 = -K_2 (u_{sc} - \hat{x}_2 i_{sc}) x_5 - K_2^2 (u_{sc} - \hat{x}_2 i_{sc})^2 - K_2 \hat{x}_3 i_{sc} \end{cases} \tag{3.89}$$

where $[k_1 \quad k_2 \quad k_3]^T = \mathbf{S}^{-1}\mathbf{H}_1(i_{sc})^T$ and the estimation of the fourth state $\hat{x}_4$ is computed by Eq. 3.85. The two differential equation sets illustrated above can be written as

$$\dot{\mathbf{z}} = G(\mathbf{z}, i_{sc}, u_{sc}) \tag{3.90}$$

where $\mathbf{z} = [S_{11} \quad S_{12} \quad S_{13} \quad S_{23} \quad S_{22} \quad S_{33} \quad \hat{x}_1 \quad \hat{x}_2 \quad \hat{x}_3 \quad \hat{x}_5]^T$, associated to an initial condition $\mathbf{z}(0) = \mathbf{z}_0$. Implementing these interconnected observers requires to invert a $3 \times 3$ symmetric matrix $\mathbf{S}$ and an algorithm to find a numeric approximation of Eq. 3.90. Several efficient numerical methods can be used to solve an ordinary differential equation defined by such a general equation. One of the most efficient one is the Bulirsch-Stoer method [118] [119] [120]. This method uses a Richardson extrapolation technique to compute the solution of this equation using a zero step-size. Compared to the EKF, the proposed IOs have a lower computational cost, because these IOs consist of two low order observers (a third-order observer and a first-order one) with 10 differential equations to solve, while the EKF is a fourth-order observer involving 14 differential equations. This allows the implementation of such an observer on a low-cost digital target.

### 3.4.4 Estimation results

The estimation results presented in this section include two parts. First of all, both observers are applied to a simulated EDLC model with preset parameters values and the estimated parameters of both observers are presented and compared. Secondly, EKF and IOs are applied to a real fresh EDLC (Nichicon 1 F/2.7 V) and the estimation results are provided. In both cases, the same PRBS (2048-bit long, shortest time interval of 0.01 s and amplitude of 2.5 mA) is added to the constant charging current in order to help the estimation of the parameters.

#### Simulation results

In the simulated case, the Nichicon EDLC with a maximum voltage of 2.7 V and a nominal capacitance of 1 F is simulated by the first order state space model represented by Eq. 3.39. According to the offline estimation results of the parameters of this type EDLC in the first chapter, the physical parameters of this model is set as shown in Table 3.1 .

Table 3.1: Physical parameters of RRC model.

| $R_s$ [$\Omega$] | $C$ [$F$] | $R_p$ [$\Omega$] |
|---|---|---|
| 1 | 1 | 3000 |

A realistic current waveform is designed and used as the input of the EDLC

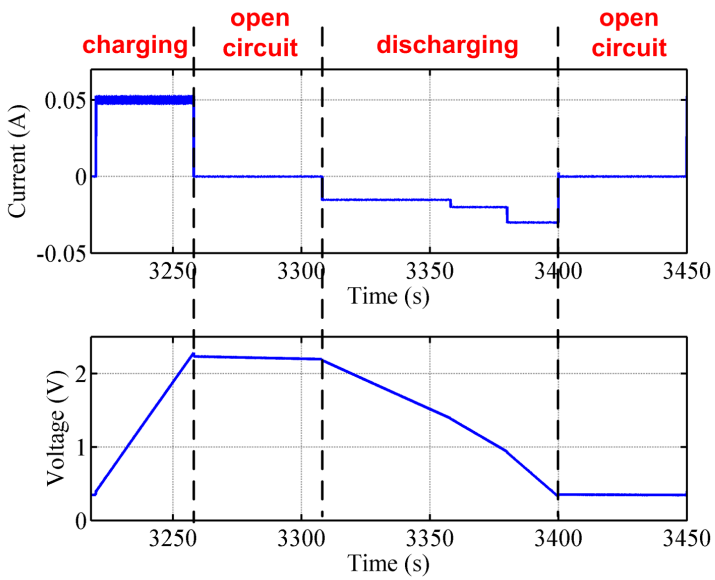


Figure 3.11: Simulated current and voltage of a RRC model of EDLC during one period.

model. The designed current waveform during one period (shown in Fig. 3.11) simulates a charging phase, a discharging phase and two open circuit phases. The corresponding output of the model (i.e. voltage) is thus obtained by solving a first-order ordinary differential equation. The reason of the chosen waveform has been explained in the previous chapter (see §2.4.1). The sampling period $T_s$ of the signals is $0.01$ s. According to the existing measurement noises in a real experiment, the voltage and current noises with respectively the noise power of $10^{-10}$ $[\mathrm{V}^2]$ and $10^{-11}$ $[\mathrm{A}^2]$ are added in the simulated signals.

Once the simulated current and voltage signals are obtained, the designed extended Kalman filter and interconnected observers can provide the state estimations of the extended EDLC model (see Fig. 3.12). Both observers are implemented with MATLAB/SIMULINK and the observers' parameters ($\mathbf{Q}$, $R$ for EKF and $\rho$, $K_2$ for IOs) are tuned before the online state estimation. The initialization and parameters of EKF in the simulation are as follows:

$$\mathbf{X}_a^{\text{init}} = [0.5,\ 0.8,\ 0.83,\ -2.5\ 10^{-4}]$$
$$\mathbf{P}^{\text{init}} = \text{diag}\,(1,\ 1,\ 1,\ 1\ 10^{-6})$$
$$\mathbf{Q} = \text{diag}\,(0.1,\ 0.5,\ 0.01,\ 1\ 10^{-6});\quad R = 1\ [\mathrm{V}^2]$$

where $\mathbf{P}^{\text{init}}$ and $\mathbf{Q}$ are $4 \times 4$ diagonal matrices and their last diagonal terms have been set to very small values because of the high parallel resistance which leads to a very small value of the state $x_4$. The parameters of the interconnected observers are chosen as: $\rho = 0.01$ $[\mathrm{s}^{-1}]$; $K_2 = 8\ 10^{-4}$ $[\mathrm{s}^{-1}\mathrm{V}^{-1}]$. Instead of tuning both $\mathbf{Q}$ and $R$, a normalized version of Eq. 3.66 is used to have only one tunning matrix $\mathbf{Q}R^{-1}$ (see Eq. 3.28) and this is why $R$ is chosen as 1.

Fig. 3.13 shows the simulated current and voltage, the estimated internal volt-

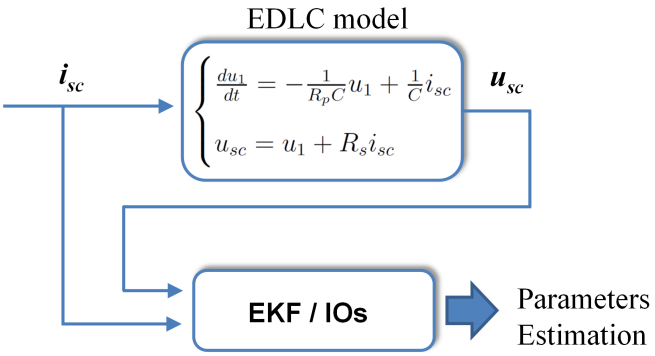


Figure 3.12: Structure of parameter estimation of an EDLC model.

age $u_1$ and the estimated parameters provided by both observers during 15 charging/discharging cycles. The results show that both observers provide good estimations of the internal voltage $u_1$. The estimations of three parameters, $R_s$, $C$ and $R_p$, all converge to the correct preset values.

Since the parameters of EDLCs evolve with their aging, it is necessary to know the dynamic performance of the designed observers. Therefore, both observers are applied to the EDLC model with varying parameters. The parameters $R_s$ and $C$ are preset to have two kinds of variation. At time $t_1$, $R_s$ has a step increase from 1 $\Omega$ to 1.1 $\Omega$ and $C$ has a step decrease from 1 $F$ to 0.95 $F$ at the same time. From time $t_2$, the series resistance increases linearly with a small slope of $1.5 \times 10^{-5}$ $[\Omega s^{-1}]$ and the capacitance $C$ decreases linearly with the same value of slope. During all the simulation process, the same tuning parameters of the observers are used. The results in Fig. 3.14 show that the parameter estimations provided by both observers can always converge to the correct values even when the parameters have step variations. It is noticed that from time $t_2$, the estimation result is not as good as that obtained in the previous case. When $R_s$ and $C$ linearly vary with time, the designed observers can almost track the parameter variation but the estimation of $R_s$ provided by the IOs and the $R_p$ estimation obtained by both observers have small oscillations. This might be explained by the inaccuracy of this model at this case because $\dot{x}_2 = 0$ and $\dot{x}_3 = 0$ in the extended EDLC model represented by Eq. 3.42 is no longer true when parameter $R_s$ and $C$ linearly vary with time. However, when monitoring the aging of EDLCs, the parameters evolution caused by aging is much slower than that we have simulated here. Therefore, the parameters can be considered as piecewise constant and thus the proposed extended model is still appropriate for aging monitoring.

### Experimental results

The simulated results presented in the previous section have clearly proved the good performance of the designed observers for parameter estimation. In this sec-

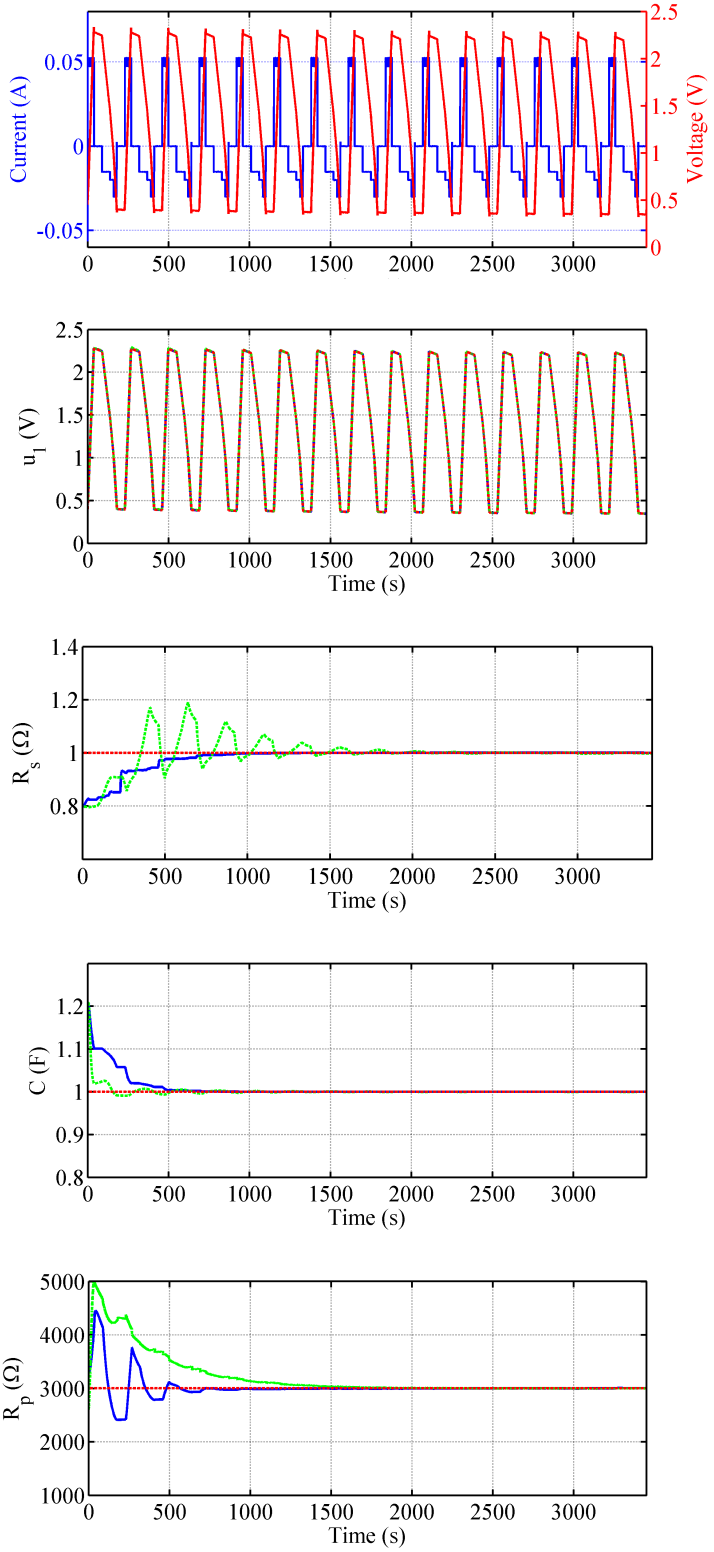


Figure 3.13: Simulated current (blue line) and voltage (red line) signals; Internal state $u_1$ and parameter estimations of an EDLC model during 15 charging/discharging periods (red dotted lines: preset $u_1$ signal and given parameters of model, blue lines: estimated by EKF, green dashed lines: estimated by IOs).

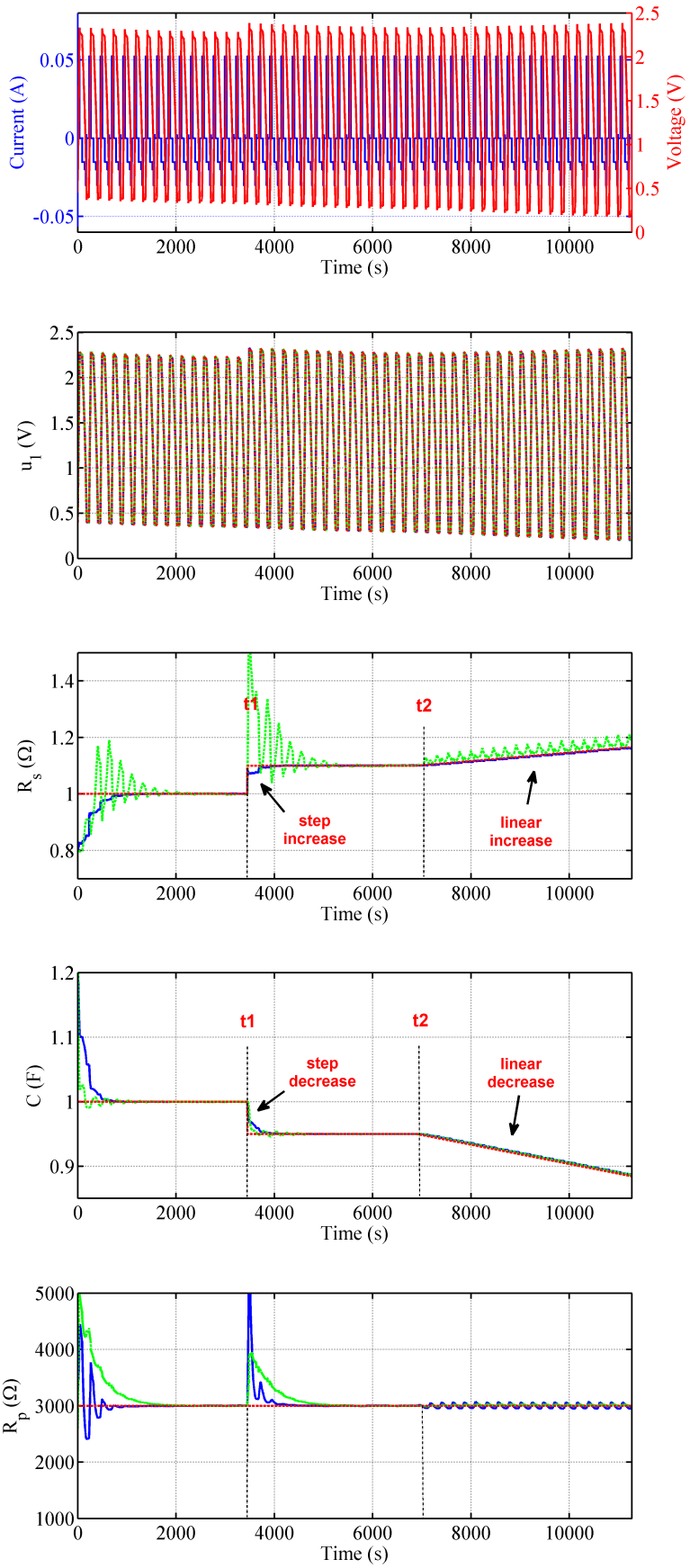


Figure 3.14: Simulated current (blue line) and voltage (red line) signals; Internal state $u_1$ and parameter estimations of an EDLC model under dynamic case (red dotted lines: preset $u_1$ signal and given parameters of model, blue lines: estimated by EKF, green dashed lines: estimated by IOs).

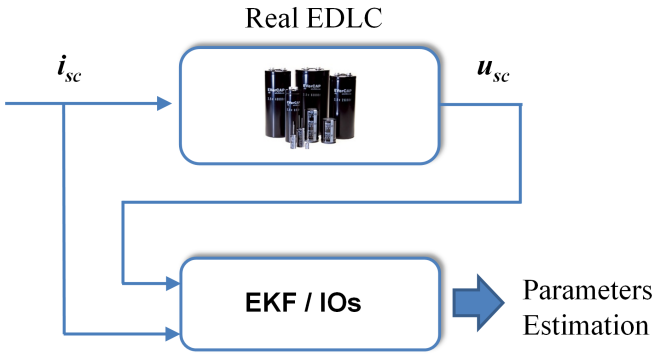


Figure 3.15: Structure of parameter estimation of a real EDLC.

tion, the experimental current and voltage signals of a real fresh Nichicon EDLC will be used to estimate its parameters (Fig. 3.15). The EDLC used here has a nominal capacitance of 1 F, a maximum voltage of 2.7 V and a nominal series resistance of 3 Ω. The initialization of the observers is the same as that in the simulated case. The parameters of EKF and IOs in the experimental case are tuned as: $\mathbf{Q} = \text{diag}\ (0.1,\ 0.5,\ 0.01,\ 1\ 10^{-6})$; $R = 1\ [\text{V}^2]$ and $\rho = 0.002\ [\text{s}^{-1}]$; $K_2 = 4\ 10^{-4}\ [\text{s}^{-1}\text{V}^{-1}]$.

To check the observability of EDLC system, the determinant of the Jacobian matrix (see Eqs. 3.17 and 3.52) has been calculated in real time. The second plot in Fig. 3.18 shows the determinant of matrix $J$ during one charging/discharging period. It clearly reveals that the extended EDLC system is locally observable at both charging and discharging phases with nonzero determinant values and unobservable during open circuit phases because of the null current signal. Since a PRBS is added to provide reliable parameter estimation and since the system is locally observable during the charging phase, it is suggested to take the estimation value at the end of the charging phase as the current parameter estimation. The estimation of the internal voltage $u_1$ and three parameters of the tested EDLC during 25 charging/discharging periods are presented in Fig. 3.16. After 3000 s, the parameter estimations almost reached their steady states. It is noticed that these estimations has some periodically fluctuations even after their steady states are reached, especially for the estimation of $R_p$. This is probably due to the non-observability during the open circuits which may provide incorrect estimations. But if we focus on the estimations at the end of charging phases (marked by red points), we can see that these estimations converge to a final value without any fluctuations. Fig. 3.17 shows the parameter estimation during one charging/discharging cycle at steady state. The estimation of capacitance $C$ remains almost constant around 1 F during the whole period, while for $R_s$ and $R_p$, the estimation values vary in a bounded range. For $R_s$ and $R_p$, EKF and IOs provide quite different values. This difference may come from the sensitivity of the observer to modelization errors.

The energy can be estimated from Eq. 3.40 with an estimated value of $C$ and an estimated $u_1$ provided by each observer. The third plot in Fig. 3.18 shows the estimated energy variation during one cycle. This plot clearly reveals the possibility to derive from the state observers an accurate energy gauge providing the SoC at any time. The last plot in Fig. 3.18 shows the output error between the measured voltage signal $u_{sc}$ and the estimated voltage $\hat{u}_{sc}$ by both observers. At the end of the charging phase, the output error provided by both observers is close to zero which demonstrates their good performances. This also supports the idea to consider the values obtained at the end of charging phase as a reliable parameter estimation.

## 3.5 Parameter estimation for the transmission line model of EDLCs

### 3.5.1 EDLC system modelization by a transmission line model

#### State space representation

The previous chapter studied different models and concluded that the second-order transmission line model with a charge redistribution branch can be a good model for online aging monitoring of EDLCs. But in this section, a fourth-order transmission line (TL) model as shown in Fig. 3.19 is used instead of the suggested model by chapter 2 to design online parameter observers. It is because this work is done before the conclusion of chapter 2 was made. However, the model used in this section is an improved model of structure S5 (see Fig. 2.18) shown in chapter 2. It has taken into account the long term behavior of the EDLCs by adding parallel resistances across each capacitance and thus it can be much better than structure S5. Therefore, this model may not be the best model for the studied EDLCs but still can be considered as a quite good model.

The fourth-order transmission line (TL) model consists of a series resistance $R_s$, three dynamic resistances $R_d/3$, four leakage resistances $4R_p$ and four voltage dependent capacitances $C_j$ $(j = 1, 2, 3, 4)$. The dynamic resistance $R_d$ results from the connection of the three $R_d/3$ resistors in series. The leakage current resistance $R_p$ results from the four $4R_p$ resistors connected in parallel and corresponds to the energy losses due to the supercapacitor self-discharge.

Since the capacitance is linearly dependent on the voltage $u_{sc}$ (see Chapter 1), it can be written as: $C = C_0(1 + \alpha u_{sc})$, where $C_0$ is the no load capacitance and $\alpha$ is a sensitivity coefficient. Thus, in the proposed model in Fig. 3.19, the capacitances of the four branches are functions of their corresponding voltages:

$$C_j = \frac{C_0}{4}(1 + \alpha u_j), \ (j = 1, 2, 3, 4) \tag{3.91}$$

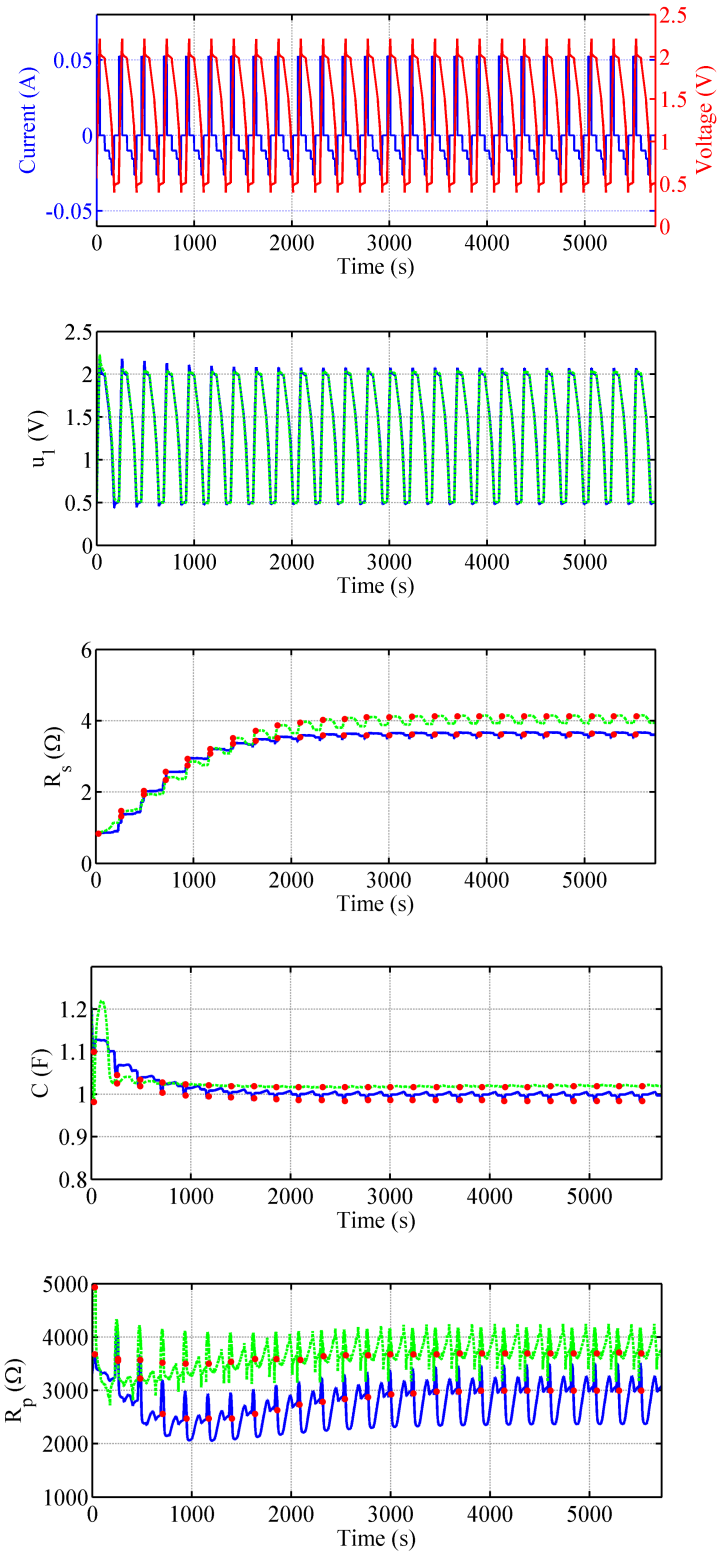


Figure 3.16: Experimental current (blue line) and voltage (red line) signals and the estimations of a fresh Nichicon EDLC (1 F/2.7 V) during 25 charging/discharging periods; Internal state $u_1$ estimation and Parameters estimation (blue lines: estimated by EKF, green dashed lines: estimated by IOs, red points: estimations at the end of each charging phase).

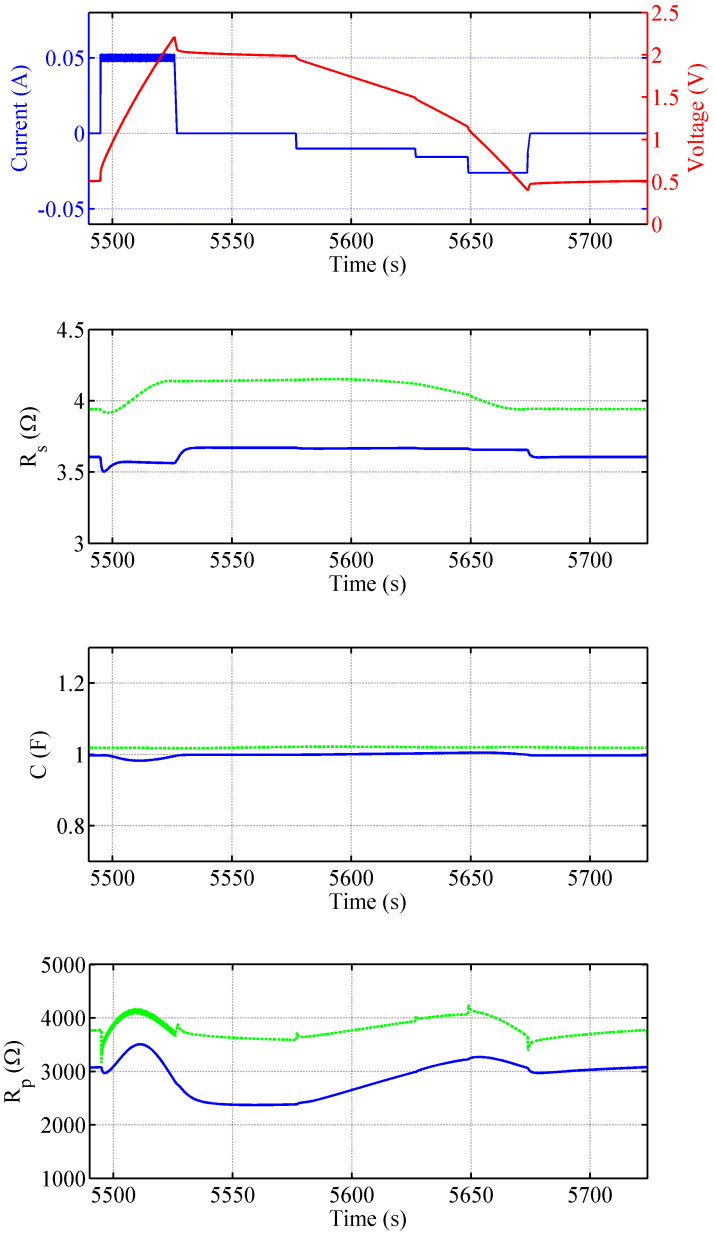


Figure 3.17: Experimental current (blue line) and voltage (red line) signals and the parameter estimations of a fresh Nichicon EDLC (1 F/2.7 V) for 1 charging/discharging period based on RRC model (blue lines: estimated by EKF, green dashed lines: estimated by IOs).

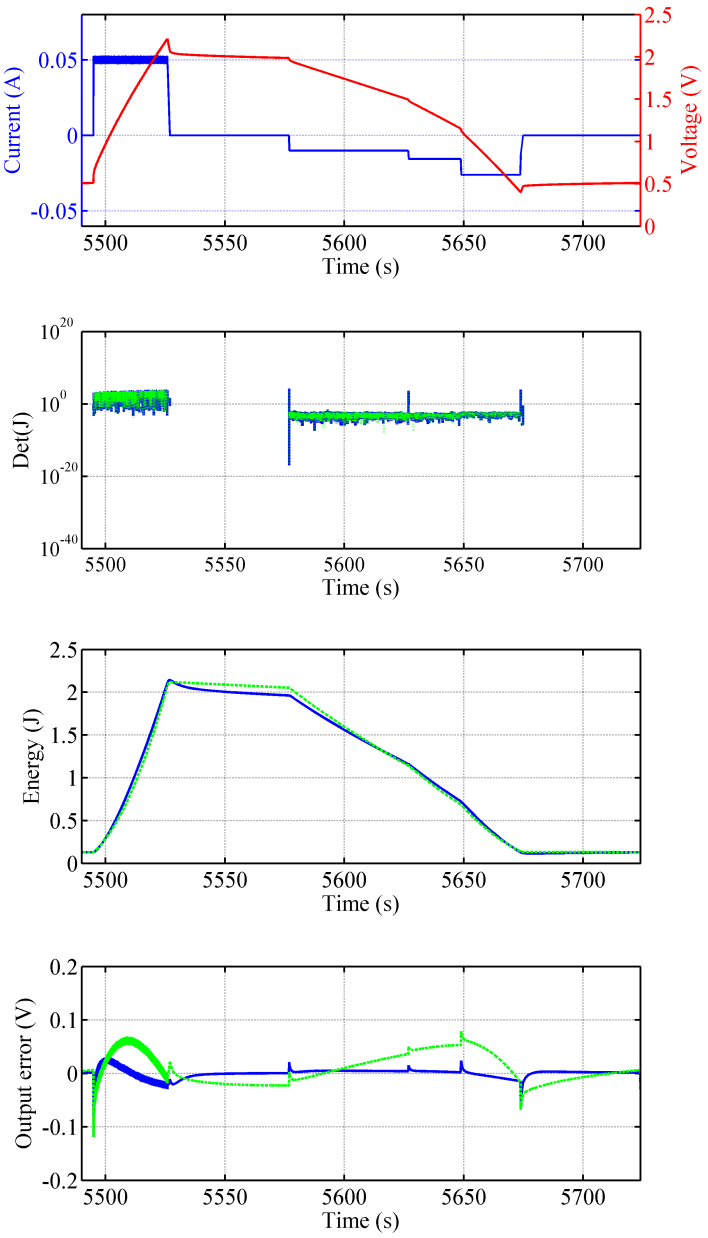


Figure 3.18: Experimental current (blue line) and voltage (red line) signals of a fresh EDLC during one charging/discharging period; The corresponding determinant of the Jacobian matrix, the stored energy and the output error obtained based on the RRC model (blue lines: estimated by EKF, green dashed lines: estimated by IOs).

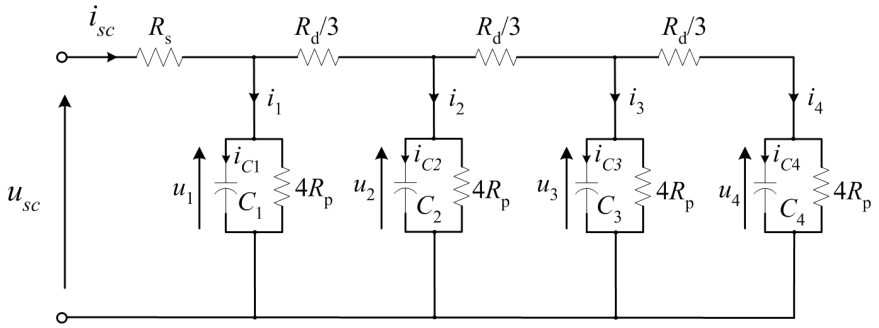


Figure 3.19: Fourth-order transmission line model of EDLC.

where $C_j$ and $u_j$ $(j = 1, 2, 3, 4)$ are the capacitance of each branch and the voltage across each capacitor. The current $i_{Cj}$ through the capacitor of each branch can be defined as:

$$i_{Cj} = \frac{dQ_{Cj}}{dt} = \frac{d}{dt}(C_j \cdot u_j) = \frac{C_0}{4}(1 + 2\alpha u_j) \cdot \frac{du_j}{dt} \tag{3.92}$$

Meanwhile, $i_j = i_{Cj} + u_j/(4R_p)$, then, the differential equation for the four capacitors is:

$$\frac{du_j}{dt} = \frac{4}{C_0(1 + 2\alpha u_j)}(i_j - \frac{u_j}{4R_p}) \tag{3.93}$$

The currents $i_j$ through each branch are calculated according to Kirchhoff's current law:

$$\begin{cases} i_1 = i_{sc} - (i_2 + i_3 + i_4) \\ i_2 = \frac{u_1 - u_2}{R_d/3} - (i_3 + i_4) \\ i_3 = \frac{u_2 - u_3}{R_d/3} - i_4 \\ i_4 = \frac{u_3 - u_4}{R_d/3} \end{cases} \tag{3.94}$$

Combining Eq. 3.93 and Eq. 3.94, the EDLC dynamic behavior can be described by

$$\begin{cases} \frac{du_1}{dt} = \frac{4}{C_0(1+2\alpha u_1)}(i_{sc} - (\frac{3}{R_d} + \frac{1}{4R_p})u_1 + \frac{3}{R_d}u_2) \\ \frac{du_2}{dt} = \frac{4}{C_0(1+2\alpha u_2)}(\frac{3}{R_d}u_1 - (\frac{6}{R_d} + \frac{1}{4R_p})u_2 + \frac{3}{R_d}u_3) \\ \frac{du_3}{dt} = \frac{4}{C_0(1+2\alpha u_3)}(\frac{3}{R_d}u_2 - (\frac{6}{R_d} + \frac{1}{4R_p})u_3 + \frac{3}{R_d}u_4) \\ \frac{du_4}{dt} = \frac{4}{C_0(1+2\alpha u_4)}(\frac{3}{R_d}u_3 - (\frac{3}{R_d} + \frac{1}{4R_p})u_4) \end{cases} \tag{3.95}$$

$$u_{sc} = u_1 + R_s i_{sc} \tag{3.96}$$

where $i_{sc}$ and $u_{sc}$ are respectively the current and the voltage of the EDLC. The former one is considered as the input of this dynamic model, and the latter as the output.

The energy stored in each capacitor of the branch in Fig. 3.19 is calculated as the integral of its power over time:

$$P_j = u_j \cdot i_{C_j} = u_j \cdot \frac{C_0}{4}(1 + 2\alpha u_j) \cdot \frac{du_j}{dt} \tag{3.97}$$

$$E_j = \int P_j \, dt = \frac{C_0}{8} \cdot (1 + \frac{4}{3}\alpha u_j) \cdot u_j^2 \tag{3.98}$$

Thus, the total energy stored in the EDLC is:

$$E = \sum_{j=1}^{4} E_j = \frac{C_0}{8} \cdot \sum_{j=1}^{4}(1 + \frac{4}{3}\alpha u_j)u_j^2 \tag{3.99}$$

**Extended EDLC model**

The mathematical model of an EDLC built in Eq. 3.95 and Eq. 3.96 is a parametric nonlinear state space model. In this model, there are five parameters, $C_0, \alpha, R_s, R_d, R_p$, and four states, $u_1, u_2, u_3, u_4$. As for the RRC model, this model will be extended to a parameterless model by considering the five EDLC parameters as additional states, in order to estimate these parameters.

To simplify Eq. 3.95, some physical parameters are replaced by new variables: $x_1 = \frac{3}{R_d}, x_2 = \frac{1}{4R_p}, x_3 = R_s, x_4 = \frac{4}{C_0}, x_5 = 2\alpha$. It is assumed that the five parameters (the series resistance $R_s$, the dynamic resistance $R_d$, the leakage resistance $R_p$, the capacitance $C_0$ and the voltage sensitivity coefficient $\alpha$) evolve with the EDLCs aging. But with respect to the electric variables $u_{sc}$ and $i_{sc}$, the variation of these parameters is very slow and unknown. Therefore, the dynamic behavior of the five parametric terms are expressed as:

$$\frac{dx_k(t)}{dt} = 0, \quad (k = 1, 2, 3, 4, 5) \tag{3.100}$$

Adjoining these five terms into the EDLC system (represented in Eq. 3.95 and 3.96), a nonlinear parameterless extended state space model of an EDLC is obtained:

$$\begin{cases} \dot{x}_1 = 0 \\ \dot{x}_2 = 0 \\ \dot{x}_3 = 0 \\ \dot{x}_4 = 0 \\ \dot{x}_5 = 0 \\ \dot{x}_6 = \frac{x_4}{1+x_5x_6}(i_{sc} - (x_1 + x_2)x_6 + x_1x_7) \\ \dot{x}_7 = \frac{x_4}{1+x_5x_7}(x_1x_6 - (2x_1 + x_2)x_7 + x_1x_8) \\ \dot{x}_8 = \frac{x_4}{1+x_5x_8}(x_1x_7 - (2x_1 + x_2)x_8 + x_1x_9) \\ \dot{x}_9 = \frac{x_4}{1+x_5x_9}(x_1x_8 - (x_1 + x_2)x_9) \end{cases} \tag{3.101}$$

$$u_{sc} = x_6 + x_3 i_{sc} \tag{3.102}$$

where $x_6 = u_1, x_7 = u_2, x_8 = u_3, x_9 = u_4$, together with $x_1, x_2, x_3, x_4, x_5$, are the state variables, the measured current $i_{sc}$ and voltage $u_{sc}$ are respectively the known input and measured output of this system.

### 3.5.2 Sensitivity and Observability study

#### Sensitivity analysis

As for RRC model, the sensitivity is studied before the design of state observers. For the proposed TL model, the capacitance in each branch in the electrical model is voltage dependent which results in the impossibility to express the impedance of this model. Therefore, the sensitivity of the impedance $Z$ at a polarization voltage value of $u_j,\ (j = 1, 2, 3, 4)$ is studied. At this case, the sensitivity of the impedance $Z$ with respect to the five parameters can be written as:

$$S^Z_{R_s}(\jmath\omega) \equiv \frac{R_s}{Z} \cdot \frac{\Delta Z}{\Delta R_s}, \quad S^Z_{R_d}(\jmath\omega) \equiv \frac{R_d}{Z} \cdot \frac{\Delta Z}{\Delta R_d}, \quad S^Z_{R_p}(\jmath\omega) \equiv \frac{R_p}{Z} \cdot \frac{\Delta Z}{\Delta R_p}$$
$$S^Z_{C_0}(\jmath\omega) \equiv \frac{C_0}{Z} \cdot \frac{\Delta Z}{\Delta C_0}, \quad S^Z_{\alpha}(\jmath\omega) \equiv \frac{\alpha}{Z} \cdot \frac{\Delta Z}{\Delta \alpha} \tag{3.103}$$

Fig. 3.20 shows the modulus of the sensitivity of the impedance with respect to the five parameters in function of frequency. The parameters of the TL model used in this sensitivity study are chosen according to the offline characterization results obtained in the first chapter: $R_s = 1.1\ \Omega$, $R_d = 2\ \Omega$, $R_p = 3000\ \Omega$, $C_0 = 0.15\ F$ and $\alpha = 0.4$. The polarization voltages across the capacitances are chosen according to the values obtained by simulating the EDLC model (Eqs. 3.95 and 3.96) with MATLAB: $u_1 = 1.15\ V$, $u_2 = 1.1\ V$, $u_3 = 1.05\ V$, $u_4 = 1\ V$. It can be concluded from the figure that high frequencies are needed to obtained good estimations of $R_s$, $R_d$ and an accurate estimation of $R_p$ requires very low frequencies. Good estimations of capacitance $C_0$ and $\alpha$ can be obtained with medium frequencies.

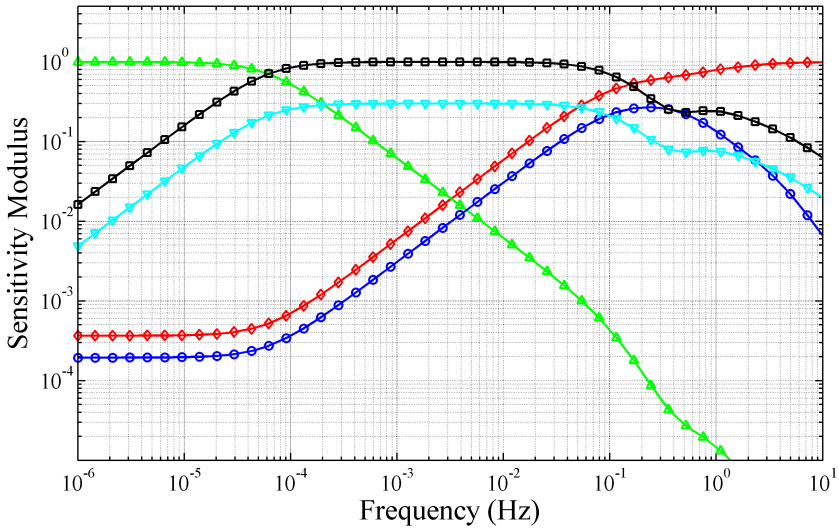


Figure 3.20: Sensitivity plot with respect to different parameters of TL model (red diamond: $R_s$, black square: $C_0$, green up triangle: $R_p$, blue circle: $R_d$, cyan down triangle: $\alpha$).

**Observability study**

To check the possibility to estimate the EDLC parameters with observers, the observability of the proposed extended model is studied. The model represented by Eq. 3.101 and Eq. 3.102 can be written as:

$$\begin{cases} \dot{\mathbf{X}}_a = f(\mathbf{X}_a, i_{sc}) \\ u_{sc} = h(\mathbf{X}_a, i_{sc}) \end{cases} \tag{3.104}$$

where $\mathbf{X}_a = [x_1\ x_2\ x_3\ x_4\ x_5\ x_6\ x_7\ x_8\ x_9]^T$ is the augmented state vector and $f(\mathbf{X}_a, i_{sc})$ and $h(\mathbf{X}_a, i_{sc})$ are the expressions at the right side of Eq. 3.101 and Eq. 3.102. In order to determine the local observability of this system, we have firstly tried to check the rank of its Jacobian matrix. However, since it is a ninth-order system, deriving the output expression and its first to eighth-order differential equations leads to a $9$ by $9$ dimensional Jacobian matrix. The determinant of this matrix has a very complicated expression with a length of hundreds of lines which causes a great difficulty to calculate its rank. Therefore, we intend to check the observability of its linearized version. If the linearized system of this nonlinear system is locally observable, the nonlinear system is also locally observable. The system linearized by the first-order Taylor approximation about the state estimation $\hat{\mathbf{X}}_a$ can be expressed as

$$\begin{cases} \dot{\mathbf{X}}_a \simeq \mathbf{F}\mathbf{X}_a + g_f(\hat{\mathbf{X}}_a, i_{sc}) \\ u_{sc} \simeq \mathbf{H}\mathbf{X}_a + g_h(\hat{\mathbf{X}}_a, i_{sc}) \end{cases} \tag{3.105}$$

where $g_f(\hat{\mathbf{X}}_a, i_{sc}) = f(\hat{\mathbf{X}}_a, i_{sc}) - \mathbf{F}\hat{\mathbf{X}}_a$, $g_h(\hat{\mathbf{X}}_a, i_{sc}) = h(\hat{\mathbf{X}}_a, i_{sc}) - \mathbf{H}\hat{\mathbf{X}}_a$ and $\mathbf{F}$ and $\mathbf{H}$ are the Jacobian matrices of the system:

$$\mathbf{F} = \frac{\partial f}{\partial \mathbf{X}_a}(\hat{\mathbf{X}}_a, i_{sc}),\ \mathbf{H} = \frac{\partial h}{\partial \mathbf{X}_a}(\hat{\mathbf{X}}_a, i_{sc}) \tag{3.106}$$

The observability of this linearized system can be determined by checking the rank of its observability matrix

$$\mathbf{O} = [\mathbf{H}\ \ \mathbf{HF}\ \ \mathbf{HF}^2\ ...\ \ \mathbf{HF}^8]^T \tag{3.107}$$

If the condition $\det(\mathbf{O}) \neq 0$ is satisfied, which means that the observability matrix $\mathbf{O}$ has full rank, the linearized system is observable [121]. Thus, the nonlinear system is also locally observable [122] which allows the parameters to be estimated online. For this extended EDLC system, the observability has been experimentally checked online as will be presented in §3.5.4.

### 3.5.3 Observers design

#### Extended Kalman filter design

As for the RRC model, a continuous-time extended Kalman filter is chosen for state estimation of TL model. As usual, the extended EDLC state and measurement model used in EKF takes the noises into account based on Eq. 3.104 [103]. The extended Kalman filter for the augmented state vector $\mathbf{X}_a$ and the output voltage $u_{sc}$ is then expressed as (see Fig. 3.21) [103] [104]:

$$\begin{cases} \dot{\hat{\mathbf{X}}}_a = f(\hat{\mathbf{X}}_a, i_{sc}) + \mathbf{K}(u_{sc} - \hat{u}_{sc}) \\ \hat{u}_{sc} = h(\hat{\mathbf{X}}_a, i_{sc}) = \hat{x}_6 + \hat{x}_3 i_{sc};\ \mathbf{K} = \mathbf{P}\mathbf{H}(i_{sc})^T R^{-1} \\ \dot{\mathbf{P}} = \mathbf{F}(\hat{\mathbf{X}}_a, i_{sc})\mathbf{P} + \mathbf{P}\mathbf{F}(\hat{\mathbf{X}}_a, i_{sc})^T + \mathbf{Q} - \mathbf{K}R\mathbf{K}^T \end{cases} \tag{3.108}$$

where $\hat{\mathbf{X}}_a = [\hat{x}_1\ \hat{x}_2\ \hat{x}_3\ \hat{x}_4\ \hat{x}_5\ \hat{x}_6\ \hat{x}_7\ \hat{x}_8\ \hat{x}_9]^T$ is an estimation of $\mathbf{X}_a$ and $\hat{u}_{sc}$ is the estimated output voltage. $\mathbf{K}$ (9 by 1 vector) is the correction gain of the observer. $R$ is a scalar while $\mathbf{Q}$ and $\mathbf{P}$ are both 9 by 9 symmetric matrices. $\mathbf{F}(\hat{\mathbf{X}}_a, i_{sc}) = \frac{\partial f}{\partial \mathbf{X}_a}(\hat{\mathbf{X}}_a, i_{sc})$ and $\mathbf{H}(i_{sc}) = \frac{\partial h}{\partial \mathbf{X}_a}(\hat{\mathbf{X}}_a, i_{sc})$ are the Jacobian matrices around the estimation, with

$$\frac{\partial f}{\partial \mathbf{X}_a}(\mathbf{X}_a, i_{sc}) = \begin{bmatrix} 0 & 0 & 0 & 0 & 0 & 0 & 0 & 0 & 0 \\ 0 & 0 & 0 & 0 & 0 & 0 & 0 & 0 & 0 \\ 0 & 0 & 0 & 0 & 0 & 0 & 0 & 0 & 0 \\ 0 & 0 & 0 & 0 & 0 & 0 & 0 & 0 & 0 \\ 0 & 0 & 0 & 0 & 0 & 0 & 0 & 0 & 0 \\ f_{61} & f_{62} & 0 & f_{64} & f_{65} & f_{66} & f_{67} & 0 & 0 \\ f_{71} & f_{72} & 0 & f_{74} & f_{75} & f_{76} & f_{77} & f_{78} & 0 \\ f_{81} & f_{82} & 0 & f_{84} & f_{85} & 0 & f_{87} & f_{88} & f_{89} \\ f_{91} & f_{92} & 0 & f_{94} & f_{95} & 0 & 0 & f_{98} & f_{99} \end{bmatrix} \tag{3.109}$$

$$\frac{\partial h}{\partial \mathbf{X}_a}(\mathbf{X}_a, i_{sc}) = \begin{bmatrix} 0 & 0 & i_{sc} & 0 & 0 & 1 & 0 & 0 & 0 \end{bmatrix} \tag{3.110}$$

$$\text{with} \quad f_{61} = \frac{x_4(x_7 - x_6)}{x_5 x_6 + 1};\ \ f_{71} = \frac{x_4\,(x_8 - 2\,x_7 + x_6)}{x_5\,x_7 + 1}$$

$$f_{81} = \frac{x_4\,(x_9 - 2\,x_8 + x_7)}{x_5\,x_8 + 1};\ \ f_{91} = \frac{x_4\,(x_8 - x_9)}{x_5\,x_9 + 1}$$

$$f_{62} = -\frac{x_4 x_6}{x_5 x_6 + 1};\ \ f_{72} = -\frac{x_4\,x_7}{x_5\,x_7 + 1}$$

$$f_{82} = -\frac{x_4\,x_8}{x_5\,x_8 + 1};\ \ f_{92} = -\frac{x_4\,x_9}{x_5\,x_9 + 1}$$

$$f_{64} = \frac{x_1 x_7 - (x_2 + x_1)x_6 + i_{sc}}{x_5 x_6 + 1}; \quad f_{74} = \frac{x_1\, x_8 - (x_2 + 2\, x_1)\; x_7 + x_1\, x_6}{x_5\, x_7 + 1}$$

$$f_{84} = \frac{x_1\, x_9 - (x_2 + 2\, x_1)\; x_8 + x_1\, x_7}{x_5\, x_8 + 1}; \quad f_{94} = \frac{x_1\, x_8 - (x_2 + x_1)\; x_9}{x_5\, x_9 + 1}$$

$$f_{65} = -\frac{x_4 x_6\,(x_1 x_7 - x_2 x_6 - x_1 x_6 + i_{sc})}{(x_5 x_6 + 1)^2}; \quad f_{75} = -\frac{x_4 x_7\,(x_1 x_8 - x_2 x_7 - 2x_1 x_7 + x_1 x_6)}{(x_5 x_7 + 1)^2}$$

$$f_{85} = -\frac{x_4 x_8\,(x_1 x_9 - x_2 x_8 - 2x_1 x_8 + x_1 x_7)}{(x_5 x_8 + 1)^2}; \quad f_{95} = \frac{x_4 x_9\,(x_2 x_9 + x_1 x_9 - x_1 x_8)}{(x_5 x_9 + 1)^2}$$

$$f_{66} = -\frac{x_4\;(x_1\, x_5\, x_7 + i_{sc}\, x_5 + x_2 + x_1)}{(x_5\, x_6 + 1)^2}; \quad f_{76} = \frac{x_1\, x_4}{x_5\, x_7 + 1}$$

$$f_{67} = \frac{x_1\, x_4}{x_5\, x_6 + 1}; \quad f_{77} = -\frac{x_4\;(x_1\, x_5\, x_8 + x_1\, x_5\, x_6 + x_2 + 2\, x_1)}{(x_5\, x_7 + 1)^2}; \quad f_{87} = \frac{x_1\, x_4}{x_5\, x_8 + 1}$$

$$f_{78} = \frac{x_1\, x_4}{x_5\, x_7 + 1}; \quad f_{88} = -\frac{x_4\;(x_1\, x_5\, x_9 + x_1\, x_5\, x_7 + x_2 + 2\, x_1)}{(x_5\, x_8 + 1)^2}; \quad f_{98} = \frac{x_1\, x_4}{x_5\, x_9 + 1}$$

$$f_{89} = \frac{x_1\, x_4}{x_5\, x_8 + 1}; \quad f_{99} = -\frac{x_4\;(x_1\, x_5\, x_8 + x_2 + x_1)}{(x_5\, x_9 + 1)^2}$$

These equations make the implementation of an online parameter estimator possible. These ordinary differential equations can be numerically solved using methods such as the Runge-Kutta or Bulirsch-Stoer algorithms.

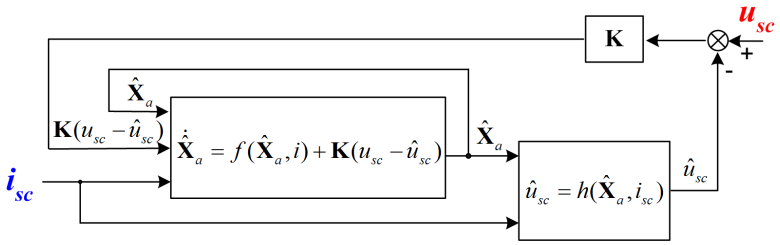


Figure 3.21: Extended Kalman filter principle.

### Braided Kalman filters design

The extended EDLC model represented by Eqs. 3.101 and 3.102 can be seen as the interconnection between two dynamic subsystems $\Sigma_1$ and $\Sigma_2$:

$$\Sigma_1 : \begin{cases} \dot{\mathbf{X}}_1 = f_1(\mathbf{X}_1, \mathbf{X}_2, i_{sc}) \\ u_{sc1} = h_1(\mathbf{X}_1, i_{sc}) \end{cases} \tag{3.111}$$

$$\Sigma_2 : \begin{cases} \dot{\mathbf{X}}_2 = f_2(\mathbf{X}_1, \mathbf{X}_2, i_{sc}) \\ u_{sc2} = h_2(\mathbf{X}_1, \mathbf{X}_2, i_{sc}) \end{cases} \tag{3.112}$$

with $\mathbf{X}_1 = [x_1\ x_3\ x_6\ x_7\ x_8\ x_9]^T$, $\mathbf{X}_2 = [x_2\ x_4\ x_5\ x_6\ x_9]^T$

$$f_1(\mathbf{X}_1, \mathbf{X}_2, i_{sc}) = \begin{bmatrix} 0 \\ 0 \\ \frac{x_4}{1+x_5x_6}(i_{sc} - (x_1+x_2)x_6 + x_1x_7) \\ \frac{x_4}{1+x_5x_7}(x_1x_6 - (2x_1+x_2)x_7 + x_1x_8) \\ \frac{x_4}{1+x_5x_8}(x_1x_7 - (2x_1+x_2)x_8 + x_1x_9) \\ \frac{x_4}{1+x_5x_9}(x_1x_8 - (x_1+x_2)x_9) \end{bmatrix}$$

$$h_1(\mathbf{X}_1, i_{sc}) = h_2(\mathbf{X}_1, \mathbf{X}_2, i_{sc}) = x_6 + x_3 i_{sc}$$

$$f_2(\mathbf{X}_1, \mathbf{X}_2, i_{sc}) = \begin{bmatrix} 0 \\ 0 \\ 0 \\ \frac{x_4}{1+x_5x_6}(i_{sc} - (x_1+x_2)x_6 + x_1x_7) \\ \frac{x_4}{1+x_5x_9}(x_1x_8 - (x_1+x_2)x_9) \end{bmatrix}$$

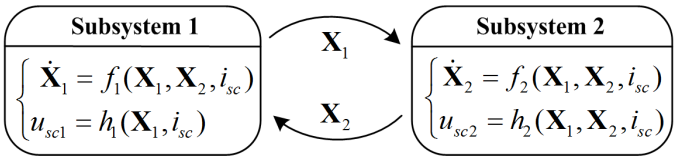


Figure 3.22: Structure of interconnected subsystems.

The partition of the proposed ninth-order state vector aims at converting the system into two lower-order subsystems, in order to reduce the computational cost. Different system partitions have been considered and the proposed partition was finally chosen because it brings enough information in both subsystems to make the state observation possible. Both subsystems are interconnected (or braided) by using the states of a subsystem as an input of the other one (see Fig. 3.22). For these

interconnected subsystems, braided Kalman filters (BKFs) can be designed [123]:

$$O_1 : \begin{cases} \dot{\hat{\mathbf{X}}}_1 &= f_1(\hat{\mathbf{X}}_1, \hat{\mathbf{X}}_2, i_{sc}) + \mathbf{K}_1(u_{sc} - \hat{u}_{sc1}) \\ \mathbf{K}_1 &= \mathbf{P}_1 \mathbf{H}_1(i_{sc})^T R_1^{-1} \\ \dot{\mathbf{P}}_1 &= \mathbf{F}_1(\hat{\mathbf{X}}_1, \hat{\mathbf{X}}_2, i_{sc})\mathbf{P}_1 + \mathbf{P}_1 \mathbf{F_1}(\hat{\mathbf{X}}_1, \hat{\mathbf{X}}_2, i_{sc})^T + \mathbf{Q}_1 - \mathbf{K}_1 R_1 \mathbf{K}_1^T \\ \hat{u}_{sc1} &= h_1(\hat{\mathbf{X}}_1, i_{sc}) \end{cases} \tag{3.113}$$

$$O_2 : \begin{cases} \dot{\hat{\mathbf{X}}}_2 &= f_2(\hat{\mathbf{X}}_1, \hat{\mathbf{X}}_2, i_{sc}) + \mathbf{K}_2(u_{sc} - \hat{u}_{sc2}) \\ \mathbf{K}_2 &= \mathbf{P}_2 \mathbf{H}_2^T R_2^{-1} \\ \dot{\mathbf{P}}_2 &= \mathbf{F}_2(\hat{\mathbf{X}}_1, \hat{\mathbf{X}}_2, i_{sc})\mathbf{P}_2 + \mathbf{P}_2 \mathbf{F_2}(\hat{\mathbf{X}}_1, \hat{\mathbf{X}}_2, i_{sc})^T + \mathbf{Q}_2 - \mathbf{K}_2 R_2 \mathbf{K}_2^T \\ \hat{u}_{sc2} &= h_2(\hat{\mathbf{X}}_1, \hat{\mathbf{X}}_2, i_{sc}) \end{cases} \tag{3.114}$$

where $\hat{\mathbf{X}}_1 = [\hat{x}_1\ \hat{x}_3\ \hat{x}_6\ \hat{x}_7\ \hat{x}_8\ \hat{x}_9]^T$ and $\hat{\mathbf{X}}_2 = [\hat{x}_2\ \hat{x}_4\ \hat{x}_5\ \hat{x}_6\ \hat{x}_9]^T$ are the estimations of $\mathbf{X}_1$ and $\mathbf{X}_2$. The linearized approximation matrices of the nonlinear systems (3.111) and (3.112) around the estimation are computed as:

$$\mathbf{F}_1(\hat{\mathbf{X}}_1, \hat{\mathbf{X}}_2, i_{sc}) = \frac{\partial f_1}{\partial \mathbf{X}_1}(\hat{\mathbf{X}}_1, \hat{\mathbf{X}}_2, i_{sc}),\ \ \mathbf{H}_1(i_{sc}) = \frac{\partial h_1}{\partial \mathbf{X}_1}(\hat{\mathbf{X}}_1, \hat{\mathbf{X}}_2, i_{sc}) \tag{3.115}$$

$$\mathbf{F}_2(\hat{\mathbf{X}}_1, \hat{\mathbf{X}}_2, i_{sc}) = \frac{\partial f_2}{\partial \mathbf{X}_2}(\hat{\mathbf{X}}_1, \hat{\mathbf{X}}_2, i_{sc}),\ \ \mathbf{H}_2 = \frac{\partial h_2}{\partial \mathbf{X}_2}(\hat{\mathbf{X}}_1, \hat{\mathbf{X}}_2, i_{sc}) \tag{3.116}$$

with

$$\frac{\partial f_1}{\partial \mathbf{X}_1}(\mathbf{X}_1, \mathbf{X}_2, i_{sc}) = \begin{bmatrix} 0 & 0 & 0 & 0 & 0 & 0 \\ 0 & 0 & 0 & 0 & 0 & 0 \\ f_{61} & 0 & f_{66} & f_{67} & 0 & 0 \\ f_{71} & 0 & f_{76} & f_{77} & f_{78} & 0 \\ f_{81} & 0 & 0 & f_{87} & f_{88} & f_{89} \\ f_{91} & 0 & 0 & 0 & f_{98} & f_{99} \end{bmatrix} \tag{3.117}$$

$$\frac{\partial f_2}{\partial \mathbf{X}_2}(\mathbf{X}_1, \mathbf{X}_2, i_{sc}) = \begin{bmatrix} 0 & 0 & 0 & 0 & 0 \\ 0 & 0 & 0 & 0 & 0 \\ 0 & 0 & 0 & 0 & 0 \\ f_{62} & f_{64} & f_{65} & f_{66} & 0 \\ f_{92} & f_{94} & f_{95} & 0 & f_{99} \end{bmatrix} \tag{3.118}$$

$$\mathbf{H}_1(i_{sc}) = \begin{bmatrix} 0 & i_{sc} & 1 & 0 & 0 & 0 \end{bmatrix} \tag{3.119}$$

$$\mathbf{H}_2 = \begin{bmatrix} 0 & 0 & 0 & 1 & 0 \end{bmatrix} \tag{3.120}$$

where $f_{61}$ - $f_{99}$ have the same expressions as presented in Eq. 3.109. Fig. 3.23

shows how BKFs work. BKFs can be also called interconnected observers as for the case of the RRC model. They are called specifically BKFs because the observers for both subsystems are Kalman filters. For EKF, the covariance matrix $\mathbf{P}$ is a 9 by 9 matrix. Since $\mathbf{P}$ is symmetric, 45 elements need to be updated at each sampling period while 21 elements of $\mathbf{P}_1$ and 15 elements of $\mathbf{P}_2$ are updated for BKFs. Therefore, BKFs have lower computational cost compared to EKF.

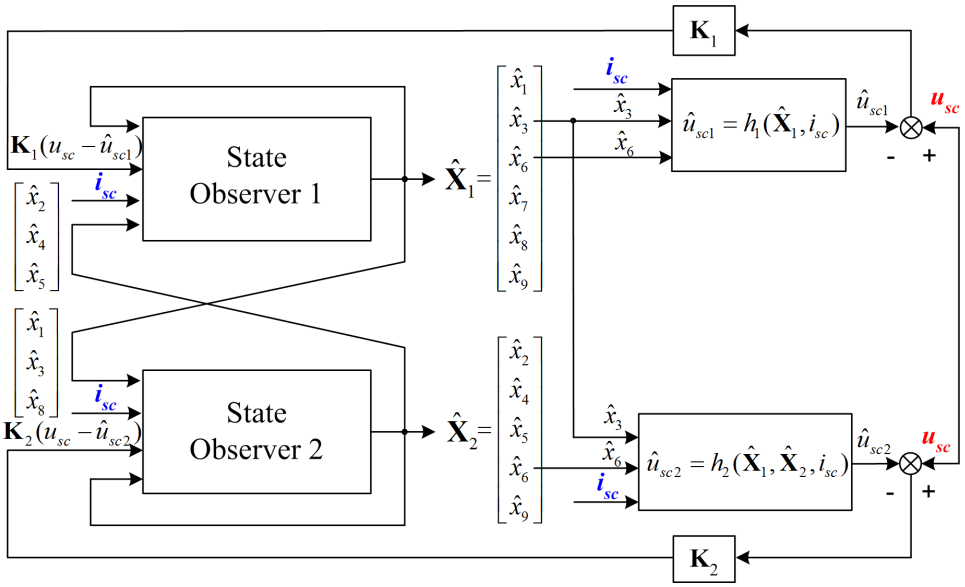


Figure 3.23: Braided Kalman filters.

### 3.5.4 Estimation results

As for the RRC model, the state estimation results presented in this section involve a simulated case and an experimental case, using the current and voltage signals from either a fourth-order transmission line model or a real EDLC.

#### Simulation results

In the simulated case, the Nichicon EDLC used in the previous sections is simulated by a fourth-order transmission line model represented by Eqs. 3.95 and 3.96. The physical parameters of this model, shown in Table 3.2, are chosen according to the offline characterization results of EDLCs. A simulated current signal similar to the one used for the RRC model is designed and used as the input of the TL model.

Table 3.2: Physical parameters of fourth-order TL model.

| $R_s$ [$\Omega$] | $R_d$ [$\Omega$] | $R_p$ [$\Omega$] | $C_0$ [$F$] | $\alpha$ |
|---|---|---|---|---|
| 1.1 | 2 | 3000 | 0.15 | 0.4 |

Both observers, EKF and BKFs, are implemented with MATLAB/SIMULINK and the parameters of the observers are tuned before the state estimation. The initialization and parameters of EKF are as follows:

$$\mathbf{X}_a^{\text{init}} = [0.75,\ 1.25\,10^{-4},\ 0.8,\ 8.33,\ 0.4,\ 0.4,\ 0.38,\ 0.36,\ 0.34]$$
$$\mathbf{P}^{\text{init}} = \text{diag}\,(1,\ 3\,10^{-6},\ 1,\ 1,\ 1,\ 1,\ 1,\ 1,\ 1)$$
$$\mathbf{Q} = \text{diag}\,(15,\ 1\,10^{-6},\ 8,\ 20,\ 2,\ 1,\ 1,\ 1,\ 1);\ \ R = 1\ [\text{V}^2]$$

where $\mathbf{P}^{\text{init}}$ and $\mathbf{Q}$ are chosen as $9 \times 9$ diagonal matrices and their second diagonal values are set quite small because of the high parallel resistance which leads to a very small value of the second state $x_2$.

The second kind of observer, BKFs, is composed of two Kalman filters. The initialization and parameters of these two Kalman filters are chosen as

$$\mathbf{X}_1^{\text{init}} = [0.75,\ 0.8,\ 0.4,\ 0.38,\ 0.36,\ 0.34]$$
$$\mathbf{X}_2^{\text{init}} = [1.25\,10^{-4},\ 8.33,\ 0.4,\ 0.4,\ 0.34]$$
$$\mathbf{P}_1^{\text{init}} = \text{diag}\,(1,\ 1,\ 1,\ 1,\ 1,\ 1)$$
$$\mathbf{P}_2^{\text{init}} = \text{diag}\,(3\,10^{-6},\ 1,\ 1,\ 1,\ 1)$$
$$\mathbf{Q}_1 = \text{diag}\,(8,\ 10,\ 1,\ 1,\ 1,\ 1);\qquad R_1 = 1\ [\text{V}^2]$$
$$\mathbf{Q}_2 = \text{diag}\,(1\,10^{-7},\ 40,\ 30,\ 1,\ 1);\ R_2 = 1\ [\text{V}^2]$$

Fig. 3.24 shows the simulated current and voltage, the estimated parameters provided by both observers based on the TL model during 25 charging/discharging cycles. The results show that the parameter estimations provided by both observers converge to the correct preset values denoted by red dashed lines. When estimating $R_p$, $C_0$ and $\alpha$, the convergence speed of BKFs is lower than that of EKF.

In order to assess the dynamic performance of the designed observers, an EDLC TL model with varying parameters is simulated. At time $t_1$, $R_s$ has a step increase from 1.1 Ω to 1.2 Ω and $R_d$ also has a step increase from 2 Ω to 2.1 Ω. At the same time, $C_0$ decreases from 0.15 F to 0.14 F. From time $t_2$, both $R_s$ and $R_d$ linearly increase with a same slope of $1.5 \times 10^{-5}$ $[\Omega\text{s}^{-1}]$ and $C_0$ decreases linearly with a slope of $-5 \times 10^{-6}$ $[\text{Fs}^{-1}]$. Fig. 3.25 shows the estimation results of both observers during the variation of the parameters. The same tuning parameters of the observers are used during all the simulation process. The results reveal a good dynamic performance of both observers because the estimation provided by both observers can always track the variation of the real parameters. The estimation for the linearly varying parameters are less satisfying because of the inaccuracy of the proposed extended model in this case: the equations $\dot{x}_1 = \dot{x}_2 = \cdots = \dot{x}_5 = 0$ in the extended EDLC model (Eq. 3.101) are no more true.

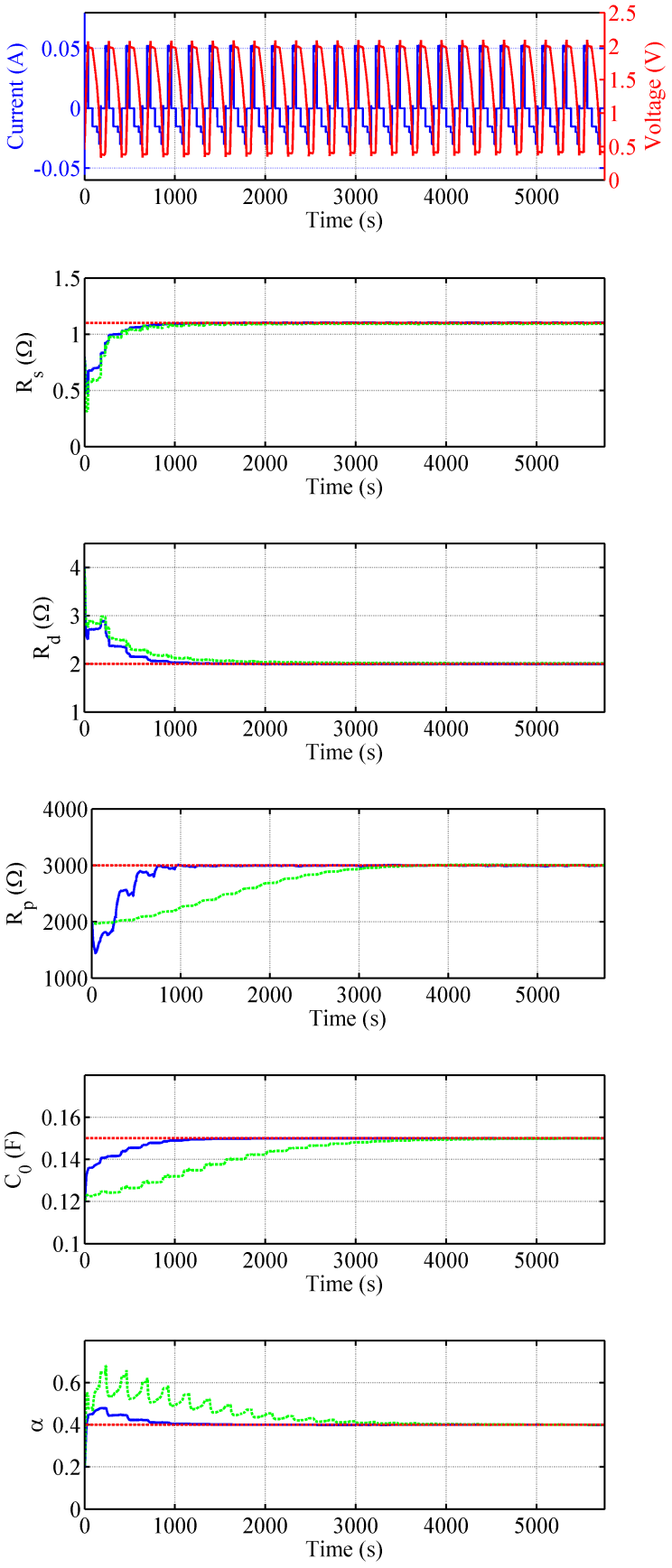


Figure 3.24: Simulated current (blue line), voltage (red line) signals and parameter estimations of a simulated EDLC during 25 charging/discharging periods based on TL model (red dashed lines: preset parameters of model, blue lines: estimated by EKF, green dashed lines: estimated by BKFs).

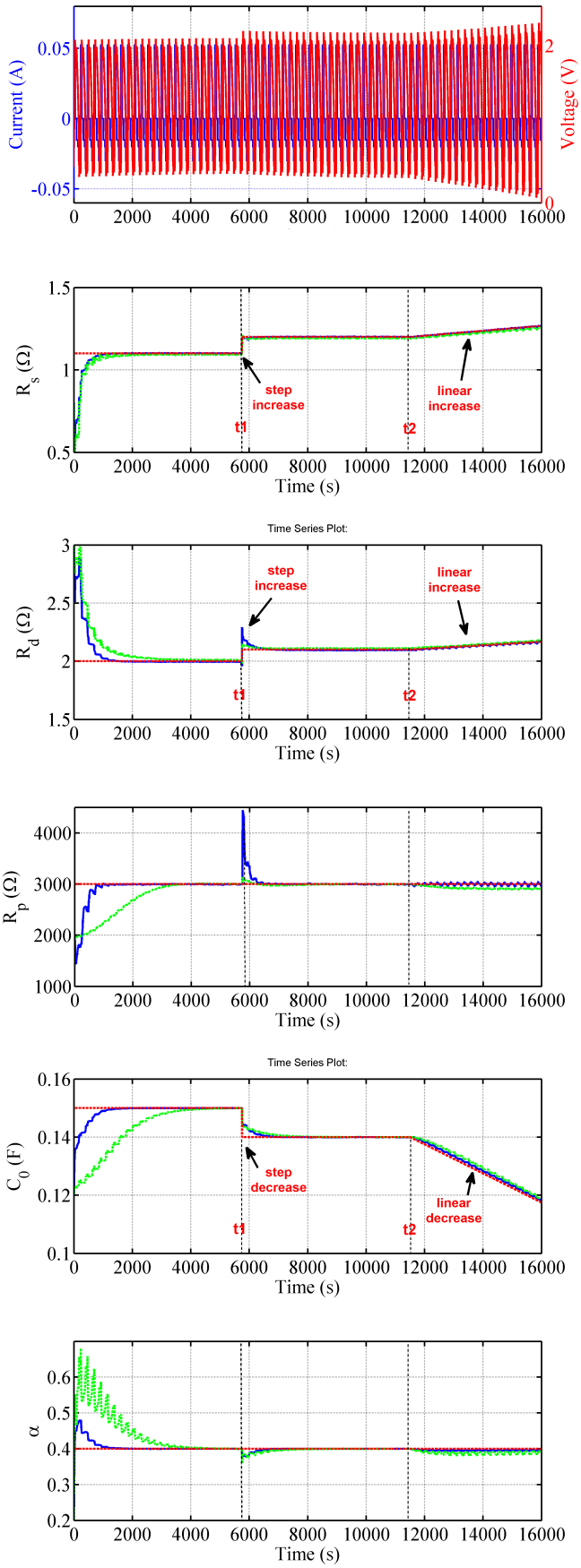


Figure 3.25: Simulated current (blue line), voltage (red line) signals and parameter estimations of a simulated EDLC during 70 charging/discharging periods based on TL model under dynamic case (red dashed lines: preset dynamic parameters of model, blue lines: estimated by EKF, green dashed lines: estimated by BKFs).

**Experimental results**

The simulated results demonstrate the good performance of the designed EKF and BKFs based on the transmission line model. These observers have also been applied to experimental current and voltage signals. The current and voltage signals used here are the same as that for RRC model. The initialization and parameters of EKF are as follows:

$$\mathbf{X}_a^{\text{init}} = [0.75,\ 8.5\,10^{-5},\ 0.8,\ 8.33,\ 0.4,\ 0.4,\ 0.38,\ 0.36,\ 0.34]$$
$$\mathbf{P}^{\text{init}} = \text{diag}\,(1,\ 3\,10^{-6},\ 1,\ 1,\ 1,\ 1,\ 1,\ 1,\ 1)$$
$$\mathbf{Q} = \text{diag}\,(0.05,\ 3\,10^{-8},\ 1,\ 5,\ 8,\ 1,\ 1,\ 1,\ 1);\quad R = 1\ [\text{V}^2]$$

The initialization and parameters of the braided Kalman filters are chosen as

$$\mathbf{X}_1^{\text{init}} = [0.75,\ 0.8,\ 0.4,\ 0.38,\ 0.36,\ 0.34]$$
$$\mathbf{X}_2^{\text{init}} = [8.5\,10^{-5},\ 8.33,\ 0.4,\ 0.4,\ 0.34]$$
$$\mathbf{P}_1^{\text{init}} = \text{diag}\,(1,\ 1,\ 1,\ 1,\ 1,\ 1)$$
$$\mathbf{P}_2^{\text{init}} = \text{diag}\,(3\,10^{-6},\ 1,\ 1,\ 1,\ 1)$$
$$\mathbf{Q}_1 = \text{diag}\,(0.05,\ 1,\ 1,\ 1,\ 1,\ 1);\quad R_1 = 1\ [\text{V}^2]$$
$$\mathbf{Q}_2 = \text{diag}\,(3\,10^{-8},\ 5,\ 0.5,\ 1,\ 1);\ R_2 = 1\ [\text{V}^2]$$

The observability of the extended system is determined online by checking the determinant of the observability matrix $\mathbf{O}$ of the linearized system. The determinant values of $\mathbf{O}$ during one charging/discharging cycle is shown in the second plot of Fig. 3.28. The extended system is locally observable at both charging and discharging phases, while it is unobservable during open circuit phases. Fig. 3.26 shows the evolution of the parameter estimations during $25$ charging/discharging cycles. The parameter estimations provided by both observers reach their steady state after $4000$ s. The periodical fluctuations of the parameters estimation at the steady state are probably caused by the incorrect estimations at the unobservable phases (open circuit phases). But we are only interested on the estimations at the end of charging phases. These estimations marked by red points reveal a clear convergence without any fluctuations. Fig. 3.27 shows the evolution of the parameter estimations during one cycle in steady state. The values at the end of the charging phase are considered as the final estimations of the parameters. The energy stored in the EDLC can be estimated by Eq. 3.99 with the estimated parameter and states. The third plot of Fig. 3.28 shows the estimated energy during one charging/discharging cycle. This allows to provide the SoC of an EDLC during its function.

The output errors between the measured voltage and the estimated voltage provided by different observers, the EKF, the first and second observers of BKFs, are calculated and shown in the fourth plot of Fig. 3.28. The plot below is the enlarged

segment of the output error during charging phase. It clearly shows that the output errors of the three observers all converge to $0$ at the end of charging phase which also demonstrates the good performance of these observers. It should be pointed out that the output error of the TL model at the end of charging phase is obviously much smaller than that of the RRC model (see the last plot of Fig. 3.18). Therefore, in accordance with the models comparison of the previous chapter, the 4th-order transmission line model of an EDLC is proved to be more accurate than the RRC model.

## 3.6 Experimental results of the EDLCs aging monitoring

In the previous sections, a fresh EDLC has been characterized by several state observers based on a RRC model and on a TL model, and the characterization results have been given and compared. In this section, all these observers will be applied to EDLCs at different aging stages to observe the parameters evolution with aging. The accelerated calendar aging process used in this chapter has been introduced in the first chapter (see §1.4.2 page 51). Each week, the same current signals as the ones used in the previous section are applied to $5$ EDLCs which are aged at $60°$ C, $2.5$ V and to $5$ other EDLCs which are aged at $60°$ C, $0$ V. Then the corresponding voltages and currents are recorded and processed by the designed state observers, in order to estimate the parameters. Therefore, the parameters evolution during the aging of EDLCs can be obtained and will be presented in the following part. These results allow to define a state of health indicator and an example of SoH gauge will be given at last.

### 3.6.1 Aging monitoring based on the RRC model

The evolution of the parameters $R_s$, $C$ and $R_p$ of the RRC model have been estimated during the EDLCs aging by the EKF and the IOs. Fig. 3.29 shows the parameters evolution of $5$ EDLCs aged at a high voltage ($2.5$ V). The red dashed lines are the linear fitting of the average estimation of the five samples and reveal the evolution rate of the estimations. Both observers show that the series resistance has a significant increase with aging and the capacitance almost doesn't evolve with time. The parallel resistance estimation decreases with aging. It can be seen from the red dashed lines that the EKF and the IOs provide a very similar evolution rate for parameters $R_s$ and $C$ but for $R_p$, the decrease with aging estimated by the EKF is much faster than that by the IOs. This difference for $R_p$ may come from the large deviation of the five EDLC samples at the ninth week and the last week which can

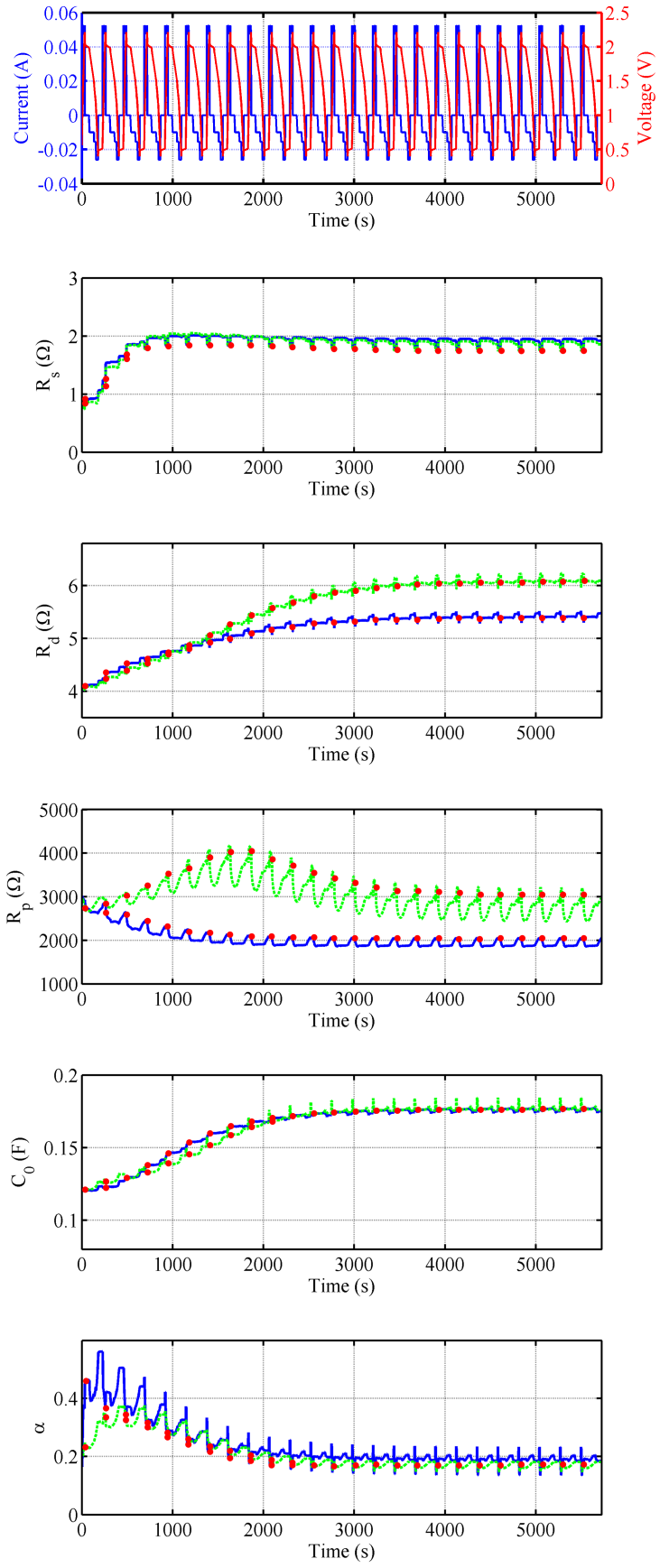


Figure 3.26: Experimental current (blue line), voltage (red line) signals and parameter estimations of a fresh EDLC during 25 charging/discharging periods based on TL model (blue lines: estimated by EKF, green dashed lines: estimated by BKFs, red points: estimations at the end of each charging phase).

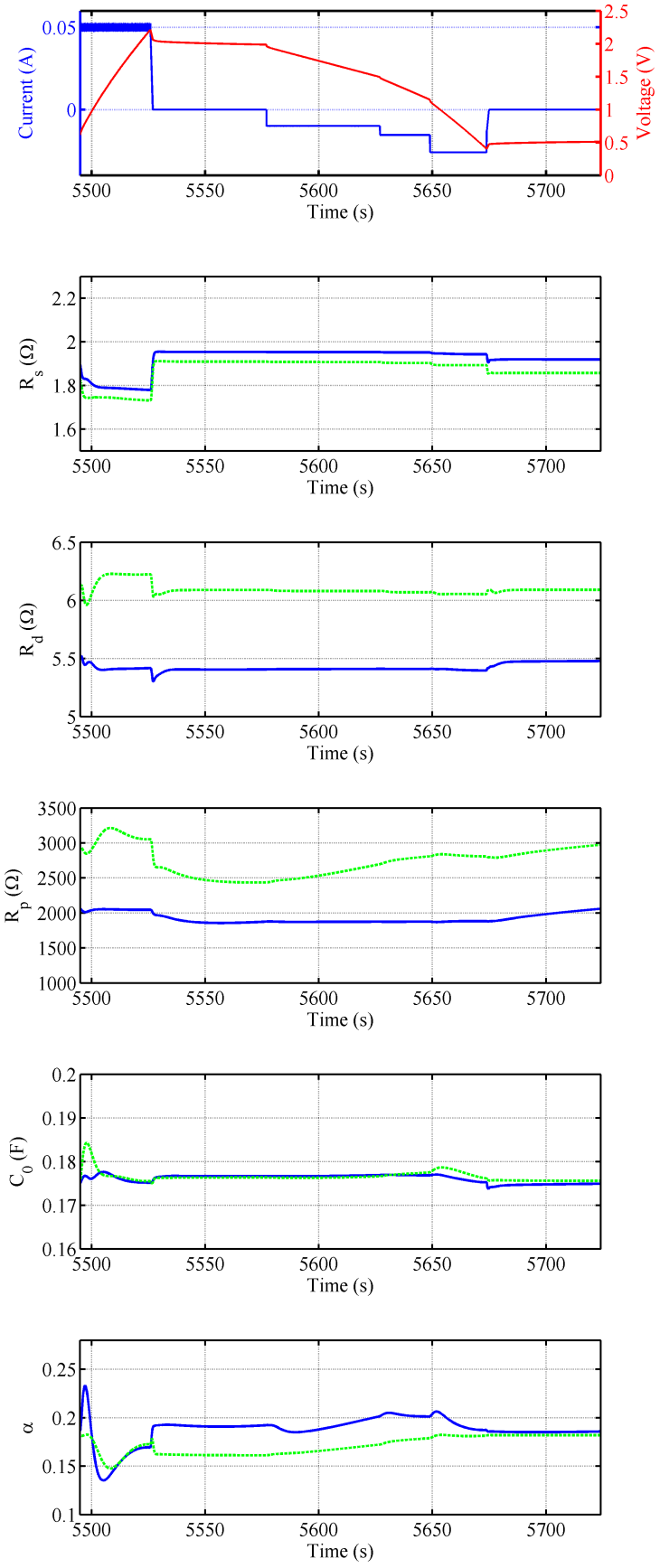


Figure 3.27: Experimental current (blue line), voltage (red line) signals and parameter estimations of a fresh EDLC during one charging/discharging period based on the TL model (blue lines: estimated by EKF, green dashed lines: estimated by BKFs).

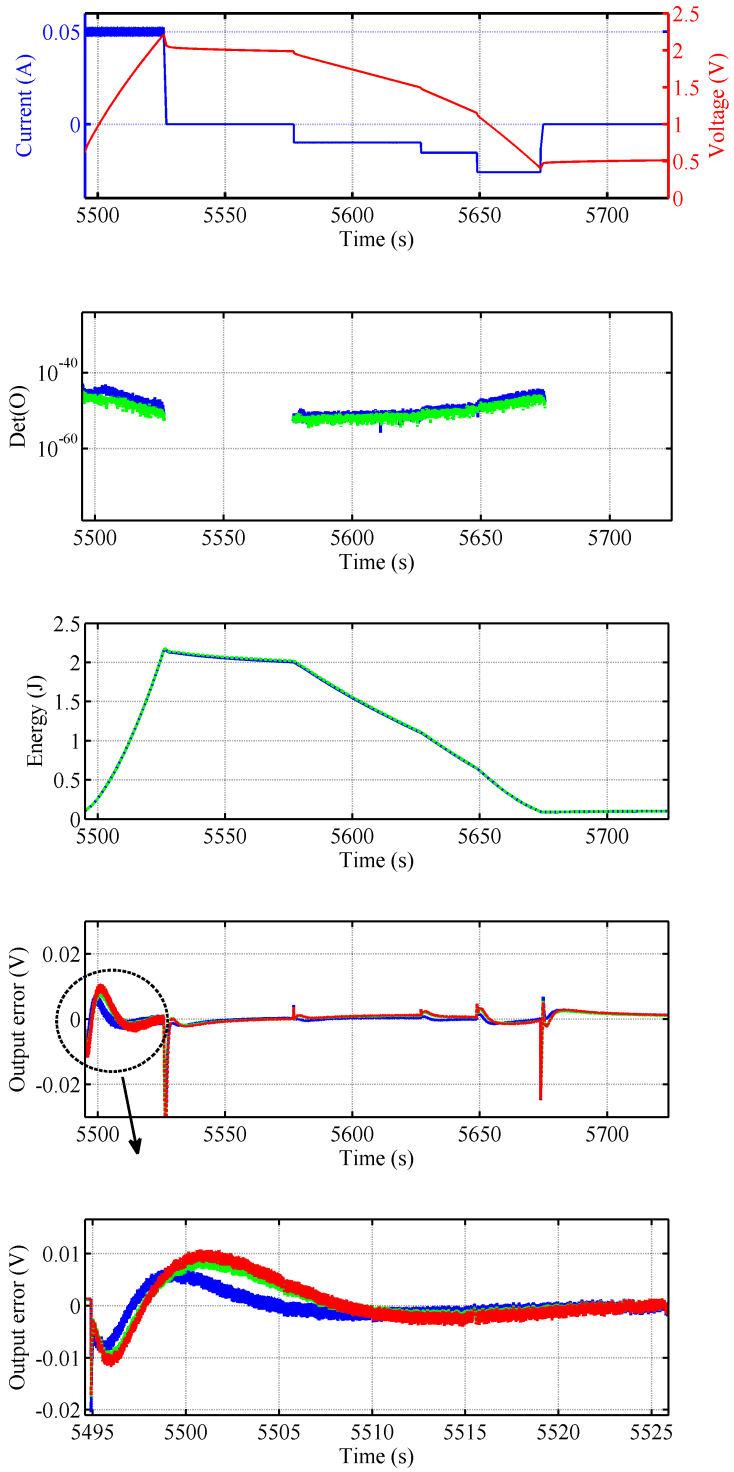


Figure 3.28: From top to bottom: experimental current (blue line) and voltage (red line) signals of a fresh EDLC during one charging/discharging period; the corresponding determinant of observability matrix; the stored energy (blue lines: estimated by EKF, green dashed lines: estimated by BKFs); the output error (blue lines: estimated by EKF, green dashed lines: estimated by the first BKF; red dashed lines: estimated by the second BKF).

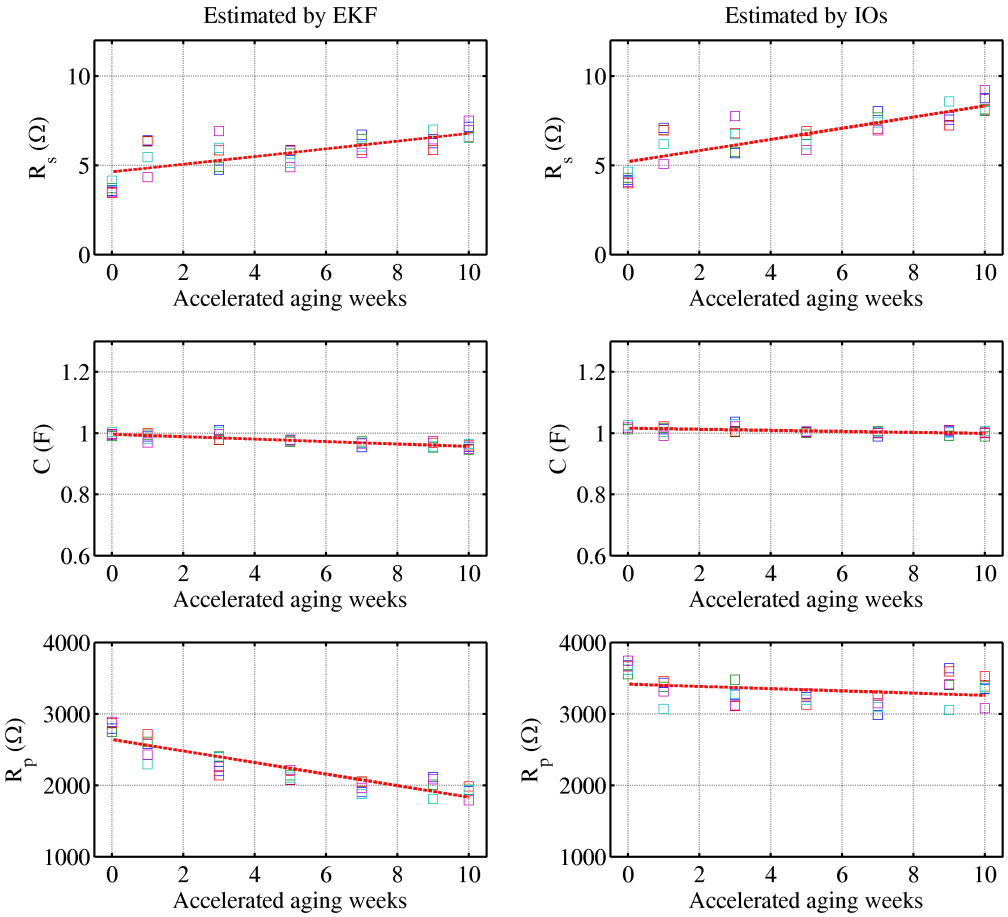


Figure 3.29: Evolution of the parameter estimations of the EDLCs in successive aging periods at 2.5 V obtained by the estimators based on the RRC model (left side: EKF, right side: IOs).

lead to a less accurate estimation. Similarly, the $R_s$ estimations of the first and the third week provided by both observers are out of the evolution path (red dashed line), probably because of their relative large samples deviation.

Fig. 3.30 shows the parameters evolution of 5 EDLCs aged at a voltage of 0 V, which is an aging case less typical than the case of EDLCs aged at 2.5 V. At this low voltage, the $R_s$ estimation increases very significantly with time while the $R_p$ estimation decreases. The estimation of capacitance $C$ has a slight increase with time. Both observers provide very similar estimations of the parameters $R_s$ and $C$. The numerical estimation values of $R_p$ provided by both observers are quite different. But their evolution rates are quite similar and thus both observers will provide a similar state of health estimation. The estimations of $R_s$ and $R_p$ at the ninth week more or less deviate from the evolution path indicated by red dashed lines, and they are probably caused by the large deviation of the samples at this week. Comparing with Fig. 3.29, it is found that the increase of $R_s$ and decrease of $R_p$ are more significant when the EDLCs are aged at a lower voltage (0 V). This is in accordance

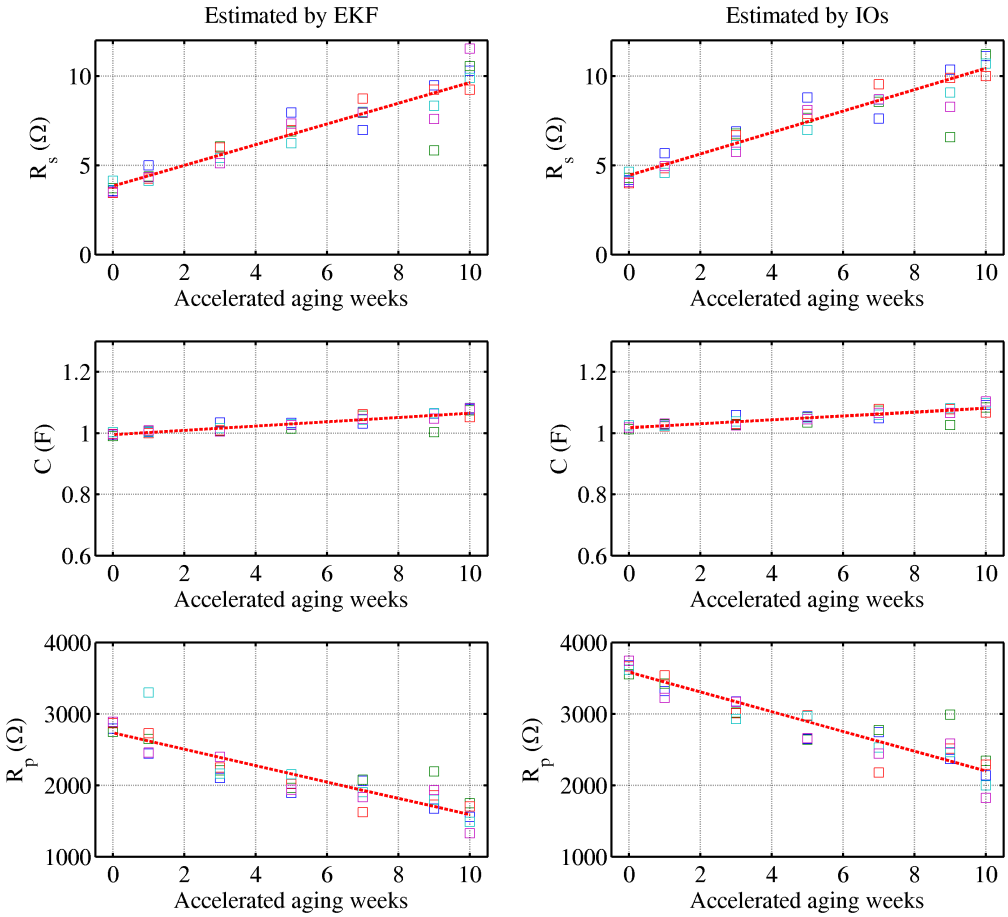


Figure 3.30: Evolution of the parameter estimations of the EDLCs in successive aging periods at 0 V obtained by the estimators based on the RRC model (left side: EKF, right side: IOs).

with the parameter evolution results obtained by offline methods in the first chapter and thus ensures the correction of the online estimations results. Usually, the capacitance of an EDLC decreases with aging but in this case, the capacitance has slightly increased. This may be because the capacitance degradation of this kind of EDLCs happens very slowly when they are aged at a special voltage of 0 V (short circuit) without any voltage potential difference between the electrodes and the electrolyte.

### 3.6.2 Aging monitoring based on TL model

This section will present the evolution of the parameters $R_s$, $R_d$, $R_p$, $C$ and $\alpha$ of the TL model estimated by EKF and BKFs during the EDLCs aging. The capacitance $C$ of an EDLC is defined as the sum of the estimated capacitances (Eq.

3.91) in the TL model:

$$C = \frac{1}{4}\sum_{j=1}^{4} \hat{C}_0(1 + \hat{\alpha}\hat{u}_j), \quad (j = 1, 2, 3, 4) \tag{3.121}$$

where $\hat{C}_0$, $\hat{\alpha}$ and $\hat{u}_j$ are respectively the estimated values of $C_0$, $\alpha$ and $u_j$ obtained at the end of the charging phase. Fig. 3.31 presents the evolution of the parameters of $5$ EDLCs aged at a high voltage ($2.5$ V). Both observers, EKF and BKFs, provide similar results. It can be seen from this plot that during the aging of EDLCs, the series resistance has a significant increase and the $R_s$ estimation of the EDLCs samples at the first and third week has a large variance and thus these estimations are not very reliable. Without regard to these two weeks, the evolution of the $R_s$ estimation can be seen as approximately linear. The capacitance $C$ has almost no variation with aging. The parallel resistance decreases with aging and the estimation result of this parameter obtained from both observers has a large difference. This difference may be caused by the large deviation of the samples at the first, third, ninth and the last week and hence the $R_p$ estimation is not very accurate. For the three parameters which are also present in the RRC model, the results obtained here are quite similar to that provided by the EKF and IOs based on the RRC model. The evolution of the additional two parameters, $R_d$ and $\alpha$, are also very significant. $R_d$ has an significant increase with aging while $\alpha$ decreases. The evolutions of these parameters are nearly linear. And it is also noticed that for both parameters, the estimated results of $5$ EDLCs samples have a quite large dispersion for the ninth and the last week. Therefore, these estimations should be carefully used to monitor the EDLCs aging. These results based on the TL model demonstrate that the series resistance and the capacitance are no longer the only two parameters which could be used for aging monitoring. Other physical parameters such as the dynamic resistance could also be good indicators to monitor the aging of EDLCs.

Fig. 3.32 shows the evolution of the parameters of $5$ EDLCs aged at a voltage of $0$ V. Both observers provide a very similar evolution of the estimations of $R_s$, $R_d$ and $C$. During the aging at $0$ V, $R_s$ and $R_d$ increase significantly while $C$ remains almost constant. Compared to the aging at $2.5$ V, the series resistance of EDLCs aged at $0$ V has a more significant increase while the dynamic resistance has a smaller variation. The voltage sensitivity coefficient $\alpha$ has a slight increase unlike the aging at $2.5$ V. All these parameter evolutions are in accordance with the offline aging monitoring results. Unexpectedly, $R_p$ estimated by EKF has increased a lot with aging especially at the end of the experiment. But it is noticed that the variance of this unexpected estimation is very large, which means that this result has a very high uncertainty and should not be trusted. Special attention should be paid to the estimation at the end of the aging experiment, for example, the ninth and the last

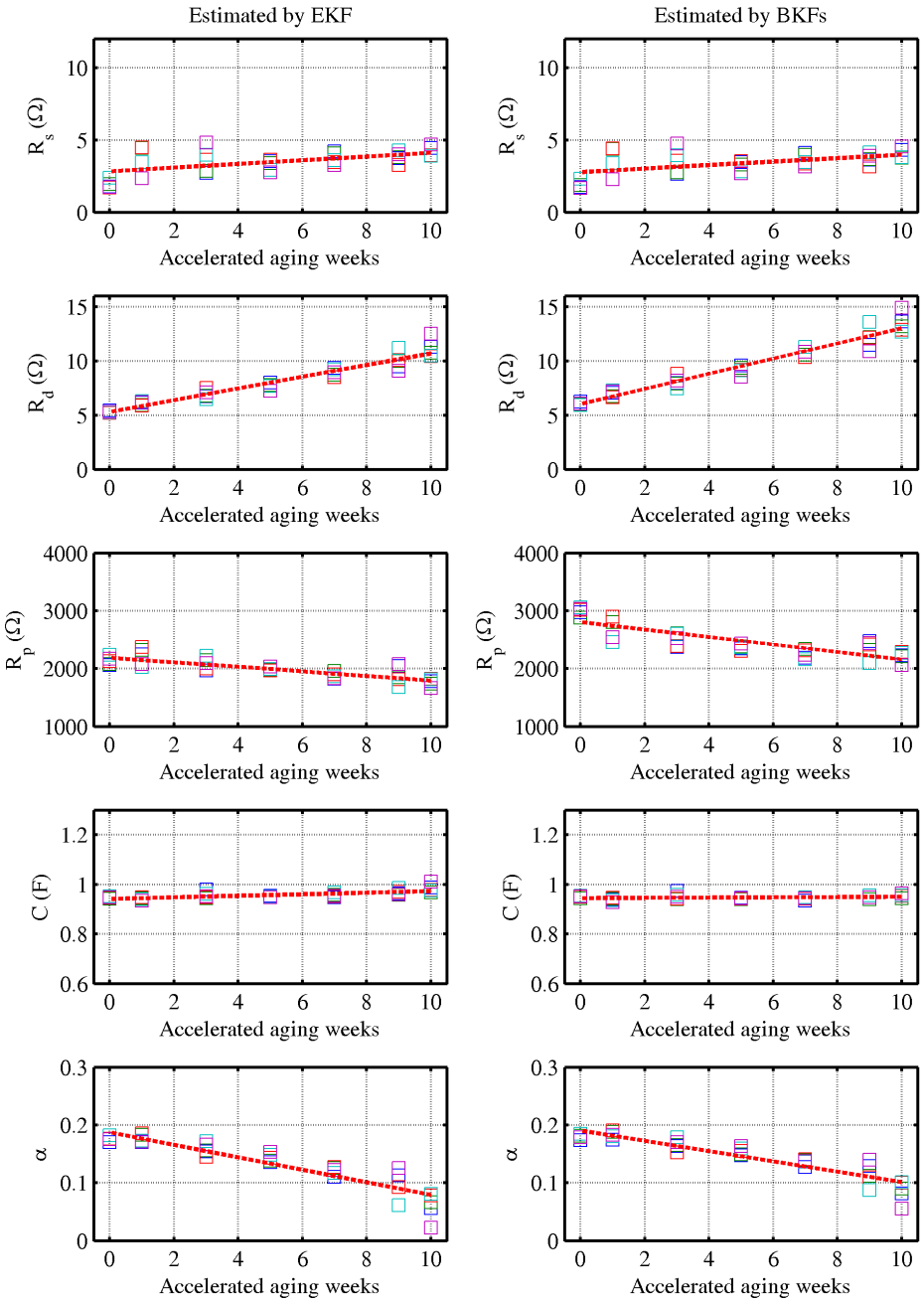


Figure 3.31: Estimation of parameters evolution of the EDLCs in successive aging periods at 2.5 V obtained by different estimators based on TL model (left side: EKF, right side: BKFs).

week. The estimations of most parameters obtained by both observers reveal a quite significant deviation of the EDLCs samples and thus they may be less reliable. It should be pointed out that this aging experiment at $0$ V is not very close to a real aging case of a practical application, because the aging of EDLCs usually happens when they are performing and their voltage is not always equal to zero. Considering this, the online monitoring results obtained with the aging experiments at $2.5$ V (shown in Fig. 3.31) should be more convincing. These results are consistent with the offline monitoring results discussed in the first chapter and thus proved that the designed observers based on the TL model are able to monitor the aging of EDLCs through their estimated parameter evolutions.

### 3.6.3 SoH estimation

Once the parameters of an EDLC are estimated online and once the end of life criterion is defined, the state of health of an EDLC can be determined. The parameter estimations obtained either offline in the first chapter or online by the observers clearly show that during the aging, the evolution rate of the parameters are different. Therefore, as discussed at the beginning of §3.2.1, the SoH can be determined by taking the variation of each parameter into account (see Eq. 3.1) or be determined by one parameter which is the fastest to reach its end of life criterion (see Eq. 3.2). In this section, an example of SoH estimation of an EDLC, obtained with both SoH definitions, during the aging process ($10$ weeks, aged at $2.5$ V and $60°C$) will be given for both the RRC and TL models.

The so called "end of life" of EDLCs does not mean they experience a true end of life but rather means that the performance is too degraded to maintain the application requirements [124]. Normally, the end of life criteria of the parameters are specified by the EDLCs manufacturers but unfortunately in our case, they are not provided. In order to show the possibility to design an online SoH indicator with the estimated parameters from the proposed state observers, it is assumed to take the average parameter estimations of the EDLCs samples at the end of the accelerated aging process as the end of life criteria.

According to Eq. 3.1 and Eq. 3.2, the state of health of an EDLC can be estimated at any time with the parameter estimations provided by a state observer. The weight of each parameter $\beta_i$ in Eq. 3.1 can be determined by the user. For example, one may set a relatively large weight for one parameter if the evolution of this parameter is related to a more serious degradation of the EDLCs performance or if the estimation of this parameter is more reliable than the others. As an example in our case, the weights of each parameter are assumed to be the same. Therefore, for the RRC model, the estimations of the three parameters, $C$, $R_s$ and $R_p$, contribute to a SoH indicator with the same weight of $1/3$ while for the TL model, the estimation

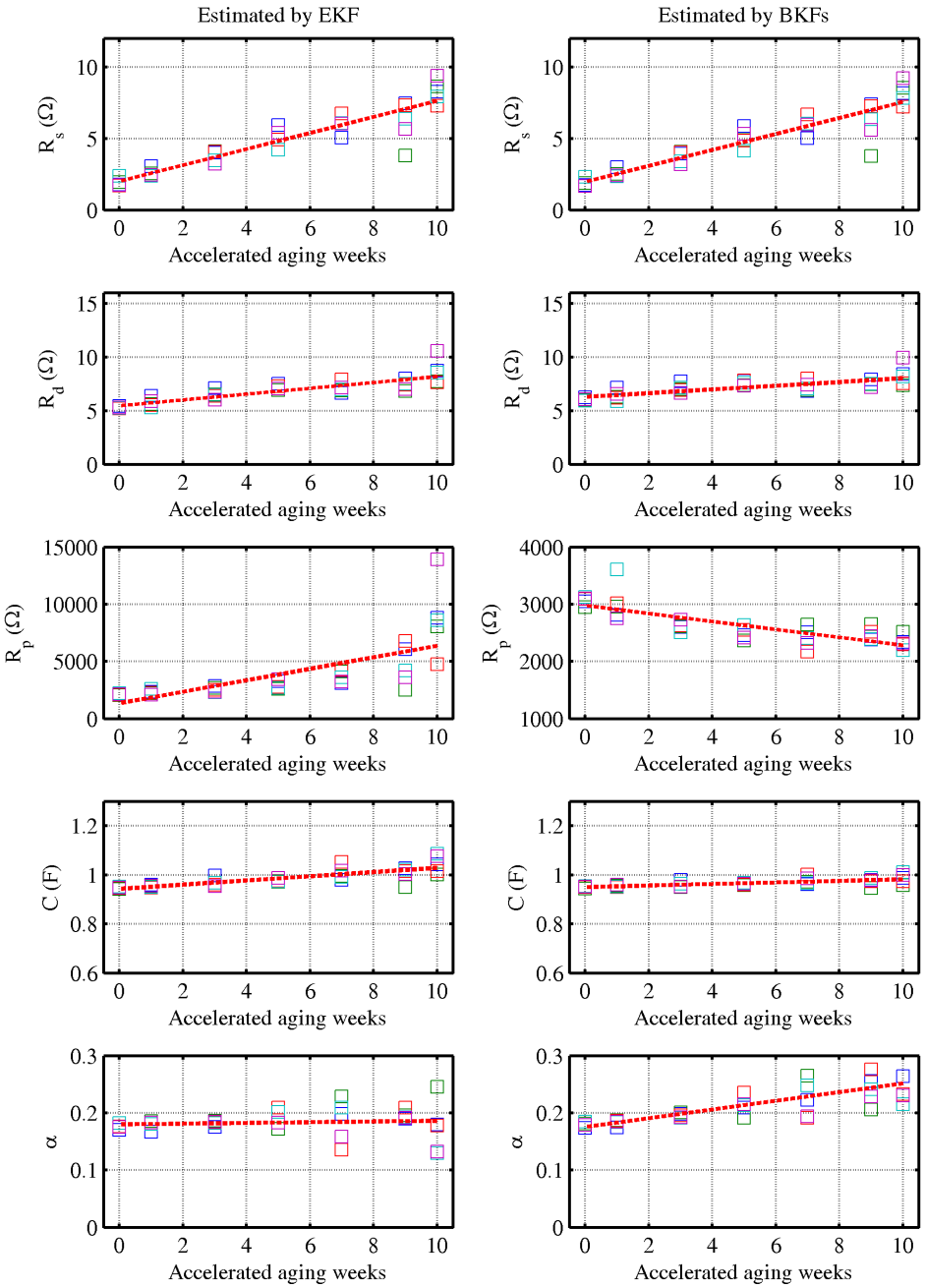


Figure 3.32: Estimation of parameters evolution of the EDLCs in successive aging periods at 0 V obtained by different estimators based on TL model (left side: EKF, right side: BKFs).

of the five parameters, $C$, $R_s$, $R_d$, $R_p$ and $\alpha$ are assumed to have the same weight of $1/5$.

Fig. 3.33 shows the SoH estimation of an EDLC during the accelerated aging experiment. The dashed lines are the linear fitting of the SoH evolutions. For the RRC and TL models, the SoH evolution with the first definition takes the evolution of several parameters into account and thus provides a quite linear decay. The one with the second SoH definition only considers one parameter which is the fastest to reach its end of life criterion. The abnormal value at the first aging week in this case is probably caused by the high inaccuracy of the $R_s$ estimation due to the large dispersion. Compared to the RRC model, the SoH estimations based on the TL model are better with a smaller estimation difference between both observers.

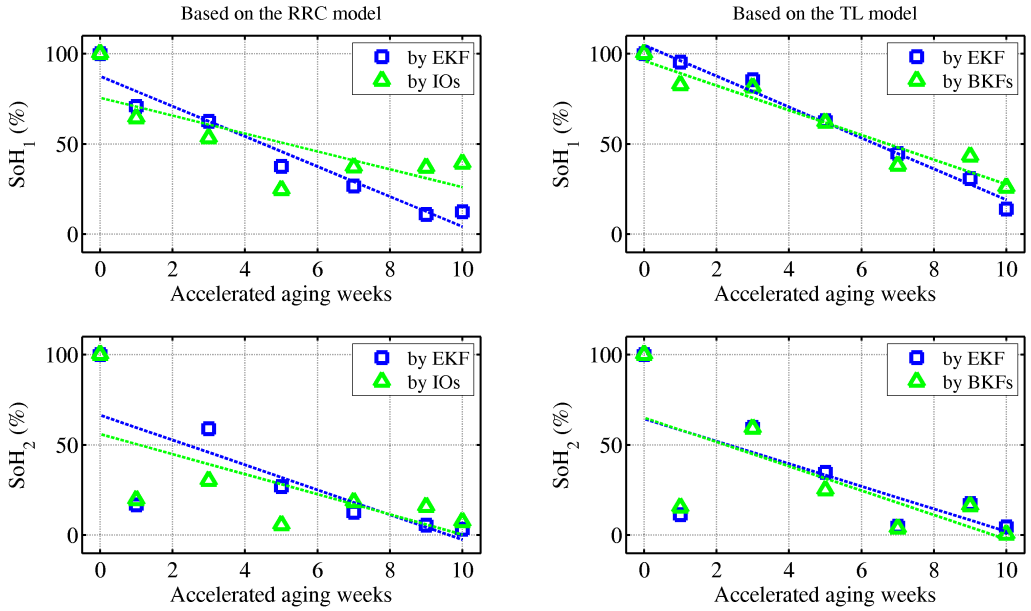


(a) Based on the RRC model (b) Based on the TL model

Figure 3.33: SoH estimations of an EDLC during aging @ 2.5 V, $60°C$.

In this chapter, different observers have been designed based on two models.

| | RRC model | | TL model | |
|---|---|---|---|---|
| | EKF | IOs | EKF | BKFs |
| Computational cost (number of differential equations) | 14 | 10 | 54 | 45 |
| Tuning parameters | 10 | 2 | 45 | 36 |
| Small output error | ★ ★ ☆ | ★ ★ ☆ | ★ ★ ★ | ★ ★ ★ |
| SoH indication ability | ★ ★ ☆ | ★ ★ ☆ | ★ ★ ★ | ★ ★ ★ |

Figure 3.34: Observers comparison based on the RRC model and the TL model.

To determine which observer based on which model can be considered as a good choice for online aging monitoring, their complexity and performance are compared from several aspects shown in Fig. 3.34. The observers based on the TL model have higher computational cost and more tuning parameters than that based on the RRC model. But the error between the estimated output and the measured output based on the TL model is much smaller than the RRC model, because the TL model is much closer to the real EDLC. Furthermore, the SoH indication ability based on the TL model is also better. Since EKF and BKFs have a similar performance with regard to the output error and SoH indication ability, the BKFs should be preferred because of their lower computational cost and fewer tuning parameters.

# Conclusion

In this chapter, an in-situ online aging monitoring system of EDLCs is proposed. The strategy is to use model-based extended observers to estimate the EDLCs parameters evolution in real time and thus to provide a knowledge of their SoH and SoC. According to the study of several models in the previous chapter, two kinds of models are used for aging monitoring. One is the simple classical RRC model with only three parameters and the other one is a 4-th order transmission line model which is much more accurate than the previous one. Different kinds of extended observers are designed based on these two models.

For the RRC model, an EKF and IOs have been designed and compared. The simulation results prove that both observers have good dynamic performances when estimating the parameters of the simulated model. Then, they have been applied to estimate the parameters and the stored energy of a real fresh EDLC using measured current and voltage signals. Compared to the EKF, IOs has less tunning parameters and a lower computational cost which may be more attractive in an industrial application.

For the TL model, an EKF and BKFs have been designed and their performances are verified with simulated experiments. Then, both observers applied to estimate the parameters of a real fresh EDLC. The result shows that both observers succeed in estimating the parameters and the stored energy of a real EDLC in real time with a very small error between the estimated output voltage and the measured voltage. Compared to the EKF, the BKFs have lower computational cost and thus should be preferred in an aging monitoring system of an EDLC application.

At last, all the designed observers based on both models have been applied to the differently aged EDLCs in an accelerated calendar aging experiment. Both observers of each model provide similar evolutions of the parameters. These results are in accordance with the offline characterization results obtained in the first chap-

ter. Based on the estimated parameters evolution of the EDLCs aged at $2.5$ V and $60^{\circ}$ C, an example of calculating the SoH of an EDLC is given, which demonstrates that the proposed model based state observers can be used for the aging monitoring through a SoH indicator. Compared to the observers based on the RRC model, the ones based on the TL model have higher computational cost and more complicated observer tunning procedure due to the high order of the system. Nevertheless, they can provide more accurate estimations when monitoring the aging of an EDLC and thus can provide a more reliable aging indicator.

# Conclusions and perspectives

## Conclusions

The supercapacitors are becoming some of the most promising energy storage devices that can be used in a wide range of applications. But the aging of the supercapacitors may cause failures and security problems. An efficient aging monitoring system of the supercapacitors is thus essential to maintain their proper functions and to enhance the reliability and safety of their industrial applications.

The EDLCs aging can be revealed from the evolution of their parameters. Most of the existing efficient methods to characterize the EDLCs need to be operated in laboratories, using some particular signals or devices. This is obviously unpractical in most cases where the EDLCs are embedded in the application, such as an electrical vehicle. The objective of this work was to design a low-cost online EDLCs aging monitoring system that can be used in-situ without interrupting the function of the EDLCs in an application.

The aim of the first part of this thesis was to study the aging of a particular kind of EDLC (Nichicon, UM series) through offline characterization methods, to propose reliable indicators for offline aging monitoring and to provide a reference used to validate the online aging monitoring results in the third chapter. Some physical parameters of EDLCs were defined as well as their uncertainties evaluating the parameter estimation quality. The numerical results of these parameters and their uncertainties were obtained for the EDLCs in an accelerated calendar aging experiment during $10$ weeks at $60°$ and under $0$ V and $2.5$ V DC polarization. The results showed that, for the EDLCs used, the integral and differential capacitances only slightly decreased, while the series and dynamic resistances had a significant increase during aging and hence can be used as good indicators for the aging monitoring. The energy efficiency was shown to be an interesting indicator for offline aging monitoring of the tested EDLCs due to its significant decrease with aging and its voltage independent character.

The aim of the second part of the work was to look for an appropriate model for online aging monitoring of the EDLCs. The main problem when modelling an EDLC is how to find a best compromise between the complexity and the per-

formance of the model. Three criteria, the small output error, the small parameter uncertainty and the high aging diagnostic ability, have been proposed to select a good model. The parameter uncertainty are calculated based on the geometric study of the hyper-surface of the output error energy. Several models concerning the voltage dependency feature of the capacitances, the charge redistribution and the transmission line effect, have been compared according to the numerical values of the proposed criteria. The second-order transmission line model combined with a charge redistribution branch has been shown to be an appropriate model for online aging monitoring of EDLCs.

The third chapter was dedicated to the design of an in-situ online aging monitoring system of EDLCs. The online aging monitoring was realized by using real-time model-based extended observers to estimate the parameters evolution of the embedded EDLCs. First of all, an extended Kalman filter (EKF) and interconnected observers (IOs) were designed based on a simple RRC model to estimate three parameters: the series resistance, the capacitance and the parallel resistance. Secondly, an extended Kalman filter (EKF) and braided Kalman filters (BKFs) were designed based on a more accurate fourth-order transmission line model to estimate five parameters: the series resistance, the dynamic resistance, the parallel resistance, the capacitance and the voltage sensitivity coefficient. Simulation results verified the good performances of both observers in each case. Compared to the EKF, IOs for the RRC model and BKFs for the TL model have a lower computational cost and thus may be more attractive in an industrial application. These designed observers have been applied to the differently aged EDLCs and the results showed that, for the tested EDLCs, the capacitance evolved slightly with aging while the series and dynamic resistances had a significant increase. These results have been validated by comparing with the offline characterization results in the first chapter. An example of calculating the SoH indicator has been given at last. Such a SoH indicator using the results of an online state observer can be easily implemented in an EDLC application, for example, by installing a low-cost preprogrammed chip.

# Perspectives

In this thesis, online aging monitoring systems of EDLCs have been preliminarily successfully designed. But there are still large possibilities to improve and to continue this work in the future. The perspectives are addressed to both theoretical and practical parts.

– *Theoretical improvement*

- The second chapter has selected a ”best” model for online aging diagnosis, which was a second-order transmission line model combined with a charge redistribution branch. But this model was not adopted to design an online state observer in the third chapter because of the lack of time. In the future, online state observers could be designed based on this suggested model to see if better aging monitoring results can be obtained.

- Some of the parameters of EDLCs are voltage and temperature dependent. The models studied in this thesis only had the capacitance depending on the voltage. A more comprehensive model taking the temperature dependent feature into account could be developed and used for online aging monitoring of EDLCs.

– *Practical improvement*

- The EDLCs studied in this thesis was not a very typical one with a small capacitance (1 F). The capacitance of this type of EDLCs seemed not evolve much with aging which was different from other high capacitance EDLCs. One can apply the same model based real-time state observers to a more typical kind of EDLCs to furthermore ensure the performance of the designed observers and to propose a SoH indicator for these EDLCs.

- The designed online observers in this work were simulated through MATLAB/SIMULINK using the recorded current and voltage signals. In the future, it could be considered to realize the implementation of the observers in an experimental platform. The algorithms of the online parameter estimation could be downloaded to a low-cost chip and then integrated into an EDLC charging/discharging experimental system.

- Instead of an accelerated calendar aging experiment, a cycling aging experiment could be considered in order to check the performance of the designed aging monitoring system.

# Contents

# List of Tables

# List of Figures

# Bibliography


[1] B. E. Conway. *Electrochemical Supercapacitors: Scientific Fundamentals and Technological Applications*. Springer, April 1999. 5, 11, 12, 13, 15, 21, 35, 36, 61, 62, 63, 64, 170

[2] R. Kotz and M. Carlen. Principles and applications of electrochemical capacitors. *Electrochimica Acta*, 45(15):2483–2498, May 2000. 5, 12, 14, 63, 64, 102, 169

[3] A. Hammar, P. Venet, R. Lallemand, G. Coquery, and G. Rojat. Study of accelerated aging of supercapacitors for transport applications. *IEEE Transactions on Industrial Electronics*, 57(12):3972–3979, 2010. 5, 22

[4] W. Lajnef, J. M Vinassa, O. Briat, H. El Brouji, S. Azzopardi, and E. Woirgard. Quantification of ageing of ultracapacitors during cycling tests with current profile characteristics of hybrid and electric vehicles applications. *IET Electric Power Applications*, 1(5):683–689, 2007. 5, 25

[5] P. Azaïs, L. Duclaux, P. Florian, D. Massiot, M. Lillo-Rodenas, A. Linares-Solano, J. Peres, C. Jehoulet, and F. Béguin. Causes of supercapacitors ageing in organic electrolyte. *Journal of Power Sources*, 171(2):1046–1053, September 2007. 5, 17

[6] R. Chaari, O. Briat, J. Y. Deletage, E. Woirgard, and J. M. Vinassa. How supercapacitors reach end of life criteria during calendar life and power cycling tests. *Microelectronics Reliability*, 51(9–11):1976–1979, September 2011. 5, 17, 22

[7] R. Kotz, P. W. Ruch, and D. Cericola. Aging and failure mode of electrochemical double layer capacitors during accelerated constant load tests. *Journal of Power Sources*, 195(3):923–928, February 2010. 5, 17, 27

[8] M. Ortuzar, J. Moreno, and J. W. Dixon. Report on fire event originated by ultracapacitors in an experimental electric vehicle. Paris, October 2004. 6, 17

[9] N. Rizoug, P. Bartholomeus, and P. Le Moigne. Study of the ageing process of a supercapacitor module using direct method of characterization. *IEEE Transactions on Energy Conversion*, 27(2):220–228, June 2012. 6, 100

[10] M. S. Halper and J. C. Ellenbogen. Supercapacitors: a brief overview. Technical Report 15055224, MITRE Coporation, USA, March 2006. 11

[11] Y. Zhang, H. Feng, X. Wu, L. Wang, A. Zhang, T. Xia, H. Dong, X. Li, and L. Zhang. Progress of electrochemical capacitor electrode materials: A review. *International Journal of Hydrogen Energy*, 34(11):4889–4899, June 2009. 11, 12, 13, 14, 15, 167

[12] P. Sharma and T. S. Bhatti. A review on electrochemical double-layer capacitors. *Energy Conversion and Management*, 51(12):2901–2912, December 2010. 12, 13

[13] G. Wang, L. Zhang, and J. Zhang. A review of electrode materials for electrochemical supercapacitors. *Chemical Society Reviews*, 41(2):797–828, January 2012. 12, 15, 16

[14] A. Schneuwly and R. Gallay. Properties and applications of supercapacitors from the state-of-the-art to future trends. Germany, 2000. 13, 14, 15, 167

[15] Vasile V. N. Obreja. On the performance of supercapacitors with electrodes based on carbon nanotubes and carbon activated material–a review. *Physica E: Low-dimensional Systems and Nanostructures*, 40(7):2596–2605, May 2008. 13

[16] S. Atcitty. Electrochemical capacitor characterization for electric utility applications, November 2006. 13

[17] V. A. Shah, J. A. Joshi, R. Maheshwari, and Ranjit Roy. Review of ultracapacitor technology and its applications. pages 142–147, Bombay, December 2008. 14, 15, 16, 167

[18] J. R. Miller and A. F. Burke. Electrochemical capacitors challenges and opportunities for real world applications. 14, 15, 167

[19] S. Trieste. *Modélisation et optimisation technico-économique d'une chaîne de conversion et de stockage d'énergie d'un navire électrique zéro émission*. Doctoral thesis, Université de Nantes, Saint Nazaire, June 2013. 15

[20] P. K. Kozhiparambil. *Development of a Supercapacitor based Surge Resistant Uninterruptible Power Supply*. Thesis, University of Waikato, March 2011. 16

[21] Maxwell Technologies. White paper: bridge power. 16

[22] R. Sadoun, N. Rizoug, P. Bartholumeus, B. Barbedette, and P. LeMoigne. Sizing of hybrid supply (battery-supercapacitor) for electric vehicle taking into account the weight of the additional buck-boost chopper. In *2012 First International Conference on Renewable Energies and Vehicular Technology (REVET)*, pages 8–14, March 2012. 16

[23] P. Thounthong, V. Chunkag, P. Sethakul, B. Davat, and M. Hinaje. Comparative study of fuel-cell vehicle hybridization with battery or supercapacitor storage device. *IEEE Transactions on Vehicular Technology*, 58(8):3892–3904, October 2009. 16

[24] R. Carter, A Cruden, and P.J. Hall. Optimizing for efficiency or battery life in a battery/supercapacitor electric vehicle. *IEEE Transactions on Vehicular Technology*, 61(4):1526–1533, May 2012. 16

[25] M. Uzunoglu O C Onar. Dynamic modeling, design and simulation of a wind/fuel cell/ultra-capacitor-based hybrid power generation system. *Journal of Power Sources*, 161:707–722, 2006. 16, 61

[26] P. Thounthong, S. Sikkabut, P. Sethakul, and B. Davat. Control algorithm of renewable energy power plant supplied by fuel cell/solar cell/ supercapacitor power source. In *Power Electronics Conference (IPEC), 2010 International*, pages 1155–1162, June 2010. 16

[27] A. M. Gee, F. V. P. Robinson, and R. W. Dunn. Analysis of battery lifetime extension in a small-scale wind-energy system using supercapacitors. *IEEE Transactions on Energy Conversion*, 28(1):24–33, March 2013. 16

[28] M. E. Choi, S. W. Kim, and S. W. Seo. Energy management optimization in a battery/supercapacitor hybrid energy storage system. *IEEE Transactions on Smart Grid*, 3(1):463–472, March 2012. 16

[29] Y. Wu and H. Gao. Optimization of fuel cell and supercapacitor for fuel-cell electric vehicles. *IEEE Transactions on Vehicular Technology*, 55(6):1748–1755, November 2006. 16

[30] M. Zhu, C. J. Weber, Y. Yang, M. Konuma, U. Starke, K. Kern, and A. M. Bittner. Chemical and electrochemical ageing of carbon materials used in supercapacitor electrodes. *Carbon*, 46(14):1829–1840, November 2008. 17

[31] T. Umemura, Y. Mizutani, T. Okamoto, T. Taguchi, K. Nakajima, and K. Tanaka. Life expectancy and degradation behavior of electric double layer capacitor part i. In *Proceedings of the 7th International Conference on Properties and Applications of Dielectric Materials, 2003*, volume 3, pages 944–948 vol.3, June 2003. 17

[32] P. Kreczanik, P. Venet, A. Hijazi, and G. Clerc. Study of supercapacitor aging and lifetime estimation according to voltage, temperature, and RMS current. *IEEE Transactions on Industrial Electronics*, 61(9):4895–4902, September 2014. 17, 22

[33] V. Lystianingrum, V.G. Agelidis, and B. Hredzak. State of health and life estimation methods for supercapacitors. In *Power Engineering Conference (AUPEC), 2013 Australasian Universities*, pages 1–7, September 2013. 17

[34] A. Hammar, P. Venet, R. Lallemand, G. Coquery, and G. Rojat. Study of accelerated aging of supercapacitors for transport applications. *IEEE Transactions on Industrial Electronics*, 57(12):3972–3979, 2010. 17, 67, 68, 170

[35] R. German, P. Venet, A. Sari, O. Briat, and J.-M. Vinassa. Improved supercapacitor floating ageing interpretation through multipore impedance model parameters evolution. *IEEE Transactions on Power Electronics*, 29(7):3669–3678, July 2014. 17

[36] Maxwell. Application notes - life duration estimation. 18

[37] Maxwell. Representative test procedure for customer evaluations. 21, 24, 169

[38] U. Retter and H. Lohse. Electrochemical impedance spectroscopy. In *Electroanalytical Methods*, Springer-Verlag, pages 159–177. 2nd edition, 2010. 22, 25

[39] A. J. Bard and L. R. Faulkner. *Electrochemical Methods: Fundamentals and Applications*. Wiley, December 2000. 22, 25

[40] Z. Shi, F. Auger, E. Schaeffer, and P. Guillemet. Evaluation métrologique des techniques de caractérisation hors-ligne des supercondensateurs. *Instrumentation, Mesure, Métrologie*, 14(1):31–46, 2014. 22, 36, 38, 105

[41] International Electrotechnical Commission. International standard IEC 62391, fixed electric double layer capacitors for use in electronic equipment, 2006. 22

[42] R. German, P. Venet, A. Sari, O. Briat, and J.M. Vinassa. Interpretation of electrochemical double layer capacitors (supercapacitors) floating ageing by multi-pore model. In *IPEC, 2012 Conference on Power Energy*, pages 218–223, 2012. 22

[43] S. Buller, E. Karden, D. Kok, and R.W. De Doncker. Modeling the dynamic behavior of supercapacitors using impedance spectroscopy. *IEEE Transactions on Industry Applications*, 38(6):1622–1626, November 2002. 22, 63, 64, 66, 170

[44] E.-H. El Brouji, O. Briat, J. M Vinassa, N. Bertrand, and E. Woirgard. Impact of calendar life and cycling ageing on supercapacitor performance. *IEEE Transactions on Vehicular Technology*, 58(8):3917–3929, October 2009. 22, 63

[45] International Electrotechnical Commission. Fixed electric double-layer capacitors for use in electronic equipment - part 1: Generic specification, 2006. 22, 23, 167, 169

[46] Nichicon Corporation. Electric double layer capacitors EVerCAP. 23

[47] P. Kreczanik, C. Matin, P. Venet, G. Clerc, G. Rojat, and Y. Zitouni. Constant power cycling for accelerated ageing of supercapacitors. In *13th European Conference on Power Electronics and Applications, 2009. EPE '09*, pages 1–10, 2009. 25, 100

[48] Autolab Metrohm. Electrochemical impedance spectroscopy (EIS ), 2011. 25

[49] A. Lasia. Electrochemical impedance spectroscopy and its applications. volume 32, pages 143–248, New York, 1999. 25

[50] R. M. Nelms, D. R. Cahela, and B. J. Tatarchuk. Modeling double-layer capacitor behavior using ladder circuits. *IEEE Transactions on Aerospace and Electronic Systems*, 39(2):430–438, April 2003. 26

[51] R. M. Nelms, D. R. Cahela, R. L. Newsom, and B. J. Tatarchuk. A comparison of two equivalent circuits for double-layer capacitors. In *Applied Power Electronics Conference and Exposition, 1999. APEC '99. Fourteenth Annual*, volume 2, pages 692–698 vol.2, March 1999. 26, 61

[52] L. G. Babe. *Nonlinear dynamic per-unit models for electrochemical energy systems : application to a hardware-in-the-loop hybrid simulation*. PhD thesis, Universidad carlos de madrid, Leganes, 2009. 26, 169

[53] P. Taberna, C. Portet, and P. Simon. Electrode surface treatment and electrochemical impedance spectroscopy study on carbon/carbon supercapacitors. *Applied Physics A*, 82(4):639–646, 2006. 27

[54] H. Gualous, M.B. Camara, B. Boudrat, R. Gallay, and B. Dakyo. Supercapacitor characterization for electric vehicle applications. In *2013 Fourth International Conference on Power Engineering, Energy and Electrical Drives (POWERENG)*, pages 1591–1596, May 2013. 27

[55] W. Lajnef, J. M. Vinassa, O. Briat, S. Azzopardi, and E. Woirgard. Characterization methods and modelling of ultracapacitors for use as peak power sources. *Journal of Power Sources*, 168(2):553–560, June 2007. 27, 30, 65

[56] BioLogic. EC-lab software: Techniques and applications, August 2013. 30

[57] H. Wang and L. Pilon. Reply to comments on "intrinsic limitations of impedance measurements in determining electric double layer capacitances" by h. wang, l. pilon [electrochimica acta 63 (2012) 55]. *Electrochimica Acta*, 76:529–531, August 2012. 30

[58] E. Barsoukov and J. Macdonald. *Impedance Spectroscopy: Theory, Experiment, and Applications*. John Wiley & Sons, April 2005. 35

[59] Joint Committee for Guides in Metrology. JCGM 104: Evaluation of measurement data - an introduction to the "guide to the expression of uncertainty

in measurement" and related documents. Technical report, JCGM, 2009. 39, 40

[60] Joint Committee for Guides in Metrology. JCGM 200: International vocabulary of metrology - basic and general concepts and associated terms (VIM) 3rd edition. Technical report, JCGM, 2012. 39, 40

[61] A. Williams S. R.L. Ellison. *Quantifying Uncertainty in Analytical Measurement (Third Edition)*. 2012. 39, 40

[62] E. Walter and L. Pronzato. *Identification of parametric models from experimental data*. Springer, 1997. 59, 60, 69

[63] L. Ljung. *System Identification: Theory for the User*. Pearson Education Canada, 1987. 59, 119

[64] M. Mensler. *Analyse et ètude comparative de mèthodes d'identification des systèmes à représentation continue : développement d'une boite à outils logicielle*. Doctoral thesis, Université de Nancy, Nancy, January 1999. 59

[65] J. C. Trigeassou. *Electrical Machines Diagnosis*. John Wiley & Sons, February 2013. 59, 69

[66] C. Huang. *Planification d'experiences pour la discrimination entre structures de modeles*. Doctoral thesis, Université Paris 11, Paris, 1991. 60

[67] J. Richalet, A. J. Rault, and R. Pouliquen. *Identification des processus par la méthode du modèle*. Gordon & Breach, 1971. 60, 69, 73, 75

[68] R. L. Spyker and R. M. Nelms. Classical equivalent circuit parameters for a double-layer capacitor. *IEEE Transactions on Aerospace and Electronic Systems*, 36(3):829–836, July 2000. 61

[69] D. Linzen, S. Buller, E. Karden, and R.W. De Doncker. Analysis and evaluation of charge-balancing circuits on performance, reliability, and lifetime of supercapacitor systems. *IEEE Transactions on Industry Applications*, 41(5):1135–1141, September 2005. 61

[70] C. T. Goh and A. Cruden. Automated high current cycling test system for supercapacitor characterisation. In *2012 International Symposium on Power Electronics, Electrical Drives, Automation and Motion (SPEEDAM)*, pages 748–753, June 2012. 61

[71] R. de Levie. On porous electrodes in electrolyte solutions: I. capacitance effects. *Electrochimica Acta*, 8(10):751–780, October 1963. 62, 64, 170

[72] E. Naswali. *Modeling and experimental validation of supercapacitors for use in an in-lab grid developed for wind integration applications*. Master thesis, Oregon State University, July 2011. Graduation date: 2012. 63

[73] H. El Brouji, J.-M. Vinassa, O. Briat, N. Bertrand, and E. Woirgard. Ultracapacitors self discharge modelling using a physical description of porous electrode impedance. In *IEEE Vehicle Power and Propulsion Conference, 2008. VPPC '08*, pages 1–6, September 2008. 64

[74] O. Bohlen, J. Kowal, and D. U. Sauer. Ageing behaviour of electrochemical double layer capacitors: Part i. experimental study and ageing model. *Journal of Power Sources*, 172(1):468–475, October 2007. 64, 65

[75] L. Du. Study on supercapacitor equivalent circuit model for power electronics applications. In *2009 2nd International Conference on Power Electronics and Intelligent Transportation System (PEITS)*, volume 2, pages 51–54, December 2009. 65

[76] Y. Y. Yao, D.L. Zhang, and D.G. Xu. A study of supercapacitor parameters and characteri stics. In *International Conference on Power System Technology, 2006. PowerCon 2006*, pages 1–4, October 2006. 65

[77] O. Bohlen, J. Kowal, and D. U. Sauer. Ageing behaviour of electrochemical double layer capacitors: Part II. lifetime simulation model for dynamic applications. *Journal of Power Sources*, 173(1):626–632, November 2007. 65

[78] N. Bertrand, J. Sabatier, O. Briat, and J. M Vinassa. Embedded fractional nonlinear supercapacitor model and its parametric estimation method. *IEEE Transactions on Industrial Electronics*, 57(12):3991–4000, 2010. 65, 100

[79] L. Zubieta and Richard Bonert. Characterization of double-layer capacitors for power electronics applications. *IEEE Transactions on Industry Applications*, 36(1):199–205, January 2000. 65, 66, 170

[80] E. Tironi and V. Musolino. Supercapacitor characterization in power electronic applications: Proposal of a new model. In *2009 International Conference on Clean Electrical Power*, pages 376–382, June 2009. 66

[81] R. German, P. Venet, A. Sari, O. Briat, and J. Vinassa. Improved supercapacitor floating ageing interpretation through multi-pore impedance model parameters evolution. *IEEE Transactions on Power Electronics*, Early Access Online, 2013. 67

[82] V. Musolino, L. Piegari, and E. Tironi. New full-frequency-range supercapacitor model with easy identification procedure. *IEEE Transactions on Industrial Electronics*, 60(1):112–120, January 2013. 67, 68, 170

[83] D. Marquardt. An algorithm for least-squares estimation of nonlinear parameters. *Journal of the Society for Industrial and Applied Mathematics*, 11(2):431–441, June 1963. 73

[84] R. Chaari, O. Briat, J.-Y. Deletage, R. Lallemand, J. Kauv, G. Coquery, and J. M Vinassa. Ageing quantification of supercapacitors during power cycling using online and periodic characterization tests. In *2011 IEEE Vehicle Power and Propulsion Conference (VPPC)*, pages 1–5, 2011. 100

[85] W. Lajnef, J. M. Vinassa, O. Briat, H. El Brouji, and E. Woirgard. Monitoring fading rate of ultracapacitors using online characterization during power cycling. *Microelectronics Reliability*, 47(9–11):1751–1755, September 2007. 100

[86] N. Rizoug, P. Bartholomeus, and P. Le Moigne. Modeling and characterizing supercapacitors using an online method. *IEEE Transactions on Industrial Electronics*, 57(12):3980–3990, December 2010. 100

[87] A. Oukaour, B. Tala-Ighil, M. AlSakka, H. Gualous, R. Gallay, and B. Boudart. Calendar ageing and health diagnosis of supercapacitor. *Electric Power Systems Research*, 95:330–338, February 2013. 100

[88] A. Eddahech, M. Ayadi, O. Briat, and J. M. Vinassa. Online parameter identification for real-time supercapacitor performance estimation in automotive applications. *International Journal of Electrical Power & Energy Systems*, 51:162–167, October 2013. 100, 101

[89] C. Chiang, J. Yang, and W. Cheng. Temperature and state-of-charge estimation in ultracapacitors based on extended Kalman filter. *Journal of Power Sources*, 234:234–243, July 2013. 100

[90] C. H. Wu, Y. H. Hung, and C. W. Hong. On-line supercapacitor dynamic models for energy conversion and management. *Energy Conversion and Management*, 53(1):337–345, January 2012. 101

[91] H. Farsi and F. Gobal. Artificial neural network simulator for supercapacitor performance prediction. *Computational Materials Science*, 39(3):678–683, May 2007. 101

[92] J. Kim and B. H Cho. State-of-charge estimation and state-of-health prediction of a li-ion degraded battery based on an EKF combined with a per-unit system. *IEEE Transactions on Vehicular Technology*, 60(9):4249–4260, November 2011. 101

[93] M. Gholizadeh and F.R. Salmasi. Estimation of state of charge, unknown nonlinearities, and state of health of a lithium-ion battery based on a comprehensive unobservable model. *IEEE Transactions on Industrial Electronics*, 61(3):1335–1344, March 2014. 101

[94] R. Hermann and Arthur J. Krener. Nonlinear controllability and observability. *IEEE Transactions on Automatic Control*, 22(5):728–740, October 1977. 105, 106, 107

[95] J. L. Casti. *Nonlinear system theory*, volume 175 of *Mathematics in science and engineering*. Academic Press, February 1985. 105

[96] C. Letellier, L. A. Aguirre, and J. Maquet. Relation between observability and differential embeddings for nonlinear dynamics. *Physical Review E*, 71(6):066213, June 2005. 106

[97] T. Saheb. *Estimation de l'état des systèmes non linéaires: application à la machine asynchrone sans capteur mécanique*. PhD thesis, Université de Nantes, Nantes, October 2004. 107

[98] D. Diallo, A Arias, and J. Cathelin. An inverter dead-time feedforward compensation scheme for PMSM sensorless drive operation. In *2014 International Conference on Green Energy*, pages 296–301, March 2014. 107

[99] A Akrad, M. Hilairet, and D. Diallo. Design of a fault-tolerant controller based on observers for a PMSM drive. *IEEE Transactions on Industrial Electronics*, 58(4):1416–1427, April 2011. 107

[100] D. G. Luenberger. Observing the state of a linear system. *IEEE Transactions on Military Electronics*, 8(2):74–80, April 1964. 108

[101] D. G. Luenberger. Observers for multivariable systems. *IEEE Transactions on Automatic Control*, 11(2):190–197, April 1966. 108

[102] D. G. Luenberger. An introduction to observers. *IEEE Transactions on Automatic Control*, 16(6):596–602, December 1971. 109

[103] M. S. Grewal and A. P. Andrews. *Kalman Filtering: Theory and Practice Using MATLAB*. John Wiley & Sons, September 2011. 109, 110, 120, 139

[104] F. Auger, M. Hilairet, J.M. Guerrero, E. Monmasson, T. Orlowska-Kowalska, and S. Katsura. Industrial applications of the Kalman filter: A review. *IEEE Transactions on Industrial Electronics*, 60(12):5458–5471, December 2013. 110, 120, 139

[105] S. Bittanti and M. Savaresi. On the parametrization and design of an extended Kalman filter frequency tracker. *IEEE Trans. on Automatic Control*, 45(9):1718–1724, September 2000. 110

[106] M. Zeitz. The extended luenberger observer for nonlinear systems. *Systems & Control Letters*, 9(2):149–156, August 1987. 111

[107] J. J. Kappl. Nonlinear estimation via Kalman filtering. *IEEE Transactions on Aerospace and Electronic Systems*, AES-7(1):79–84, January 1971. 111, 112

[108] B. De Fornel and J. Louis. *Electrical Actuators: Applications and Performance*. John Wiley & Sons, March 2013. 112

[109] H. W. Bode. *Network Analysis and Feedback Amplifier Design*. Van Nostrand, 1945. 114

[110] I. M. Horowitz. Fundamental theory of automatic linear feedback control systems. *IRE Transactions on Automatic Control*, 4(3):5–19, December 1959. 114

[111] R. Rohrer and M. Sobral. Sensitivity considerations in optimal system design. *IEEE Transactions on Automatic Control*, 10(1):43–48, January 1965. 114

[112] M. Fink, J. J. Batzel, and H. Tran. A respiratory system model: Parameter estimation and sensitivity analysis. *Cardiovascular Engineering*, 8(2):120–134, June 2008. 114

[113] G. Besancon, J. De Leon-Morales, and O. H. Guevara. On adaptive observers for state affine systems. *International journal of Control*, 79(06):581–591, 2006. 121

[114] G. Besancon and H. Hammouri. On observer design for interconnected systems. *Journal of Mathematical Systems, Estimation and Control*, 8(3):1–25, 1998. 121

[115] M. A. Hamida, J. De Leon, A. Glumineau, and R. Boisliveau. An adaptive interconnected observer for sensorless control of PM synchronous motors with online parameter identification. *IEEE Transactions on Industrial Electronics*, 60(2):739–748, February 2013. 121, 122

[116] H. Hammouri and J. de Leon Morales. Observer synthesis for state-affine systems. In , *Proceedings of the 29th IEEE Conference on Decision and Control, 1990*, pages 784–785 vol.2, December 1990. 122

[117] A. El Magri, F. Giri, G. Besançon, A. El Fadili, L. Dugard, and F. Z. Chaoui. Sensorless adaptive output feedback control of wind energy systems with PMS generators. *Control Engineering Practice*, 21(4):530–543, April 2013. 122

[118] R. Bulirsch and J. Stoer. Numerical treatment of ordinary differential equations by extrapolation methods. *Numerische Mathematik*, 8(1):1–13, March 1966. 125

[119] W. H. Press, S. A. Teukolsky, and W. T. Vetterling. *Numerical Recipes 3rd Edition: The Art of Scientific Computing*. Cambridge University Press, Cambridge, 3 edition edition, September 2007. 125

[120] T. Zhang, A. Shen, and F. Auger. An advanced simulation of a PMSM control system based on a bulirsch-stoer implementation with an arduino due. In *2013 IEEE 4th International Conference on Electronics Information and Emergency Communication (ICEIEC)*, pages 197–200, November 2013. 125

[121] C. Letellier, L. Aguirre, and J. Maquet. How the choice of the observable may influence the analysis of nonlinear dynamical systems. *Communications in Nonlinear Science and Numerical Simulation*, 11(5):555–576, August 2006. 138

[122] X. Wang, P. Cui, and H. Cui. Local observability of nonlinear systems based on linearization. In *2nd International Symposium on Systems and Control in Aerospace and Astronautics, 2008. ISSCAA 2008*, pages 1–4, December 2008. 138

[123] M. Barut, S. Bogosyan, and M. Gokasan. Experimental evaluation of braided EKF for sensorless control of induction motors. *IEEE Transactions on Industrial Electronics*, 55(2):620–632, 2008. 142

[124] Maxwell Technologies. Product guide - maxwell technologies BOOSTCAP ultracapacitors, 2009. 156

l'université nantes angers le mans
COMMUNAUTÉ D'UNIVERSITÉS ET ÉTABLISSEMENTS

UNIVERSITÉ DE NANTES

# Thèse de Doctorat

Zhihao SHI

## Modélisation et surveillance en ligne du vieillissement de supercondensateurs

## Modeling and online aging monitoring of supercapacitors

**Résumé**

Cette thèse a pour objectif de concevoir des systèmes de surveillance en ligne du vieillissement de supercondensateurs, utilisables dans des applications industrielles de stockage d'énergie. Un vieillissement calendaire accéléré a d'abord été effectué sur une population de 100 supercondensateurs Nichicon (1F /2.7V) du commerce. Ces supercondensateurs ont ensuite été caractérisés par des méthodes hors ligne à chaque phase de vieillissement et l'évolution de leurs paramètres caractéristiques et leurs incertitudes sont analysées et discutées. Pour surveiller leur état de santé, des modèles dynamiques sont ensuite comparés selon des critères proposés et un bon modèle est retenu pour faire de la surveillance en ligne. Différents types d'observateurs, tels que des observateurs de Kalman et des observateurs interconnectés, sont enfin conçus en s'appuyant sur deux modèles, un modèle RRC du premier-ordre et un modèle de ligne de transmission du quatrième ordre, afin d'estimer les paramètres d'un supercondensateur en temps réel et sur son site d'application. Les résultats expérimentaux obtenus par les observateurs proposés dans cette thèse montrent une bonne estimation de l'évolution des paramètres, comparable avec les résultats des méthodes de caractérisation hors ligne.

**Mots clés**

Supercondensateurs, vieillissement, état de santé, état de charge, caractérisation hors ligne, modélisation, identification, surveillance en ligne, observateurs d'état, observateurs de Kalman, observateurs interconnectés.

**Abstract**

The aim of this thesis is to design online aging monitoring systems for supercapacitors that could be used for industrial energy storage applications. To investigate the supercapacitors' aging, accelerated calendar aging experiments have been first carried out on Nichicon 1F/2.7V commercial EDLCs. Offline characterizations methods have been used at each aging phase and the parameters evolution and their uncertainties during the aging process are analyzed and discussed. To provide an online estimation of the state of health of an EDLC, different model structures are first compared according to some proposed optimal criteria, and an appropriate model is finally suggested for the online aging monitoring of EDLCs. Different nonlinear state observers, such as Kalman observers and interconnected observers, are designed to estimate EDLCs' parameters in real time. They are based on two kinds of EDLC models: a first-order RRC model and a fourth-order transmission line model. Experimental results demonstrate a good estimation of the parameters evolution provided by the proposed online observers, in accordance with that obtained by offline methods.

**Key Words**

Supercapacitors, aging, state of health, offline characterization, modeling, identification, online monitoring, state observers, Kalman filters, interconnected observers, braided Kalman filters.